Etude expérimentale du pouvoir d'arrêt des ions dans la matière tiède et dense: mesure de la distribution des états de charges d'un faisceau d'ions émergeant de la matière tiède et dense

Maxence Gauthier

THÈSE DE DOCTORAT

présentée à l'École Polytechnique pour obtenir le grade de

DOCTEUR DE L'ÉCOLE POLYTECHNIQUE

Discipline : physique des plasmas

Par

Maxence GAUTHIER

Experimental Study of Ion Stopping Power in Warm Dense Matter: Charge-state Distribution Measurements of Ions Leaving Warm Dense Matter

Soutenue le 6 Août 2013 devant le jury composé de :

M. Robert CAUBLE	Examinateur
M. Gérald FAUSSURIER	Directeur de thèse
M. Julien FUCHS	Directeur de thèse
M. Gilles MAYNARD	Rapporteur
M. Jose Manuel PERLADO	Président du jury
M. Patrick RENAUDIN	Rapporteur

Remerciement / Acknowledgement

Les personnes que je souhaiterai remercier étant pour la plupart francophones d'origine ou d'adoption, j'ai l'outrecuidance d'écrire ces quelques remerciements dans ma langue maternelle. Lecteur adepte de la langue de la tragédie plutôt que de celle de la farce rassure-toi, ces quelques pages de français seront les seules du manuscrit à l'être (même si, il me faut l'admettre, mon anglais a parfois une fâcheuse tendance à traverser la manche).

En préambule à ce mémoire, je souhaite adresser mes remerciements les plus sincères aux personnes qui m'ont apporté leur aide et qui ont contribué à l'élaboration de ce mémoire ainsi qu'à la réussite de cette formidable aventure que constitue la thèse.

Je tiens tout d'abord à remercier François Amiranoff et Daniel Vanderhaegen, les directeurs respectifs du LULI et du DPTA pour leur accueil au sein de leur unité et leur soutien indispensable à la bonne conduite de ma thèse. Un grand merci à l'ensemble du personnel administratif du LULI, du CEA mais aussi de l'école doctorale pour leur écoute et aide afin de nous simplifier les nombreuses démarches que nous sommes amenées à effectuer tout au long de la thèse.

J'exprime également toute ma reconnaissance et gratitude à l'égard des équipes techniques (laser et expérience) du LULI et du JLF pour leurs efforts à nous garantir les meilleures conditions afin de réaliser nos expériences et ainsi de nous permettre de triompher des nombreuses chausse-trappes que nous réserve le tumultueux couple laser-plasmas. Ma pensée va en particulier à ceux que j'ai côtoyés le plus souvent, Sandra, Edouard, Harumi, Julie, Mathieu, Olivier, Emilie, Fabien, Luc, Johanna.

Je remercie les membres du jury pour avoir lu avec attention mon mémoire et s'être déplacé à Paris en plein mois d'Août afin de juger mon travail de recherche. Les rapports élogieux et constructifs, ainsi que les questions posées lors de la soutenance, m'ont permis d'avoir une meilleure idée de la portée de mes recherches, mais surtout des perspectives qu'elles offrent.

Je tiens à exprimer ma profonde reconnaissance à mes deux directeurs de thèse. A travers les nombreuses expériences auxquelles j'ai participé pendant ma thèse, Julien et son enthousiasme à toute épreuve, m'a permis d'acquérir les bases, si ce n'est plus, de ce qui fait un bon chercheur-expérimentateur. Très bon pédagogue, il a toujours été à mon écoute que cela soit pour expliquer des méthodes expérimentales et d'analyse, ou bien pour rassurer quand les résultats se faisaient durs à extraire. Autant la partie expérimentale fut le domaine de Julien, autant la partie théorique fut celui de Gérald. Il sut captiver mon intérêt sur nombre de sujets théoriques et répondre aux interrogations de l'ignare que j'étais. Les longues discussions que nous eûmes d'expérimentateur à théoricien me

furent d'un grand secours pour toucher du doigt ce qui se cache derrière le mot « pouvoir d'arrêt » et pour trouver une manière de le « manipuler » expérimentalement. Doué d'une grande rigueur, il a apporté, tout du moins je l'espère, un peu de mesure à mon enthousiasme débordant et parfois oublieux des contraintes des équations. Je tiens également à les remercier tous les deux pour leurs conseils dans la rédaction du mémoire et les corrections apportées. Vos remarques constructives m'ont permis d'améliorer substantiellement la qualité du manuscrit, mais aussi, peut-être le plus important, ma qualité de rédaction.

Un travail de recherche ne peut s'accomplir sans aide, d'autant plus quand il est en grande partie réalisée sur des installations laser d'avant-garde où le maître-mot est précision. Je tiens à remercier les chercheurs du LULI et tout particulièrement ceux avec qui j'ai travaillé: Tommaso, Jean-Raphaël, Alessandra, Sophia, Lorenzo, Patrick, le premier à s'émouvoir (à raison ?) de la santé des thésards. Je souhaiterai également remercier les personnes auprès desquelles j'ai travaillé au CEA, Christophe, Philippe, mon voisin de bureau des premiers jours, merci pour ta patience, ta bonne humeur et tes conseils avisés, Patrick et sa protégée Esther, l'autre Patrick, Laurent, et Laurence, l'intérêt porté à mon sujet de thèse, ainsi que ton soutien tout au long de ma thèse m'a touché. Merci également à tous les chercheurs et étudiants issus d'autres laboratoires avec qui j'ai collaboré et qui ont eux-aussi grandement contribué à la réussite de cette thèse. Merci tout particulièrement à: Céline, Fabien, François, Emmanuel, et Claude du CELIA, Dominique Vernhet, Emilie Lamour, Jean-Pierre Rozet de l'INSP, Tiberio et Vincent du CEA, Stéphanie, Thomas, Medhi et Fasia du CENBG, Manuela, Christian, Marco et Tomas d'Allemagne, Domenico d'Irlande (et d'Italie), Ronny, Hui, Andy, et Jim des Etats-Unis, Patti et Feliciana d'Italie.

Que ne serait une thèse sans le soutien amical et mutuel qu'il existe entre stagiaires, thésards et post-doc ? Je tiens à remercier ceux qui de collègues sont souvent passés à un statut d'ami : Motoaki, qui j'espère n'a pas trop souffert de mes cours de Français, Ana et Livia, mes prédécesseurs qui ont assisté, les premières, à mes prouesses en matière d'accélération de protons et de découpage de RCF, Anna, Sébastien, Hans Peter, Frédéric, ce passionné d'étymologie, Daniel, Mikayel, Drew, Bruno, ce gentleman révolutionnaire aux idées nouvelles dont j'ai partagé à la fois le directeur de thèse et le bureau, Floriane, celle qui partagea ma passion pour la mystérieuse patate bleue et la capricieuse mouche Binit, enfin tout le groupe de docteurs en devenir, Vincent, Clément, Anne-Claire, Marc, Laura, la touche féminine et énergique du bureau, Raphaël, Adrien, Roman, Anaïs, Claire, Clément II et Diouf. Un grand merci pour toute la sympathie, les conseils et les encouragements que vous avez pu me prodiguer.

Un merci spécial pour des amis extraordinaires, qui m'ont écouté d'une oreille attentive et compatissante avec une égale constance, aussi bien pour m'enflammer à propos de mon sujet de thèse que pour m'épancher sur les difficultés de la recherche : Pierre-Emmanuel, Julien, Cécile, Nicolas, Alan, les anciens rennais à la grande soif (de culture), Marc, koukou, Jean-marie, pupuce, Alexiss, Alexis, Vincent, Rémi, Hervé. Vos constants efforts pour me faire sortir de temps en temps de ma bulle et vos encouragements toujours renouvelés ont beaucoup compté pour moi.

Je voudrais finalement remercier profondément toute ma famille qui m'a accompagné tout au long de cette thèse comme à chaque étape de ma vie et pour qui je n'ai pas de mot assez fort pour exprimer ma gratitude.

Sur ce, place à la physique et bonne lecture à tous !

« Ce n'est pas dans la science qu'est le bonheur, mais dans l'acquisition de la science. »

Edgar Allan Poe

INDEX

INTRODUCTION

This thesis aims at exploring the stopping power properties of ions propagating in warm dense matter. We will first present the context in which this study takes place. Then, the objectives and the plan of the thesis will be presented.

Context

The broad context of this thesis lies within the scope of thermonuclear fusion research and more particularly the approach brought upon by the discovery and development of laser technology that is called inertial confinement fusion (ICF). In ICF, the pellet of combustible, composed of two isotopes of hydrogen, deuterium (^2_1H) and tritium (^3_1H), is compressed to typically 100-1000 times the solid density. For this, are used either (1) high-energy laser beams, this is the direct drive approach [1], or (2) laser-generated X-rays, this is the indirect drive approach [2]. Both heat the outer layer of the DT pellet, which then expands outward. The remainder part of the pellet is then compressed inward by the rocket-like blow-off of the hot plasma surface. This inward spherical compression of the pellet leads finally to the heating of the converging central region of the plasma, called the hot spot, to high temperature.

The fusion reactions between deuterium and tritium that occur in the hot spot release 17.6 MeV of energy per reaction in the form of fast alpha particles and neutrons:

$$^2_1H + ^3_1H \rightarrow ^4_2He\ (3.5\ MeV) + n\ (14.1\ MeV)$$

Provided the fusion reactions in the hot spot occur at a sufficient rate (which is determined by the hot spot thermodynamic conditions), these energetic particles can then deposit enough energy inside the denser and colder surrounding combustible to initiate a chain of fusion reactions that will burn the whole pellet.

This scheme could be used to produce electricity provided that the energy released by the fusion reactions is larger than the power brought to compress and ignite the combustible. To optimize the process, it is of obvious importance to determine how the produced alpha (^4_2He) deposit their energy and help to maintain a high temperature in the plasma pellet [3].

Determining accurately the stopping power of ions in dense plasmas is even more important in the context of fast ignition (FI). This approach is based on separating the compression phase and the heating phase of ICF, with a potential increase in energy gain [4, 5]. In this frame, recent publications have proposed to use short-pulse laser-accelerated ion beams to heat the pre-compressed fuel and

ignite the target [6,7] (see Figure 0-1). Indeed ions, compared to fast electrons for instance, are expected to have an excellent coupling efficiency with the fuel. This comes from the fact that they deposit their energy in a very narrow volume at the end of their range (which only depends on the ion initial energy (Bragg Peak)) and also that they can be focused into a very small spot [8, 9]. The short time duration of the short-pulse laser-produced ion beams, their laser-to-ions high energy conversion (10-12 % demonstrated) coupled with their high flux make them a suitable candidate for FI [10].

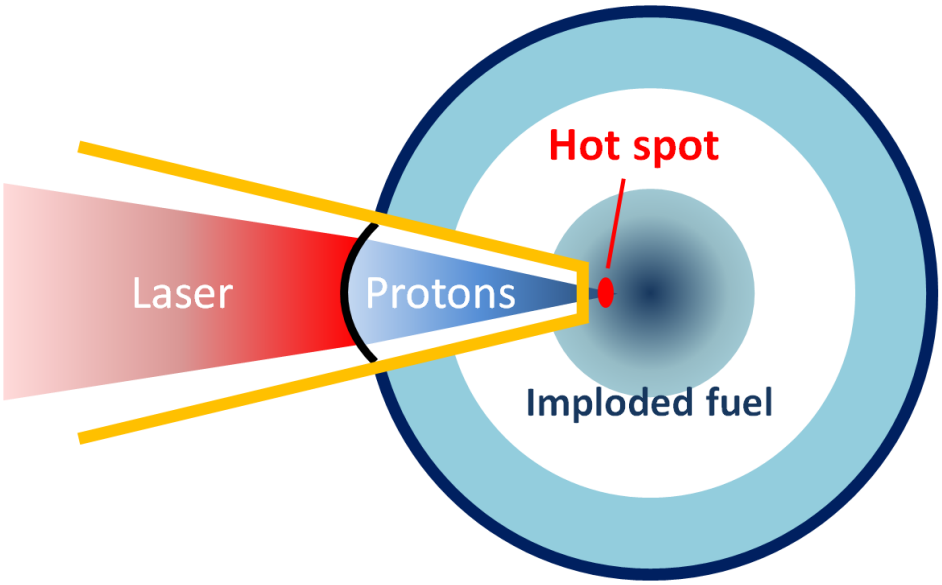

Figure 0-1: Illustration of a FI scheme using a laser-generated ion beam. The pre-compressed imploded fuel is heated and ignited by a short pulse laser-generated proton beam. In order to decrease the energy requirement, a cone is used to bring the proton source closer to the imploded fuel [7].

High-energy conventional ion accelerators are also of interest as possible alternative drives for ICF within the ion-driven inertial fusion scheme [11]. In the most direct approach, ion energy-deposition would simply replace laser heating of the small pellet of combustible [12]. In a more indirect one, the pellet would be compressed by X-rays generated by the interaction of focused ion beams with a Holhraum [6]. Although, at the moment, this scheme suffers from problems related to the ion flux, the ion beams spot size, the pulse duration and the pointing of the beam [7,13], the expected efficient coupling of beam energy into the target, the high efficiency and high repetition rate of beam generation make it a good candidate for ICF as well [11]. High-energy ion accelerators that could provide the required ion beams are currently under investigations [14, 15].

As a result, within ICF, a very obvious concern is the physics of ion energy-deposition in the target plasma. Indeed, evaluation of the scenarios mentioned above requires detailed information about ion ranges, and energy-deposition in matter that passes quickly through different regimes from cold solid to highly compressed and hot plasma where fusion reactions take place [16, 17].

Using as a benchmark numerous and trustable data on a large range of projectile energy on many materials [18, 19] methodically obtained through experiments carried out with accelerators, scientists are nowadays able to predict accurately the stopping power in cold solid material through theoretical and empirical methods [20]. However, far less is known about the stopping power in warm and hot dense matter.

From a theoretical point of view, the stopping power is actually expected to change with the target thermodynamic state. For instance, the ionization of a projectile propagating at a given velocity is expected to rise with the plasma temperature, increasing its interaction with the plasma. Another effect is the modification at high temperature of the plasma screening properties. Those are fundamental when evaluating the stopping power. Determining and including those effects in the calculation of the stopping become very difficult in the case of warm and hot dense matter (temperature above 1 eV and density close or higher than solid density), where the plasma is strongly coupled, partially ionized, and degenerated [21].

Although several theories have been developed [22, 23, 24, 25, 26], none of them has ever been tested in warm and hot solid-density matter. Indeed, due to the experimental complexity of containing heated matter long enough to (1) perform the measurement before thermal expansion takes place and (2) properly characterize the studied medium, no experimental data actually exist in dense plasma at temperature higher than 1 eV.

A way to circumvent those difficulties could be to use again short-pulse laser-produced ion beams. Indeed, exceptional properties have been observed for ion beams accelerated by such lasers from planar targets, such as high brightness, high spectral cut-off, high directionality, low emittance, and short duration (a few ps at the source) [27]. These characteristics can be used to generate WDM. Indeed laser generated ion beams can heat isochorically thin foils and produce quasi-uniform WDM during hundreds of ps with negligible thermal expansion [8,28].

In the present study, we use the unique properties exhibited by ion beams generated by short-pulse lasers in order to both produce warm dense matter and probe it, with the aim of investigating the stopping power of ions in warm dense matter.

Goal and plan:

The main objective of this thesis is to develop and exploit an experimental platform to study the stopping power of ions in warm dense matter, more particularly when the density is close to solid.

The first two chapters are aimed at presenting the subject and theories that are used in this thesis:

- in the first chapter, the context of warm dense matter is recalled from a theoretical and experimental point of view. The different methods to generate experimentally WDM are also reviewed with a particular interest on the method that is used in this thesis, i.e., based on ion heating.
- the second chapter is devoted to the stopping power of ions in dense matter. We presented one of the theories that have been developed to predict the proton stopping power in WDM and the results it provides on the effect of the temperature. Using Gus'kov et al. approach, we enlightened the great influence of the temperature-dependent projectile ionization on the stopping power of carbon projectiles.

The third chapter is dedicated to the study of the principal experimental tool of our platform aimed at studying the stopping power, the laser-generated ion beams. The first part concerns the well-documented and studied process of ion acceleration using a solid-density target. The theoretical aspects of the production of such ion beam from the laser-matter interaction to the energetic ions are recalled. We pay a particular attention to the property of the ion source (symmetry, number of ions, energy cut-off) with respect to the platform developed in chapter IV. We emphasize in particular the issues concerning their low reproducibility and laser-to-ion conversion efficiency. In the second part, we focus our attention on ion beam acceleration using short-pulse laser interacting with lower-than-solid density targets which exhibits interesting properties with respect to the issues mentioned above. We study the ion beams produced with a high intensity short pulse laser when interacting with two different kinds of lower-than-solid-density targets.

- With helium gas jet targets: we demonstrate that helium beams can be generated perpendicularly to the laser propagation axis with very similar spectrum. This characteristic can be used in our experimental platform as a way to obtain a good ion-beam reproducibility: we can use the beam symmetric to the probe beam as a reference providing the spectrum of the probe beam before interaction. Although the energy cut-off displayed by the two beams are not close enough for direct stopping power measurements, we emphasize that they can be used in the experiments related to projectile charge measurements as detailed in chapter IV.
- With laser-exploded targets: Using a long-laser pulse to explode a thin target and playing on the intensity of the long pulse and on the delay between the long and the short-laser pulse, we explore various plasma gradient conditions. We demonstrate that, contrary to what is currently thought, high energy protons (3-4 MeV) can be produced with target having long

gradient plasma at the back side. In addition, we observe that under certain laser and exploded foil conditions, it was possible to accelerate protons to the same energies (7-8 MeV) as using solid-density targets in the standard TNSA mechanism.

In the fourth and last chapter which constitutes the core of this thesis, the stopping power in WDM is studied from the experimental aspect. The first part is devoted to the direct measurement of the stopping power in WDM generated by proton heating. Using stopping power theoretical predictions detailed in chapter II, we find out that, to be observable, the effect of the temperature on the stopping power in heated solid-density aluminum requires higher temperature conditions (typically above 40 eV) and diagnostics of our higher precision than what is achievable with our current experimental means. Therefore, we have focused our experimental study on the equilibrium mean charge of a projectile propagating through the matter, an important parameter of the stopping power that is predicted to be modified in our temperature regime. We describe two experiments based on the same principle: a thin solid-density aluminum foil is heated using a laser-generated energetic proton beam, while it is simultaneously probed by a second laser-generated ion beam, the mean charge of which is measured.

- In a first experiment performed at LULI 100 TW facility with a carbon beam as a probe, we validate our experimental set-up by reproducing in a single shot and with a reasonable agreement the carbon equilibrium mean charge in cold solid-density aluminum obtained in conventional accelerator. In addition, we measure the equilibrium mean charge in WDM heated up to 1 eV, according to the spectrum of the heating proton beam, and observe that, in this temperature regime, the equilibrium mean charge is not different from the one in cold solid-density matter in the energy range from 0.04 to 0.5 MeV/u. We conclude on the importance of performing similar measurements at higher temperature, so that we can observe some modifications in the equilibrium mean charge.
- In a second experiment performed using the TITAN laser at the Lawrence Livermore National Laboratory, we use the helium-ion source detailed in chapter III to probe WDM. Interestingly, we establish that our helium ion source delivers an ion beam that is already equilibrated in helium gas. We reproduce on a single shot the helium mean equilibrium charge in cold solid-density aluminum obtained using accelerators for energies from 0.1 to 0.6-0.7 MeV/u.

Finally, in the conclusion, the main results are summarized and some of the future perspectives regarding the study of stopping power in WDM are presented.

References

[1] S. Bodner et al., Phys. Plasmas **5**, 1901 (1998)
[2] J. D. Lindl, AIP Conf. Proc. **318**, 635 (1994)
[3] S. Skupsky, Phys. Rev. A **16**, 727 (1977)
[4] C. Labaune, W. J. Hogan, and K. A. Tanaka, Inertial Fusion Science and Applications (Elsevier, New York/Amsterdam, 1999)
[5] M. Tabak *et al.* Phys. Plasmas **12**, 057305 (2005)
[6] M. Roth et al., Phys. Rev. Lett. **86**, 436 (2001)
[7] M. Temporal et al., Phys. Plasmas **9**, 3098 (2002)
[8] P. K. Patel et al., Phys. Rev. Lett. **91**, 125004 (2003)
[9] S. N. Chen et al., Phys. Rev. Lett. **108**, 055001 (2012)
[10] J.J. Honrubia et al., 35th EPS conf. Plasma Phys. **32D**, P5.125 (2008)
[11] C. Deutsch & I. Hofman, C. R. Acad. Sci. Paris, **1**, 758 (2000)
[12] L.R. Grisham, Phys. Plasmas **11**, 5727 (2004)
[13] D. Keefe, Ann. Rev. Nucl. Part. Sci. **32**, 391 (1982)
[14] R. Bock, GSI report 95-15, February 1995
[15] R.O. Bangerter & T.J. Fessenden, Heavy-ion driven inertial fusion, in: E. Panarella, Current Trends in International Fusion Research (Plenum Press, New York , 1997)
[16] C. K. Li & R. D. Petrasso, Phys. Rev. Lett. **70**, 3059 (1993)
[17] C. Deutsch et al., Open Plasma Phys. J. **3**, 88 (2010)
[18] Particle interactions with matter, http://www.srim.org/#SRIM
[19] Stopping Power for Light Ions, http://www.exphys.jku.at/stopping/
[20] J. F. Ziegler J. Appl. Phys. / Rev. Appl. Phys. **85**, 1249 (1999)
[21] R. W. Lee et al., J. Opt. Soc. Am. B **20**, 770 (2003)
[22] E. Nardi et al., Phys. Fluids **21**, 574 (1978)
[23] T. A. Mehlhorn, J. Appl. Phys. **52**, 6522 (1981)
[24] T. Peter & J. Meyer-Ter-Vehn, Phys. Rev. A **43**, 1998 (1990)
[25] G. Maynard and C. Deutsch, Phys. Rev. A **26**, 665 (1982); **27**, 574 (1983)
[26] P. Wang et al., Phys. Plasmas **5**, 2977 (1998)
[27] J. Fuchs et al., Nature Phys. **2**, 48 (2006)
[28] A. Mancic et al., High Energy Dens. Phys. **6**, 21 (2010)

I. WARM DENSE MATTER

I.1 Introduction

Warm dense matter is a state of matter that is neither solid, gas, liquid nor ideal plasma. As such it cannot be treated using well-established theoretical frames, like condensed matter or plasma physics [1], and its study from a theoretical point of view is very challenging. Warm dense matter is roughly characterized by densities varying from 0.1 to 10 times the solid density, and temperatures from 1 to 100 eV (see Figure I-1).

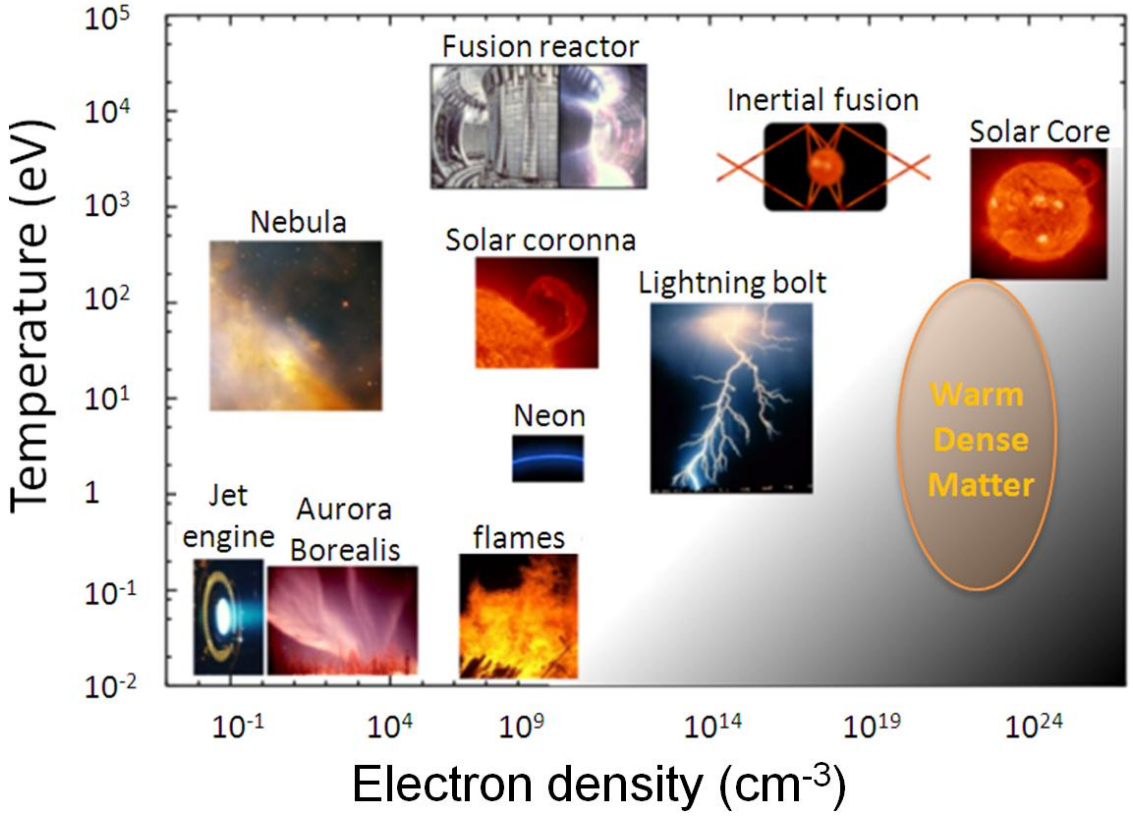

Figure I-1: Diagram (extracted from Ref. [2]) in temperature and electron density, situating the domain of warm dense matter (see the orange shaded region) with respect to other common forms of plasmas.

Warm dense matter can be found in several domains and applications, therefore understanding its properties is of considerable interest. This regime is present in a large collection of physical environments like in the center of telluric planets or in the core of giant planets [3], but also in plasma created from interactions between high-intensity lasers and solid-density foils [4], or in inertial confinement fusion (in both direct and indirect drive schemes) [5].

In this chapter, the warm dense matter (WDM) regime is defined with respect to different parameters encountered in plasma physics. The characteristic difficulties and challenges posed by this transient state in both theoretical and experimental studies are emphasized. Then, two different approaches, which are used to treat WDM in this thesis, are described. Their respective strong points and limits are underlined. The last part is focused on the generation of warm dense matter in the laboratory. The different means to produce warm dense matter and to measure its thermodynamic characteristics are presented.

I.2 Definition

A plasma can be considered as a globally neutral gas composed of charged (and possibly neutral) particles interacting with each other through Coulomb forces, and presenting a collective behavior [6]. A globally neutral gas means that there is, on average, the same amount of negative and positive charges in the gas. We can distinguish different categories of plasmas with respect to density and temperature. To classify the different plasma regimes, one can use non dimensional parameters. We will here introduce them with respect to the plasma density and temperature, using hypotheses described below.

I.2.1 Hypotheses

We will restrict ourselves to single or multi species plasmas that are entirely ionized, composed of electrons (charge $-e$, mass m_e) and ions (charge Ze, mass m_i). These plasmas are characterized by several macroscopic values such as electron and ion densities (n_e and n_i) and temperatures (T_e and T_i). For a single-species plasma, the global neutrality of the plasma gives,

$$n_e \cong Z n_i. \tag{1.1}$$

When considering plasmas composed of different kinds of ions, one defines the ion average charge [6],

$$\mathrm{Z}^* = \frac{\sum_j n_j Z_j}{\sum_j n_j}, \tag{1.2}$$

where Z_j and n_j are respectively the charge and the density of the ions of the species j. The equation associated with the plasma global-neutrality then becomes,

$$n_e \cong \mathrm{Z}^* n_i. \tag{1.3}$$

We consider that the electrons and the ions are in thermal equilibrium, i.e., the electron and ion temperatures are equal [6]:

$$T_e \cong T_i \cong T. \tag{1.4}$$

I.2.2 Characteristic lengths

Let us now introduce two different characteristic lengths that will help us to circumscribe the domain in which WDM lies:

- the Wigner-Seitz radius is defined as the radius of a sphere that contains on average only one particle [6]:

$$r_\alpha = \left(\frac{3}{4\pi n_\alpha}\right)^{1/3}, \tag{1.5}$$

  where α index designs the electrons or the ions. In the case of ions, r_i is called the ion-sphere radius. The average distance between two particles α is then approximately $2r_\alpha$.

- the Fermi Energy is defined as the highest occupied energy levels in a fully degenerate electron gas at 0K. It gives an order of magnitude of the electron energy in a degenerate system [7]:

$$E_F = \frac{\hbar^2}{2m_e}(3\pi^2 n_e)^{2/3} = k_B T_F\,, \tag{1.6}$$

  where $\hbar = h/2\pi$, h is the Planck constant and m_e, the mass of an electron. T_F is called the Fermi temperature. This gives numerically with respect to the electrons:

$$E_F[eV] \cong \left(\frac{n_e[cm^{-3}]}{4.53 \times 10^{21}}\right)^{2/3}. \tag{1.7}$$

I.2.3 Degeneracy factor

To determine if quantum effects have to be taken into account when treating interactions between electrons, one may compare the electron thermal energy with the Fermi energy [8]. Quantum effects in the interactions between electrons will obviously be negligible provided that,

$$\theta = \frac{k_B T}{E_F} = \frac{T}{T_F} \gg 1. \tag{1.8}$$

The parameter θ is usually named the degeneracy factor. Numerically, the above criterion yields:

$$\boxed{\theta \cong T[eV]\left(\frac{4.53\times 10^{21}}{n_e[cm^{-3}]}\right)^{-\frac{2}{3}} > 1.} \quad (1.9)$$

If this condition is fulfilled, the plasma is then considered classical. From (1.9), one can see that classical plasmas are found at high temperature and low density. Conversely, for $\theta < 1$, the electrons are degenerate and the plasma is considered degenerate.

We note that, in the framework of this thesis, the ions can be considered as non-degenerated.

I.2.4 Coupling parameter

The plasma dynamic is a result of a competition between the thermal agitation of the particles, which increases the plasma entropy, and the collective features of the Coulomb interactions between particles, which, at the opposite, tends to organize them [9]. This feature can be quantified by the degree of so-called coupling between the plasma species. The plasma coupling parameter is defined as the ratio of the Coulomb-interaction average potential energy between particles to the average kinetic energy, $\langle E_k \rangle$ [8]:

$$\Gamma = \frac{\langle \mathrm{V} \rangle}{\langle E_k \rangle}. \quad (1.10)$$

- In the case of non-degenerate (with respect to electrons) plasmas, the particles follow the Maxwell-Boltzmann law. The average kinetic energy per particle is thus calculated as $\frac{3}{2}k_B T$, which we take as $k_B T$ in an order-of-magnitude estimate. We consider the Coulomb-interaction average potential energy between ions [8],

$$\langle \mathrm{V} \rangle \approx \frac{Z^2 e^2}{4\pi\varepsilon_0 r_i}, \quad (1.11)$$

where ε_0 is the vacuum permittivity. The coupling parameter is then given by:

$$\Gamma_{nd} \approx \frac{\frac{Z^2 e^2}{4\pi\varepsilon_0 r_i}}{\mathrm{k}_B \mathrm{T}}. \quad (1.12)$$

This is expressed numerically by:

$$\boxed{\Gamma_{nd} \approx 2.32\times 10^{-7}\frac{Z^{5/3}(n_e[cm^{-3}])^{1/3}}{T[eV]}.} \quad (1.13)$$

For $\Gamma_{nd} \ll 1$, the plasma is non-degenerate and weakly coupled; the motion of the plasma charged particles is weakly influenced by the Coulomb interactions with the other electrons of the plasma. Such plasmas are usually designated as kinetic [6]

For $\Gamma_{nd} \geq 1$, the plasma is non-degenerate and strongly coupled. Coupled means the interactions between electrons are strong and the electrons are considered correlated, i.e., the position in the phase-space of one particle strongly depends on the positions of the other electrons of the plasma.

- In the case of degenerate plasmas, it is more relevant to redefine the coupling parameter as obtained by comparing the Coulomb-interaction average potential energy between electrons [7],

$$\langle \mathrm{V}_{ee} \rangle \approx \frac{e^2}{4\pi\varepsilon_0 r_e}, \tag{1.14}$$

with the Fermi energy. This gives numerically,

$$\boxed{E_F[eV] \cong \left(\frac{n_e[cm^{-3}]}{4.53 \times 10^{21}}\right)^{2/3}}. \tag{1.15}$$

The coupling parameter is therefore given by,

$$\boxed{\Gamma_d \approx \frac{\langle \mathrm{V}_{ee} \rangle}{k_B T_F} \approx \left(\frac{2.57 \times 10^{23}}{n_e[cm^{-3}]}\right)^{1/3}}, \tag{1.16}$$

For $\Gamma_d \ll 1$, the plasma is degenerate and weakly coupled.

For $\Gamma_d \geq 1$, the plasma is degenerate and strongly coupled.

These four plasma regimes are presented in the temperature-density diagram of a hypothetical fully-ionized hydrogen plasma shown in Figure I-2. On one hand, we observe that the plasma coupling increases with the electron density and decreases with the temperature in non-degenerate plasmas. On the other hand, when the plasma is degenerate, the plasma coupling decreases with the electron density and the limit between weakly and strongly coupled plasma does no longer depend on the temperature.

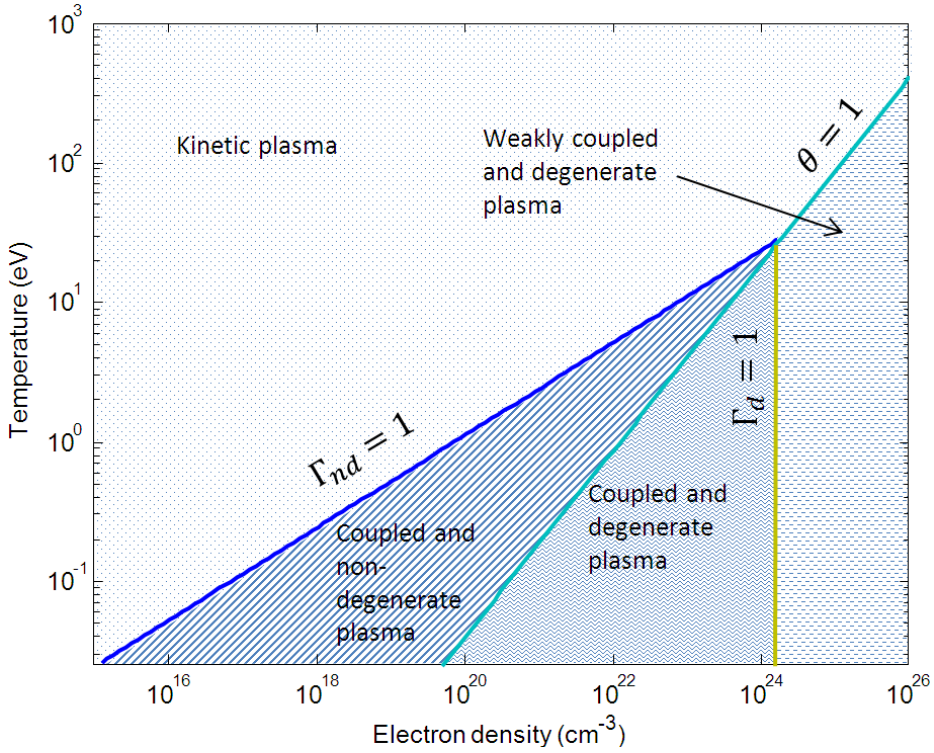

Figure I-2: Temperature density diagram of a hypothetical fully-ionized plasma of hydrogen. The different regimes are separated by the dimensionless parameters of the plasma defined above.

I.2.5 Warm dense matter

As mentioned in the introduction, warm dense matter is a transient regime that lies at the confluence of plasma, gas, liquid and solid and shares properties of all four [1]. Like in liquids and condensed matter, in this regime, classical Coulomb forces between atoms cannot be neglected. In addition, the electrons need to be treated quantum-mechanically. Last, the temperature is high enough to excite thermally the electrons and ionize them creating a plasma and increasing the electron density at constant ion density (see Figure I-3).

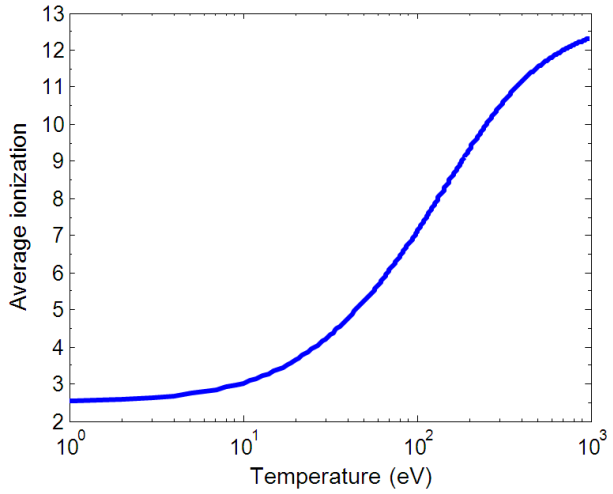

Figure I-3: Average ionization of solid-density aluminum predicted by the Thomas-Fermi statistical model (see Ref. [10]) as a function of temperature.

Warm dense matter is roughly located in the diagram of density-temperature where all of these effects cannot be neglected, i.e., where the matter is (1) partially degenerate; (2) weakly to strongly coupled; (3) partially ionized. In the case of aluminum, this regime is typically found inside the orange area in the diagram presented in Figure I-4.

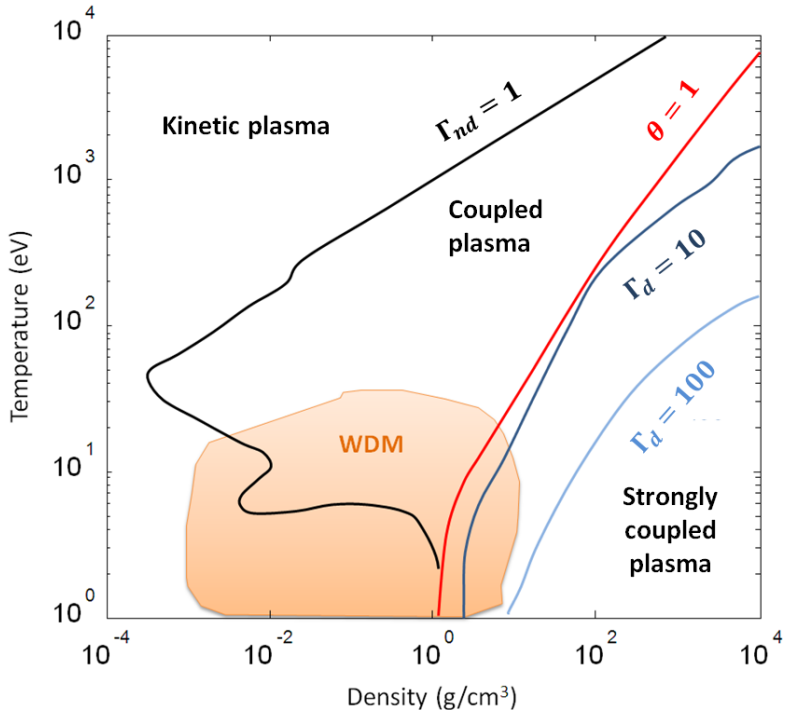

Figure I-4: Temperature density phase diagram for aluminum. The so-called warm dense matter area also corresponds to the region of greatest uncertainties with respect to the available models [11].

In WDM, all of the above-mentioned effects are of comparable magnitude which presents a great difficulty to reliable modeling since no simplification can be made. The electronic or ionic structures of WDM are not well-known and we also have a limited knowledge of transport properties, such as

electrical and thermal conductivities [2]. It is therefore fundamental for the predictions that can be made in this regimes, regarding e.g. optical (opacities, reflectivity) and mechanical properties (viscosity, strength) or its equation of state[1] (EOS), to be tested and improved using experimental data [11]. However, WDM properties are also very difficult to measure in the laboratory [2]. Indeed this transient regime typically lasts a few hundreds of picoseconds before hydrodynamic expansion occurs and induces significant target density decrease. Furthermore, the high plasma density causes the matter to be optically thick. Thus, many experimental techniques commonly used in plasma physics cannot be applied to diagnose and characterize the generated plasma [1].

I.3 Theory

As mentioned earlier, the complicated nature of warm dense matter makes the modeling of its properties very challenging.

In order to accurately describe warm dense matter, a model should be able to calculate the average electron-density profile around an ion in the matter, determine self-consistently the average ionization of the matter, and compute the interaction between ions, the total Helmholtz free energy of the matter and a very large set of ionic and electronic transport coefficients [12, and references therein]. The model should also be valid and robust enough to ensure a transition, as smooth and physically correct, between the well-understood density-temperature domains [1].

In order to approach the WDM regime, different theories have been (and are being) developed based on models that have been developed in adjacent regions (e.g. models used in SESAME [13]), as e.g. condensed matter and plasma physics [2].

Within the frame of calculating stopping power in warm dense matter, we present here two different models based on first principles: one coming from solid-state physics and the other one from dense plasma physics. After briefly presenting the density functional theory on which they both rely to treat the quantum interactions between electrons, each code is presented with respect to its potentialities and limits within the framework of modeling warm dense matter.

[1] EOS is the equation that relates pressure, temperature and density of a material.

I.3.1 Density Functional Theory

The density functional theory (DFT) is one of the most widely used methods for *ab initio* calculations of the atoms and molecules structures, and of their interactions [14]. The concept of the approach relies on the fact that the properties of a many-electron system at zero temperature, i.e., in the ground state, can be determined exactly from the knowledge of the spatial distribution of the electron density. The name DFT comes from the use of the electron density functional. Extended to finite-temperature, the DFT can be used to compute the thermodynamic properties of the system [15].

At 0 K, this theory is based on the two theorems formulated by Hohenberg and Kohn [16]. In the first one, it is shown that the Hamiltonian of a many-electron system in the ground state can be written as a functional of the electron density function (in the ground state), $n_{e0}(\vec{r})$. This result allows working with the electronic density function as a variable instead of the many-electron wave-functions. All the system properties can therefore be determined with respect to $n_{e0}(\vec{r})$. In the second theorem, they demonstrate that $n_{e0}(\vec{r})$ is the density function that minimizes the system energy.

The energy functional of a system of electrons can be split up into a sum of density functionals [17],

- $\mathrm{E}_K[n_e(\vec{\mathrm{r}})]$, the kinetic energy of the non-interacting electron gas in its ground state,
- $\mathrm{E}_{ee}[n_e(\vec{\mathrm{r}})]$, the Coulomb potential energy between the electrons of the system,
- $E_{ext}[n_e(\vec{\mathrm{r}})]$, the external potential energy of the system which corresponds to the interactions between nuclei and electrons,
- $\mathrm{E}_{\mathrm{XC}}[n_e(\vec{\mathrm{r}})]$, the exchange-correlation functional. It corrects the difference between the kinetic energy of a non-interacting electron gas and of an interacting one,

giving the following expression [17],

$$\mathrm{E}[n_e(\vec{\mathrm{r}})] = \mathrm{E}_K[n_e(\vec{\mathrm{r}})] + \mathrm{E}_{ee}[n_e(\vec{\mathrm{r}})] + E_{ext}[n_e(\vec{\mathrm{r}})] + \mathrm{E}_{\mathrm{XC}}[n_e(\vec{\mathrm{r}})]. \tag{1.17}$$

To determine the density of the system according to the Hohenberg and Kohn's theorems, one needs to solve $\frac{\delta \mathrm{E}[n_e(\vec{\mathrm{r}})]}{\delta n_e(\vec{\mathrm{r}})} = 0$. Using the Kohn-Sham (KS) formulation [17], this equation can be reduced to a set of one-electron Schrödinger equations, the KS equations, in which each electron interacts with an effective potential composed of the sum of the external potential, the Coulomb potential between the electrons and the potential relative to the exchange correlation functional (see Figure I-5). The many-electron problem is now replaced by an exactly equivalent set of self-consistent one-electron equations that is easier to handle.

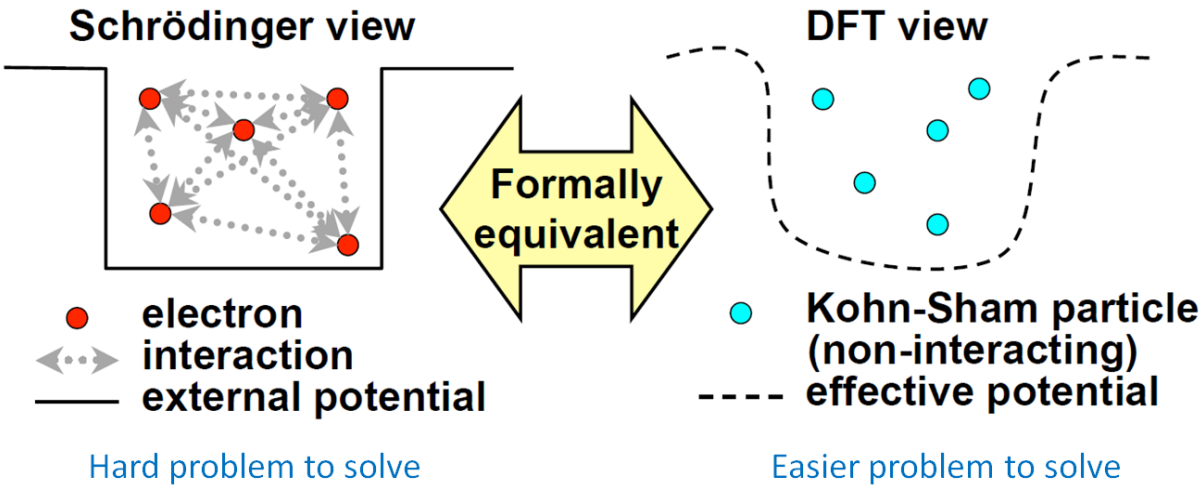

Figure I-5: Illustration of the principle of the DFT, extracted from Ref. [18].

One should note that the sole approximation that is made in the DFT is related to the determination of the exchange-correlation functional $\mathrm{E_{XC}}[n_e]$. Among the different approaches that exist to estimate it, one can use the Local (Spin) Density Approximation (L(S)DA) [19]. One approximates $\mathrm{E_{XC}}[n_e]$ by a function of the local electron density $\mathrm{E_{XC}}(n_e)$. Its values (with respect to n_e) are then estimated empirically using Monte-Carlo quantum simulations of a homogeneous electron gas at zero temperature [20].

In computational simulations, the electronic structure is found numerically by iteration using the so-called self-consistent field method (see Figure I-6) based on the convergence of $n_e(\vec{\mathrm{r}})$ [14] (since the density function is considered in the KS equations as both the input and the output),

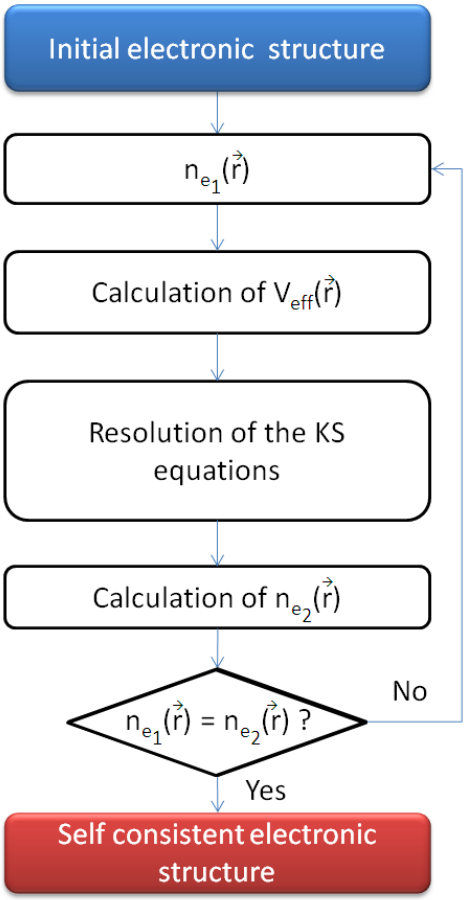

Figure I-6: Illustration of the self-consistent field method.

To treat the case of a finite-temperature system, one replaces the total energy, E, by the free energy of the system [15].

I.3.2 Quantum Molecular Dynamics (QMD)

Quantum Molecular Dynamics (QMD) calculations provide a means to understand and to predict the interactions between atoms and molecules, and to model chemical reactions [21].

Firstly introduced by Car and Parrinello [22], this approach is based on a successful combination of DFT with classical Molecular Dynamics (MD) simulations for the heavy particles (ions), which is possible within the Born-Oppenheimer approximation (or adiabatic approximation) [23]. This approximation makes possible to decouple the ion motion from the electrons. Ions are much more massive than electrons, thus ions can be considered as essentially static relative to the electrons. The ions are then treated classically, whereas electrons are treated quantum-mechanically (see Figure I-7). QMD allows generating the ions trajectory by alternating electronic structure and molecular dynamics calculations.

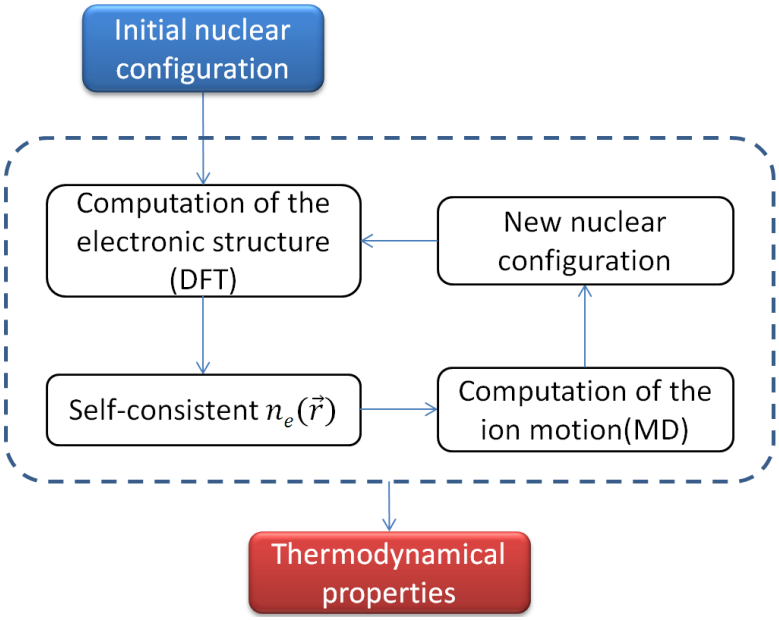

Figure I-7: illustration of the convergence loop in the QMD code ABINIT.

QMD codes are commonly used to compute the different thermodynamic quantities of the warm dense matter, such as the pressure and the total energy of the system. They have indeed demonstrated to be able to provide the structural, thermodynamic, and optical properties of WDM in good agreement with experimental results obtained in coupled systems [24, 25, 26, 27, 28].

Such code uses the pseudopotential method to reduce the computational time required to solve the KS equations in the DFT [29]. Due to the computational method used to determine the electronic wave-functions, an "all-electrons" calculation (all electrons are taken into account in the calculation) can necessitate a vast amount of computational time. To reduce it, one can use pseudopotentials in QMD calculations. The pseudopotential approximation is based on the fact that core electrons strongly bounded to the nuclei are very weakly affected by their environment [30]. Thus, they can be considered frozen: the core electronic wave-function is replaced by the wave-function they have in an isolated atom. To calculate the valence electrons wave-functions, the interaction potential between the core electrons and the nuclei is replaced by a pseudopotential (weaker potential) mimicking the resulting effective potential felt by the valence electrons (see Figure I-8). A detailed review of the method can be found in Ref. [31, 32].

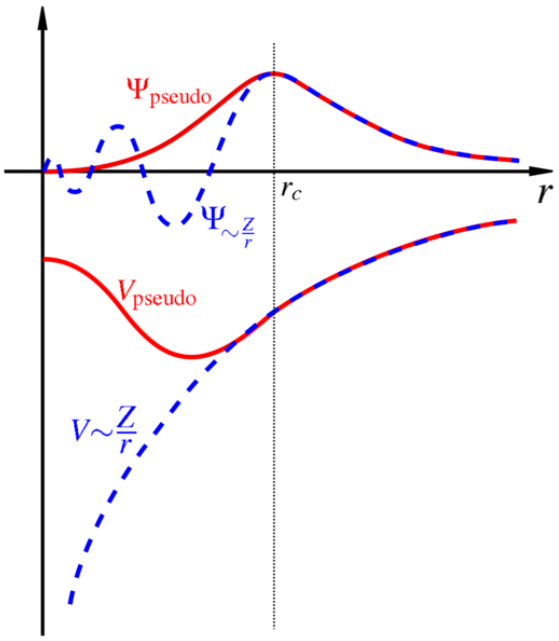

Figure I-8: Comparison of a wave-function (Ψ) in the Coulomb potential of the nucleus (blue) to the one (Ψ_{pseudo}) in the pseudopotential (red) (extracted from Ref. [33]). The real and the pseudo wave-functions and potentials match above a certain cut-off radius r_c that can be viewed as a border between core (frozen) and valence electrons.

In this thesis, we used the QMD code ABINIT [33] to determine the electron density function required to calculate the stopping power within the dielectric theory presented in the next chapter.

I.3.3 Self-Consistent Approach for Astrophysical and Laboratory Plasmas (SCAALP)

SCAALP [34, 35] is an average-atom model [36]. Such kind of model is used to calculate the thermodynamical properties in the intermediate regime located between the Debye-Hückel (low density) and Thomas-Fermi (high density) approaches. It computes the average electron structure for the ions by simplifying the influence of the plasma environment. This model presents a spherical symmetry and thus is not able to describe any molecular states or crystal structure.

In SCAALP, the plasma is modeled as an effective classical system of virtual neutral particles, i.e., a collection of Neutral Pseudo Atoms (NPAs) [37] interacting via an interatomic effective pair potential, $\phi_{eff}(\vec{R})$ (see Figure I-9). The electronic structure and density are assumed to be identical for each NPA. Each NPA is composed of one nucleus of charge Z_N and Z_N electrons which screen the nucleus, such that the NPA average charge is zero [34]. These electrons can be either in bound or in continuum states.

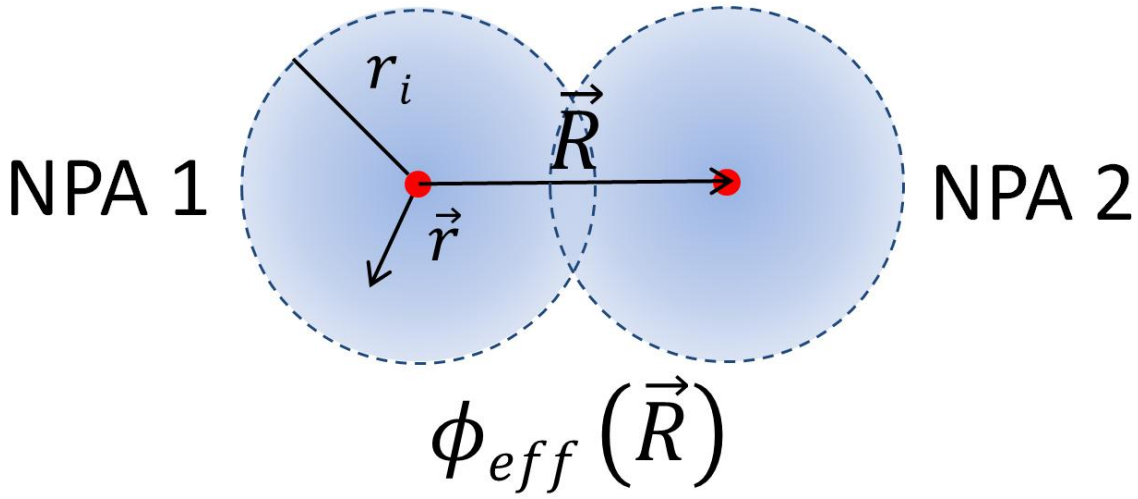

Figure I-9: Representation of the interactions between two NPAs. We distinguish here $\vec{r}$ as the spatial parameter within the NPA from $\vec{R}$ the spatial parameter of the system of NPAs.

Like in DFT, the electronic structure of the NPAs is determined by solving a system of one-electron Schrödinger equations in an effective potential, V_{eff}. The electrons follow the Fermi-Dirac distribution function,

$$f_{FD}(E) = \frac{1}{1 + \exp\big(\beta(\mathrm{E} - \mu)\big)}, \tag{1.18}$$

where $\beta = 1/k_B T$ and μ, the chemical potential. The electronic density in each NPA is thus given by,

$$n_e(\vec{\mathrm{r}}) = \sum_i |\varphi_{\mathrm{i}}(\vec{\mathrm{r}})|^2 f_{FD}(\varepsilon_{\mathrm{i}}), \tag{1.19}$$

where the $\varphi_{\mathrm{i}}(\vec{\mathrm{r}})$ are the eigenvectors of the Schrödinger equations mentioned above.The neutrality of the NPA over the Wigner–Seitz cell of radius r_i determines the chemical potential, μ, so that,

$$\int_0^{r_i} 4\pi r^2 n_e(\mathrm{r})\, dr = \mathrm{Z}_N. \tag{1.20}$$

The collection of NPAs is described with respect to a reference system of hard-spheres (HS) with the packing-fraction η as parameter [38]. This model is widely used in statistical mechanics to describe fluids and the transition between solid and fluid states [39].

Within the Born-Oppenheimer approximation (the nuclei are treated classically and the electrons quantum mechanically), the expression of the free energy of the system per NPA is given by [35]:

$$\mathrm{F}_{tot} = F_I^{id} + F_{HS}^{ex}(\eta) + \frac{n_i}{2}\int g\big(\eta, \vec{R}\big)\phi_{eff}\big(\vec{R}\big)d\vec{R} + F_e\,, \tag{1.21}$$

where F_I^{id} is the ideal free energy of a non-interacting gas, $F_{HS}^{ex}(\eta)$ is the excess free energy of the HS reference system that corrects the difference between the free energy of a non-interacting ion gas

and of an interacting one, $g(\eta, \vec{R})$ is the radial pair distribution function of the HS reference system, and F_e is the electronic contribution to the free energy.

To solve the system of equations for a given material, density and temperature, one needs to determine self-consistently both the effective potential $V_{eff}(\vec{r})$ and the packing-fraction η. This is done by applying the Gibbs-Bogolyubov inequality [35] to our system: the total free energy of the system at thermodynamic equilibrium (T, n_i and Z_N are fixed) is minimal for any variations of, respectively, the electronic and ionic structure [35], i.e., $\frac{\partial \mathrm{F}_{tot}}{\partial \eta} = 0$ and $\frac{\delta \mathrm{F}_{tot}}{\delta n_e(\vec{\mathrm{r}})} = 0$. From these two conditions, one obtains, respectively, the best packing fraction and effective potential to represent the effective ionic structure of the reference system.

As shown in Figure I-10, the electronic and ionic structures (embodied, respectively, in the electron density and the pair distribution functions) are obtained numerically by iteration based on the convergence of both the average ionization, defined in the code as,

$$\mathrm{Z}^* = \frac{n_e(r_i)}{n_i}, \tag{1.22}$$

and the packing fraction. Once done, one can compute thermodynamic properties of the system, such as pressure, internal energy, entropy, calorific heating, or sound speed, by differentiating the plasma total free energy [40]. The electron transport coefficients are also calculated using the Ziman-Evans formula at finite-temperature (electronic resistivity) [41] and the Mestel method (thermal conductivity) [42].

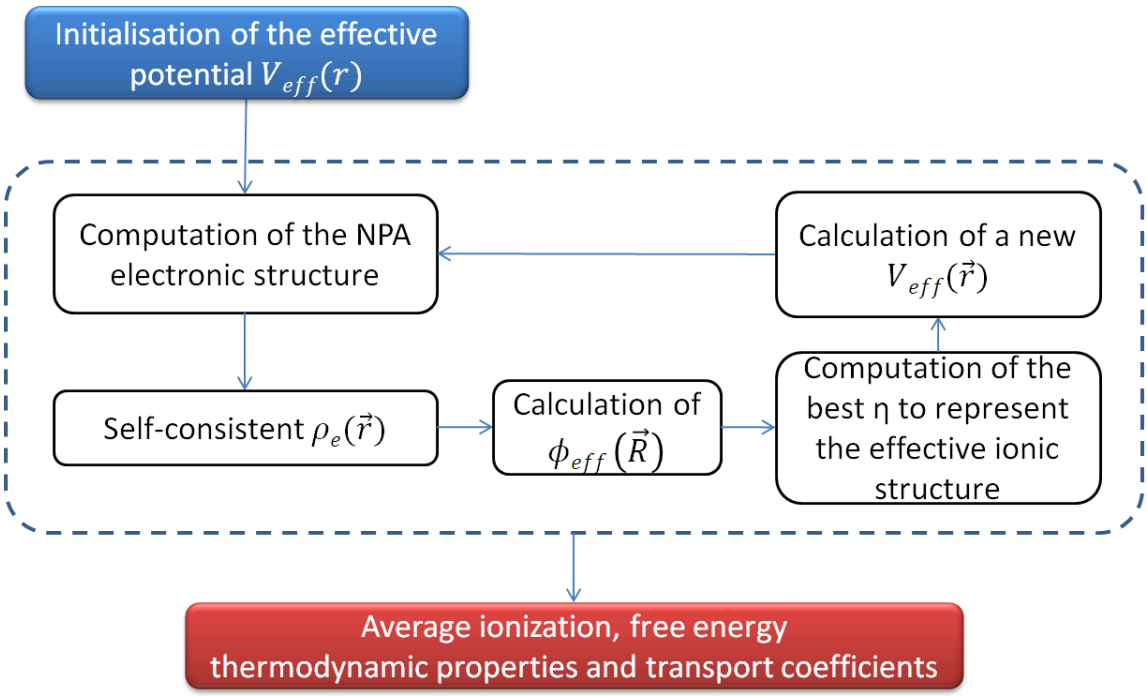

Figure I-10: Illustration of the convergence loop in SCAALP.

This atom model gives a self-consistent description of dense plasmas from first principles and provides thermodynamic and transport properties for a wide range of high energy density physics applications [35] with a reduced computational time compared to QMD. Nevertheless, it is limited not only by its spherical symmetry, but also by the reference system used to treat the ionic structure. Indeed, due to the neutrality imposed inside the NPA, the potential $\phi_{eff}(\vec{R})$ between two NPAs is zero when they do not overlap ($R > 2r_i$), thus long range interactions are neglected [35].

I.4 Generation of WDM

We have mentioned earlier that modeling warm dense matter is very challenging. The solution brought by *ab initio* codes to come back to first principles in order to lower the uncertainties is very promising. However, it needs experimental results to be tested. Furthermore, generating warm dense matter in a laboratory would allow to directly studying the matter under certain conditions relevant to a number of research areas such as ICF or planetology. Nowadays, simply producing warm dense matter is still relatively difficult, but does not require the most powerful and cutting edge facility. Indeed pulsed beams delivered by table top laser facilities are enough to produce warm dense matter when irradiating a basic solid target. However, in order to be studied, warm dense matter produced in the laboratory needs also to be well-characterized, i.e., one needs to control the electron and ion densities and temperature. Furthermore, since, in laboratory, matter passes very briefly through this regime, it needs to be maintained in a WDM state during enough time, so that its properties can be probed.

When heated, a solid-density sample sees its density decreasing rapidly due to hydrodynamic expansion. The time the foil density stays close to solid-density, i.e., the time of confinement, is roughly given by the ratio of the dimension of the heated zone, *d*, to the ion sound velocity c_s, i.e., the typical speed of the plasma expansion [6],

$$\tau \approx \frac{d}{c_s}. \tag{1.23}$$

Using this expression for a 10 µm thick solid-density plasma with a temperature of 10 eV, one finds that the time of confinement is of the order of 100 ps.

One way to reach both the temperature and density required by warm dense matter is to heat isochorically the sample: the energy is deposited within a time scale shorter than the time of confinement. Another issue is to keep the heated target as homogeneous as possible, making it easier to study and to use in experiment. In this paragraph, we will briefly go through the different methods and approaches that have been developed to achieve such conditions.

I.4.1 Direct laser heating

With the discovery of chirped-pulse amplification technique [43], optical laser pulses have been able to reach very high intensity with a subpicosecond time duration. At first glance, this seems to be the good candidate to produce warm dense matter: according to their short-pulse duration, these lasers could heat solid material to elevated temperatures with minimal hydrodynamic expansion [44]. Furthermore, they can be used directly or indirectly as a diagnostic to probe any plasma with a very good temporal resolution.

However solid-density targets are optically thick to optical laser. The laser light is reflected at the surface and penetrates into the solid target over the typical laser skin depth (the length over which the evanescent electromagnetic field penetrates). For 1 µm wavelength light, it is typically equal to 10-100 nm. Consequently, the laser can only heat the surface of the target while the inner parts are heated by thermal conduction occurring over the same time scale than the thermal expansion of the plasma. In addition, since the laser is reflected at the target surface, the coupling between the laser and the target remains very poor and the energy deposition small compared to the energy delivered. Even if P-polarized laser light can be used to increase the energy coupling through resonant absorption mechanism (see chapter III), this mechanism generates suprathermal electrons which deposits their energy deep inside the target if thick enough, and generates large spatial temperature and density gradient within the target [45].

I.4.2 Electron heating

Short-pulse laser generated suprathermal electrons can also be used to heat WDM since they penetrate into high-density matter and can deposit their energy before thermal expansion occurs.

High-intensity short-pulse laser interacting with solid-density targets generates suprathermal electrons through various acceleration processes, such as resonant absorption or ponderomotive acceleration, which are further described in chapter III (section III.2.2). These so-called hot electrons propagate at near-relativistic speed forward inside the target and can deposit energy in zones beyond the reach of the laser.

Two kinds of phenomena are involved when speaking of the hot electron transport inside the target. First, hot electrons are subject to collisions with the background electrons (associated principally with their slowing down) and ions (associated with their angular deflection) of the target. Second, if the hot electron current is dense enough, typically for laser intensities above $10^{17}\ W/cm^2$ [46], collective effects come into play. The charge separation associated with the acceleration of the electrons from the target surface towards the inside of the target generates a restoring electrostatic field. In addition, the hot electron current inside the target causes the fast rise of an azimuthal magnetic field. It induces an electromotive field which contributes to the hot electron slowing down, but also to the generation of a return current carried by the background electrons. All of these processes have to be taken in account when estimating the energy deposition of the electrons.

In order to increase the heating efficiency and uniformity, one uses targets much thinner than the hot electrons mean free path. The hot electrons pass through the target with a negligible energy loss and produce a charge separation at the target edge resulting in a large electrostatic sheath field that causes their longitudinal refluxing [47]. The hot electrons are then trapped inside the target and recirculate, transferring their energy to the target until being thermalized. To illustrate the process of thermalization and estimate its time scale, let us look at the evolution of the temperature of, respectively, the hot electrons, the background electrons and the ions of a 10 µm solid-density initially cold (300 K) aluminum sample induced by a hot electron typically generated by a $10^{18}\ W/cm^2$ short-pulse laser with a 1 D simulation using the code described in Ref. [48]. One can see in Figure I-11 that the hot electrons transfer their energy to the background electrons which in turn heat the ions at a slower rate. In our example, the target thermalizes within approximately 20 ps to a temperature of 30 eV.

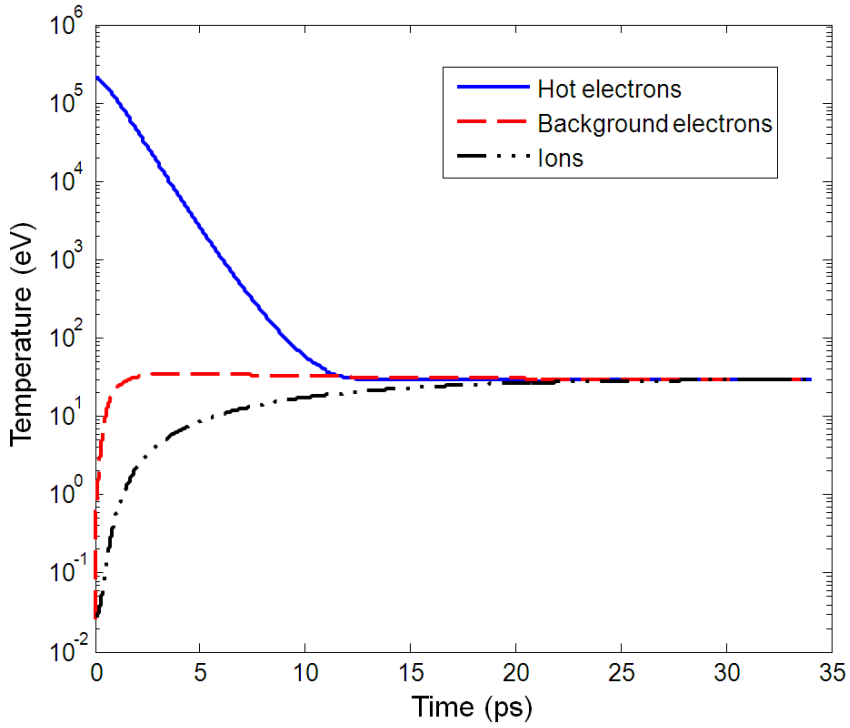

Figure I-11: Evolution of the hot electrons (blue), background electrons (red) and ion (black) temperatures induced in a 10 µm solid-density cold aluminum by hot electrons typically generated by a $10^{18}\ W/cm^2$ short-pulse laser.

However, as shown in Ref. [46], due to electron scattering, the resulting temperature is not spatially uniform. The spreading of the hot electrons creates a radial temperature gradient in the foil with a temperature ten times higher in the central laser spot compared to the surrounding region. This effect can be reduced and the heating enhanced if one uses small-mass targets having size of the order of the laser focal spot [49]. The hot electrons are then also trapped in the transverse dimension along which they gain in uniformity and density.

Nevertheless, the confinement at high-density of the target is still limited by both the hot electrons temperature and the thickness of the sample. To increase the confinement time, buried-layer targets, i.e., in which the WDM zone is sandwiched by foils of other material which decompress less, are commonly used [50]. Currently, dense plasmas have been isochorically heated by electrons up to 200 eV [51, 52, 53]. It should be noted that temperature gradients along the laser axis are still observed, the temperature decreasing from the region of laser interaction to the rear side of the irradiated target [54].

I.4.3 Shock compression

Two different approaches exist to compress a solid and have access to plasma densities higher than the solid one. The first one is static [55]. It consists in compressing a solid-density material between two anvils. Currently, one usually uses diamond anvils: it allows reaching pressures up to 300 Gbar, but also presents the advantage that, due to the transparency of diamond, optical probing can be used to study the properties of the compressed material.

The second method is dynamic [56]. The principle is to launch a shock wave inside the matter which can then reach very high densities during a few nanoseconds. On the contrary to the static approach, this method increases not only the pressure but also the temperature of the material: matter passes then very quickly from a cold solid (or gas) state to a very dense and high temperature plasma. The pressure reached in the material can be very important, but is limited by the simultaneous temperature increase. Indeed contrary to the static method, the compression generated by the shock wave is adiabatic. The compression is therefore counteracted by the increase of the internal energy of the compressed matter. As a consequence, in the best case, i.e., if there is no other source of heating, a shock wave cannot compress more than four times the target initial density [57]. The coordinates in density and temperature reached by the compression are always located on a Rankine-Hugoniot curve entirely determined by the initial condition of the target. To reach higher density with a moderate increase in temperature, it is also possible to compress the sample quasi-isentropically by launching successive shocks inside the matter instead [58].

Shock waves can be generated by different methods: gas guns [59], Z-pinch machines [60] or high energy lasers [61]. It should be noted that one can couple both static and dynamic methods to reach higher densities and different Rankine-Hugoniot curves [56]: the foil is precompressed using static methods and then shock-compressed. The final compression factor is then equal to the product of both method factors.

Regarding the laser-shock compression method, the shock wave is generated by irradiating the solid target with a nanosecond laser beam. The target is generally composed of a pusher and a sample that one wants to compress. The high intensity laser irradiates the pusher and creates a hot plasma at the front target surface. When the plasma relaxes into vacuum, as a reaction, a shock wave is generated and launched into the target, compressing it: this is called the rocket effect. This is actually the method employed in inertial fusion to compress and heat the targets. The laser and the target characteristics can be adjusted to uniformly compress and heat the sample [62, 63]. Note that the

laser temporal profile can also be modified in order to switch from adiabatic to quasi-isentropic compression with the ramp compression method [58].

This technique is currently one of the best to generate the high-pressure (of the order of 10 Mbar) and low-temperature (of the order of 1 eV) plasmas that can be found, for instance, in planetary interiors [3]. Several studies have demonstrated its validity to study EOS [64] or shock compressed material structural properties. To conclude, the laser-induced shock compression method allows creating homogeneous and thick WDM samples of density above the solid-density and during several ns. Studies are currently conducted to enhance the ability to control the density and temperature conditions that can be reached [65].

I.4.4 X-ray heating

X-rays have a wavelength in the range of 0.01 to 10 nm, corresponding to frequencies in the range $3\times10^{16\text{-}19}$ Hz and energies in the range 100 eV to 100 keV. They are commonly divided into two classes: soft X-rays (below 5-10 keV) and hard X-rays (above 5-10 keV). In our case we will remain in the soft X-ray regime. Contrary to optical rays, X-rays (photons) are able to penetrate further inside high density, and thus allows both probing and volumetrically heating high-density matter (see Figure I-12). The main mechanism of absorption is expected to be X-ray photoabsorption which produces a vacancy in the inner-shell. Rapid Auger decay (of the order of 1 fs) as well as radiative decay processes transfers energy to the electrons resulting in heating. The initial non thermal electron energy distribution then relaxes to a thermal one, producing a warm dense plasma on a short time scale (typically 1-5 ps for an aluminum foil heated by soft X-rays to 13-15 eV [66]). We will present three different techniques that are currently used to heat solid-density matter with X-rays.

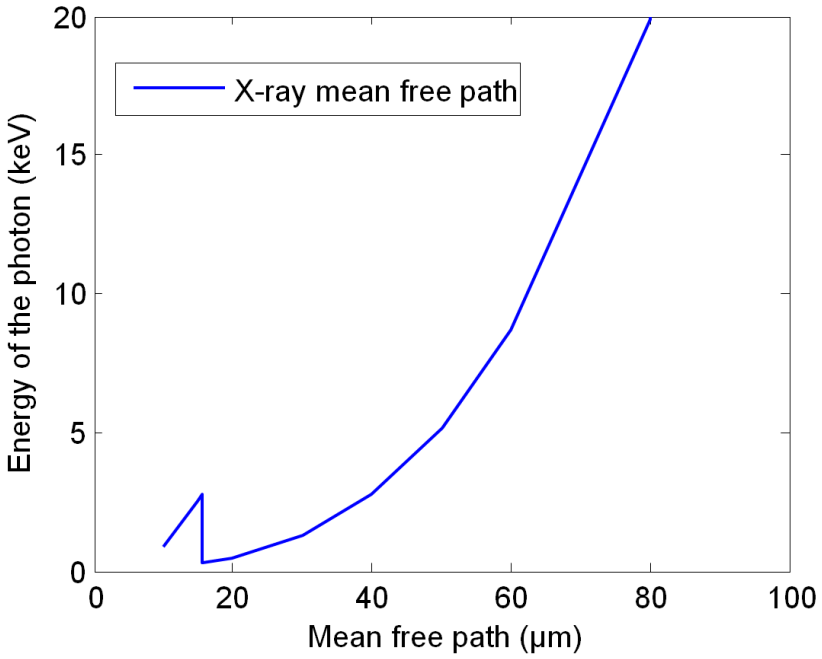

Figure I-12: X-ray photon energy as a function of the photon mean free path in cold solid-density aluminum [69].

I.4.4.1 X-ray generated by laser

The first technique uses high power lasers to generate X-ray fluxes. It is currently used in the frame of the indirect scheme of inertial fusion. The principle is simple: when irradiating a high-Z material by a high-energy laser, a part of the absorbed energy is re-emitted at a higher wavelength, depending on the temperature of the heated foil in an isotropic manner. Using high-intensity lasers, the temperature is typically of several tens of eV and the emission in the soft X-ray regime (0.5-2 keV). This radiation is then used to heat the sample.

This technique can be greatly improved in term of heating efficiency and uniformity by using Hohlraums instead of a planar foil to generate the X-rays [67]. A Hohlraum is a cavity whose walls are in radiative equilibrium with the radiant energy within the cavity. The sample to be heated is generally located in the center of the cavity. When heated, the cavity emits a uniform blackbody radiation with a peak in the soft X-ray regime. As soon as the sample thickness is shorter than the penetration length of the X-rays peak, the radiation is capable of heating volumetrically and quasi-uniformly the sample. It should be noted that this process induces a shock wave toward the center of the Hohlraum that compresses the target and increases its density before heating it. Targets are usually very thin (< µm) and tamped by low Z material in order to minimize density gradients and improve the homogeneity of the heated sample. In experiments using aluminum sample, a maximum thermal temperature of about 93 eV was achieved 1.5 ns after the laser impinged on the Hohlraum (for a 1 ns duration laser pulse) [68]. However, the thermal expansion of the sample caused the sample to be

diluted with respect to the solid, with a density around 0.03 g/cm^3 at maximum temperature. In addition, similarly to the direct heating by lasers, the small skin depth of X-rays (typically 3 µm skin depth in aluminum for 1 keV X-ray [69]) does not allow to create large volumes of uniform hot, dense plasma.

I.4.4.2 X-ray generated by Z pinch

The oldest technique to heat matter to WDM conditions is to use a Z pinch machine [70]. It uses the fact that two parallel wires carrying current in the same direction will be pulled toward each other by the Lorentz force. A Z pinch machine consists in a cylinder composed of an array of wires oriented along a z-axis. During a very short time, a very high current is launched inside the wires, vaporizing them into plasma. The high current conducted by the plasma generates a powerful magnetic field that compresses the plasma along the z-axis. When converging on axis, its initial kinetic energy is transferred into heating. This very hot plasma emits soft X-rays by blackbody radiation which can then be used to heat a sample. With this technique, temperatures up to approximately 60 eV have been reached for solid aluminum using a tamped foil to keep the solid density [71]. As mentioned with the Hohlraum, the small skin depth of soft X-ray radiations requires thin targets to make the heating isochoric. It should also be noted that the characteristic time scale of the heating is several tens of ns.

I.4.4.3 X-ray generated by X-FEL

The last technique, i.e., using X-ray free-electron laser (X-FEL) facilities to heat up matter, is the most recently developed. These facilities typically deliver mono-energetic, short duration (10-200 fs) and high brightness (up to 10^{13} photons/pulse) X-ray pulses with photon energies starting in the soft X-rays to hard X-ray regimes (up to approximately 20 keV for SACLA [72]) at a high repetition rates (kHz) [73]. With higher energy photons, the penetration depth is much larger than using thermal soft X-rays as in the two previous sections and allows heating thicker sample (e.g. for 10 keV photons, the penetration depth in Al is above 100 µm [69]). Furthermore, if the sample thickness is shorter than the photon mean free path, the energy of the photons can be considered almost constant while going through the matter, the energy deposition (which depends only on the photon energy) is then very uniform inside the matter. Nevertheless, it should be noted that in such case, the energy used to heat the matter is small compared to what is actually delivered by the free electron laser.

As a result, the heating is isochoric (short duration) and homogeneous along the free electron laser axis. In a recent experiment that took place at LCLS [66,74], silver foils of 0.5 µm thickness were irra-

diated by 9 keV X-ray pulses of 60 fs FWHM (full width at half maximum) duration. The 1.05 to 1.55 mJ bunch was focused to 14x17 μm^2 FWHM at the sample plane. The optical measurements of the heated foil expansion supported by numerical projections indicate a target temperature of 11 to 15 eV depending on the X-ray irradiance, i.e., 4.4 to 6.5×10^{15} W/cm² (which corresponds approximately to 10^{12} photons/pulse) with a remarkable uniformity of density and temperature in the longitudinal plane of the laser. It is worth noticing that, based on K alpha emission measurements coupled with a radiative-collisional code, S. M. Vinko et al. reported as well the experimental creation of solid-density aluminum plasma to non-equilibrate radiation temperatures above 100 eV using also the LCLS X-ray free-electron laser [75]. The 1 µm thick aluminum target was typically heated by 80-fs X-ray pulses at photon energies in the range 1.56–1.83 keV with a similar irradiance (10^{12} photons).

I.4.5 Ion heating

The energy deposition of an energetic ion is very typical. Contrary to X-rays, energetic electrons and optical photons, the projectile deposits most of its energy at the end of its range. In Figure I-13, the different functions of energy deposition per unit length in water for X-rays, electron and protons are shown [76]. The deposited energy by the X-rays is proportional to their number. Therefore the energy deposition is the highest in the first layers of the irradiated material and gradually decreases in deeper layers with the photons getting absorbed or scattered by the medium. When fast electrons and ions moves through matter, they lose and deposits energy along their path. Nevertheless, due to their light mass, incident electrons are scattered by (mostly) nuclei of the medium [77]. The electron energy deposition is therefore spread in the transverse direction as the electrons progress forward in the initial direction, decreasing the average energy deposition per unit length in the material. Consequently, the relative dose they deposit along their path decrease with the thickness. At the opposite, ions are barely affected by the scattering until the very end of their range where their velocity is getting close to the velocity of the target electrons (approximately 0.1 MeV for protons in aluminum), at which stage, they propagate in straight lines [78]. As we will see later, in this velocity domain, the interaction cross-section of a charged particle with the medium increases as the particle velocity, v, (or energy) decreases and becomes proportional to $1/v^2$ [78]. The ion energy deposition therefore increases with the penetration depth and they deposit most of their energy at the end of their range in a very narrow peak known as the **Bragg peak** [79] (see Figure I-13). Note that the latest figure concerns the energy deposition in cold matter, it may be very different when the energy is deposited in hot matter [80].

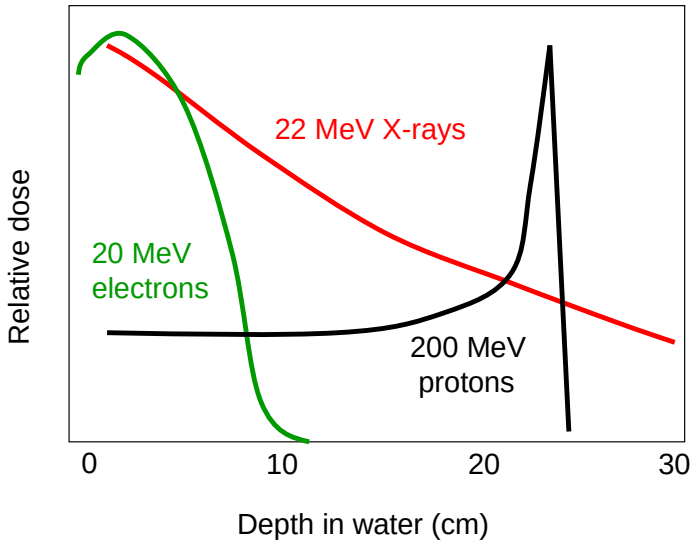

Figure I-13: Diagram of the energy deposition of electron, X-ray and proton monoenergetic collimated beams in cold water (extracted from Ref. [76]).

Two different sources of collimated ion beams currently exist: they are generated either by conventional accelerator or by high-power short-pulse lasers.

I.4.5.1 Ion beams generated by conventional accelerator

A conventional accelerator such as a cyclotron or synchrotron basically delivers mono-energetic light or/and heavy ion (up to uranium) beams up to very high energies (e.g. up to 3.5 TeV protons at LHC or 1 - 2 GeV per nucleon at GSI). Working on the same principle as X-rays and electrons, the energy deposition of such a beam in a thin target, i.e., a target with a thickness well below the projectile range, would lead to a volumetric and even more uniform heating with respect to what has been already presented. Furthermore, as we will see after, the energy deposition of such very high energy particles is well-known and little sensitive to the temperature of the sample. However this method suffers from major drawbacks: first, since the particle energy is far from the one that corresponds to the Bragg peak, we use only a very small part of the energy that is actually delivered by the accelerator. Second, the ion flux accessible with conventional accelerator is pretty low with respect to what is actually needed to heat the matter to high temperature (e.g. in Ref. [81], SIS-18 (GSI) is said to deliver around 10^8 uranium ions per cm² per ns with an energy of a few hundreds MeV per nucleon. Such a beam would roughly induce an increase of temperature of 13 K per ns in a 10 µm thick solid-density aluminum target. Third, the ion pulse duration ranges from a few nanoseconds to hundreds of nanoseconds at constant flux. With such a time scale, thermal expansion needs definitely to be taken into account. Because of the reasons listed above, up to now, to our knowledge, conventional accelerator ion beams have never been used experimentally to produce warm dense matter. Generally, the warm dense matter is generated by a pump laser; the ion beam is then used to probe the medium

[82]. With the upcoming of new facilities delivering higher ion flux, simulations have been performed to estimate what density and temperature would be achievable. Using as an input a hundred nano-second duration, uranium ion beam (U^{28+}) composed of 2 x 10^{11} ions accelerated to 200 MeV per nucleon and collimated on a spot of 0.5 mm diameter FWHM, one predicts that a cylindrical solid hydrogen sample tamped by a carbon layer will be isochorically heated up to 1 eV along the ion beam axis [81]. According to the simulation, the thermal expansion is predicted to cause the density of the hydrogen in the center of the sample (the part most exposed to the radiation) to be reduced at the beginning of the irradiation. This effect is counteracted by the expansion of the tamper which tends to compress the hydrogen sample. After 100 ns, the density of hydrogen is found to be equal to 80 % of the solid density.

I.4.5.2 Ion beams generated by short-pulse laser

As we will see in chapter III, ion beams generated by high-intensity short-pulse laser are fundamentally different from those delivered by conventional accelerators. Although these ion beams exhibit modest energies (up to approximately 65 MeV at present [83]) compared to the beams generated in the accelerators, their main advantage rely on their broadband spectrum (see Figure I-14) and on being produced on a very short time scale, i.e., a few ps.

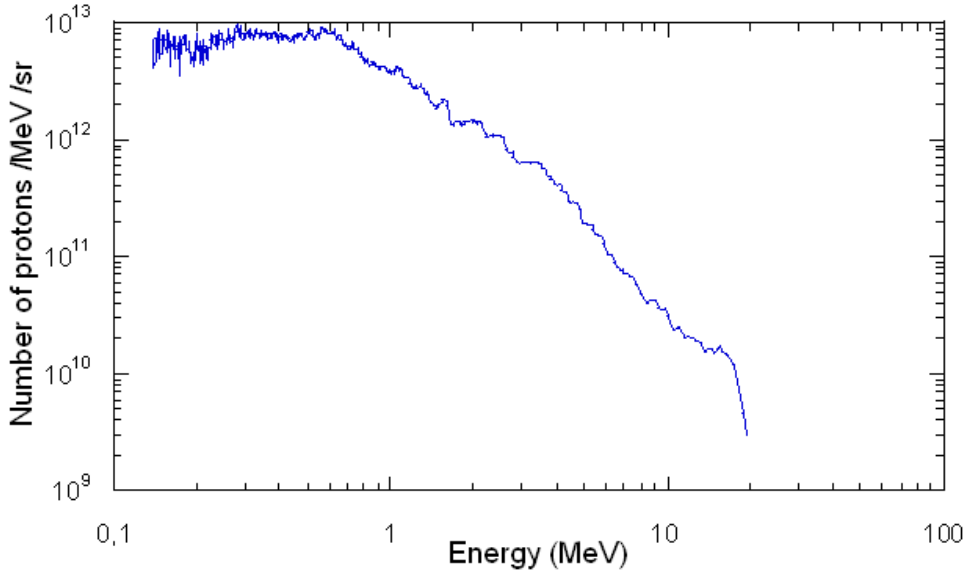

Figure I-14: Typical proton beam spectrum generated by the 100 TW high-intensity short-pulse laser at LULI (1 µm wavelength, 400 fs, 25 J, intensity around 5×10^{19} W/cm^2 on a 10 µm gold target).

On one hand, the broadband aspect allows efficient and volumetric heating of a thin sample, since the ions of the low energy part of the spectrum are stopped inside the thin target. Indeed, each projectile of the continuous ion distribution will deposit most of its energy at a certain depth determined

by its energy. When integrating over the whole distribution, the sample is quasi-homogeneously heated (see Figure I-15).

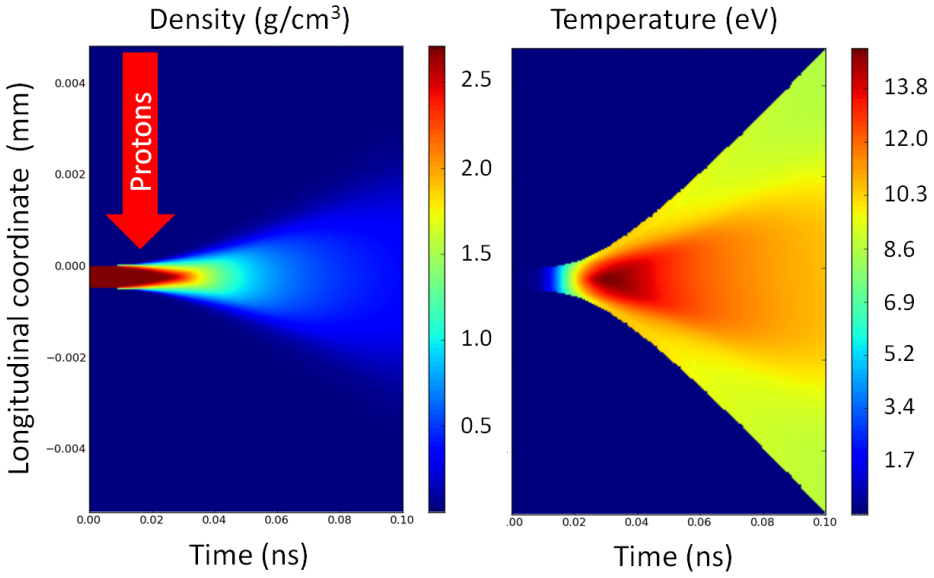

Figure I-15: Temporal evolution of the density and temperature (obtained from the 1D hydrodynamic code, ESTHER (see chapter IV)) along the target longitudinal coordinate of a 10 µm solid-density aluminum foil heated by the proton beam shown in Figure I-14.

On the other hand, the very short duration of the beam at the source allows to heat the sample before the target starts its thermal expansion. The heating time scale is therefore almost determined by the different times of flight of the beam ions from their source to the target to be heated. As an example, after 300 µm of propagation, there are only approximately 20 ps of debunching time between protons with 0.5 MeV and 5 MeV, energies that were produced simultaneously. Since the proton energy deposition time (few tens of ps) is shorter than the hydrodynamic expansion time (of the order of a 100 ps for a 10 µm solid-density aluminum foil), the sample that is heated by the laser-accelerated proton beam can stay close to its initial density, i.e., above 10 % of it, during more than 100 ps (see Figure I-16), which is a sufficient time to perform thermodynamic measurements. These two aspects make proton heating to be currently one of the most interesting methods to create warm dense matter.

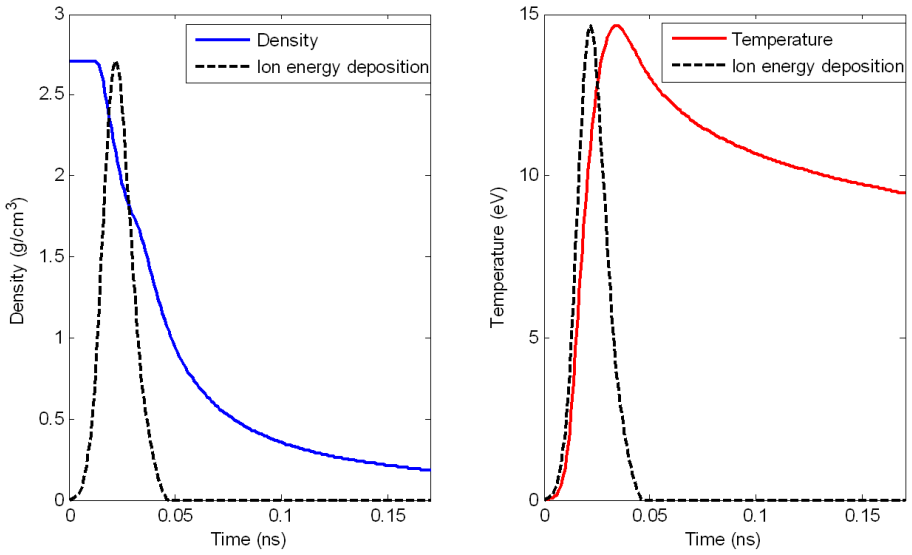

Figure I-16: Temporal evolution of the temperature and density in the center of a 10 µm thick solid-density aluminum target heated by a laser-generated proton beam (obtained from the 1D hydrodynamic code, ESTHER (see chapter IV)). The energy deposition of the ion beam (normalized to its maximum) is plotted as a reference in order to show its short time scale with respect to the target expansion.

The isochoric heating by a high-intensity laser accelerated proton beam was first demonstrated by P. Patel et al. [84] on the LLNL 100 TW Janus laser, operating at 800 nm and delivering 10 J of energy in a 100 fs duration pulse and focused to a 5 µm FWHM laser spot. In this experiment the laser spot was defocused to a 50 µm in diameter with an average intensity of 5 x 10^{18} W/cm^2 in order to optimize the proton beam for the application. Two source target geometries were studied: planar and hemispherical. The heated target was an aluminum foil positioned respectively, at 250 and 160 µm from the proton source target (in the hemispherical case, the heated Al foil is placed in a plane coinciding with the geometric center of the shell; the radius of the hemisphere is therefore 160 µm). The purpose of the hemispherical target was to obtain a more concentrated proton beam, i.e., to enhance the flux on the target [85]. From the emission measurements coupled to a hydrocode (LASNEX [86]), it was estimated that the 10 µm thick Al foil was heated up to 4±1 eV over an area of around 200 µm in diameter. In the hemispheric geometry, the heating was localized to a 50 µm diameter area with a temperature up to 23±6 eV.

Later, P. Antici at al. [87], using the 100 TW laser at LULI, Ecole Polytechnique, demonstrated that the heating decreases with the increasing target thickness. It was also shown that with the atomic number Z of the target the heating increases as well. This is expected since the stopping power of the protons increases with higher Z targets.

It is worth noticing that R. Snavely [88] reported reaching isochoric heating temperatures of 81 eV in 15 µm thick Al slab. Their experiment was performed on the Gekko PW laser using 1 µm light at an intensity of 3×10^{18} W/cm^2 incident on a hemispherical aluminum shell.

I.4.6 Conclusion

Among all the methods presented above, shock compression, X-ray heating and ion heating have shown to be the best methods to generate uniform, solid-density warm samples. Using these methods, one can achieve a density close or even above the solid one (through shock compression for the latter) with temperatures from 1 to 100 eV. The characteristic of the heated matter are however not all the same. On one hand, using X-FEL and ion beam generated by laser techniques, the energy is deposited uniformly inside the sample in a very short time scale. As a result, the sample stays in the warm dense matter regime before the thermal expansion occurs (e.g. for a 10 µm aluminum foil heated up to 10 eV, it corresponds to approximately 100 ps). On the other hand, the other techniques, i.e., shock compression, ion heating using accelerator beams, X-ray heating using Holhraums or Z pinch, allows the matter to stay in the warm dense regime over nanoseconds, even 100 ns in the case of ion heating using accelerator beams, but at the expense of higher complexity of target design and higher energy input to reach the same temperature.

I.5 Conclusion

In this chapter, we have introduced WDM from both theoretical and experimental points of view.

The two different *ab initio* codes, SCAALP and ABINIT, that will be employed to model WDM in this thesis, have been presented. They will be particularly used in the next chapter to estimate the behavior of a charged particle propagating inside WDM.

Among the different methods presented in this chapter to produce WDM, we will choose to use solid-density targets heated by short-pulse laser-generated proton beams as our preferred method to study stopping power in WDM.

References

[1] R. W. Lee et al., J. Opt. Soc. Am. B **20**, 770 (2003)
[2] DOE report, High Energy Density Laboratory Physics Research Needs workshop, Rockville, MD (2009), https://e-reports-ext.llnl.gov/pdf/307164.pdf
[3] B. A. Remington et al., Rev. Mod. Phys. **78**, 755 (2006)
[4] T. Ao et al., Phys. Rev. Lett. **96**, 055001 (2006)
[5] J. Ye et al., Phys. Plasmas **18**, 032701 (2011)
[6] P. Mora, lecture notes, *Introduction to Plasma Physics,* École Polytechnique, Palaiseau (2009)
[7] N. W. Ashcroft & N. D. Mermin, *Solid State Physics,* Philadelphia: Saunders College (1976)

[8] L.D. Landau, E.M. *Lifshitz. Statistical Physics, Part 1. Vol. 5*, Oxford: Butterworth–Heinemann (1980)
[9] M. Rax, *Physique des plasmas*, Paris: Dunod (2005)
[10] S. Atzeni & J. Meyer-ter-Vehn, *The Physics of Inertial Fusion*, Oxford: Oxford University Press (2004)
[11] R. M. More*, Applied Atomic Collision Physics* Vol. 2*,* New York: Academic Press (1982)
[12] F. Perrot & M.W.C. Dharma-Wardana, Phys. Rev. E **52**, 5352 (1995)
[13] S. P. Lyon & J. D. Johnson, *T-1 Handbook of the SESAME Equation of State* , LANL report LA-CP-98-100 (1998)
[14] A. E. Mattsson et al., Model. Simul. Mater. Sci. Eng. **13**, R1 (2005)
[15] N. D. Mermin, Phys. Rev. A **137**, 1441 (1965)
[16] P. Hohenberg & W. Kohn, Phys. Rev. **136**, B864 (1964)
[17] W. Kohn & L. J. Sham, Phys. Rev. **140**, A1133 (1965)
[18] M. Desjarlais, Quantum Molecular Dynamics Calculations of Warm Dense Matter and Application to Pulsed Power Experiment, WDM Winter School, LLNL (2008), http://hifweb.lbl.gov/wdmschool/talks/09_Desjarlais.pdf
[19] R. M. Martins, *Electronic Structure: Basic Theory and Practical Methods*, Cambridge: Cambridge University Press (2008)
[20] D. M. Ceperley & B. J. Alder, Phys. Rev. Lett. **45**, 566 (1980)
[21] B. Saha et al, ACS Nano **3**, 2241 (2009)
[22] R. Car & M. Parrinello, Phys. Rev. Lett. **55**, 2471 (1985)
[23] M. Born & R. Oppenheimer, Annalen der Physik **389**, 457 (1927)
[24] T. R. Mattsson & M.P. Desjarlais, Phys. Rev. Lett. **97**, 017801 (2006)
[25] L. A. Collins et al., Phys. Rev. B **63**, 184110 (2001)
[26] M. P. Desjarlais, Phys. Rev. B **68**, 064204 (2003)
[27] M. P. Desjarlais et al., Phys. Rev. E **66**, 025401 (2002)
[28] J. Clerouin et al., Phys. Rev. B **71**, 064203 (2005)
[29] J. C. Phillips & L. Kleinman, Phys. Rev. **116**, 287 (1959)
[30] R. M. Martins, *Electronic Structure: Basic Theory and Practical Methods*, Cambridge: Cambridge University Press (2008)
[31] J. Ihm et al., J. Phys. C **12**, 4409 (1979)
[32] P. Denteneer & W. van Haeringen, J. Phys. C **18**, 4127 (1985)
[33] M. C. Payne et al., Rev. Mod. Phys. **64**, 1045 (1992)
[34] C. Blancard & G. Faussurier, Phys. Rev. E **69**, 016409 (2004)
[35] G. Faussurier, Phys. plasma **17**, 052707 (2010)
[36] R.P. Feynman et al., Phys. Rev. **75**, 1561 (1949)
[37] J. M. Ziman, Advances Phys. **13**, 89 (1964)
[38] J. P. Hansen and I. R. McDonald, *Theory of Simple Liquids*, London: Academic Press (1986)
[39] K. J. Runge & G. V. Chester, Phys. Rev. B **38**, 135 (1988)
[40] R. P. Drake, *High Energy Density Physics*, New York: Springer (2006)
[41] J. M. Ziman, Philos. Mag. **6**, 1013 (1961)
[42] L. Mestel, Proc. Cambridge Philos. Soc. **46**, 331 (1950)
[43] D. Strickland & G. Mourou, Opt. Commun. **56**, 219 (1985)
[44] Y. Ping et al., High Energy Dens. Phys. **6**, 246 (2010)
[45] P. Audebert et al., Phys. Rev. Lett. **89**, 265001 (2002)
[46] F. Pérez, Ph.D. thesis, École Polytechnique, Palaiseau (2011)
[47] A. Forsman et al., Phys. Rev. B **58**, R1248 (1998)
[48] P. Antici et al., to be submitted to New J. Phys.
[49] S. D. Baton et al., High Energy Dens. Phys. **3**, 358 (2007)

[50] M. Edwards et al., Phys. Rev. Lett. **97**, 35001 (2006)
[51] P. M. Nilson et al., Phys. Rev. E **79**, 016406 (2009)
[52] G. Gregori et al., Contrib. Plasma Phys. **45**, 284 (2005)
[53] S. N. Chen et al., Phys. Plasmas **14**, 102701 (2007)
[54] M. H. Key et al., J. Phys. IV (France) **133**, 371 (2006)
[55] A. W. Lawson & T.Y. Tang, Rev. Sci. instrum. **21**, 815 (1950)
[56] P. Loubeyre et al., High Press. Res. **24**, 25 (2004)
[57] L. F. Henderson, *Handbook of Shock Waves, Vol. 1*, San Diego: Academic Press (2001)
[58] M. Bastea et al., App. Phys. Lett. **95**, 241911 (2009)
[59] S. T. Weir et al. , Phys. Rev. Lett. **76**, 1860 (1996)
[60] M. D. Knudson et al., Phys. Rev. Lett. **87**, 225501 (2001).
[61] G. W. Collins et al., Science **281**, 1178 (1998)
[62] M. Koenig et al., Phys. Rev. E **50,** R3314 (1994)
[63] A. Benuzzi et al., Phys. Plasmas **5**, 1 (1998)
[64] L. B. Da Silva et al., Phys. Rev. Lett. **78**, 483 (1997)
[65] K. T. Lorentz et al., High Energy Dens. Phys. **2**, 113 (2006)
[66] A. Levy et al., Phys. Rev. Lett. (submitted)
[67] T. S. Perry et al., Phys. Rev. E **54**, 5617 (1996)
[68] J. Zhang et al., Phys. Rev. E **79**, 016401 (2009)
[69] NIST, X-ray attenuation database, http://www.nist.gov/pml/data/xraycoef/index.cfm
[70] M.A Liberman et al., *Physics of High-Density Z-Pinch Plasmas,* New York: Springer (1999)
[71] J. J. MacFarlane et al., Phys. Rev. E **66**, 046416 (2002)
[72] http://xfel.riken.jp/eng/sacla
[73] https://portal.slac.stanford.edu/sites/lcls_public/Pages/Default.aspx
[74] J. Dunn, et al., Proc. SPIE **8140**, 81400O (2011)
[75] S. M. Vinko et al., Nature **482**, 59 (2012)
[76] J. Fuchs, Production de plasmas d'Al denses et dégénérés par faisceau de protons accélérés par laser, IRMDSP workshop, Saclay, France (2008)
[77] ICRU Report 37, Stopping Powers for Electrons and Positions (1984)
[78] ICRU Report 49, Stopping Powers and Ranges for Protons and Alpha Particles (1993)
[79] W. H. Bragg & R. Kleeman, Phil. Mag. S **6**, 726 (1904)
[80] J. D'Avanzo et al., Nucl. Fusion **35,** 210 (1995)
[81] A. Kozyreva et al., Phys. Rev. E **68**, 056406 (2003)
[82] A. Franck et al., Phys. Rev. B **81**, 026401 (2010)
[83] S. A. Gaillard et al., Phys. Plasmas **18**, 056710 (2011)
[84] P. K. Patel et al., Phys. Rev. Lett. **91**, 125004 (2003)
[85] S. N. Chen et al., Phys. Rev. Lett. **108**, 055001 (2012)
[86] G. B. Zimmerman & W. L. Kruer, Comments Plasma Phys. Controlled Fusion **2**, 85 (1975)
[87] P. Antici et al., J. Phys. IV (France) **133**, 1077 (2006)
[88] R. Snavely et al., Phys. Plasmas **14**, 092703 (2007)

II. ION STOPPING POWER IN WARM DENSE MATTER

From the end of the 19th century and the first observations performed by Thomson on this topic [1] to our days, the theory of the propagation of charged particles through matter has been a subject of continuing interest [2]. This interest is driven by at least two things: first, the desire of physicists to be able to calculate the energy lost by a particle when propagating through matter and, second, the need for understanding such process because of its role in nuclear physics [3], radiation chemistry [4], and radiation biology [5].

After defining the notion of stopping power and the different parameters that play a role in stopping power studies, we focus on the theoretical calculation of the stopping power in cold material based on the dielectric theory developed by Lindhard and co-workers [6]. The use of "cold" should be here understood as representative of temperatures well-below the Fermi temperature of the electrons, i.e., temperatures around room temperature [7]. Then, we present how this theory can be extended to treat matter at higher temperature. Finally, the impact of temperature on the stopping power in solid-density aluminum is estimated according to the dielectric theory using the average-atom model SCAALP and the QMD code ABINIT.

II.1 Definition

When an ion propagates as a projectile through matter, it loses energy through interactions with the medium. This energy is transferred to the medium through different processes [8]: electronic excitation and ionization of the medium, projectile excitation and ionization, electron capture, nuclear stopping and electromagnetic radiation. The contribution of each process depends on the following quantities [8]: mass and velocity of the projectile-ion, constituents of the medium, density or temperature of the medium.

The stopping power of a projectile propagating through matter is defined as its average energy-loss $-dE$ per unit path length *dl* when passing through matter in straight line [8], noted, $-\frac{dE}{dl}$.

One can also find in literature the stopping power reduced to the mass density of the medium, ρ, called mass stopping power or stopping power per target mass unit [8],

$$-\frac{1}{\rho}\frac{dE}{dl}, \tag{2.1}$$

It can also be reduced to the atomic density of the medium n_i, giving the stopping cross-section, S, which corresponds to the average energy-loss per target atom [8],

$$S = -\frac{1}{n_i}\frac{dE}{dl}. \tag{2.2}$$

The average energy-loss being the result of stochastic processes, a number of identical particles starting out under identical conditions will show a distribution of energies and trajectories as they propagate inside matter. The fluctuation in energy-loss per unit path length is characterized by the straggling parameter W [8],

$$W = \frac{1}{n_i}\frac{d\langle(\Delta E - \langle\Delta E\rangle)^2\rangle}{dl}, \tag{2.3}$$

where $\langle(\Delta E - \langle\Delta E\rangle)^2\rangle$ is the variance of the energy loss after a given path length l.

In the context of many applications such as radiation protection [8], material analysis by ion beams [9], ion implantation in semiconductor technology [10] or hadron therapy [5], determining the particle range, i.e., the length of penetration of a charged particle until it comes to rest, is of tremendous importance. Different ranges are defined in Ref. [8], we introduce here the three most common:

- the Continuous-Slowing-Down Approximation (CSDA) range, *R*: this range is calculated assuming that the energy loss by the projectile at every point along its path is given by the average stopping power (see Figure II-1). In this approximation, energy-loss fluctuations are therefore neglected. The CSDA range is thus calculated by integrating the reciprocal of the total stopping power. In matter at zero-temperature, the CSDA range is,

$$R(E_{initial}) = \int_0^{E_{initial}} \left(-\frac{dE'}{dl}\right)^{-1} dE' = \int_0^{E_{initial}} \frac{dE'}{n_i S(E')}, \tag{2.4}$$

  where $E_{initial}$ is the initial energy of the projectile.

  A particle propagating inside a finite-temperature matter ends up thermalized in the matter at energy E_{th} [11, 12]. If $E_{initial} > E_{th}$, the CSDA range is calculated as followed:

$$R(E_{initial}) = \int_{E_{th}}^{E_{initial}} \frac{dE'}{n_i S(E')}. \tag{2.5}$$

  If $E_{initial} < E_{th}$, the projectile gains energy from the target and the stopping power becomes negative,

$$R(E_{initial}) = \int_{E_{initial}}^{E_{th}} \frac{-dE'}{n_i S(E')}. \quad (2.6)$$

- the projected range, R_p: it represents the average maximum penetration depth with respect to the initial direction of motion (see Figure II-1). In this definition, the shortening of the penetration depth due to multiple scattering of the projectiles is taken in account.
- the range straggling, R_W: it corresponds to the variance of the projected range.

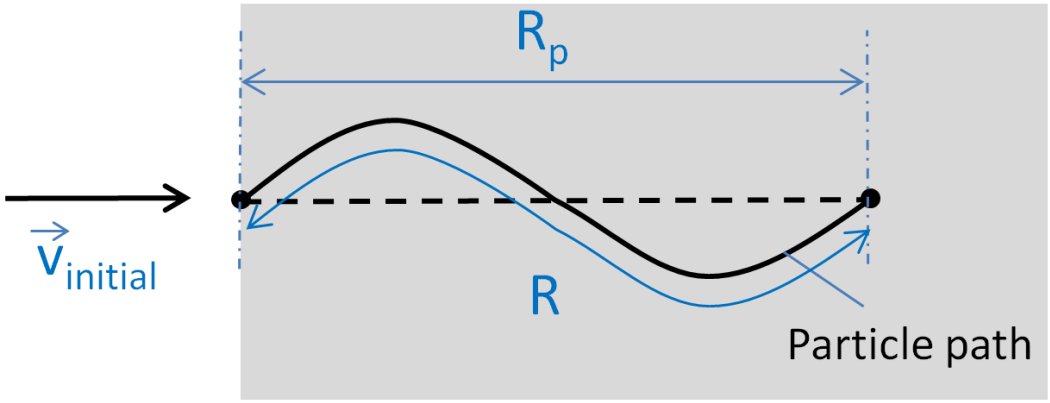

Figure II-1: Illustration of the concept of CSDA and projected ranges. In this illustration, $\vec{V}_{initial}$, the initial speed of the incident particle is directed normally to the target surface. The effect of the scattering is exaggerated in order to show the difference between the CSDA and the projected ranges.

II.2 Framework of our study

In our calculation of the ion stopping power, the ion is assimilated to a point charge eQ_1, where e is the elementary charge, of mass M_1 propagating at constant speed $\vec{v}_{10}$ through matter in straight line (see Figure II-2). This means that the path length *dl,* along which the stopping is calculated, is small enough so that the energy *-dE* transferred to the medium is negligible with respect to the projectile energy. The effect of scattering along *dl* is also neglected.

A theoretical description of the energy-loss would require taking into account the changes in the electronic configuration of the projectile ion by the various processes of ionization, electron capture and excitation occurring when interacting with the matter [13]. One can define an equilibrium mean charge state $\langle Q_1 \rangle_{eq}$ as the average projectile charge state where the ionization rate is equal to the recombination rate [14]. Assuming (i) the projectile slowing down is negligible during the time of equilibrium, the necessary time for the projectile to reach its equilibrium charge, keeping its velocity constant, and (ii) the contribution of such atomic processes to the total energy-loss is negligible, we

can separate the stopping power from the dynamics of the projectile ionization [13][2]. Thus, first we calculate the stopping power for a fixed projectile charge state Q_1, to which we add, in a second phase, the influence of the projectile charge state.

In addition, we consider that the particle passes through matter at thermal equilibrium: the atomic density, n_i, and the temperature, T, are well-defined and uniform along dl. Since we will not treat compound targets in this thesis, we restrict our calculations to single-species matter with atomic number Z_2 and mass M_2.

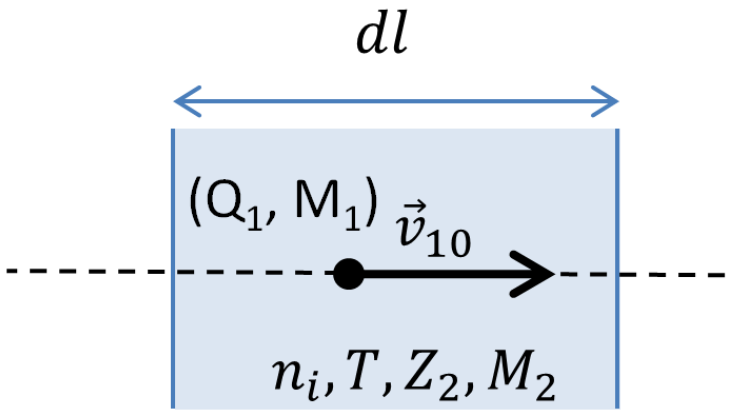

Figure II-2: Illustration of the framework of our study.

In literature, the energy-loss of ions propagating through matter is traditionally divided into two components [8]: the elastic and the inelastic loss. The elastic loss is defined as the energy-loss due to elastic Coulomb collisions in which the recoil energy is transferred to atoms of the target material. The inelastic loss is defined as the energy-loss due to inelastic collisions with the target electrons, whether bound or free. The elastic loss is also called nuclear stopping power and the inelastic loss, electronic stopping power [2].

It is known that the nuclear stopping power has an importance only at low projectile velocity with respect to the free-electron average-velocity in the medium [11, 15]. For instance, the nuclear stopping power of protons in cold (300 K) solid-density aluminum becomes only significant with respect to the electron stopping power for energy below 1 keV, where its contribution to the total stopping power is above 10 % (see Figure II-3) [15]. Furthermore, according to the predictions given in Ref. [11], it is expected to stay below 2 % of the total stopping power for energies above 10 keV for medium temperatures below 100 eV.

[2] Such assumption is discussed in chapter IV.

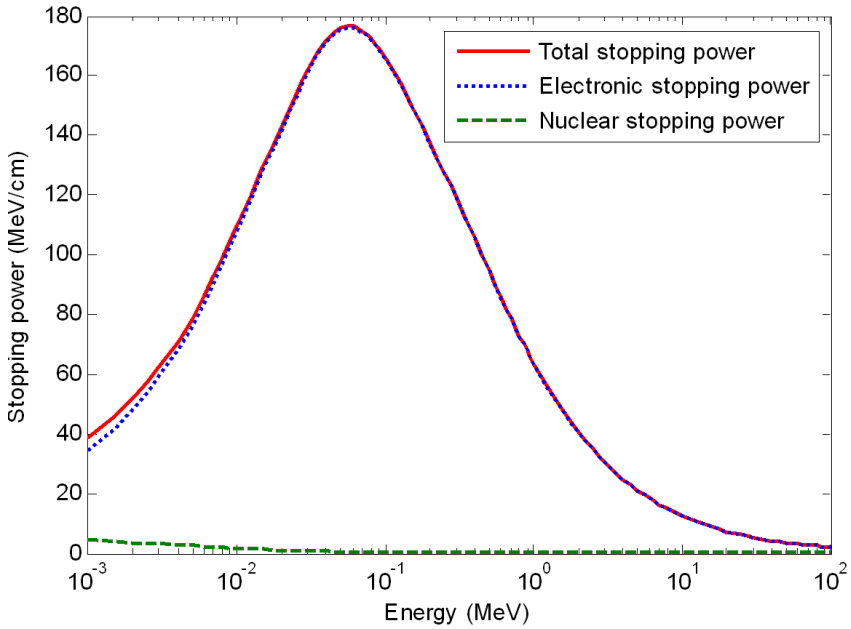

Figure II-3: Electronic, nuclear and total stopping power of proton in solid-density aluminum at 300 K from Ref. [15].

Note that very high velocity ions, typically above 1 GeV for protons, can also lose energy through emission of Bremsstrahlung. In such case, we are dealing with radiative stopping power [8].

In this thesis, we treat only the electronic stopping power which represents the main contribution to the stopping in the energy domain that is common for ions generated by short pulse laser interaction with matter and that are studied in our experiments (typically from several tens of keV to several tens of MeV for protons). Obviously, considering these energies, we neglect relativistic effects.

II.3 Ion stopping power in cold matter

Based on decades of experimental and theoretical studies (summarized in Ref. [8]), the knowledge of ion stopping power in cold matter is nowadays important [16]. The experimental stopping powers and the theories developed based on them have allowed producing stopping power tables covering a wide range of projectiles, target materials and energies (e.g. [15, 17]).

Several methods have been developed to express the electronic stopping power. The first approaches [18] based on the works of Bohr [19] and Bethe [20] were only taking in account the energy loss by binary collisions, i.e., the energy lost by the projectile while colliding with a single atom of the medium. It is only after the work of Lindhard et al. [6], on the stopping power of slow projectiles, that the energy-loss via collective effects has been taken into account. The latter is related to the motion of the collective answer of the target electrons to the projectile propagating inside the matter, increasing its energy-loss. This effect have been shown to be particularly important with respect to the bina-

ry collision contribution to the energy-loss for slow projectiles, i.e., when the target electrons have the time to screen the projectile [8].

We will here concentrate our study on the dielectric model proposed by Lindhard and Winter [21] that treats the electronic stopping power in dense matter. Contrary to models based on binary collisions between the projectile and the electrons (e.g. in Ref. [16, 22]), in the dielectric approach, one considers the energy loss is due to the polarization cloud the charged projectile creates in its wake. Thus, it automatically includes the collective effects [8].

Following Lindhard' s work, we will first present the stopping power at zero-temperature in a spatially uniform free electron gas and, in a second phase, extend it to dense matter.

II.3.1 Stopping power in a cold free electron gas

A free electron gas is defined as a plasma which electrons are embedded in a uniform neutralizing background of positive charges [23]. We consider here a homogeneous electron gas with a uniform density n_e at a zero-temperature. The approach and the computation developed in this paragraph are detailed in Ref. [23].

When propagating through a free electron gas, a charged particle induces an electric field, $\vec{E}_{ind}$, which polarizes the medium. Indeed electrons are slightly displaced into the wake of the projectile, the effect being stronger behind the projectile than in front of it (see Figure II-4). Consequently, this field will tend to act back on the particle and cause it to loose kinetic energy. The frictional force caused by the induced electric field and felt by the projectile of charge (M_1, Q_1) at the position $\vec{r}$ and time t is then,

$$\vec{F}_{ind} = Q_1 e \vec{E}_{ind}(\vec{r}, t). \qquad (2.7)$$

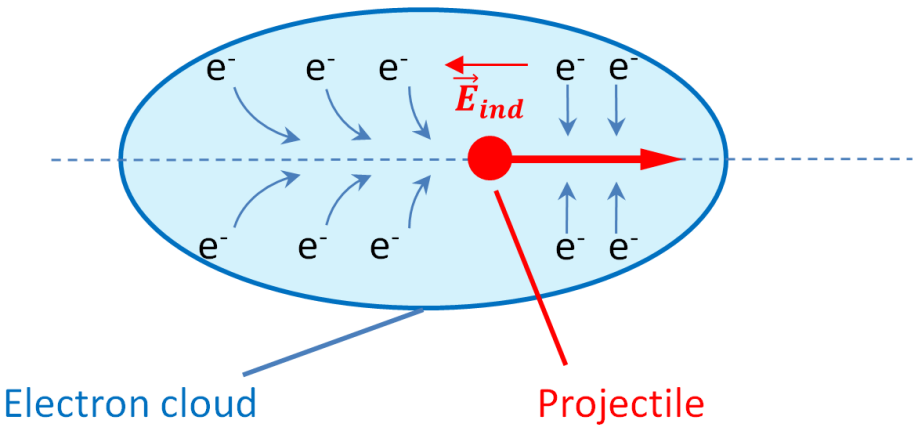

Figure II-4: Illustration of the dynamic screening of a positively charged projectile by a free electron gas.

The energy lost by the projectile propagating at a constant speed $\vec{v}_{10}$along a distance *dl* corresponds to the work of the frictional force:

$$-dE = -\vec{F}_{ind}(\vec{r},t).\overrightarrow{dl} = -Q_1 e\vec{E}_{ind}(\vec{r},t)\cdot\frac{\vec{v}_{10}}{v_{10}}dl\,. \qquad (2.8)$$

The stopping power is then given by,

$$-\frac{dE}{dl} = -Q_1 e\vec{E}_{ind}(\vec{r},t)\cdot\frac{\vec{v}_{10}}{v_{10}}. \qquad (2.9)$$

With this reasoning, the computation of the stopping power reduces to the calculation of the electric field induced by an external charge propagating in straight line at a constant velocity $\vec{v}_{10}$. Thus, we can choose our reference frame[3] so that $\vec{r} = \vec{v}_{10}t$ is the position of the projectile in space at time t. The projectile (M_1, Q_1, $\vec{v}_{10}$) can be viewed as an external and point-like space-charge density,

$$\rho_{ext}(\vec{r},t) = Q_1 e\delta(\vec{r} - \vec{v}_{10}t). \qquad (2.10)$$

Passing Eq. (2.10) in the Fourier space, one obtains,

$$\rho_{ext}(\vec{k},\omega) = \int_{-\infty}^{+\infty}\iiint_{\mathbb{R}^3} dt\, d^3r\, \rho_{ext}(\vec{r},t)e^{-i(\vec{k}\cdot\vec{r}-\omega t)} \qquad (2.11)$$

$$= 2\pi Q_1 e\delta(\omega - \vec{k}\cdot\vec{v}_{10}).$$

The external potential induced by the point charge is calculated using the Poisson equation in the Fourier space:

[3] This choice greatly simplifies the mathematical operations developed after.

$$\varphi_{ext}(\vec{k},\omega) = \frac{\rho_{ext}(\vec{k},\omega)}{k^2\varepsilon_0} = \frac{Q_1 e}{k^2\varepsilon_0} 2\pi\delta(\omega - \vec{k}\cdot\vec{v}_{10}). \quad (2.12)$$

If we assume that the plasma answers linearly to the perturbation, the response of the plasma to the external potential is determined by the dielectric function of the free electron gas, ε. This yields in the Fourier space [23],

$$\varphi_{total}(\vec{k},\omega) = \frac{\varphi_{ext}(\vec{k},\omega)}{\varepsilon(\vec{k},\omega)}, \quad (2.13)$$

where φ_{total} is the total potential inside the gas.

The Coulomb potential induced by the projectile is then equal to the total potential subtracted by the external potential,

$$\begin{aligned}\varphi_{ind}(\vec{k},\omega) &= \varphi_{total}(\vec{k},\omega) - \varphi_{ext}(\vec{k},\omega) \\ &= \varphi_{ext}(\vec{k},\omega)\left(\frac{1}{\varepsilon(\vec{k},\omega)} - 1\right) \\ &= \frac{Q_1 e}{k^2\varepsilon_0} 2\pi\delta(\omega - \vec{k}\cdot\vec{v}_{10})\left(\frac{1}{\varepsilon(\vec{k},\omega)} - 1\right).\end{aligned} \quad (2.14)$$

The induced electric field in the Fourier space is then calculated from the induced Coulomb potential,

$$\vec{E}_{ind}(\vec{k},\omega) = -i\vec{k}\varphi_{ind}(\vec{k},\omega). \quad (2.15)$$

After Fourier inverting Eq. (2.15) to get the induced electric field at the projectile position ($\vec{r} = \vec{v}_{10}t$) and some simplifications, we can deduce from Eq. (2.9) the following expression of the stopping power [23],

$$\left(-\frac{dE}{dl}\right)_{cold} = \frac{i(Q_1 e)^2}{(2\pi)^2\varepsilon_0 {v_{10}}^2}\int_0^\infty \frac{dk}{k}\int_{-kv_{10}}^{kv_{10}} \omega\left(\frac{1}{\varepsilon(k,\omega)} - 1\right)d\omega. \quad (2.16)$$

If we introduce the Bohr velocity, $v_B = \frac{e^2}{4\pi\varepsilon_0\hbar}$ and the electron gas plasma frequency, ${\omega_{pe}}^2 = \frac{n_e e^2}{\varepsilon_0 m_e}$, we obtain,

$$\left(-\frac{dE}{dl}\right)_{cold} = \left[\frac{4\pi\hbar^2}{m_e}\frac{{Q_1}^2{v_B}^2}{{v_{10}}^2}\, n_e\right] L_{diel,cold}, \quad (2.17)$$

where the stopping number in cold matter, $L_{diel,cold}$, is given by,

$$L_{diel,cold} = \frac{i}{\pi{\omega_{pe}}^2}\int_0^\infty \frac{dk}{k}\int_{-kv_{10}}^{kv_{10}} \omega\left(\frac{1}{\varepsilon(k,\omega)} - 1\right)d\omega, \quad (2.18)$$

In literature, the expression of the stopping power is generally presented as a product of two quantities, the prefactor and the stopping number [8]. The prefactor, enclosed in square brackets in Eq.

(2.17), has the dimension of the stopping power and is independent of the model used to calculate the stopping number. On the contrary, the stopping number in cold matter, $L_{diel,cold}$, is a model dependent dimensionless quantity that captures the slowing down behavior of the charged particle by the host medium. The calculation of the stopping number in a free electron gas now only relies on the determination of the frequency- and wavenumber-dependent dielectric function.

Using the Rayleigh-Schrödinger time-dependent perturbation theory to the lowest order, an analytical expression of the dielectric function can be found with respect to the electron distribution function [24]. This approach is called the Random Phase Approximation (RPA) [25]: it assumes a weak coupling between the particles and fails for strongly coupled medium where the local field corrections can be taken into account [26, 27]. These effects turn out to be important for very low projectile velocity and can be handled by applying a local field correction term into the expression of the dielectric function [28 and references therein].

Using the Fermi-Dirac distribution function, Lindhard and Winter [21] obtained an analytical expression for the stopping number in a zero-temperature electron gas[4]. This expression can be simplified:

- in the case of a **low velocity** projectile [21], i.e., when its speed is well below the average electron velocity ($v_{10} \ll v_e$), one finds,

  $$L_{diel,cold} \propto (v_{10})^3. \tag{2.19}$$

  Using Eq. (2.17), one can see that the stopping power behaves like a frictional force that is proportional to the particle velocity,

  $$\left(-\frac{dE}{dl}\right)_{cold} \propto v_{10}. \tag{2.20}$$

- in the **high velocity** case ($v_{10} \gg v_e$), one finds [21],

  $$L_{diel,cold} \cong \ln\left(\frac{2{m_e}{v_{10}}^2}{\hbar\omega_{pe}}\right) \cong \ln\left(\frac{2{m_e}^{3/2}{\varepsilon_0}^{1/2}{v_{10}}^2}{\hbar e\, {n_e}^{1/2}}\right). \tag{2.21}$$

  If we focus on the dependence of the stopping number on the projectile velocity, we obtain,

[4] The problem is then simplified: at T = 0 K, the Fermi Dirac distribution function reduces to the Heaviside function $\mathrm{H}(k_F - k)$ with k_F, the Fermi electron wave-vector defined with respect to the Fermi energy ($E_F = \hbar^2 {k_F}^2/2m_e$).

$$L_{diel,cold} \propto \ln(v_{10}). \tag{2.22}$$

The stopping power scales as $\ln(v_{10})/{v_{10}}^2$.

To have an idea of the boundary between the high and low velocity domain, since we consider a zero-temperature system, we can use the Fermi velocity,

$$v_F[m/s] = \sqrt{\frac{2E_F}{m_e}} \cong 10^6 \left(\frac{n_e[cm^{-3}]}{2.16 \times 10^{22}} \right)^{1/3}, \tag{2.23}$$

to give an order of magnitude of the electron velocity in a degenerate system. As an example, the Fermi velocity is 2.03×10^6 m/s in cold solid-density aluminum. The energy of a proton moving at such velocity is approximately 20 keV.

In order to see the influence of the density, the stopping number is shown in Figure II-5 as a function of the density and for various projectile energies from 10 keV/u to 10 MeV/u, where /u means per nucleon. Each curve presents the same trend shifted with respect to the projectile velocity. At low electron densities, we find ourselves in the high velocity case, i.e., the average velocity of the electrons is much lower than the projectile speed ($v_{10} \gg v_F$). According to Eq. (2.21), the stopping number is slightly decreasing with density. When density increases, the average velocity of electrons is getting close to and exceeds the projectile speed ($v_{10} \leq v_F$): we pass in the low velocity domain. The electrons have time to rearrange around the propagating projectile. The slowing down of the projectile is related to the electric field it induces in the electron gas while propagating. As this field is reduced if the electrons can quickly screen the propagating projectile, the stopping number is strongly reduced in a high-density electron gas [29].

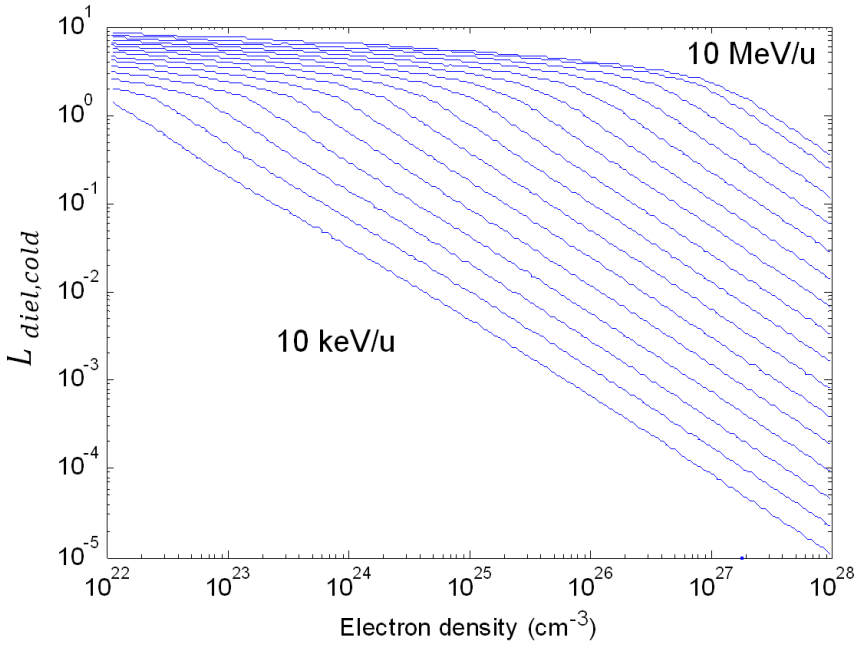

Figure II-5: Evolution of the stopping number in a free electron gas at zero-temperature as a function of the electron density for various projectile energies from 10 keV/u to 10 MeV/u (extracted from Ref. [29]).

II.3.2 Stopping power in cold and dense inhomogeneous matter

In order to evaluate the electronic stopping power in dense matter in which the electron gas is no longer uniform, Lindhard et al. [30] suggest to combine the dielectric approach with the local-density-approximation (LDA). The main idea of this approximation is that the projectile passing in a volume element d^3r at position $\vec{r}$ transfers its energy to the nearby electron gas which has locally a uniform electron density, $n_e(\vec{r})$. In practice, the non-uniform electron gas is divided into small independent volume elements of free electron gas and the electron density distribution in each volume is assumed to be uniform. The stopping power for a charged particle is calculated in each volume element, and the final stopping power is computed by averaging over these elements, weighted by their distribution in matter [29].

If we consider the atomic density to be locally uniform, the integration can be performed in a Wigner-Seitz (WS) cell (the volume of a WS is $1/n_i$). Recalling the plasma to be composed of a single species and assuming the average-atom approximation to be valid, we obtain the following expression for the stopping power,

$$\left(-\frac{dE}{dl}\right)_{cold} = \frac{4\pi\hbar^2}{m_e}\frac{{Q_1}^2{v_B}^2}{{v_{10}}^2} n_i \iiint_{WS} n_e(\vec{r}) L_{diel,cold}(n_e(\vec{r}))\, d^3r, \tag{2.24}$$

with $n_e(\vec{r})$, the electron density inside the WS cell, so that,

$$\iiint_{WS} n_e(\vec{r}) d^3r = Z_2. \tag{2.25}$$

By analogy with the general expression of the stopping power, this expression can be written,

$$\left(-\frac{dE}{dl}\right)_{cold} = \frac{4\pi\hbar^2}{m_e} \frac{{Q_1}^2 {v_B}^2}{{v_{10}}^2} n_i L_{atom,cold}\,, \tag{2.26}$$

where the atomic stopping number $L_{atom,cold}$ is given by,

$$L_{atom,cold} = \iiint_{WS} n_e(\vec{r}) L_{diel,cold}\left(n_e(\vec{r})\right) d^3r. \tag{2.27}$$

Lindhard's approach then remains correct provided that the electron density is varying smoothly in space. In Figure II-6, one compares the electron radial densities of an isolated atom given by the Thomas Fermi atom model and by the more precise Kohn-Sham one [31]. One observes that even for an isolated atom, the electron density is not so smooth according to the Thomas-Fermi Fermi model and oscillates strongly close to the nuclei according to the more precise Kohn-Sham one. In solids and partially ionized plasmas, the spatial variation is even more dramatic, such that the application of the LDA to estimate the stopping power becomes questionable. However, it has been successfully applied to explain the stopping power in cold solids, at low and high velocities [32].

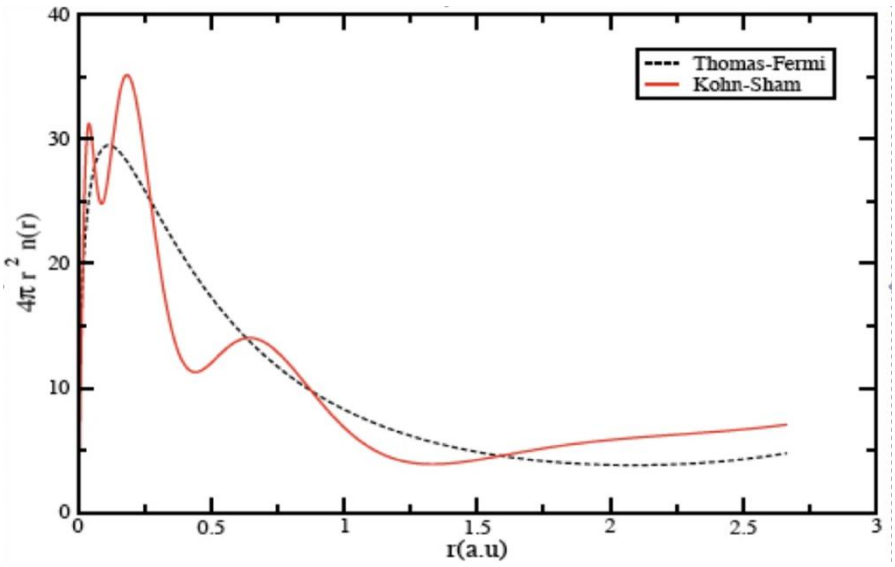

Figure II-6: Electron radial density in atomic unit of an isolated atom obtained using, respectively, the Thomas Fermi model (dashed line), the Kohn Sham model (plain line).

For a better understanding of the results provided by this approach, let us calculate $L_{atom,cold}$ by integrating the product of the $L_{diel,cold}$ by the radial electron density, $4\pi r^2 n_e(r)$, over the cell radius.

To visualize the contribution to $L_{atom,cold}$ of the different electron densities along the radius, r, we plot in Figure II-7, the radial density $4\pi u^2 n_e(u)$, and the function,

$$g(r) = \frac{\int_0^r 4\pi u^2 n_e(u) L_{diel,cold}\big(n_e(u)\big) du}{L_{atom,cold}}, \qquad (2.28)$$

for various projectile energies. $g(r)$ represents the cumulative contribution of the electrons (integrated from the nucleus) to the atomic stopping number, $L_{atom,cold}$. Note that the electron density and the radial electron density shown in Figure II-7 are obtained using SCAALP for solid-density aluminum at 1 eV. At this temperature, the electron density has barely changed with respect to the cold case[5] and, as we will see later, the stopping power is still the same (with respect to the cold case). Figure II-7 illustrates the fact that the higher the projectile energy, the more the inner-shell electrons contribute to its stopping number. This comes simply from the fact that:

- as shown in Figure II-5, the dependence of $L_{diel,cold}$ on the electron density becomes weaker for higher energy projectiles,
- inner-shell electrons are of higher radial density than the outer-shell ones (see the blue curve in Figure II-7).

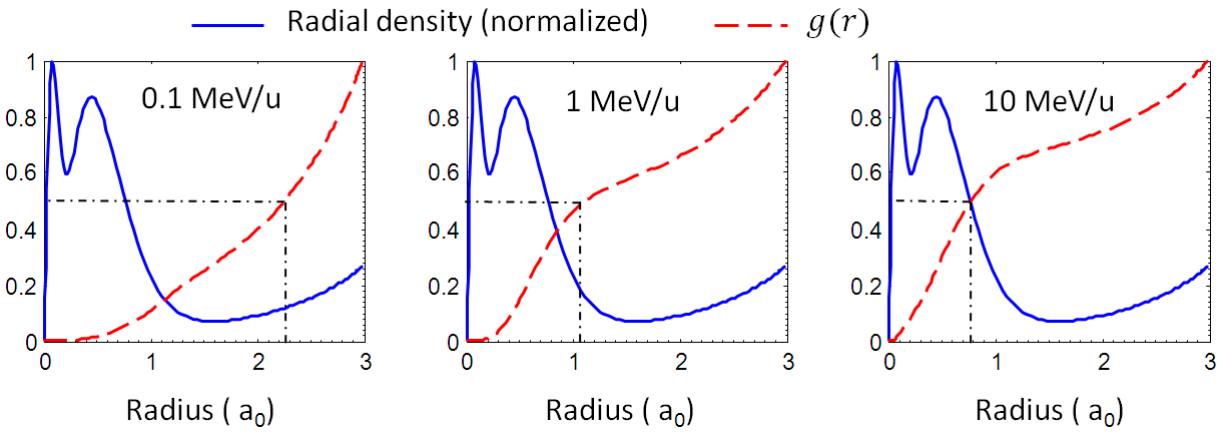

Figure II-7: Radial electron density (plain line) and g(r) (dashed line) as a function of the cell radius (in atomic units) in solid-density aluminum for, respectively, 0.1, 1 and 10 MeV/u projectiles [33].

[5] The temperature of the plasma, T = 1eV, is still well below the electron Fermi temperature: $T \cong T_F/9$.

II.4 Extension to finite-temperature matter

A great deal is known about ion stopping power in cold matter, but this quantity is expected to change with the temperature. There are currently no experimental measurements of ion range propagating in warm and hot dense matter. However, it is of tremendous importance, since in most hypothetical ion-driven targets, the ions deposit their energy in material at or near solid-state density, which is predicted to reach several hundreds of eV temperatures [34]. In such a regime, there are more free electrons than in cold solid-density matter.

II.4.1 Stopping number

In order to estimate $L_{diel,fT}$, the stopping number in a finite-temperature electron gas, an extension of Lindhard's approach has been developed by Gouedard and Deutsch [35]. It basically consists in extending the Lindhard expression of the dielectric function to the case of finite-temperatures. Maynard and Deutsch proposed a way to compute numerically the full RPA dielectric function of a free electron gas at finite-temperature and derived a general expression of the stopping power at finite temperature [36].

II.4.2 Stopping power

Following the work of Wang et al. [29], the stopping power in warm dense matter can be estimated by using the stopping power expression in a finite-temperature free electron gas (see section II.4.1) within the LDA approximation (see section II.3.2). We obtain then the following expression of the stopping power,

$$\left(-\frac{dE}{dl}\right)_{fT} = \frac{4\pi\hbar^2}{m_e}\frac{{Q_1}^2{v_B}^2}{{v_{10}}^2}n_i L_{atom,fT}, \tag{2.29}$$

with,

$$L_{atom,fT} = \iiint_{WS} n_e(\vec{r}) L_{diel,fT}(\vec{r}) d^3r, \tag{2.30}$$

where n_i is the ionic density of the plasma and n_e, the electron density in the WS cell.

The calculation of the stopping power now depends on the determination of the electron density, which can be evaluated using an average-atom model (such as SCAALP) taking in account the effect of the temperature.

II.5 Comparison between stopping power in cold and hot matter

In the following paragraphs, the impact of the temperature on the stopping power is studied using the dielectric approach coupled with the *ab initio* average-atom model SCAALP [35]. To check the validity and the consistency of the code, we first compare the stopping power obtained using SCAALP at 300 K with the well-known cold dense matter results (for which experimental data are available). Then, we study the impact of the temperature on the stopping power curves according to the dielectric theory.

To illustrate the evolution of the stopping power with the temperature, we choose to put the focus on the stopping power of projectiles propagating in solid-density aluminum. Indeed, this is the material that we commonly used in experiment.

II.5.1 Cold stopping power obtained from the dielectric theory compared to experimental data

In Figure II-8, proton stopping power measurements in aluminum at 300 K gathered by Paul [37] are compared with three different approaches:

- a fit formula given by the National Institute of Standards and Technology (NIST),
- dielectric approach calculation using SCAALP electron density function,
- dielectric approach calculation using ABINIT electron density function.

The NIST curve is extracted from the PSTAR database [15]. At high energies, NIST stopping powers of proton in aluminum are evaluated using Bethe's stopping power formula that appears to be in agreement with experimental data [20]. At low energies, a semi-empirical formula fitting the experimental proton stopping power data is used. The stopping power for the intermediate energy protons region, typically from 0.2 to 0.5 MeV, is computed by interpolation of a single cubic spline fitting the experimental stopping powers. This procedure gives a precision from 1 % to 2 % in the high velocity regime. Nonetheless, uncertainties are estimated to increase in the low velocity regimes [38]: 2 % to 5 % at 1 MeV, 5 % to 10 % at 100 keV, 10 % to 15 % at 10 keV, and at least 20 % to 30 % at 1 keV. This way of computing the stopping power explains why the NIST curve passes through the center of the cloud formed by the experimental data points even in the intermediate region where the spreading is important.

The last two curves are obtained within the LDA approximation using the method developed in section II.4. The SCAALP curve is computed using the electronic density provided by the average atom model SCAALP. The integration is performed over the WS cell.

The computation of the ABINIT curve follows the same method, but now the electron density is provided by the QMD model. The integration is performed over the simulation box (in 3 D) and normalized to the number of atoms (108 in the present case). There, we assume the ion charge to be equal to 1 in the velocity range we are looking at [15].

In Figure II-8, one can distinguish three different velocity regions. Consistently with what has been shown for low velocity projectiles in a free electron gas (section II.3.1), we observe that below 20 keV, the stopping power is proportional to v_{10}. Furthermore, the scaling in $\ln(v_{10})/{v_{10}}^2$ of the stopping power in the high velocity limit (section II.3.1) is retrieved for projectile energy above 200 keV, as observed. Between these two domains, from 20 keV to 200 keV, lies what is commonly called the intermediate velocity region [8]. In this domain, the stopping power reaches its maximum at around 50 keV, where the projectile velocity is roughly equal to the average of the target electron velocity [39].

As all the experimental data shown in Figure II-8 have not been measured at the same time, and as they also do not use the same set-up or diagnostics, this likely explains the scattering observed in Figure II-8, especially in the intermediate and low velocity regimes, below 300 keV, where the uncertainties on the stopping power measures become important [8]. It should be noted that the points that are clearly breaking away from the others in the intermediate regime have not been measured in the same experiment or by the same experimental team [37].

One can see in Figure II-8 that all three curves agree well with each other at low and high energies. Although we find that the energy, at which the maximum stopping power is reached, is identical in all curves, the dispersion of results is particularly noticeable in the intermediate velocity region where this maximum is reached. Even if a few experimental data are found to be in agreement with the SCAALP calculations, most of them are 10-20 % below. This difference could come from the spherical symmetry of the average atom model used to describe the medium. However the QMD calculation, which does not rely on the same assumption, is observed to be in remarkable agreement with SCAALP over the entire energy range. Therefore, it seems that 3D effects cannot explain the difference between SCAALP and experiment. One can then again wonder if the LDA approximation is trustable to estimate the stopping power in this regime. Full QMD simulations would be a good help to shed light on this issue. Such kind of simulations are currently under development and may bring

information in a near future to understand the discrepancy observed in the vicinity of the maximum stopping power [40, 41].

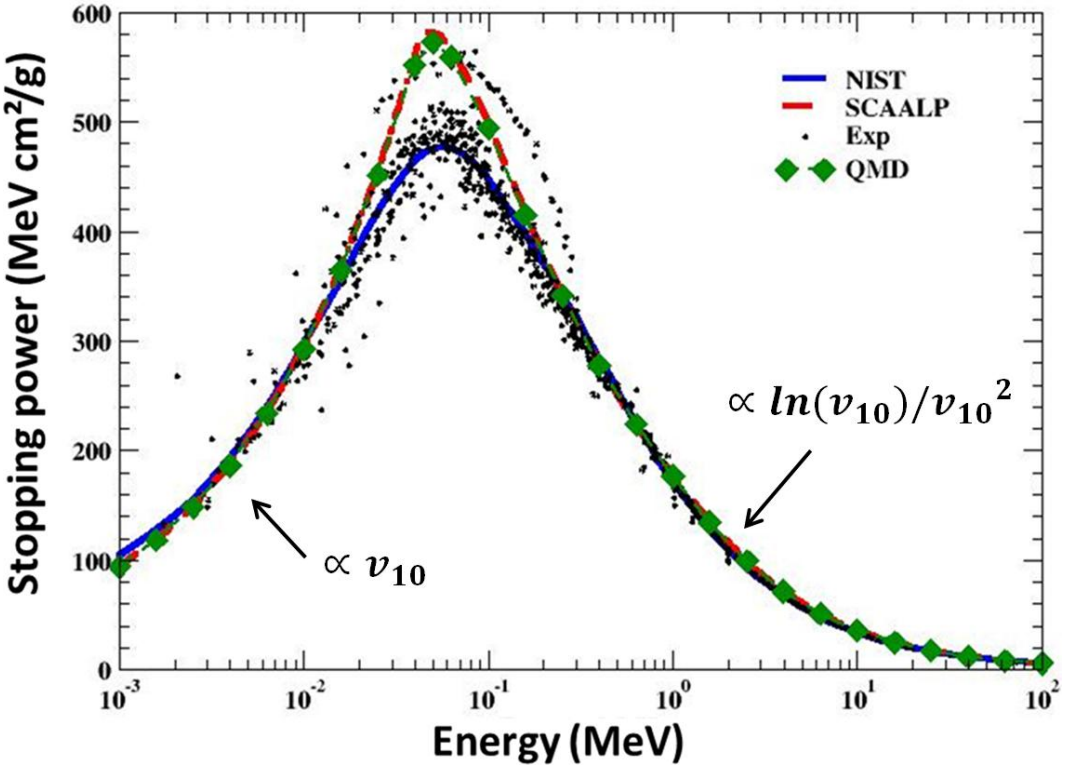

Figure II-8: Electronic stopping power of proton in solid-density aluminum at 300 K. Theoretical calculations using the SCAALP model and QMD simulation are compared to the NIST reference values and experimental data points.

II.5.2 Influence of the temperature on the stopping power in dense plasma

II.5.2.1 Proton stopping power

The influence of the temperature on the proton stopping power in solid-density aluminum estimated using the SCAALP model is shown in Figure II-9. Note that the ion charge is again assumed to be equal to 1 in the velocity range we are looking at.

First, one can see that both the proton energy location, as well as the value of the maximum of the stopping are very sensitive to the temperature. Its maximum value is reduced by a factor of 10 % at 5 eV, 40 % at 50 eV and 60 % at 100 eV. Second, one observes that the location of the stopping power maximum is shifted to higher projectile energy with the temperature, going from 50 keV at 1 eV to 0.3 MeV at 100 eV. Third, one notices that on one hand the stopping power slightly increases with temperature in the high velocity range, but on the other hand quickly decreases in the low velocity range.

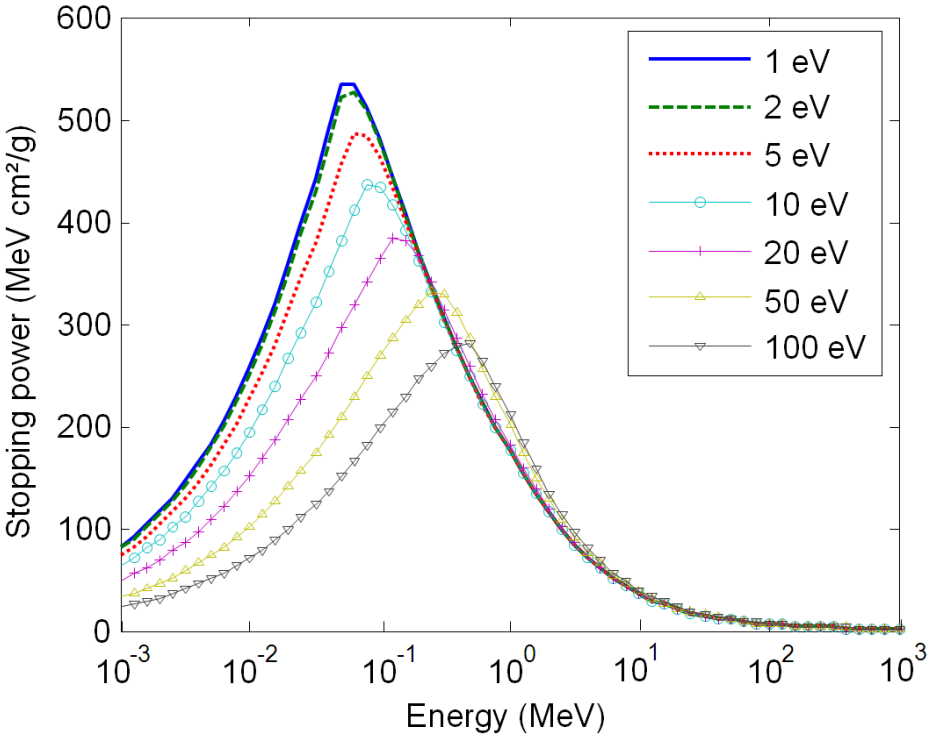

Figure II-9: Electronic stopping power of proton propagating through solid-density aluminum obtained using SCAALP as a function of the proton energy for temperature from 1 to 100 eV, extracted from Ref. [42].

II.5.2.2 Heavy ion stopping power

Since we assumed the ion projectile charge to be constant and equal to 1, the influence of the temperature on the stopping power of the protons is solely correlated to the influence of the temperature on the stopping number (the prefactor is not temperature dependent). In order to estimate the influence of the temperature on the stopping power of heavier projectiles, the influence of the temperature on the projectile charge, Q_1, needs to be taken in account as well. Indeed, the stopping power is proportional to Q_1^2, therefore determining how it is modified by temperature is of fundamental importance in the calculation of the electronic stopping power.

II.5.2.2.1 Effective charge

A common way to include this effect is to introduce the notion of projectile effective charge state, Z_{eff} [16]. This value is defined as the square root of the ratio of the stopping power of a given heavy projectile, $\left(-\frac{dE}{dl}\right)_{Z_1}$, to the stopping power of the proton propagating at the same velocity (or energy per nucleon) in the same medium, $\left(-\frac{dE}{dl}\right)_{proton}$ with $Q_1 = 1$ for proton. The stopping power is then,

$$\left(-\frac{dE}{dl}\right)_{Z_1}(v_{10}) = {Z_{eff}}^2 * \left(-\frac{dE}{dl}\right)_{proton}(v_{10}). \qquad (2.31)$$

In cold matter, numerous experiments aiming at measuring Z_{eff} have revealed that, in the high velocity regime, $v_{10} \gg v_e$, the effective charge depends mainly on the ratio between the projectile velocity v_{10} and the relative velocity of the electrons of the projectile [43, 44, 45, 46]; the latter can be estimated from the projectile atomic number Z_1 according to the Thomas-Fermi model [45]: $Z_{eff}(Z_1, v_{10})$. The effective charge is found to be practically independent of the chemical composition and density of the medium in which it propagates [45]. Based on these experimental results, several semi-empirical formulas have been proposed (e.g. Moak and Brown formula [46]).

In the low velocity regime, v_{10} of the order of or below v_e , the medium electron velocity is no longer negligible with respect to the projectile velocity. The medium electron velocity and density are therefore playing an important role in the determination of the effective charge of the projectile.

Recently, a method has been proposed by Gus'kov et al. [47] to extend Moak and Brown formula [46] from high velocity to low velocity projectiles propagating in hot dense matter. The overall idea is that the electrons of the medium contribute (as well as the electrons of the projectile) to the process that lead to the projectile having an effective charge, Z_{eff}. Hence, in this approach, the semi-empirical formula is applied on each electron of the medium in the reference frame of the projectile, i.e., the ion velocity v_{10} is replaced in the Moak and Brown formula by $|\vec{v}_{10} - \vec{u}|$, the norm of the ion velocity relative to the velocity of the electron ($\vec{u}$). The resulting semi-empirical formula, $Z_{eff}(Z_1, |\vec{v}_{10} - \vec{u}|)$ weighted by $|\vec{v}_{10} - \vec{u}|$ in order to take into account the projectile-electron collision frequency (proportional to $|\vec{v}_{10} - \vec{u}|$), is then averaged over the electron Fermi-Dirac distribution. An expression of the effective charge as a function of the projectile atomic number, the projectile velocity, the temperature and the Fermi temperature of the free electrons of the medium ($Z_{eff}(Z_1, v_{10}, T, T_F)$) is derived from the numerical results. The practical formula that is fitted from the numerical results differs from them by at most 5 % [47].

The effective charge of a carbon ion propagating through a solid-density aluminum predicted by Gus'kov et al. for various temperatures is shown in Figure II-10. To compute T_F, we use the ionization degree given in Ref. [48]. Once again, we observe three different regimes (see Figure II-10):

- the effective charge at high velocity, above 7-8 MeV/u, (zone 1 in Figure II-10) is constant and equal to the atomic number of the projectile. The projectile is therefore assumed to be fully stripped and interact with the target electrons as a bare nucleus. Note that the extent of this high velocity region does not change with the temperature.
- at low velocity (zone 2 in Figure II-10), especially when the temperature rises, the effective charge remains almost constant with respect to the projectile energy. Furthermore, we observe that the size of the low velocity zone increases with the temperature. Indeed, when the projectile velocity goes below the average velocity of the free electron of the target material, the effective charge proposed by Gus'kov et al. gets closer to the thermal ionization state of the projectile which can then be treated as a static impurity in the plasma.
- the transition between these two regions (zone 3 in Figure II-10) is smooth and continuous.

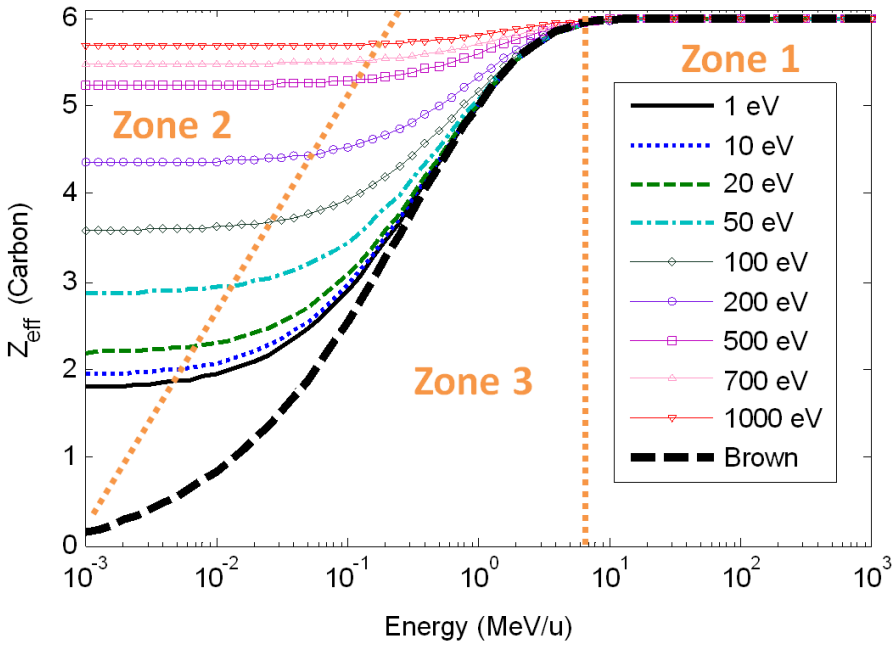

Figure II-10: Effective charge of a carbon projectile propagating in a solid-density aluminum sample for various temperatures as a function of the projectile energy as predicted by Gus'kov et al. [47]. The result is compared with the effective charge in cold aluminum proposed by Moak and Brown. For comparison purpose, we extended artificially this semi-empirical formula to low velocity (beyond its range of validity) [46]. The dashed (orange) lines roughly delimitate the various regions discussed in the text.

Note that this method to treat the variation of the projectile charge does not take into account the electronic structure of the projectile in a detailed way. This would require a much more complex treatment [49]. In the present study, Gus'kov formula will be used to calculate the stopping power of heavy ions. Since this formula is based on many approximations and has never been tested experi-

mentally [47], heavy ion stopping power curves presented in Figure II-11 are most useful to illustrate the variation of the stopping power with temperature rather than to estimate with precision the stopping power of carbon. Indeed, as shown in Ref. [33], there is already a non-negligible discrepancy at 300 K between the stopping power of heavy projectiles ($Z_1 > 1$) calculated using the Gus'kov effective charge formula combined with the proton stopping power computed in the previous section and available experimental data in the intermediate and low velocity regime. We should note that the agreement between them improve with the projectile atomic number [33].

II.5.2.2.2 Stopping power

The stopping power of carbon in solid-density aluminum for various temperatures is shown in Figure II-11. Contrary to protons, the variation of the maximum value of the stopping power of carbon along the energy axis does not respond monotonously to temperature. When the temperature increases, the peak of the stopping power starts to increase, reaching its maximum at 100 eV and decreases after. Furthermore, one observes that for temperatures above 50 eV, the peak slightly shifts toward lower velocity.

The behavior of the stopping power is determined by the product of Z_{eff}^2 by the proton stopping power (which dependence on the temperature is embodied in $L_{atom,fT}$). At fixed energy, these two factors however tend to vary in opposite manner as a function of temperature: Z_{eff}^2 increases with temperature (see Figure II-10), while the proton stopping power decreases with temperature (see Figure II-9):

- In the domain of low temperatures, the increase of Z_{eff}^2 with temperature is however stronger than the decrease of the proton stopping power. Hence the stopping power of carbon increases with temperature. This is actually what is happening for temperatures below 100 eV.
- In the domain of high temperatures, the reverse happens: Z_{eff}^2 saturates while the proton stopping power continues to decrease with temperature. Hence, the stopping power of carbon decreases with temperature. The carbon stopping power therefore follows the same trend as the proton one.

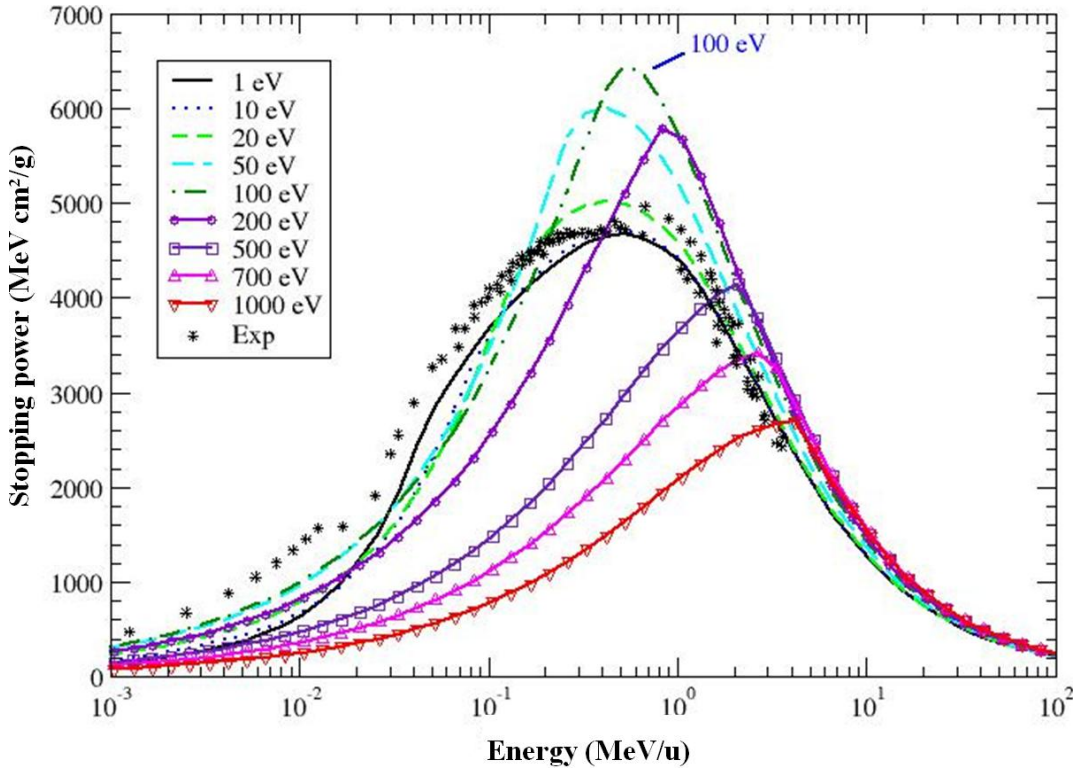

Figure II-11 : Stopping power of carbon propagating through solid-density aluminum obtained using the SCAALP atom model as a function of carbon energy per nucleon for temperatures from 1 to 1000 eV and compared to experimental data obtained in cold solid-density aluminum.

II.6 Summary

We computed in this chapter the electronic stopping power of protons in warm and hot solid-density aluminum using the dielectric approach extended to finite temperature plasmas. This method allows us to avoid making any distinction in the treatment of bound and free electrons. This is essential in the context of warm dense matter where these populations greatly evolve with respect to the target temperature and density. Nevertheless, this computation necessitates a good knowledge of the electron density profile inside matter. In our case, we use the electron density calculated using the average-atom model SCAALP and ABINIT (the last one solely for cold stopping power).

The proton stopping power obtained in this approach fits well the well-known cold stopping curve and only differs at intermediate projectile velocities where the average electron velocities equals the projectile one ($v_{10} \approx v_e$). This difference could be due to the LDA approximation.

When the temperature increases, the proton stopping power decreases in the low velocity regime ($v_{10} \ll v_e$) and the peak in the stopping power shifts to higher energy. In the high velocity regime ($v_{10} \gg v_e$), the stopping power slightly increases due to the thermal ionization of the core electrons. This trend is accompanied by a shift to higher projectile energy with the temperature of the intermediate zone due to the increase of the velocity of the medium electrons.

Assuming that the stopping number and the projectile can be determined independently, we use here Gus'kov et al. approach to estimate the stopping power for heavier projectiles. When the temperature increases, the stopping is predicted to rise due to the ionization of the projectile charge. At higher temperature, once the projectile is almost fully ionized, it follows the trend observed for protons.

References

[1] J. J. Thomson, *Conduction of Electricity Through Gases*, Cambridge: Cambridge University Press (1903)
[2] E. Bonderup, lecture notes, *Penetration of Charged Particles Through Matter*, University of Aarhus (1978)
[3] A. Adamo et al., Nucl. Phys. A 558, 665 (1993)
[4] A. O. Allen, Annu. Rev. Phys. Chem. **3**, 57 (1952)
[5] S. V. Bulanov, Phys. Lett. A **299**, 240 (2002)
[6] J. Lindhard and M. Scharff, Mat. Fys. Medd. K. Dan. Vidensk. Selsk. **27**, 15 (1953)
[7] N. W. Ashcroft & N. D. Mermin, *Solid State Physics,* Philadelphia: Saunders College (1976)
[8] ICRU Report 73, *Stopping Ions Heavier Than Helium* (2005)
[9] C. Jeynes et al., Rev. Accl. Sci. Tech. **4**, 41 (2011)
[10] D. K. Brice, *Ion Implantation Range and Energy Deposition Distributions, vol. 1, High Energies*, New York: Plenum Press (1975)
[11] G. Faussurier et al., Phys. Plasmas **20**, 012705 (2013)
[12] R. L. Singleton & L. S. Brown, Plasma Phys. Control. Fusion **50**, 124016 (2008)
[13] G. Zwicknagel et al., Phys. Reports **309**, 117 (1999)
[14] G. Maynard, et al., Il Nuovo Cimento, **106A**, 1825 (1993)
[15] NIST, Proton stopping power database,
http://physics.nist.gov/PhysRefData/Star/Text/PSTAR.html
[16] J. F. Ziegler, J. Appl. Phys / Rev. Appl. Phys. **85**, 1249 (1999)
[17] Particle interactions with matter, http://www.srim.org/#SRIM
[18] F. Bloch, Zeit. J. Phys. **81**, 363 (1933)
[19] N. Bohr, Phil. Mag. **25**, 10 (1913)
[20] H. A. Bethe, Ann. Phys. **5**, 325 (1930)
[21] J. Lindhard and A. Winther, Mat. Fys. Medd. K. Dan. Vidensk. Selsk. **34**, 4 (1964)
[22] U. Fano, Annu. Rev. Nucl. Sci. **13**, 1 (1963)
[23] S. Ichimaru, *Statistical Plasma Physics : vol. 1 Basic Principles*, Westview: Bounder Press (2004)
[24] L. D. Landau & E.M. Lifshitz, *Statistical Physics*, Oxford: Pergamon Press (1969)
[25] G. Maynard and C. Deutsch, Phys. Rev. A **26**, 665 (1982); **27**, 574 (1983)
[26] G. Gregori et al., Phys. Rev. E **67**, 026412 (2003)
[27] M. D. Barriga-Carrasco, Phys. Rev. E **79**, 027401 (2009)
[28] S. Ichimaru & K. Utsumi, Phys. Rev. B **24**, 7385 (1981)
[29] P. Wang et al., Phys. Plasmas **5**, 2977 (1998)
[30] J. Lindhard and M. Scharff, Mat. Fys. Medd. K. Dan. Vidensk. Selsk. **27**, 15 (1953)
[31] W. Kohn & L. J. Sham, Phys. Rev. **140**, A1133 (1965)
[32] A. Sarasola et al., Nucl. Meth. Phys. Res. B **182**, 67 (2001)
[33] M. Gauthier et al., High Energy Dens. Phys. **9**, 488 (2013)
[34] C. Deutsch & I. Hofman, C. R. Acad. Sci. Paris, **1**, 758 (2000)

[35] C. Gouedard & C. Deutsch J. Math. Phys. **19**, 32 (1978)
[36] G. Maynard & C. Deutsch, J. Phys. (France) **46**, 1113 (1985)
[37] H. Paul et al., Nucl. Instrum. Meth. Phys. Res. B **61**, 261 (1991)
[38] ICRU Report 49, *Stopping Powers and Ranges for Protons and Alpha Particles* (1993)
[39] R. A. Lews et al., Phys. Rev. A **44**, 392 (1991)
[40] A. A. Correa et al., Phys. Rev. Lett. **108**, 213201 (2012)
[41] M. Ahsan Zeb et al., Phys. Rev. Lett. **108**, 225504 (2012)
[42] G. Faussurier et al., Phys. Plasma **17**, 052707 (2010)
[43] H. D. Betz & L. Grodzins, Phys. Rev. Lett.. **25**, 211 (1970)
[44] L. C. Northcliffe, Phys.Rev. **120**, 1744 (1960)
[45] J. F. Ziegler et al., *The Stopping and Range of Ions in Solids*, New York: Pergamon (1985)
[46] M. D. Brown & C. D. Moak, Phys. Rev. B **6**, 90 (1972)
[47] S. Y. Gus'kov et al., Plasma Phys. Rep. **35**, 709 (2009)
[48] W. Ebeling et al, *Thermophysical Properties of Hot Dense Plasmas*, Stuttgart: Teubner (1991)
[49] T. Peter & J. Meyer-Ter-Vehn, Phys. Rev. A **43**, 2015 (1991)

III. IONS GENERATION BY LASER-MATTER INTERACTION

III.1 Introduction

The first observation of energetic ions produced by laser-matter interactions goes back to the early 1960's [1]. The ion beams were typically of the order 100 keV/u to a few MeV/u and emitted into a large solid angle [2]. At that time, the laser intensities were going from 10^{11} to 10^{17} W/cm² and the pulse were ns to several ps long. These beams were seen as an issue for future direct drive laser fusion and only used as a diagnostic to measure the hot electrons temperature of the irradiated target [3]. In the late 1980's, the implementation of the so-called chirped pulse amplification (CPA) technique in high power lasers has made available new intensity regimes that were previously inaccessible in laboratory: it was possible to produce picoseconds duration pulses of intensities higher than 10^{18} W/cm^2, the relativistic threshold for an electron oscillating in a 1 µm-wavelength radiation [4]. The consequences were very important on ion acceleration performance, since the ion beams accelerated by ultra-intense, short laser pulses were considerably improved in terms of energy, quantity and quality, raising a renewed interest for potential in industry as well as in science.

The first highly collimated beams with multi-MeV energies [5, 6, 7, 8], produced in 2000, have shown remarkable degree of collimation and laminarity, high cutoff energy, short duration, and emission along the normal to the rear surface of the irradiated target. These characteristics were interesting and complementary compared to what can be obtained in conventional accelerators. Lasers actually allow us to generate nowadays dense, high energy and charge neutralized picoseconds ion bunches in a much more compact and cheaper device than standard accelerator techniques, but is, up to now, still limited to much lower energies. Such ion beams are currently commonly used as pump source (e.g. for isochoric heating [8, 9 , 10, 11]) or probe (e.g. for proton radiography [12, 13]) in plasma experiments. As an example, it gives scientists the possibility to recreate in laboratory stellar matter conditions [14, 15] or to study the fields generated by ultra-short laser beams interacting with targets on a picosecond time scale [16, 17].

Furthermore, many other interesting applications are in view such as using laser-produced ion beam as an injector for accelerators [18], or for cancer therapy [19] and ICF [20], but have requirements which have not yet been achieved in laboratory. In this context, studies are being conducted to improve the already-known acceleration mechanisms or to propose new acceleration mechanisms capable of producing ion beams that could be used successfully in future applications like those mentioned above.

In this chapter, an overview of the existing and demonstrated mechanisms of laser acceleration is presented as well as their performances and potentialities. Laser plasma interactions can be broadly categorized into either under-dense or over-dense interactions depending on whether or not the laser beam can propagate through the plasma (respectively n_e below n_c and n_e above n_c, where n_e is the plasma density and n_c the critical density with respect to the laser wavelength, its expression is given further in Eq. (3.13)). The first part of the chapter deals with the most common and developed method of accelerating ions using lasers: the interaction of a short-pulse laser beam with solid-density targets. The second part is devoted to a very promising, but still young, way of accelerating ions using lower-than-solid density targets in which the laser propagates mostly in sub to near-critical density plasma ($n_e \lesssim n_c$).

III.2 Ion acceleration in solid-density targets

For current laser intensities, the laser cannot directly accelerate ions; indeed their mass does not allow them to reach a speed close the laser-light group velocity [21], such that they could interact directly with the laser. Note that, although they do not currently exist, very high-intensity lasers (intensity above 10^{24} W/cm²) are predicted to be able to directly accelerate ions by light pressure [22]. In our case, the laser energy is first transferred to the electrons that are accelerated at the beginning of the acceleration process. These electrons, called hot or suprathermal, then electrostatically transfer their energy to the ions, accelerating them in turn.

In the following paragraphs, the basics of relativistic laser-matter interaction are firstly reminded. Then, we briefly go through the different mechanisms of electron acceleration in solids, since it plays an essential role in the ion accelerating process. Subsequently, the principal mechanisms of ion acceleration are shortly explained. Their characteristics, best performances up to now and potentialities are presented as well.

III.2.1 Laser-matter interaction

High-intensity short-pulse lasers generally typically deliver a light pulse with intensities up to a few 10^{19} - 10^{20} W/cm² during around 100 fs to a few ps. It always arrives with a ns pulse of lower intensity preceding the main pulse, called pre-pulse. It is generally due to the Amplified Spontaneous Emission (ASE) existing in the amplifier stages of the laser chain. Its duration of 0.5 to 5 ns in most cases is fixed by the shutter speed of the Pockels cells used in the laser chain. The intensity ratio between the main pulse and the ASE is called the contrast (or contrast ratio) of the beam. The ASE irradiates the target before the main pulse and heats the electron of the surface, generating a hot pre-plasma. For

instance, the high-intensity short laser pulse at ELFIE (LULI) is typically a 350 fs pulse with intensities up to 10^{19} W/cm² on target. Its temporal profile is plotted in Figure III-1. The contrast is estimated to be lower than 10^{-6}, which corresponds to an ASE intensity of around 10^{13} W/cm².

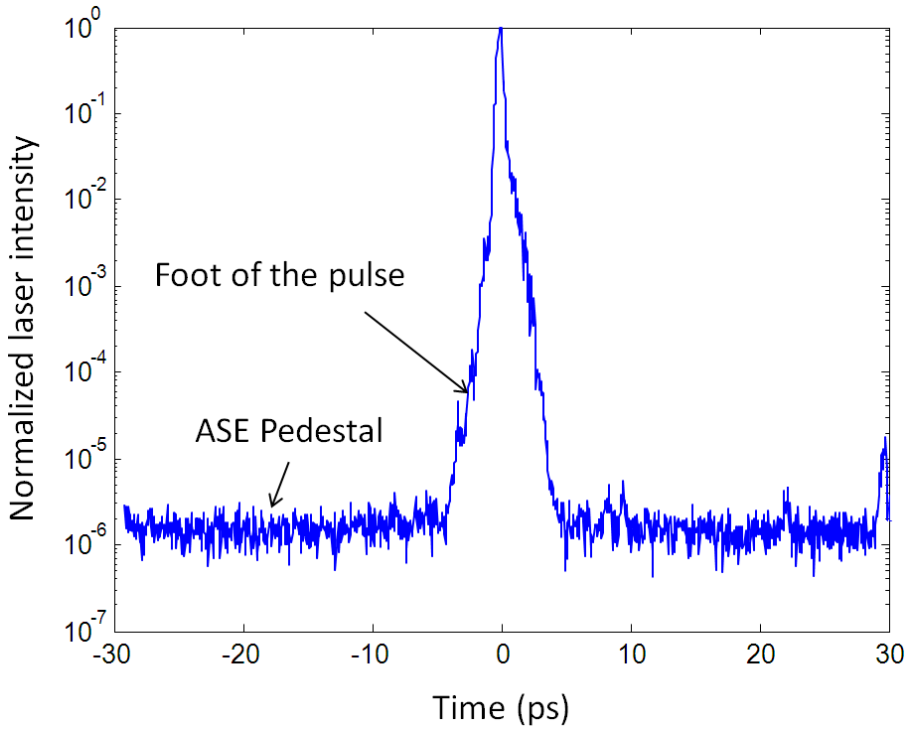

Figure III-1: Temporal profile of the ELFIE compressed beam obtained using a 3ω autocorrelator, where ω is the laser frequency. The intensity is normalized to the maximum intensity of the pulse. The curve corresponds to an ASE contrast below 4 x 10^{-6}, the noise limit of the measuring device.

Knowing the plasma formation threshold[6] to be around 10^{11} W/cm² [21], the main pulse is thus always interacting with a pre-plasma if the laser-contrast is not improved by any additional method. The electron density profile in the pre-plasma can be approximated with the following exponential law:

$$n_e = n_{e0} \exp\left(-\frac{x}{L_G}\right), \qquad (3.1)$$

[6] The breakdown mechanism is due to an electron avalanche ionization caused by the electrostatic field of the laser beam. The field threshold is dependent on the laser duration, but can be estimated between 10^6-10^7 V/m in our case. It corresponds to an intensity of 10^{11} W/cm².

where n_e is the electron density, n_{e0} is the electron density in the solid and L_G is the gradient characteristic length. The origin of the x-axis corresponds to the edge of the solid-density target before irradiation.

The electrons of the target front surface oscillate in the electromagnetic field generated by the laser. Their motion is described by the Lorentz equation:

$$\frac{d\vec{p}}{dt} = m_e \frac{d}{dt}(\gamma \vec{v}) = -e\left(\vec{E} + \vec{v} \times \vec{B}\right), \tag{3.2}$$

where $\vec{p}, \vec{v}, m_e$ and γ are, respectively, the momentum, the velocity, the mass and the Lorentz factor of the electron,

$$\gamma = \frac{1}{\sqrt{1 - \frac{v^2}{c^2}}} = \sqrt{1 + \frac{p^2}{{m_e}^2 c^2}}, \tag{3.3}$$

where c is the light speed. Assuming that the electron oscillation is due to a progressive and planar laser-wave, one finds from Eq. (3.2) projected along the direction transverse to the propagation axis of the laser [21],

$$\frac{p_\perp}{m_e c} = \frac{eE_0}{m_e c \omega_0} \equiv a_0 , \tag{3.4}$$

where $p_\perp$ is the transverse electron momentum, ω_0 the laser frequency and E_0 the amplitude of the laser wave. a_0 corresponds to the ratio of the classical velocity of the oscillating electron by the light speed:

$$a_0 = \frac{v_{classic}}{c} = 0.85\sqrt{I_{18}{\lambda_{0,\mu m}}^2}, \tag{3.5}$$

where I_{18} is the laser intensity normalized to 10^{18} W/cm² and $\lambda_{0,\mu m}$ the laser-wavelength normalized to 1 µm. Averaging γ over a laser period, one finds,

$$\bar{\gamma} = \sqrt{1 + \frac{a_0^2}{2}} \tag{3.6}$$

From Eq. (3.5), we observe that the electrons start to be accelerated to near-relativistic speeds, when a_0 is close to 1. For 1 µm-wavelength lasers, it corresponds to laser intensity around 10^{18} W/cm².

At near-relativistic electron velocities, the magnetic term in the Lorentz equation can no longer be neglected. The electrons are then not only oscillating transversally, but also drifting along the laser propagation axis at speed v_D [21],

$$\frac{v_D}{c} = \frac{a_0^2}{4 + a_0^2}. \quad (3.7)$$

The interaction between the laser beam and the electrons of the plasma perturbs the electron density creating locally small charge separations. The free electron population of the plasma responds by collectively oscillating at the electron plasma frequency ω_{pe} [23]:

$$\omega_{pe}\ [rad.s^{-1}] = \sqrt{\frac{n_e e^2}{\varepsilon_0 m_e}} \cong 5.64 \times 10^4 \sqrt{n_e[cm^{-3}]}, \quad (3.8)$$

Let us take the advantage of mentioning charge separations in plasma to introduce the electron Debye length, the characteristic length over which a charge is screened in a classical plasma at electronic temperature, T_e [23],

$$\lambda_D[cm] = \sqrt{\frac{\varepsilon_0 k_B T_e}{n_e e^2}} \cong 743 \sqrt{\frac{T_e[eV]}{n_e[cm^{-3}]}}. \quad (3.9)$$

It corresponds also to the characteristic distance travelled by the electrons when oscillating at ω_{pe}:

$$\lambda_D = \frac{v_{the}}{\omega_{pe}}, \quad (3.10)$$

with the thermal velocity of the electrons in plasma [21],

$$v_{the} = \sqrt{\frac{k_B T_e}{m_e}}, \quad (3.11)$$

When writing the dispersion relation of the laser-wave propagating through the plasma, one finds that it cannot propagate if its frequency is lower than ω_{pe} [23]:

$${k_0}^2 c^2 = {\omega_0}^2 - {\omega_{pe}}^2, \quad (3.12)$$

where k_0 is the wave-number of the laser wave propagating inside the plasma. Indeed, in such a case, the plasma electrons would have time to screen the oscillating field of the laser. This condition corresponds to a maximum electron density above which the laser electromagnetic wave cannot propagate, the so-called critical density[7]:

[7] For relativistic laser intensities ($a_0 \geq 1$), the electron mass becomes γm_e, which reduces the electron plasma frequency to $\omega_{pe}^{rel} = \frac{\omega_{pe}}{\gamma}$. The critical density is therefore shifted to higher values (γn_c) allowing the laser to penetrate into higher density regions. This effect is known as the self-induced transparency.

$$n_c(\omega_0)[cm^{-3}] = \frac{m_e \varepsilon_0 {\omega_0}^2}{e^2} \cong \frac{1.11 \times 10^{21}}{{\lambda_{0,\mu m}}^2}. \quad (3.13)$$

The remaining penetration of the laser through the overdense plasma is just evanescent. It is characterized by its skin depth l_s [23]*:*

$$l_s[\mu m] \approx \frac{c}{\omega_{pe}} \cong \sqrt{\frac{2.8 \times 10^{19}}{n_e[cm^{-3}]}}. \quad (3.14)$$

III.2.2 Hot electron heating

Various mechanisms of electron acceleration in a laser field exist. Their relative importance depends strongly on I, the intensity of the laser beam, and on the density profile of the plasma it is interacting with.

III.2.2.1 Collisional absorption

For laser beams of intensity below 10^{16} W/cm^2, the main mechanisms of energy absorption are collisional [21]. The collisions between electrons and ions result in a frictional drag of the electron motion, introducing a phase shift between the electron flux (or current), $\vec{J}$, and the electric field, $\vec{E}$. The average over a cycle of the product, $< \vec{J} \cdot \vec{E} >$, is then no longer null: the energy of the electromagnetic wave is dissipated by Joule effect. Physically, a photon is absorbed during the collision between an electron and an ion. This mechanism is called inverse Bremsstrahlung. The electron-ion collision frequency is proportional to ${n_e T_e}^{-3/2}$ [24]. For higher laser intensity (I above 10^{16} W/cm²), although the electron temperature is quickly increasing to hundreds of eV and thus reduces the electron-ion collision frequency, the speed of the electrons allows them to go deeper inside the plasma than the laser skin depth. Therefore the absorption zone expands to higher density regions, and hence increases the total energy transferred from the laser to the electrons. It is called anomalous skin effect [21].

This first type of absorption takes place in the coronal plasma ($n_e \leq n_c$) provided that the electron temperature remains low. For intensity higher than 10^{15} W/cm², the surface temperature of the irradiated target rises so fast (the coronal plasma typically reaches a temperature of 400 eV after 10 fs of irradiation [21]), that collisions become very quickly ineffective during the interaction. In addition, the electrons quiver-velocity, i.e., the oscillating velocity due to the laser field, becomes comparable to the thermal velocity, thus reducing the effective collision frequency even further.

For short and high-intensity laser beam, the dominant processes are thus collisionless and are due to the collective answer of the plasma to the laser-wave.

III.2.2.2 Resonant absorption

The resonant absorption is a collisionless absorption process that arises at moderate intensity (above 10^{15} W/cm²) when the laser makes an angle, θ, with the direction of the target normal (i.e., with the main plasma density gradient axis denoted x here). This mechanism occurs in the region close to the critical density. If one decouples the p-component and s-component of the laser, the dispersion relation (3.12) becomes [21]:

$$\begin{aligned}(s)\ \ & k^2(1-sin^2(\theta))c^2 = {\omega_0}^2 - {\omega_{pe}}^2(x),\\ (p)\ \ & k^2(1-cos(\theta)sin(\theta))\,c^2 = {\omega_0}^2 - {\omega_{pe}}^2(x).\end{aligned} \qquad (3.15)$$

The electromagnetic wave cannot propagate for density above $n_c cos(\theta)$ and is thus reflected before reaching the critical density. However if the density gradient is steep enough, the evanescent electric wave tunnels through the critical surface. Its p-component produces small electron density fluctuations along the gradient density axis which are capable of driving up a plasma wave. This plasma wave is resonantly pumped by the laser, inducing its amplitude to grow over a few laser periods. It results in large density fluctuations (see Figure III-2). This amplification is damped and saturated due to collisions at low intensity, but mostly by non-linear mechanisms such as wave breaking or particle trapping for higher intensities [25]. These mechanisms accelerate electrons carrying with them a high kinetic energy inside the target, forming a hot electron population.

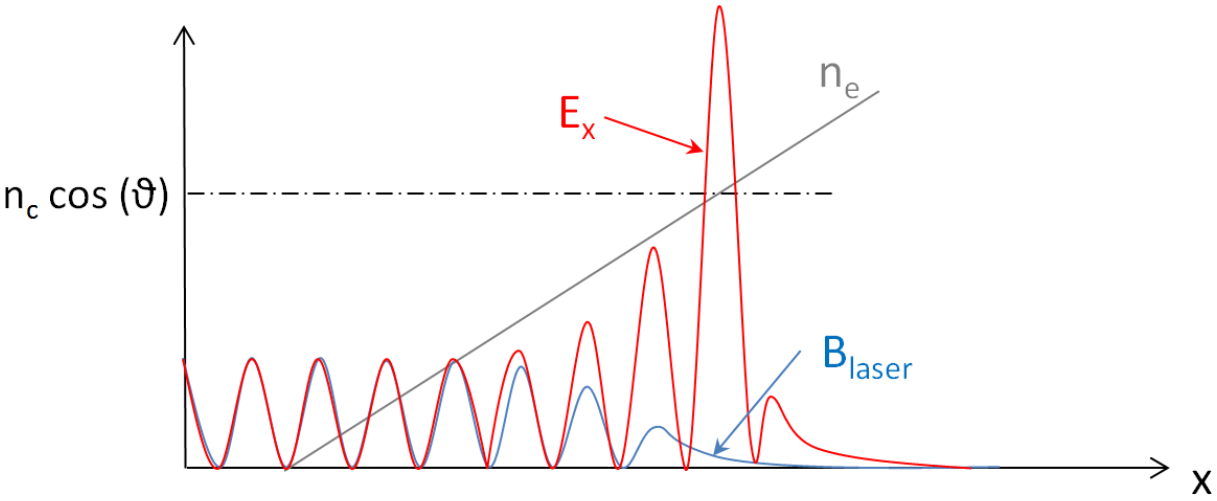

Figure III-2: Resonant acceleration mechanism. The laser magnetic field amplitude, B, decreases when getting close to the critical density. The resonance between the p-component of the laser beam and the plasma makes the plasma electric field E_x diverging close to the critical density.

III.2.2.3 $\vec{J} \times \vec{B}$ heating

It is the principal mechanism of electron heating in our laser intensity and pre-plasma domain. Therefore, we dwell upon it more than with the others. The previous collisionless mechanisms were linear, i.e., the electrons were answering linearly to the electric field of the laser and the current was collinear to the electric field [23]. At intensities higher than 10^{17} W/cm², the plasma answer is no longer linear, and non-linear terms related to the B-field component of the laser cannot be neglected in the equation of motion,

$$\frac{d\vec{p}}{dt} = -e\left(\vec{E} + \vec{v} \times \vec{B}\right), \tag{3.16}$$

where $\vec{p}$ is the electron momentum ($\vec{p} = \gamma m_e \vec{v}$), $\vec{E}$ and $\vec{B}$, respectively, the electric and magnetic field of the laser. These non-linear effects give rise to the so-called ponderomotive force on which is based the so-called $\vec{J} \times \vec{B}$ heating.

III.2.2.3.1 Ponderomotive force

If we introduce the electromagnetic potential vector $\vec{A}$ in Eq. (3.16)[8] , we obtain,

$$\frac{\partial \vec{p}}{\partial t} + \left[\vec{v} \cdot \vec{\nabla}\right]\vec{p} = e\left(\frac{\partial \vec{A}}{\partial t} - \vec{v} \times \left(\vec{\nabla} \times \vec{A}\right)\right). \tag{3.17}$$

We decompose the momentum vector $\vec{p}$ into 2 components of different timescales. The fast component, $\overrightarrow{p_f}$, represents the transverse component of the electron momentum, while the slow one, $\overrightarrow{p_s}$, represents the electron momentum averaged over a laser period.

$$(fast)\ \ \frac{\partial \overrightarrow{p_f}}{\partial t} = e\left(\frac{\partial \vec{A}}{\partial t}\right) \Rightarrow \overrightarrow{p_f} = e\vec{A}, \tag{3.18}$$

$$(slow)\ \ \frac{\partial \overrightarrow{p_s}}{\partial t} + \frac{\left[\left(\overrightarrow{p_s} + \overrightarrow{p_f}\right) \cdot \vec{\nabla}\right]\left(\overrightarrow{p_s} + \overrightarrow{p_f}\right)}{m_e \gamma} = -e\frac{\left(\overrightarrow{p_s} + \overrightarrow{p_f}\right) \times \left(\vec{\nabla} \times \vec{A}\right)}{m_e \gamma}. \tag{3.19}$$

[8] We assume the plasma to be neutralized, thus $\vec{E} = -\partial \vec{A}/\partial t$.

On fast timescales, one finds the basic solution of an electron oscillating in a planar laser wave. We use Eq. (3.18) to remove $\vec{A}$ in Eq. (3.19). After averaging over a laser period and simplifications[9], one gets,

$$\frac{\partial \overrightarrow{p_s}}{\partial t} = -\frac{\vec{\nabla}|p_f|^2}{2m_e\gamma}. \tag{3.20}$$

Averaging the Lorentz factor over the laser period T_0, one finds,

$$\vec{\nabla}\bar{\gamma} = \vec{\nabla}\left(\sqrt{1+\frac{{p_f}^2}{{m_e}^2c^2}}\right)_{T_0} = \frac{\vec{\nabla}|p_f|^2}{2\gamma{m_e}^2c^2}. \tag{3.21}$$

Using (3.20) and (3.21), we finally obtain the expression of the ponderomotive force, $\overrightarrow{F_P}$:

$$\overrightarrow{F_p} \equiv \frac{\partial \overrightarrow{p_s}}{\partial t} = -m_e c^2 \vec{\nabla}\bar{\gamma}. \tag{3.22}$$

The ponderomotive force derives from a ponderomotive potential ϕ_P: $\overrightarrow{F_P} = -\vec{\nabla}\phi_P$, expressed as[10]:

$$\phi_P = (\bar{\gamma} - 1)mc^2 \tag{3.23}$$

Using (3.4) and assuming the electrons to be nonrelativistic ($\frac{{a_0}^2}{2} \ll 1$), the expression of the ponderomotive force and potential can also be written as a function of the laser intensity, I:

$$\overrightarrow{F_p} = -\frac{1}{2cn_c}\vec{\nabla}I, \tag{3.24}$$

$$\phi_P = \frac{I}{2cn_c}. \tag{3.25}$$

It should be noted that the same calculation can be performed for the ions. However, since the ponderomotive force is inversely proportional to the mass, the ion motion is negligible on electron timescales (see the classical expression of the ponderomotive force in Eq. (3.26)). More details regarding the ponderomotive force can be found in Ref. [26, 27].

At first sight, the principal effect of the ponderomotive force is to eject the electrons from the areas of high intensity. Indeed, a focused laser beam is associated to a radial intensity gradient directed toward the center of the beam as illustrated in Figure III-3 . The electrons are thus radially drifting away from the center of the focused beam.

[9] Assuming that the slow term is negligible compared to the fast one, we keep only the slow terms of the lowest order.

[10] The constant of the potential is chosen so that the potential is zero when the particle is at rest ($\gamma = 1$).

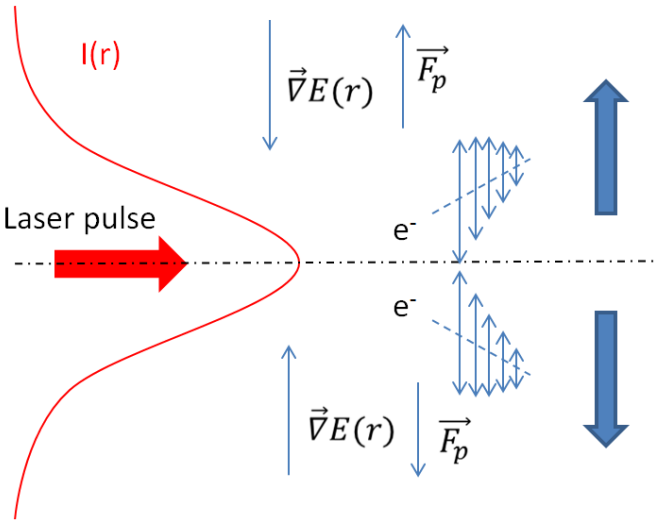

Figure III-3: The ponderomotive force drives away the electrons from the high-intensity zone.

III.2.2.3.2 Electron heating

For high laser-intensity and steep plasma density gradients, the ponderomotive force can also accelerate electrons inside the target [28]. Indeed, the laser-field amplitude results in an intensity gradient along the propagation axis and thus, generates a ponderomotive force in this direction. To illustrate the physics of the mechanism, let us look at an example. For a planar and linearly-polarized laser-wave oscillating at ω_0, propagating along the x-axis with an intensity gradient, the expression of the longitudinal component of the non-linear forces acting on the electron motion in the nonrelativistic case is given by [28],

$$\overrightarrow{F_{NL}} = -\frac{e^2}{4m_e\omega_0}\frac{\partial|E(x)|^2}{\partial x}(1-\cos(2\omega_0 t))\,\vec{x}. \qquad (3.26)$$

When averaging Eq. (3.26) over a laser period, one finds back the expression of the ponderomotive force calculated before in Eq. (3.24). The fast component can be viewed as the effect of an electrostatic wave $\overrightarrow{E_p}$, oscillating along the propagation axis at $2\omega_0$,

$$\overrightarrow{E_p} = \frac{e}{4m_e\omega_0}\frac{\partial|E(x)|^2}{\partial x}\cos(2\omega_0 t)\,\vec{x}. \qquad (3.27)$$

This fast component is responsible of heating the plasma. Although the oscillating component of the electron motion is not coming directly from the laser, its effect is very analogous to the vacuum heating. The electrons are accelerated backward, and then reinjected inward the target. Some of them escape the electrostatic field continuing their travel inside the target. This process, called $\vec{J}\times\vec{B}$ heating, generates twice a laser period hot electron bunches with a Maxwellian energy distribution [28]. The temperature of the hot electron distribution (or the electron average energy) follows the pon-

deromotive potential associated with the pure transverse motion and can be estimated by the following expression [29]:

$$T_{e,hot}[\mathrm{keV}] = m_e c^2 \left(\sqrt{1 + {a_0}^2} - 1\right) \cong 511\left(\sqrt{1 + \frac{{I_{18}\lambda_{0,\mu m}}^2}{1.37}} - 1\right). \quad (3.28)$$

The temperature is shown to depend only on the product of the intensity by the square of the wavelength, called the laser irradiance usually noted ${I\lambda_0}^2$.

Various diagnostics and methods have been developed to experimentally measure the hot electron distribution and retrieve the hot electron temperature [30]. One way is based on the measurement of the X-ray Bremsstrahlung emission induced by the hot electrons. It consists in comparing the experimental X-ray spectrum with the one obtained by numerical computations for different electron temperature. Using this method, and varying the laser intensity from 10^{17} to 10^{19} W/cm², Beg *et al.* found an empirical law [31] which significantly differs from Eq. (3.28) (see Figure III-4):

$$T_{e,hot}[\mathrm{keV}] = 215\left({I_{18}\lambda_{0,\mu m}}^2\right)^{1/3}. \quad (3.29)$$

As pointed out in Ref. [33], the Bremsstrahlung emission is only sensitive to electrons between 300 keV à 2 MeV and the higher energy part of the distribution is unknown. Note that on a recent study [30], electron temperatures inferred from measurements of 4 different diagnostics, i.e., spectrometry of electrons, spectrometry of protons and optical probing of these beams expanding into vacuum, have shown to be also in agreement with Beg's law (see Figure III-4). Moreover, A theoretical model recently developed by Haines [32] supports Beg's scaling (see Figure III-4). The difference between Wilks' and Haines' models relies on the fact that Haines' electrons experience only a fraction of the acceleration induced during a laser-light period before being moving beyond the laser light's penetration region. The new scaling found by Haines is then:

$$T_{e,hot}[\mathrm{keV}] = m_e c^2 \left(\sqrt{1 + a_0\sqrt{2}} - 1\right) \cong 511\left(\sqrt{1 + 1.2\sqrt{{I_{18}\lambda_{0,\mu m}}^2}} - 1\right). \quad (3.30)$$

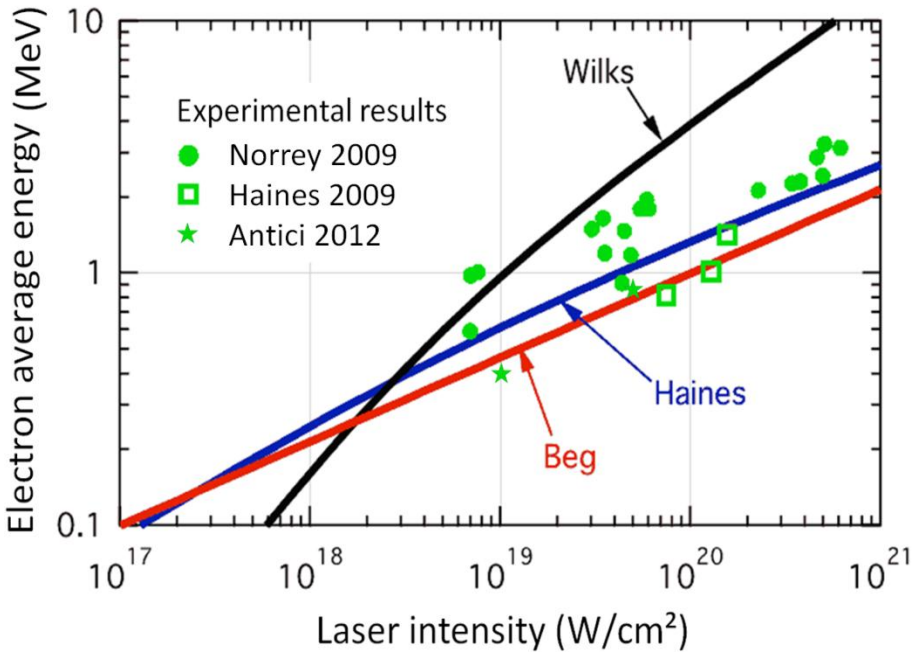

Figure III-4 : Comparison of different models of the electron average energy, as a function of the laser intensity with experimental results found in Refs. [30, 33].

Considering the experimental laser conditions encountered during the present thesis and the different scalings proposed, the hot electron temperature is estimated to range between a few hundreds keV to a few MeV.

Note that the expressions (3.28), (3.29) and (3.30) cannot be used for long plasma density gradients ($L_G \gg \lambda_0$, recalling L_G is the characteristic length of the density gradient). In such a case, the laser beam interacts with the under-dense plasma and triggers other non-linear mechanisms of absorption such as forward and backward Raman scattering that are not discussed here (see [3] and references therein).

III.2.2.4 Vacuum heating

This last mechanism concerns only very-contrast laser which generates very steep plasma density gradients at the front surface of the irradiated target due to their low intensity pre-pulse. Such plasmas are too steep for plasma waves to grow; hence, heating mechanisms based on them such as resonant absorption can no longer work [21]. However, the electrons located near the edge of the plasma density step between the target and the vacuum are directly exposed to the evanescent laser field. Instead of resonating, the electrons are dragged out into the vacuum well beyond the plasma Debye length by the p-component of the field. As the field reversed, they are injected back into the dense plasma with a high velocity. Since the laser has a short skin depth, the electrons continue their travel, penetrating deeper inside the overdense plasma without being slowed down by the reversing

field of the laser wave. They eventually lose their energy further by collision or any other mechanisms. This particular heating, called Brunel mechanism [34] or vacuum heating, is dominant for plasmas with L_G below 10 % of the laser wavelength, λ_0 [21].

III.2.3 Ion acceleration mechanisms

The ions are too heavy to be directly accelerated by the laser light, their charge-to-mass ratio being more than 1836 times lower than the electron one. Therefore, ions cannot follow the field oscillations. This prevents them from being subject to any of the above mechanisms. However, they are affected by the collective motion of the hot electrons accelerated by the laser and by the charge separation it induces. The different mechanisms presented after describe how hot electron energy is transferred to ions.

III.2.3.1 Sweeping acceleration

As mentioned in the previous paragraph, when a high-intensity laser pulse irradiates a solid-density target, the laser pulse propagates up to the relativistic critical density. In the focused zone, the ponderomotive force sweeps electrons and pushes them inward the target, creating a space charge separation (see Figure III-5).

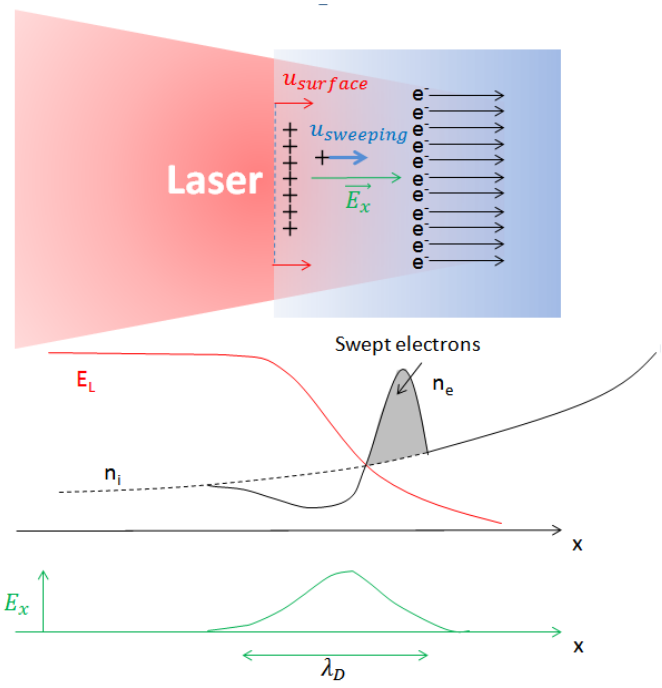

Figure III-5: Sweeping acceleration mechanism. E_L is the magnitude of the laser field and E_X the magnitude of the electrostatic field inside the plasma.

The sweeping length is of the order of the Debye length and the number of electrons is determined by the balance between the ponderomotive and the electrostatic potential induced by the swept electrons [35]. The strong electrostatic field induced in proximity of the critical front surface accelerates (sweeping acceleration) the ions (mass m_i) to a maximum velocity of:

$$u_{sweeping} = c\left(\sqrt{\frac{2m_e}{m_i}\left(1+\frac{I_{18}\lambda_{0,\mu m}{}^2}{1.37}\right)}-1\right). \tag{3.31}$$

In addition, the laser-light continuously pushes the surface by its pressure and the interface is moving during the sweeping process at the velocity [29] (see Figure III-5):

$$u_{surface} = c\sqrt{\frac{1+R}{2}\frac{n_c}{n_e}\frac{Qm_e}{m_i}\,a_0{}^2}, \tag{3.32}$$

where n_e is the electron density of the recessing surface, Q the ion charge state, n_c the critical density and R the reflection coefficient of the laser beam.

The ions are therefore accelerated in a moving frame, which gives a maximum velocity for the ions,

$$v_{max} \approx u_{surface} + u_{sweeping}. \tag{3.33}$$

Using a more comprehensive approach on the sweeping process, Ref. [35] finds a maximum velocity,

$$v_{max} \cong u_{surface} + 1.5\,u_{sweeping}. \tag{3.34}$$

For laser intensities typically above 10^{22} W/cm², the ion front surface velocity is predicted to exceed the ion sound velocity,

$$c_s = \sqrt{QkT_{e,hot}/m_i}\,. \tag{3.35}$$

Consequently, a shock wave would build up and, according to simulations, ions of higher energy would be generated, reaching twice the shock speed [36,37]. However such laser intensity has not been reached yet, so this last mechanism has never been measured and confirmed.

III.2.3.2 Target normal sheath amplification - Plasma expansion mechanism

III.2.3.2.1 Forward

III.2.3.2.1.1 Acceleration mechanism

The Target Normal Sheath Acceleration (TNSA) mechanism is currently the most efficient ion acceleration mechanism in terms of generating the most energetic and highest ions flux, and so has been theoretically and experimentally studied through many aspects.

At the opposite of the sweeping acceleration, the TNSA [38,39] is based on the expansion of the plasma at the target surface and accelerates ions from the target surfaces into vacuum. It takes place on both surfaces, but it is more efficient in terms of maximum ion energy if the surface has a sharp interface with vacuum, hence it is generally more efficient at the rear side of the irradiated target (at the opposite of the surface interacting with the laser). Note that for strong laser pre-pulse, the relatively hot pre-plasma generated on the front side of the target expands into vacuum, sending a shock wave through the target that heats the rear surface which loses its sharpness before the acceleration occurs, reducing its efficiency.

Mainly due to $\vec{J} \times \vec{B}$ heating, hot electrons are accelerated forward inside the target, with relativistic energy. At such energies, the hot electron population is slowed down a little inside the target. Indeed the hot electrons are much faster than the cold electrons of the target, and are consequently interacting weakly with them. Hence, the fast electrons reach the rear surface of the target almost without losing energy. This approximation works only if the mean free path of the hot electrons is much larger than the target thickness. In laser-produced ion beam experiments, the irradiated gold target is typically micrometric thick, while the hot electron temperature is around 1 MeV with a mean free path close to 0.4 mm [40].

Whereas inside the target the electron beam is neutralized by the medium, outside the target, the ions cannot follow the light electrons. While the first and fastest electrons escape the target, setting up a strong electrostatic sheath field, most of the hot electrons are retained by the strong field, forming a non-neutralized electron cloud over a Debye length (the maximum distance the plasma can support a charge separation). Assuming that the hot electron density $n_{e,hot}$ follows the Boltzmann equilibrium,

$$n_{e,hot} = n_{e0,hot} \exp\left(\frac{\phi e}{k_B T_{e,hot}}\right), \tag{3.36}$$

where $n_{e0,hot}$ is the hot electron density of the unperturbed plasma and ϕ is the electrostatic potential, the initial electrostatic field amplitude, E_{init}, at the interface can be calculated as [38],

$$E_{init} = \frac{k_B T_{e,hot}}{e\lambda_D}\sqrt{\frac{2}{\exp(1)}} \sim \sqrt{n_{e,hot} T_{e,hot}}\,. \qquad (3.37)$$

This strong electrostatic field, typically of a few TV/m, (1) ionizes the outermost atom layers of the target rear surface by barrier suppression [41][11] and (2) accelerates them normally to the rear surface. Physically, the electrons transfer their energy to the ions through the electrostatic field they generate. During the irradiation, the hot electron temperature is maintained by the laser which launches continuously hot electrons bunches into the plasma. The accelerated ions are locally neutralized by electrons. The induced electron rarefaction inside the target creates a positive layer at the target surface. One can distinguish three regions (Figure III-6):

1. at the front, a negative structure formed by the interface between the ion front and the hot electron Debye sheath, where the electrostatic field peaks,
2. a quasi-neutral layer where the electrostatic field is quasi-uniform,
3. a positive sheet located at the beginning of the expansion, where the electrostatic field is increasing linearly.

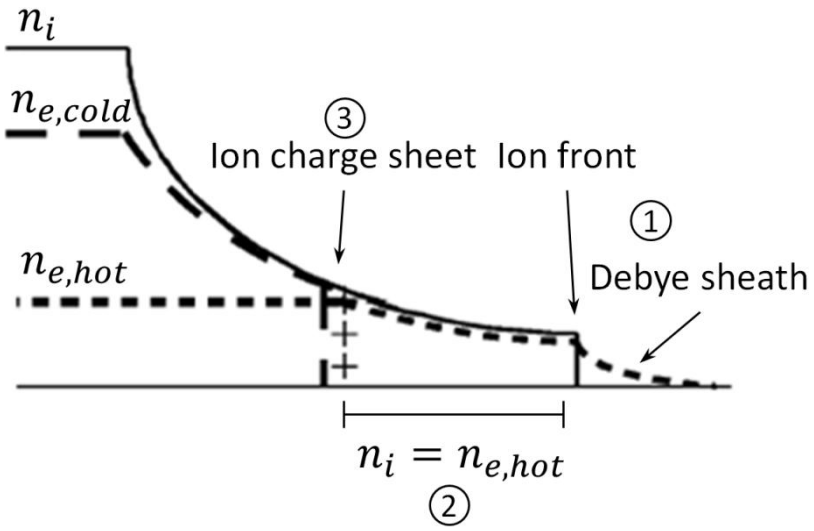

Figure III-6: Ion and hot/cold electron densities, respectively, $n_i, n_{e,cold}$ and $n_{e,hot}$ of the expanding plasma at the rear surface of the irradiated target (extracted from ref. [38]).

When the laser stops feeding the hot electron sheath, the regime passes from isothermal to adiabatic. The hot electrons continue to transfer their energy to the ions but their temperature decreas-

[11] The hot electrons can also directly ionize the atom when passing through the target. This process is negligible for short pulse laser (ps) interaction, but becomes predominant for ns pulses.

es. As a consequence, the electrostatic field decreases until ions and electrons reach equilibration, ending the acceleration process. Finally, it ends up with a dense ion bunch of short duration (of the order of a few ps), charge-neutralized by co-moving electrons [42].

III.2.3.2.1.2 Ion beam spectrum

The plasma expansion mechanism has been studied using two different 1D models: one isothermal, working at the early times of the process [38], the other adiabatic to model the plasma after the laser irradiation [43]. In these hydrodynamic models, the cold electrons, hot electrons (those accelerated by the laser) and ions are distinguished. The electron inertia is neglected, i.e., their density follows the Boltzmann equilibrium and keeps a Maxwellian distribution. The populations are only interacting through electrostatic forces. Those models consist in studying the collision-less expansion of the plasma into vacuum. They have been shown to be in good agreement with experimental results [44]. According to those models, the final ion spectrum is a semi-Maxwellian distribution,

$$\frac{dN}{dE} = \frac{n_{i0} c_s \tau}{\sqrt{2EZk_B T_{e,hot}}} \exp\left(-\sqrt{\frac{2E}{Qk_B T_{e,hot}}}\right), \tag{3.38}$$

where c_s is the sound velocity of the hot electrons plasma with a given $T_{e,hot}$, the temperature of the hot electrons at the beginning of the acceleration, Q, the ion charge, n_{i0}, the ion density of the unperturbed target. While in the adiabatic model, no formula exists for the energy cut-off, the isothermal model gives,

$$E_{max} \cong 2Qk_B T_{e,hot} ln\left(\tau + \sqrt{\tau^2 + 1}\right), \tag{3.39}$$

where τ is the normalized time of τ_{acc} , the ion acceleration duration,

$$\tau = \frac{\omega_{pi}}{\sqrt{2\exp(1)}} \tau_{acc}, \tag{3.40}$$

where ω_{pi} is the ion plasma frequency in the sheath. τ_{acc} depends on the duration of the laser pulse. It has been estimated from experimental results to [45],

$$\tau_{acc} = \alpha(\tau_{laser} + t_{min}), \tag{3.41}$$

where $t_{min} = 60\ fs$, τ_{laser} is the laser pulse duration, and α varies linearly from 3 at the intensity 2×10^{18} W/cm² to 1.3 at 3×10^{19} W/cm² and stays constant at 1.3 for higher intensities.

Spectra obtained in experiment usually do not follow perfectly the semi-Maxwellian predictions. Indeed a typical spectrum displays two, sometimes three, hot electron temperatures, those tempera-

tures increasing with ion energy [46]. One can easily identify them by measuring the different slopes of the ion spectrum using a Thomson parabola (TP) (see):

$$\frac{dN}{dE} \sim K_1 \frac{\exp\left(-\sqrt{\frac{2E}{QT_{e,hot\,1}}}\right)}{\sqrt{EQT_{e,hot\,1}}} + \mathrm{K}_2 \frac{\exp\left(-\sqrt{\frac{2E}{QT_{e,hot\,2}}}\right)}{\sqrt{EQT_{e,hot\,2}}} + K_3 \frac{\exp\left(-\sqrt{\frac{2E}{QT_{e,hot\,3}}}\right)}{\sqrt{EQT_{e,hot\,3}}}, \tag{3.42}$$

where K_1, K_2 and K_3 are three constants.

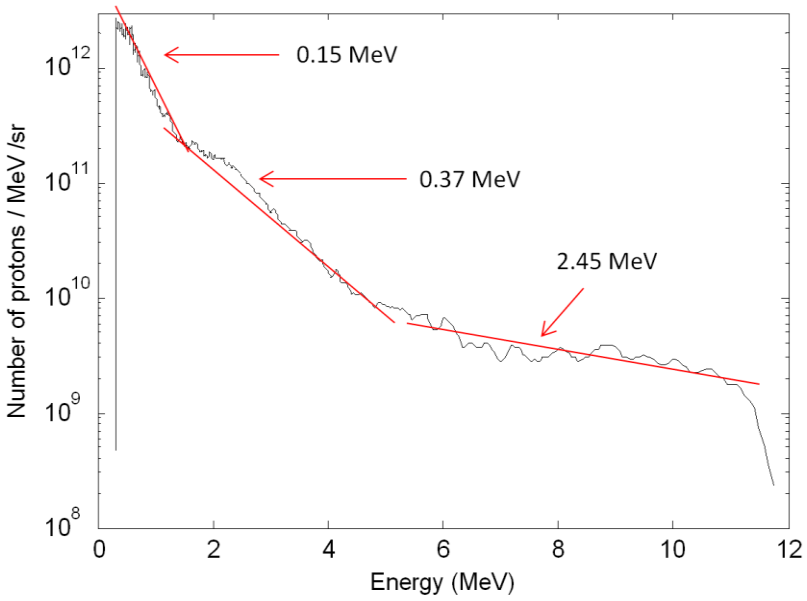

Figure III-7: Typical proton spectrum obtained using a TP and measured on the ELFIE laser during the October 2011 experimental campaign. The target was 10 µm thick Au and the 1 µm-wavelength laser intensity was approximately 3×10^{19} W/cm².

While the slope of the distribution is determined by the hot electron temperature(s), it has been shown that the energy cut-off is mainly proportional to the irradiance, $I\lambda_0^2$, of the laser interacting with the solid-density planar target (see Figure III-8). Note the different trend in ion maximum energy for ultrashort laser (below 150 fs) and short laser pulse (above 150 fs). It should be mentioned that other models and scaling laws have also been developed in order to reproduce experimental spectra and maximum (cut-off) energy (see references included in [44]).

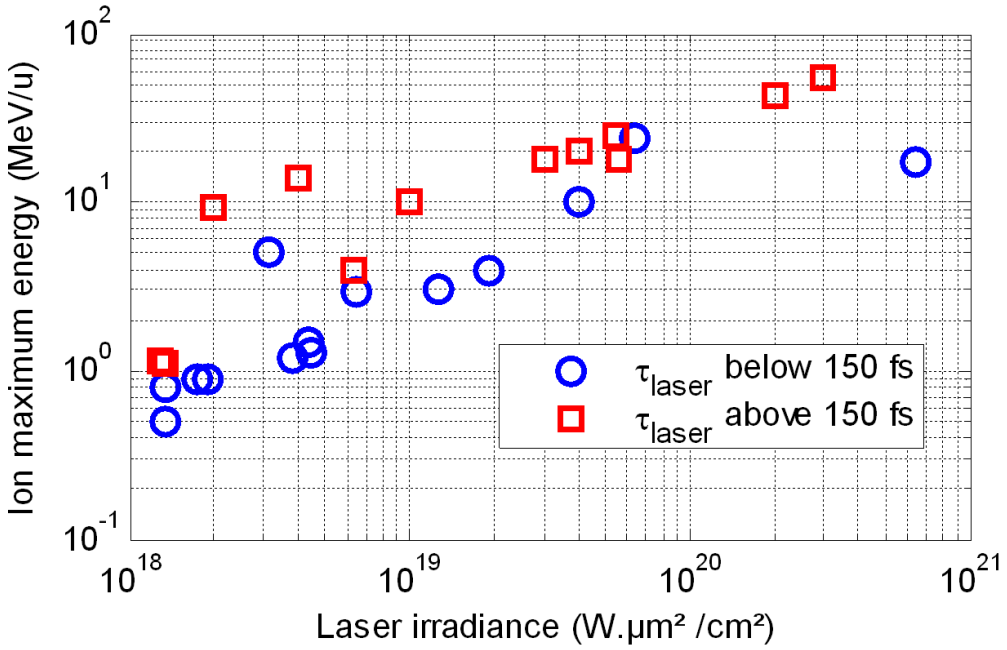

Figure III-8: Measured maximum ion energy plotted as a function of laser irradiance. Red squares and blue circles represent, respectively, the maximum ion energy measured during experiments using short and ultra-short laser pulse (data are extracted from Ref. [44, 45]).

III.2.3.2.1.3 Ion beam angular characteristics

Other characteristics of the ion beam generated by TNSA are their good directionality and laminarity. While the ion energy is dependent on the electrostatic field, the axis of proton emission depends on the geometry of the sheath field related to the hot electron spatial distribution.

The hot electrons accelerated at the front surface are little interacting with thin targets when passing through. Consequently, their divergence is equal to the one induced by the accelerating mechanism. It has been demonstrated that this divergence increases with the plasma gradient length [32, 33] and the laser intensity [47]. Nevertheless, in the case of small pre-plasma, the divergence is mainly due to the ponderomotive force transverse component [48]. The divergence angle is then comprised between 40° to 60° according to the electron energy, the value decreasing with the electron energy. When leaving the target, the electrons form an electron sheath at the solid-vacuum interface. Its spread depends on the hot electron divergence and the target thickness. The electron sheath exhibits a bell-shape due to the combination of the lateral spreading of the hot electrons and of the electron refluxing (see Figure III-9). Thus, electrons are concentrated along the principal propagation axis of the electrons [49].

Ions are accelerated normally to the isopotential and so follow the curvature of the bell shaped electron sheath (see Figure III-9). As a consequence, the ion beams accelerated by TNSA have a small

divergence: the ions are emitted normally to the target rear surface in a half-cone angle of 15°-20°, the angle decreasing with the ion energy [8]. The geometry of the sheath field explains as well the ion beam very good laminarity (the trajectories of the ions do not cross or overlap) [50].

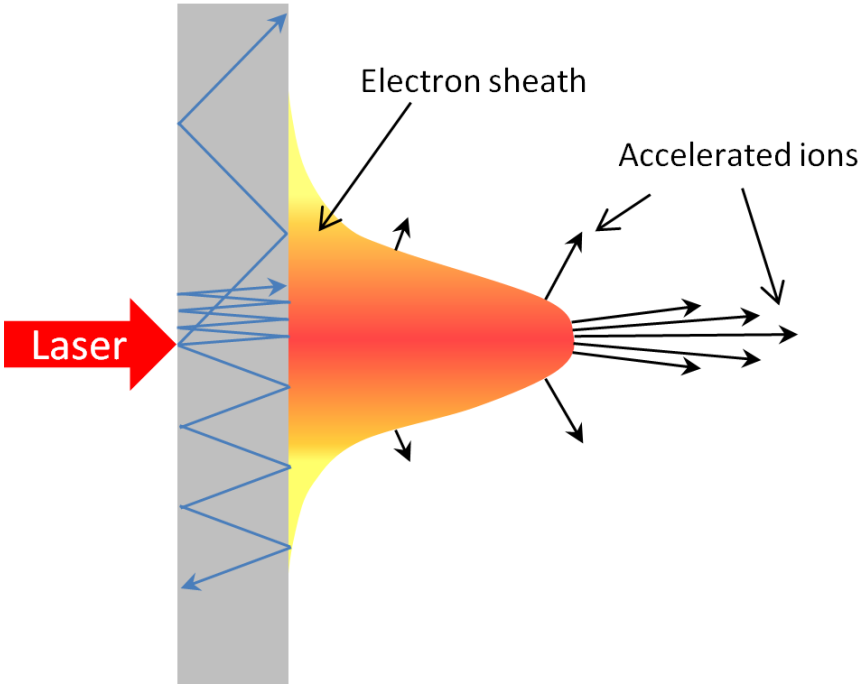

Figure III-9 : Illustration of the electron sheath at the target rear surface. The trajectory of 3 electrons injected inside the target at 3 different angles. One can see that, due to refluxing, electrons injected with a small angle compared to the target normal axis stay in the proximity of the center (with respect to the laser irradiation), while those injected with a big angle spread on a large surface. The electron density is therefore the highest in the center of the target. Due to the bell-shape of the electron sheath, it is also the region of the best directionality.

III.2.3.2.2 Backward

The same process appears at the front side of the irradiated foil. Indeed, hot electrons are accelerated backward due to the reflected laser light interacting with the plasma gradient and the hot electrons accelerated forward inside the target are partly reflected by the strong sheath field at the rear side of the target and come back to the front side. The front surface can then experience the same expansion mechanism. However, contrary to the forward acceleration for which the acceleration takes place from an unperturbed and planar surface (if the target is thick enough to prevent the shock wave induced by the pre-pulse to reach the rear surface before ion acceleration occurs), the front surface is irradiated by the laser. The laser pre-pulse can perturb the front surface before the arrival of the main laser pulse. Therefore, the front plasma expands before the arrival of the hot electrons. The electrostatic field is no longer proportional to $1/\lambda_D$, but to the inverse of the characteristic length of the plasma gradient $1/L_G$ (recalling L_G is the) [51], which reduces the energy cut-off [52]. Furthermore non uniformities in the laser intensity spatial profile tend to degrade the bell-

shape of the expanding plasma and so worsen the laminarity of the accelerated ion beam. These problems are resolved when the contrast of the laser beam is high (above 10^{-10}). The pre-pulse is then too weak to significantly perturb the front surface. In such a case, the backward ion beam is improved, but does not reach the quality level of the forward one [35]. It has also been shown that for thin enough targets (i.e., thin enough targets with respect to the electron mean free path), the hot electrons build up the same electrostatic field on both side of the irradiated target. The backward and forward ions are then almost identical [53]. This interesting characteristic has been used in chapter IV (see section 171).

III.2.3.2.3 Multi-charged and multi-species ion beams accelerated by TNSA

During this thesis, the problem of accelerating efficiently multi-charged ions, not only protons, was important. Since the main acceleration mechanism used during this thesis is the TNSA, we focus on it. Note that what is written on TNSA may apply to other mechanisms as well, since most of the acceleration mechanisms presented here take place at the target surface.

The accelerated ions originate from the atoms located on the foil surface, but, above all, from the contaminant always present on target surfaces, such as hydrocarbon or water vapor [3,54]. If the laser pulse is short (ps, fs), the main ionization process at the target rear side is the so-called tunnel ionization [41]. The electrostatic field created by the charge separation is high enough to be able to lower the potential barrier that maintains the electrons in orbit around the nucleus [55, 56]. The electrons have then a non-zero probability to get over it (see Figure III-10). If the electrostatic field is strong enough, the potential barrier could be completely canceled and the bound electron is ejected: this is called ionization by barrier suppression [57, 58]. Assuming the atomic potential to be the Coulomb potential, the potential balanced by an electric field, E, gives a resulting potential,

$$V(r) = -\frac{Ze^2}{4\pi\varepsilon_0 r} - eEr, \tag{3.43}$$

where Z is the charge of the nucleus, r the distance from the nucleus. One can estimate when the maximum of the potential is reached by solving $\frac{\partial V}{\partial r}(r_M) = 0$:

$$r_M = \sqrt{\frac{Ze}{4\pi\varepsilon_0 E}}. \tag{3.44}$$

The maximum of the atomic potential when not interacting with an electric field is equal to the ionization potential, U_i,

$$U_i = -\frac{Ze^2}{4\pi\varepsilon_0 r_M}. \quad (3.45)$$

The barrier is cancelled if and if only $V(r_M) = 0 = U_i + eEr_M$, which gives, E_{th}, the electric field threshold,

$$E_{th} = \frac{4\pi\varepsilon_0}{Ze^2} {U_i}^2. \quad (3.46)$$

It should be noted that in the case of longer pulses (ns), the ionization due to collisions with hot electrons has to be taken into account as well.

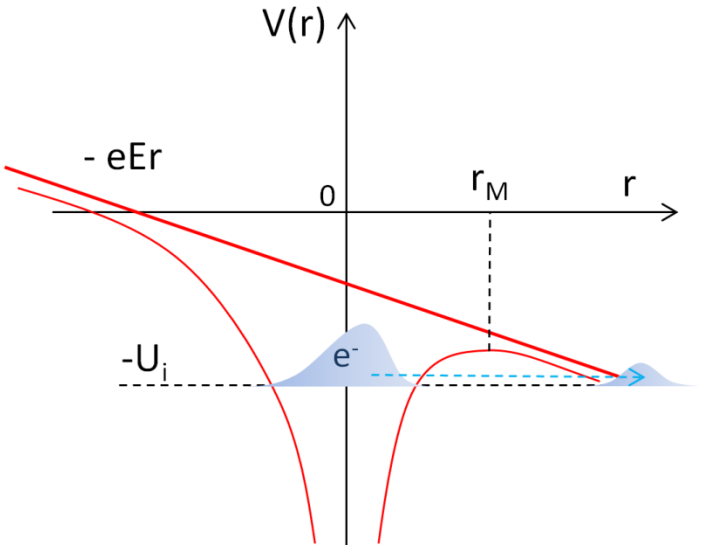

Figure III-10: Schematic picture of tunneling ionization by a strong external laser electric field, E.

While the outermost layers of the target experience a high electrostatic field, the deeper ones are screened by the ionized surface layers and are seeing an electrostatic field quickly dropping with the distance from the layer to the surface [59]. As a consequence, the highest charge of the different accelerated ions increases with the electrostatic field. The threshold for the minimum field strength needed for the ionization of the kth ionic state can be estimated using (3.43),

$$E_k = \frac{{U_k}^2 4\pi\varepsilon_0}{e^2 Z}, \quad (3.47)$$

where U_k is the ionizing potential of the kth ionic charge state and Z, the atomic number of the nuclei. According to this estimation, a laser-beam irradiating an aluminum target and generating a sheath field of 2 TV/m can generate e.g., protons, carbon ions up to C^{4+}, oxygen ions O^{6+} and aluminum ions up to Al^{6+} with E_k, respectively, of approximately 0.18 ($U_4(C) \cong 64.5\ eV$), 1.7 ($U_6(O) \cong 138.1\ eV$) and 1.9 ($U_6(Al) \cong 190.5\ eV$) TV/m [60]. The acceleration process has an impact on the output spectra as well. Indeed the velocity increase during the acceleration process is proportional to the ion charge (Qe) to mass (m_i) ratio:

$$\frac{d\vec{v}}{dt} = \frac{Qe}{m_i}\vec{E}, \tag{3.48}$$

where $\vec{E}$ is the electrostatic sheath field. The accelerated protons, i.e., the ions with the highest charge-to-mass ratio, followed by the other light contaminants are located at the ion front. They experience the highest electrostatic field and shield the heavier and slower ions. Therefore the hot electrons are transferring preferentially their energy to the lightest and most ionized particles. The results is an ion bunch composed of a Maxwellian spectrum for each accelerated ions with a number of particle and a maximum energy decreasing with the charge-to-mass ratio. It should be mentioned that the accelerated ions can also be ionized or may capture some electrons during the expansion phase when propagating in the near-critical plasma. This effect is discussed in chapter IV (see section IV.2.4.6).

To obtain a greater proportion of heavier ions, one can remove the contaminants of the surface layer by heating it prior to the main pulse irradiation using a CW laser [61] or by Ohmic heating [62] (without damaging to much the target planarity). A temperature above 1000°C is needed to remove all of the contaminants [3], but a temperature of 300-400°C is enough to considerably reduce the hydrocarbon contamination [61].

III.2.3.3 Radiation pressure acceleration mechanism

Radiation pressure acceleration (RPA) is the acceleration of ions at a surface irradiated by intense light, where the accelerating force is determined by the radiation pressure of the irradiating light. This principle of the mechanism is very close to the sweeping mechanism. The only difference lies in the target size. Indeed the RPA requires the target thickness to be below the laser skin depth.

Like in the sweeping mechanism, the electrons are quickly accelerated to relativistic speed by the laser field and piled up in front of the laser pulse. They leave behind a charge depletion layer, giving rise to an electrostatic field back holding them and in turn accelerating the ions. In the case of very thin targets, the electrons are ejected from the target and transfer most of their energy to the ions. Since the target is very thin, all of the ions are experiencing an electrostatic field and are accelerated to the same velocity forming a quasi-monoenergetic ion layer [63]: the accelerated foil, which consists of the electron and the ion layers, can be regarded as a relativistic plasma mirror co-propagating with the laser pulse [22]. In fact, the laser continuously pushes the electron layer, which in turn accelerates the ions through the charge separation field. This very efficient process allows laser-to-ions high energy conversion and leads to the generation of a mono-energetic ion bunch. Particle in cell (PIC) simulations [22, 64] have shown that at intensities above 5×10^{21} W/cm^2, RPA starts to dominate

over TNSA, and that at intensities above 10^{23} W/cm^2 and using thin foil targets, an efficient generation of GeV ions and a linear scaling of ion energy with the pulse energy may be obtained.

Although this very interesting mechanism has been recently pointed out experimentally [65, 66], it remains very challenging:

- a high electron temperature may perturb the mechanism. In such a case, the electrons significantly spread in energy and the electron density is considerably reduced where the laser is interacting. In addition the acceleration by the sheath field of the expanding electrons (TNSA) becomes predominant. This issue can be overcome by using a circularly polarized laser so that the heating component of the ponderomotive force is cancelled [67].
- very thin target may be damaged/destroyed by the laser pre-pulse before the main pulse arrives. A contrast of less than 10^{10} at 10ps before the main pulse is required [68].
- transverse Rayleigh-Taylor like instability grows on the foil causing spectral broadening of the ion beam and the accelerated foil to break [67]. To prevent such instabilities, a short rise time is required.
- lasers of intensity close to several 10^{21} W/cm² exist, but nowadays suffer a very low contrast.

III.2.4 Main results and issues toward applications

Exceptional properties have been observed for ion beams accelerated from planar targets such as high brightness, high spectral cut-off, high directionality, low emittance, and short duration (a few ps at the source) [69]. These characteristics have already been used successfully in fundamental research experiments to generate warm dense matter as explained in chapter I or to measure the temporal evolution of high fields present in low-density plasmas with a precision of a few ps in time and a few µm in space, through the so-called proton radiography technique [70, 71]. Furthermore, many other interesting applications are in view such as in the medical field [72, 73, 74], nuclear physics [75, 76], accelerators [77], astrophysics [14] and in ICF experiments [78], but have requirements which have not yet been achieved in laboratory. Those can be summarized by the following points: (i) higher energy, (ii) enhanced control of the spectrum width, (iii) higher number and (iv) enhanced stability and repetition rate.

In this context, many studies have been conducted to improve our understanding of the acceleration mechanisms and thus control the properties of the emitted ion beam. Since the hot electrons are

essential in the ion accelerating process, the principal way to enhance laser-generated ion beams is to play on the hot electrons characteristics. One recalls that the initial electrostatic field in TNSA is proportional to $\sqrt{n_{e,hot}T_{e,hot}}$. The hot electron density and temperature can be enhanced by changing the laser parameters, or by modifying the irradiated target properties.

Studies about the influence of different interaction parameters have demonstrated that the maximum energy of laser-generated ions, E_{max} is strongly dependent on the laser intensity [27]. For short pulse longer than 300 fs, E_{max} is proportional to the square root of the intensity, while for shorter pulse the dependence is linear, those dependences following the one of the hot electron temperature with the laser intensity [31]. The highest energy cut-off has been obtained using a PW (10^{15} W) short pulse laser with energy up to 60-67.5 MeV [8, 79], but with a very low number of ions at that energy (5×10^6 protons/MeV). The pulse duration also plays an important role in so far as it increases the acceleration duration and thus the final energy cut-off. This can also be viewed as an increase of the laser energy deposited in the foil. Finally, as mentioned previously, the laser contrast also plays a role in the sense that a too intense ASE can damage thin targets and thus reduce dramatically the acceleration.

The design of the target interacting with the high-intensity short pulse has shown to have a significant impact on the generated ion beam as well.

Since the ion beam has a too large envelope divergence [8], a way to increase the proton flux is to focus the beam. It can be done by using curved targets in a hemispherical shape [9,80]. Indeed the plasma expansion follows the target shape and thus the electrostatic field induced by the hot electrons is directed toward the hemisphere focal point. Therefore the protons converge in a ballistic mode at the center of the sphere to a few tens of micron spot, increasing the flux by almost a factor of magnitude. However, it has been recently shown that filamentation occurs during the focusing. This could potentially limit the focalization and degrade the low emittance of the ion beam [81].

The proton divergence can also be enhanced by guiding and collimating the hot electron upstream. Proton beam generated using flat cone target composed of a cone target with a small and flat foil at the tip have shown maximum energies 1.3 times in excess of flat-foil targets [82]. The cone target indeed concentrates hot electrons at its tip, leading to a better collimation of the hot electrons, but also a higher flux [5], and thus improves the ion acceleration. Nevertheless those interesting results have shown to be significantly sensitive to the laser contrast ratio [83].

Increasing the electron flux can also be managed by reducing the target thickness [84]. Using a thin target reduces indeed the longitudinal and transverse dilution of the electrons passing through,

hence increases the hot electron density at the surface [13]. Finally, a huge proportion of the hot electrons (more than 90%) emerging from the rear side does not escape the target, but is thrown back inside the foil by the high electrostatic field located at the surface. This phenomenon is called electron recirculation. It allows the superposition of electrons accelerated at different times and thus increases the amplitude of the electrostatic field and the proton energy. A thin target allows the re-circulating electrons to do several back-and-forth between the front and the rear surface of the irradiated target, increasing the effect of electron superposition. The thinner the target is, the more important the recirculation effect. Nevertheless, as already explained with RPA, very thin targets may be damaged by the laser pre-pulse (ASE pedestal) before the main pulse arrives.

Although the hot electrons are principally accelerated in the longitudinal direction, the transverse component of their velocity induces a noticeable transport of the hot electrons in the target transverse dimension over hundreds of μm [85]. In the case of very thin targets, this transverse dilution is increased by the recirculation. It can be counteracted by using Reduced Mass Targets (RMS) [86]. Besides being thin, those targets have a limited size in the transverse direction. Consequently the transverse dilution of the recirculating electrons is limited. The electron density is increased, strengthening the electrostatic field. In addition, the confinement of the hot electrons extends the acceleration duration.

The last target parameter on which one can play is the target composition. Metallic targets yield higher maximum proton energy. This is related to the dependence of the fast electron transport through solid-density matter on the initial conductivity of the material [87]. A double layer target has been proposed to generate both mono-energetic and higher energy ion beams [88]. It consists on a high-Z substrate with very thin coating of low-Z atoms. The high Z substrate actually interacts with the laser and controls the electrostatic field strength: the number of low-Z ions in the second layer is so low that it does not have any significant effect on the electrostatic field. The light ions, which have a higher charge-to-mass ratio, are accelerated much more efficiently than the heavy ions. The low Z atomic layer is therefore completely expelled from the substrate by the electrostatic field, forming a quasi mono-energetic ion beam. This type of target has been used successfully in ref. [62], but the ions of the mono-energetic beam were low in number (around 10^9 /MeV/sr) and in energy (3 MeV/u) to be used in any application.

To conclude, despite all of the research on target design, using laser-generated ion beams for any of the practical applications mentioned before is still not possible. The key points remain the laser intensity, energy and contrast. Building higher repetition rate, higher intensity and more energetic laser facilities is limited by the technology and the price [89]. Furthermore, the best existing high-

intensity short pulse lasers are still currently considered as prototypes. This affects their performances and stability. In addition, the compactness of the laser, which is one their best qualities, would be lost by increasing the size of the laser in the proportions anticipated for the future facilities delivering higher energy and intensity laser. One way to bypass this technology issue would be to increase the laser-to-ion conversion efficiency (currently around 1-7 % [27]) [89]. This is actually the objective of the research conducted about lower-than-solid density targets developed in the next part.

III.3 Ion acceleration in lower-than-solid density targets

It was recently shown that a promising way to accelerate ions forward to high energies and in a collimated beam is to use sub- or near-critical density targets (electron density below or close to n_c) instead of solid ones [68, 90, 91, 92, 93]. Despite the low performance in terms of energy and number of particles measured up to now, under-dense targets have a great potential: the energy conversion from the laser to the near-critical density target is much more important than with a solid target [94]. The laser transfers most efficiently its energy to the electrons in near-critical density plasmas, through plasma wave generation (e.g. parametric instabilities) and resonant absorption before being reflected at the critical density. Comparatively, when interacting with a solid target, a laser interacts little with the very thin near-critical plasma region located at the target surface and most of its energy is reflected there. On the contrary, in a near-critical density target, the laser passes through the whole target and transfers efficiently most of its energy to the plasma. As a consequence, in the scope of any applications mentioned above, less energetic lasers are needed. Less energetic lasers means also a shorter cooling-off time for the laser amplifiers, thus a higher repetition rate. In the case of gas jet targets, the density and the material of the target can be easily adjusted according to the request. In addition, the alignment process is also considerably reduced and the time between two shots is no longer determined by the time required to change from one target to another. Finally the mechanisms of acceleration have shown to be less susceptible to the laser pre-pulse and obviously to the problem of target surface contamination that prevents single-species ion-beam acceleration when using solid-density targets. However, from the experimental point of view, it remains difficult to operate over or close to the critical density. The pulse can undergo severe propagation instabilities [95 and references therein] and loses energy through inverse Bremsstrahlung absorption, ionization, and plasma scattering instabilities.

Our experimental study about ion acceleration in lower-than-solid density targets concerns the interaction of a short-pulse-laser with two very different target conditions. The first section is devoted to the interaction with an under-dense ($\mathrm{n}_e < \mathrm{n}_c$) gas jet target in which ions are accelerated radially

with respect to the laser propagation axis by Coulomb explosion. The second section is dedicated to a very promising longitudinal ion acceleration mechanism that is predicted to occur in near–critical density target with a smooth density gradient. In order to study this collisionless shock acceleration mechanism, we performed an experiment in which the short pulse laser interacts with an exploded foil reproducing the conditions required for this mechanism to occur.

III.3.1 Ion acceleration in a subcritical density gas jet target

Our experimental study deals with a 1 µm-wavelength high-intensity (intensity of several 10^{18} W/cm²) short-pulse laser irradiating helium gas jet targets of density from 1 to 20 % of the critical density (once ionized). Our objective is to estimate the potentialities of such a set-up to produce two similar high energetic ion beams. After explaining the theory about the principal ion acceleration process that occurs with such target and laser conditions, i.e., the Coulomb explosion acceleration mechanism, its main characteristics are underlined. Subsequently, we describe the experiment we performed at the Lawrence Livermore National Laboratory (LLNL) and present the results we obtained. We pay a specific attention to the rotational symmetry (around the laser propagating axis) exhibited by the ion beam generated through the Coulomb explosion acceleration mechanism. Finally, we discuss the potentiality offered by this interesting characteristic in the scope of experiments aimed at studying the stopping power and more particularly regarding the one presented in chapter IV (see section IV.2.5).

III.3.1.1 Theory

III.3.1.1.1 Ionization

Let us first look at how the irradiated gas becomes a plasma, i.e., the ionization process of the gas. When a high-intensity laser pulse interacts with a gas, the gas response depends strongly on the intensity of the laser beam. An electron can be ejected from an atom if it receives a large enough energy to be stripped off from its bound state to a free continuum state.

- It can do this by absorbing a single photon of high energy, hν, (i.e., high frequency, ν). This process is called the photoelectric effect (see Figure III-11a). For a 1 µm-wavelength laser, this effect is very limited since the energy of the photons is relatively low, around 1 eV. Recall that e.g., the binding energy of the electron in hydrogen is 13.6 eV.
- Another possibility is multi-photon ionization [55]. If the photon density, i.e., light intensity, is high enough, an electron can simultaneously absorb several low frequency photons to

overpass its binding energy (see Figure III-11b). The ionization rate depends strongly on the light intensity and this process becomes noticeable for laser intensity above 10^{10} W/cm^2 [96].

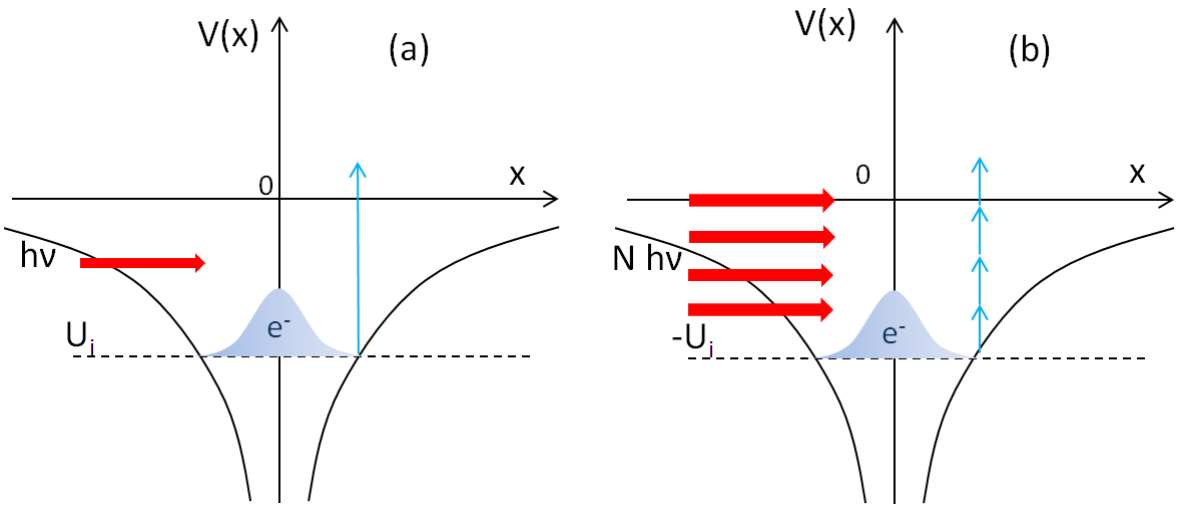

Figure III-11 Schematic pictures of the photoelectric effects (a) and multi-photoionization by N photons (b)

- When the laser field becomes strong enough to disturb the Coulomb field created by the nucleus and felt by the electron, the electrons can be ionized by barrier suppression ionization [55] (see section III.2.3.2.3).

One can estimate the rate of the latest ionization process using the Ammosov–Delone–Krainov (ADK) model [41, 56]:

$$\nu_{ADK}[s^{-1}] \cong 6.6 \cdot 10^{16} \left(\frac{q^2}{n_{ef}^{4.5}}\right) exp\left[-\frac{2q^3}{3n_{ef}^3}\frac{E_{at}}{E}\right]\left\{10.87\frac{q^3}{n_{ef}^4}\frac{E_{at}}{E}\right\}^{\frac{2}{n_{ef}^{1.5}}}, \quad (3.49)$$

where E is the ionizing field, E_{at}, the atomic unit of electric field (0.51 TV/m), q, the charge of the created ion and $n_{ef} = q/\sqrt{U_k/U_H}$, U_K and U_H being the ionization potentials of respectively the ionized species and hydrogen.

For example, the ionization rates for helium can be estimated for different laser intensities using the ionization potentials of the electron which are respectively 24.59 eV and 54.42 eV [60] and are exposed in **Erreur ! Source du renvoi introuvable.**.

Light intensity (W/cm²)	Ionization rate (ADK) for He^{+} in ps^{-1}	Ionization rate (ADK) for He^{2+} in ps^{-1}
10^{14} W/cm²	2.6×10^{-26}	2.6×10^{-32}
10^{15} W/cm²	**13**	1.7×10^{-3}
10^{16} W/cm²	3×10^{8}	**3.5×10^{5}**
10^{17} W/cm²	6×10^{9}	3×10^{7}
10^{18} W/cm²	1×10^{9}	2.5×10^{7}

Table III-1: Rate of tunnel ionization of helium as a function of the laser intensity.

The table shows that the gas is quickly ionized by barrier suppression for intensities above approximately 10^{15} W/cm² and fully-ionized for intensity above approximately 10^{16} W/cm². This is consistent with the results obtained in Ref. [97].

The predominant mechanism between multi-photon ionization and tunnel ionization can be identified using the Keldysh parameter [55]:

$$\gamma_K = \left(\frac{U_k}{2\phi_p}\right)^{1/2}, \qquad (3.50)$$

where ϕ_p, the ponderomotive potential.

$\gamma_K > 1$ indicates that the electric field is not high enough to suppress the potential barrier, we are then in the regime of multi-photon ionization. At the opposite, when $\gamma_K < 1$, tunnel ionization is predominant. In the context of our study, we used short-pulse lasers with peak intensity above 10^{18} W/cm². This corresponds to a ponderomotive potential over 0.15 MeV and a Keldysh parameter of the order of 100. Therefore, we can consider the irradiated gas to be quickly fully-ionized by tunnel ionization to a plasma state within a few fs. It should be noted that laser pulses are usually preceded by low-intensity pre-pulses arriving before the main pulse, this leads to a partial ionization of the gas by multi-photon ionization prior to the main pulse occurring. Furthermore, since 10^{16} W/cm² is enough to fully ionize the helium gas, the ionization process takes place at the foot of the pulse. From now on, we thus consider that our laser pulse is directly interacting with a fully-ionized plasma.

III.3.1.1.2 Self-focusing and plasma channel formation

The interaction between a high-intensity laser pulse and a low-density plasma results in the self-focusing of the radiation. Two factors contribute to this focusing on a femtosecond time scale: the relativistic increase of the electron mass and the ponderomotive force.

The laser causes the electrons to oscillate at relativistic speeds and thus, decreases locally the plasma frequency. Writing the dispersion relation (Eq. (3.51)), for a relativistic light wave, one obtains,

$$\omega_0{}^2 = c^2 k_0{}^2 + \omega_{pe}^{rel\,2} = c^2 k_0{}^2 + \omega_{pe}{}^2/\gamma\,. \tag{3.51}$$

Recalling that the refraction index is given by,

$$\eta \equiv \frac{ck_0}{\omega_0} = \sqrt{1 - \frac{\omega_{pe}{}^2}{\gamma \omega_0{}^2}}, \tag{3.52}$$

one can see that the refraction increases with the Lorentz factor and so with the laser intensity (see Eq.(3.3)), i.e., the phase-velocity of the laser-wave ($v_\varphi = c/\eta$) decreases with the intensity. Therefore, the phase front travels more slowly at the center of a Gaussian laser-beam than at its edge (see Figure III-12). The curvature of the wave front causes the rays to bend proportionally to the relative path difference leading to a self-focusing of the beam. This effect is enhanced by the transverse ponderomotive force that induces the electrons to drift away from the beam axis at relativistic speed. The plasma frequency is therefore reduced at the center of the laser-beam ($\omega_{pe} \sim \sqrt{n_e}$), increasing even more the refractive index.

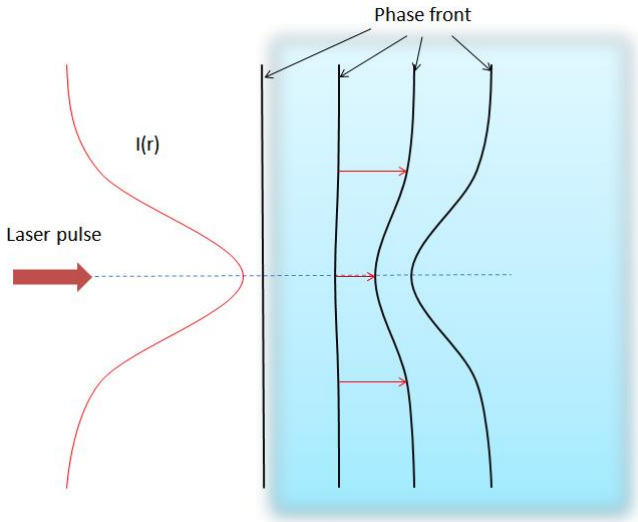

Figure III-12: Front bending of the laser due to relativistic self-focusing.

This effect is counteracted by the natural beam spreading due to diffraction[12]. The threshold for the laser power, P_L, above which a Gaussian beam is self-focused in a plasma with a uniform density can be estimated by [98],

$$P_L[GW] \cong 16.2\, n_c/n_e. \tag{3.53}$$

[12] If the target is not fully-ionized (lower intensity or targets with a high Z_N), refraction due to the ionization process may occur as well: in the center of the beam (where the intensity is the highest), the ionization process is more important and thus increases the electron density and the refraction index in this zone.

Note that n_c is the nonrelativistic critical density. One can also extract from Eq.(3.53) a condition on the electron density,

$$n_e[cm^{-3}] \cong \frac{6.85 \times 10^{16}}{{\lambda_{0,\mu m}}^2 P_L\,[TW]}. \tag{3.54}$$

The relativistic self-focusing becomes stronger when the laser beam decreases in diameter and becomes more and more intense.

It ends up in a self-focused channel which structure is governed by the balancing between the ponderomotive force and the Coulomb forces caused by the electron depletion on the laser axis leaving a large positively space charge area around the focal laser spot. Indeed the heavier ions moves much more slowly than the electrons and are not directly affected by the laser field. Note that, for a laser power slightly more important than P_L (approximately $1.1\ P_L$), the electrons are completely ejected from the plasma channel which then exhibits a radius of the order of the plasma skin depth [99].

III.3.1.1.3 Coulomb explosion mechanism

Ions are violently expelled from the positively charged zone created by the laser. This mechanism is called Coulomb explosion. Physically, within a time scale of $1/\omega_{pe,}$, most of the fast electrons are retained by the electrostatic field induced by the charge separation and transfer their energy to the ions through this electrostatic field. Hence, the ions are accelerated radially, i.e., in the direction of the electrostatic field, and move away from the laser axis, spatially neutralized by some co-moving electrons.

Since the charge separation is due to the ponderomotive force that drives the electrons away from the high-intensity area, the energy transfer to an ion reaches its maximum when the ponderomotive force and the force due to the charge separation compensate [100]:

$$\frac{\partial \overrightarrow{p_e}}{\partial t} = e\vec{E} - m_e c^2 \vec{\nabla}\bar{\gamma} = 0, \tag{3.55}$$

where $\overrightarrow{p_e}$ is the electron momentum, $\vec{E}$ the electrostatic field given by $\vec{\nabla} \cdot \vec{E} = \mathrm{e}\delta\mathrm{n}_e/\varepsilon_0$, with $\delta\mathrm{n}_e$ the charge density of the charge separation zone and $m_e c^2 \vec{\nabla}\bar{\gamma}$, the ponderomotive force as defined in Eq. (3.22). One obtains for the ions of charge Q:

$$\frac{\partial \overrightarrow{p_i}}{\partial t} = Qe\vec{E} = Qm_e c^2 \vec{\nabla}\bar{\gamma}, \tag{3.56}$$

where $\overrightarrow{p_i}$ is the ion momentum.

The maximum energy actually corresponds to the relativistic ponderomotive energy:

$$U = Qm_e c^2(\bar{\gamma} - 1). \tag{3.57}$$

Recalling $\bar{\gamma} = \sqrt{\left(1 + \frac{{a_0}^2}{2}\right)}$, this result clearly indicates that the maximum energy reached depends only on the intensity of the laser beam. The plasma density has only an impact on the self-focusing effect that may increase the laser intensity. Indeed a higher plasma density means a shorter laser skin depth ($\sim {n_e}^{1/2}$), thus a smaller focal spot diameter and a higher intensity. The accelerated particles being the ones located in the un-neutralized space charge area, the density plays also a role on their number.

The intensity gradient of the laser pulse is radial, so the resulting momentum gained by the electrons is mainly perpendicular to the laser propagation axis. As a consequence, the ions are preferentially emitted transverse to the direction of the laser beam propagation (see Figure III-13).

It is important to note that, at relativistic intensities, instabilities (e.g. parametric instabilities such as Stimulated Raman Scattering (SRS) [101], filamentation [102]) may occur as well and can perturb the laser beam profile and reduce the focalization, and so limit the acceleration process [99, 103, 104].

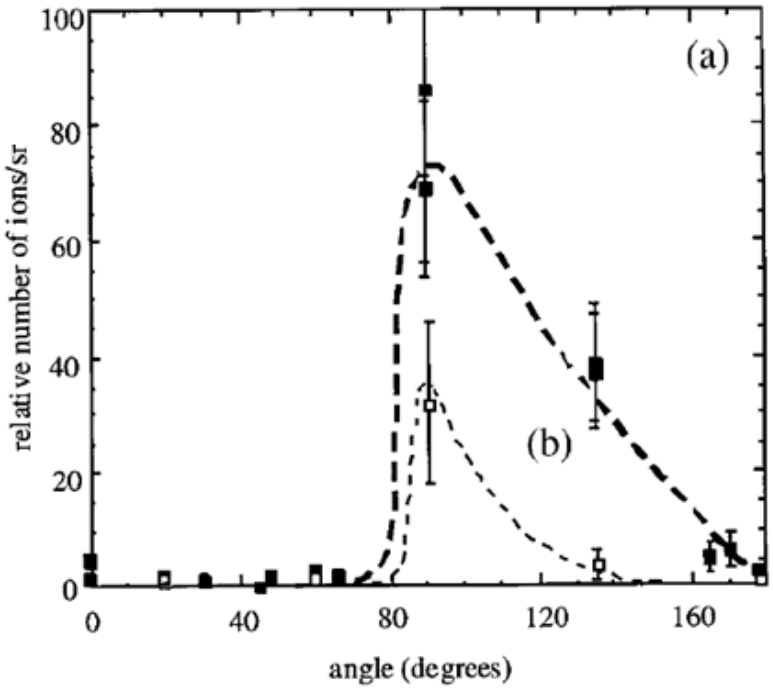

Figure III-13: Angular emission of energetic ions; distribution of helium ions with energy greater than (a) 400 keV, (b) 2 MeV (figure extracted from Ref. [100]).

The first measurements of high energy ions accelerated this way reported in Ref. [100] have shown a maximum energy of 3.6 MeV for helium using a laser of 50 J and duration of 0.9 ps at a wavelength of 1.054 µm. The laser pulse was focused to a 5 µm diameter spot into a gas jet target with an electron density of 5.3×10^{19} cm^{-3}.

III.3.1.2 Experimental study

III.3.1.2.1 Our measurements: objective and set-up

In the scope of measuring the stopping power of energetic ions in warm dense matter, knowing with a good precision the incoming probe ion beam is fundamental. However the diagnostics commonly used to measure broadband laser accelerated beam are disruptive (magnetic selector) or even destructive (TP). The rotational symmetry of the Coulomb explosion caused by the focusing of a high-intensity laser beam in a gas jet could be a solution to our problem. Indeed the incoming probe ion beam emitted at a certain angle, can then be inferred from the disruptive measurement of another ion beam emitted at the same angle compared to the laser axis. The study of the reliability of this symmetry is the main focus of the study presented here. Those measurements were also needed for the charge equilibration experiment that is presented in chapter IV. This experiment aimed at measuring the best compromise between the different parameters of the interaction: (1) the density of the gas jet, (2) the laser pulse parameters and (3) the position of the laser focus compared to the gas jet location, all this in order to get a reproducible and symmetric high-energy helium beam. Such measurements could be also useful for future experiments using the same set-up.

The experiment we present the result of was carried out using the TITAN laser at the Lawrence Livermore National Laboratory (LLNL) working in the chirped pulse amplification (CPA) mode at a wavelength λ_0= 1.064 µm. The experimental set-up is shown in Figure III-14.

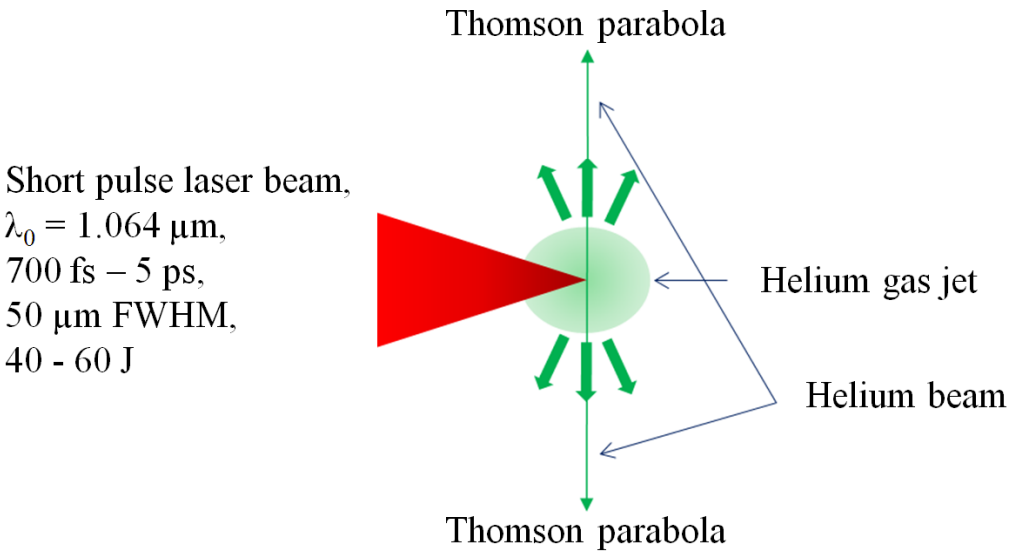

Figure III-14: Experimental set-up.

The helium ion beams were measured by two TPs located on both sides of the gas jet. They were looking at the emission of ions accelerated at 90° compared to the laser propagation axis.

III.3.1.2.2 Parameters of the experiment

III.3.1.2.2.1 Gas Jet

The gas jet system (see Figure III-15) is composed of: a bottle containing the compressed gas; a pressure transducer in charge of adjusting the pressure of the gas-jet, a tube that connects the transducer to a fast solenoid valve in charge of switching on or off the gas flow into the nozzle; a trigger box in charge of triggering the valve before the shot; a nozzle which is here a 10 cm tube ended by a 1 mm diameter size hole from where the gas is ejected. The nozzle is oriented vertically and the gas expelled toward the bottom. The high-intensity laser beam of 40-60 J energy (the energy range corresponds to shot-to-shot fluctuations) is focused using an f/3 (i.e., the f-number[13] is 3), off-axis parabola to a 50 µm diameter focal spot full width of maximum (FWHM) inside the helium gas and accelerates helium ions by Coulomb explosion. The two TPs are located on both side of the gas jet, 1 m away from the ion source to measure the spectra of the helium beam accelerated at 90° compared to the laser axis.

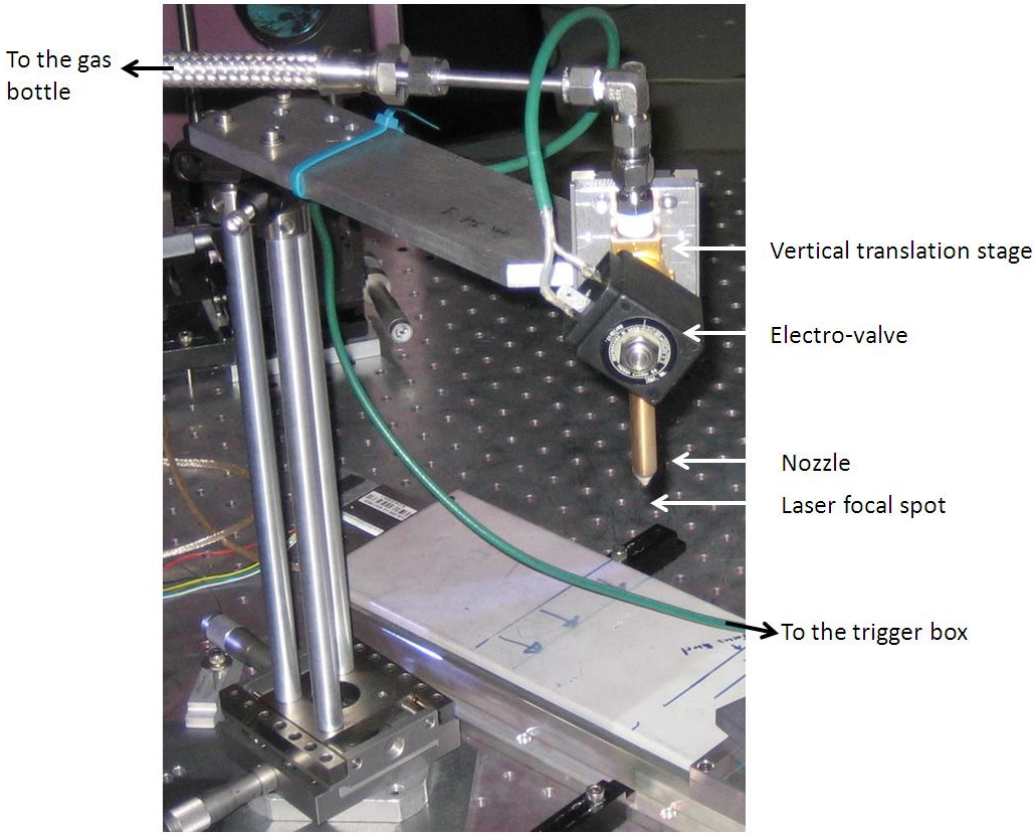

Figure III-15: Photo of the gas jet system used during the TITAN July 2012 campaign.

[13] The f-number is defined by the ratio of the focal length to the optical diameter of the parabola.

(1) To look at the impact of the gas jet density, we played on two parameters:

- the gas pressure inside the nozzle: 20 or 100 bar,
- the vertical distance between the nozzle exit and the focus of the beam.

(2) Two different positions of the focus compared to the nozzle center were used to measure the impact of the laser focus inside or outside the gas:

- in the center of the gas just above the exit of the nozzle,
- at the edge of the gas at 0.5 mm from the center.

It should be noted that this parameter modifies also the gas density where the ionization takes place.
(3) Since our best focal spot was already too wide compare to what can be done using such a laser beam, it was not interesting to play on it. However, we used two laser beam durations: 700 fs and 5 ps. It has an impact not only on the duration of the accelerating process, but also on the intensity of the beam, respectively, estimated around 3×10^{18} and 6×10^{17} W/cm² in vacuum.

III.3.1.2.2.2 Thomson Parabola

A TP is a diagnostic that is used to obtain absolute energy spectra for all of the different ions of the beam. The particles are deflected by a pair of permanent magnets located inside a soft iron yoke (to improve the field strength and homogeneity) to differentiate particles of different velocity, i.e., energy per nucleon along one dimension, and by a pair of electrodes to differentiate particles of different charge-to-mass ratio (Q/m_i) along the other dimension (see Figure III-16). Then, the particles are collected on the detector – an image plate (IP), providing a 2D image of continuous spectra of all the ions within the beam. A pinhole is located at the entrance of the TP in order to extract a low divergence point-like beam that can be diagnosed much easier. Since having too many particles can saturate the detector, one can play on the diameter of the pinhole to decrease the flux. Coming from the same source, X-rays, γ-rays and neutral particles pass through the TP without being deflected. They produce a projection of the pinhole on the detector, providing an important reference for the measurement of the spectrum, called the "0^{th} order". It is central to note the incapacity of this diagnostic to measure any neutral projectile distribution. Details on the basic working principles of particle deflection are given in appendix.

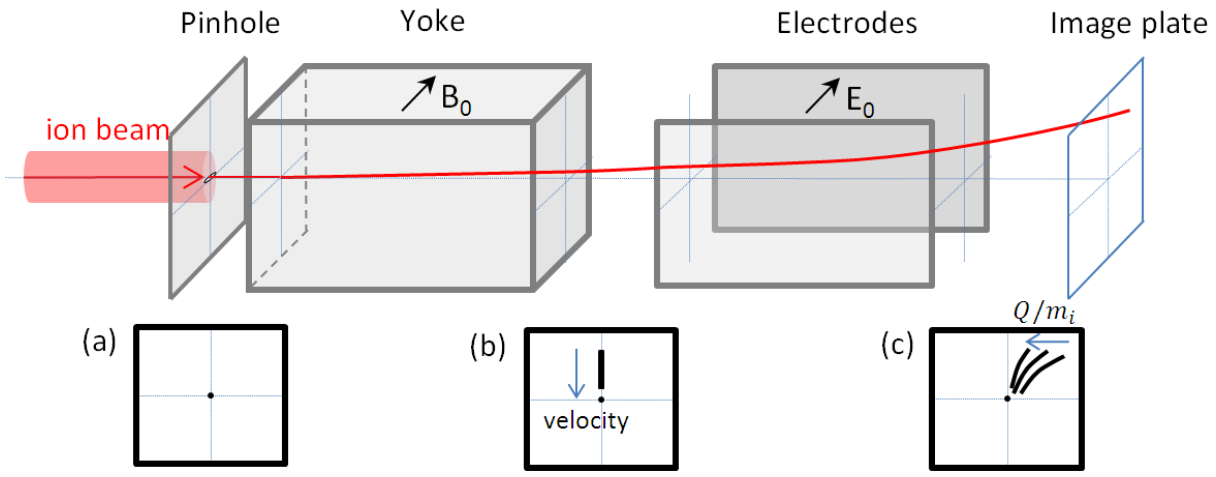

Figure III-16: Concept of the TP. The red line represents the trajectory of one ion. The three black square images, what would be recorded by an image plate (in case of a broadband multispecies ion beam) if located just after (a) the pinhole, (b) the magnetic yoke and (c) the electrodes.

The characteristics of the two TPs we used in this experiment are different in term of magnetic field, electric field and distances from the interaction to the image plate. We call them East and West, according to their position inside the target chamber. Both ion beams detected by the East and West TPs are passing through a 100 µm diameter pinhole located, respectively, 42 and 37 cm away from the helium source. Then, they are deflected by respectively 0.37 and 0.55 T magnetic field and by an electric field of respectively around 350 and 150 kV/m. Both TPs are calibrated in energy using a set of aluminum and copper filters. The method is described in appendix. The particles are then collected on an image plate detector.

III.3.1.2.2.3 Image Plate

An image plate is a film-like radiation image sensor composed of specially designed phosphors that trap and store radiation energy in metastable excited states. Initially developed for digital X-ray medical imaging systems [105], later on they were found to be also effective for the detection of a wide range of radiations (UV, ions [106], electrons [107], gamma rays, etc.). The stored radiation energy can be retrieved by photo-stimulation of the metastable excited states using a scanning laser beam. The energy released is then emitted in the form of a light that is collected by a photomultiplier tube and converted into electric signal which is then digitized, leading to a photo-stimulated luminescence (PSL) value for each scanned pixel. The main advantages of an IP are its insensitivity to electromagnetic noise, its versatility as a radiation detector, a higher sensitivity and a wider dynamic range compared to photographic emulsion, a linear response and a good spatial resolution (limited by the scanning system, typically 25 µm). Also, it is reusable after erasing it with a uniform visible light source.

We have used IPs of the type BAS-TR 2025 from Fuji Photo Film Co. Ltd since they are the most sensitive image plate existing on the market, i.e., they have no protective layer covering the detection phosphor and thus allow detection of very low energy particles. The scanner FUJI FILM BAS-7000 was used as a reader for the IPs. The intensity of the signal on the IP is decreasing in time, i.e., there is a fading effect and because of this, the IPs were always scanned, during this experiment, at a fixed time of approximately 15 min after exposure to the ion source. One estimates from Ref. [106] that we lose this way less than 10% of the original signal recorded on the IP. The signal deposited by a particle varies with its energy. Therefore, we used an absolute calibration in number of helium ions according to the amount of signal read on the IP. It was performed using an accelerator [108]. It should be noted that the calibration range is 0.7 to 5 MeV. In our case, the accelerated particles have never reached energy above 5 MeV. To get the number of particle for energy below 0.7 MeV, we expanded the calibration in number assuming the response of an IP to ion to be linear at low energy, an assumption which has been verified using a Monte Carlo code, GEANT4 [109, 110]. An imprecision is not really important in our case since our final measurement depends on the comparison between reference and through spectra measured by, respectively, East and West TPs using the same IP detector.

III.3.1.2.3 Results

III.3.1.2.3.1 Target density profiles

The spatial density and temporal profile of the flow emitted by a given gas jet depends strongly on the shape of the nozzle and on the valve used, but is fully reproducible from shot-to-shot. The same nozzle is used during the whole experiment. This reproducibility allows us to measure independently before or after the experiment, the characteristic profiles of the jet density. The temporal profile is measured via a 1D Schlieren shadowgraph method (see Figure III-17). A lens is positioned to image the top of the nozzle, i.e., where you want to know the temporal density profile, on a fast photodiode. The gas jet is illuminated by a collimated beam. A knife with a sharp edge is then positioned just right at the focus of the lens, so that it blocks the light that goes in a straight path above the nozzle: only noise is then detected on the photodiode.

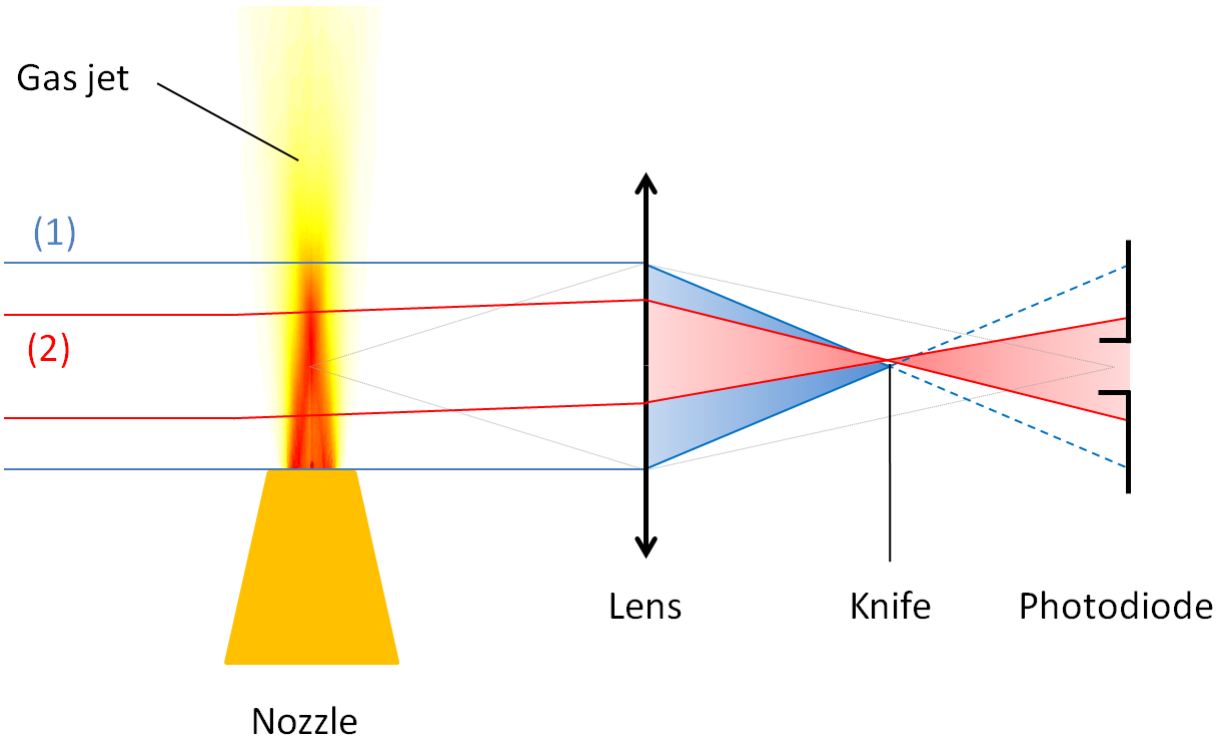

Figure III-17: 1D Schlieren shadowgraph: (1) are rays of the collimated beam in vacuum (or air) blocked by the knife; (2) are rays of the same beam deflected when passing through the gas jet.

The gradient of density caused by the gas jet, expanding from the nozzle when it is pulsed, changes the refractive index of the medium along the collimated beam path; it is then deflected from the direction it had in vacuum. The deflected part of the beam is then not anymore hidden by the sharp edge and illuminates the photodiode. The stronger the gradient and the denser the gas, the more the light is deflected, and the higher the signal on the photodiode. The evolution of the diode voltage as a function of time gives us the temporal profile of the flow in the gas jet. From Figure III-18, one can see that the gas jet density increases very quickly (over approximately 0.5 ms) and remains almost constant during 25 ms before expanding. Finally, the gas jet trigger is set so that the laser beam passes through the gas jet when the density is almost constant and the flow in a steady state.

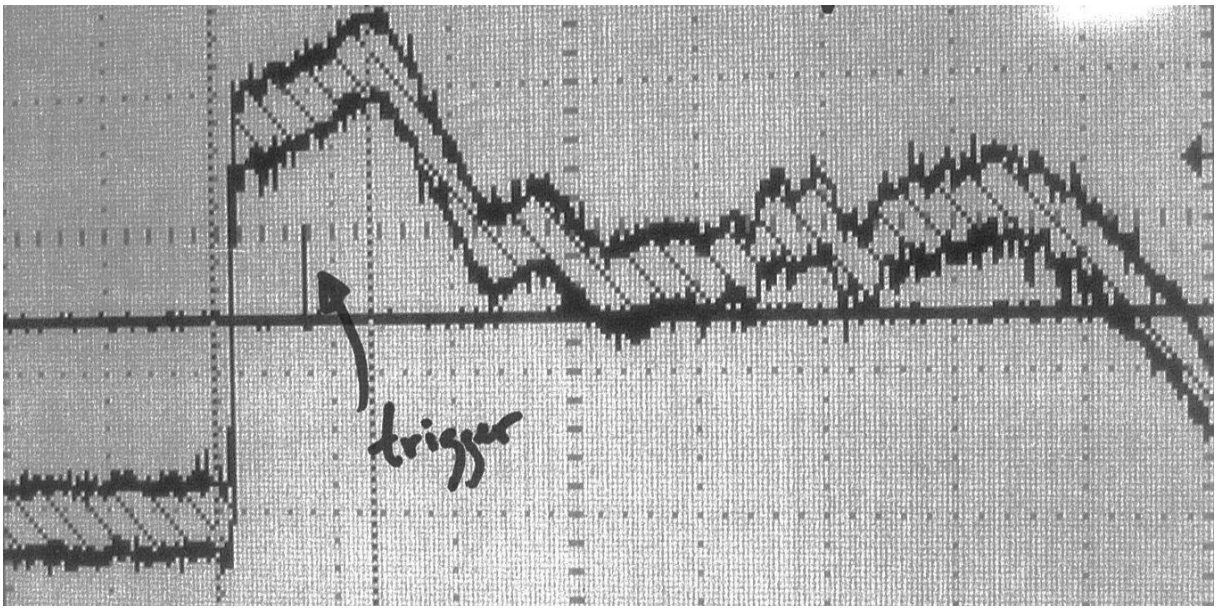

Figure III-18: Voltage of the photodiode obtained by Schlieren shadowgraphy; the time goes horizontally from left to the right, one division represents 25 ms, the other axis is the voltage of the photodiode with 2 V per div. The signal of the trigger (pointed by an arrow) indicates when the main CPA laser beam is passing through the gas jet.

The spatial distribution of the gas-jet density in the output of the nozzle was independently measured through interferometry using a Mach-Zehnder interferometer. Basically, the refraction index of a gas increases with the gas atomic density [111,112]: it takes more time for the light to go through it. This delay induces a phase shift that is measured by interferometry, from which an atomic density profile is calculated. In our pressure range, the atomic density is found to be proportional to the backing pressure and a 2D density profile relative to the pressure can be obtained (Figure III-19).

This 2D profile can be divided in two parts. From the tip of the nozzle to 1.5-2 mm upward, the gas density stays high and even slightly increases in the center, while at the boundary, the gas quickly expands in vacuum. The narrowing of the gas jet from 0 to 1.5 mm is typical of supersonic flows [113]. It is the results of oblique shock wave generated at the nozzle exit and directed inward toward the center line of the nozzle. This effect is counteracted by the natural expansion caused by the density gradient between the vacuum and the ejected gas. Therefore, the “converging effect” caused by the supersonic flows passing through the nozzle (a cone passing from 0.5 to 1 mm toward the exit) decreases with the distance from the nozzle tip. As a consequence, the density plateau sees its width slowly decreasing with the distance and finally disappears at about 1.5-2 mm from the nozzle. After 2 mm, the gas is simply expanding.

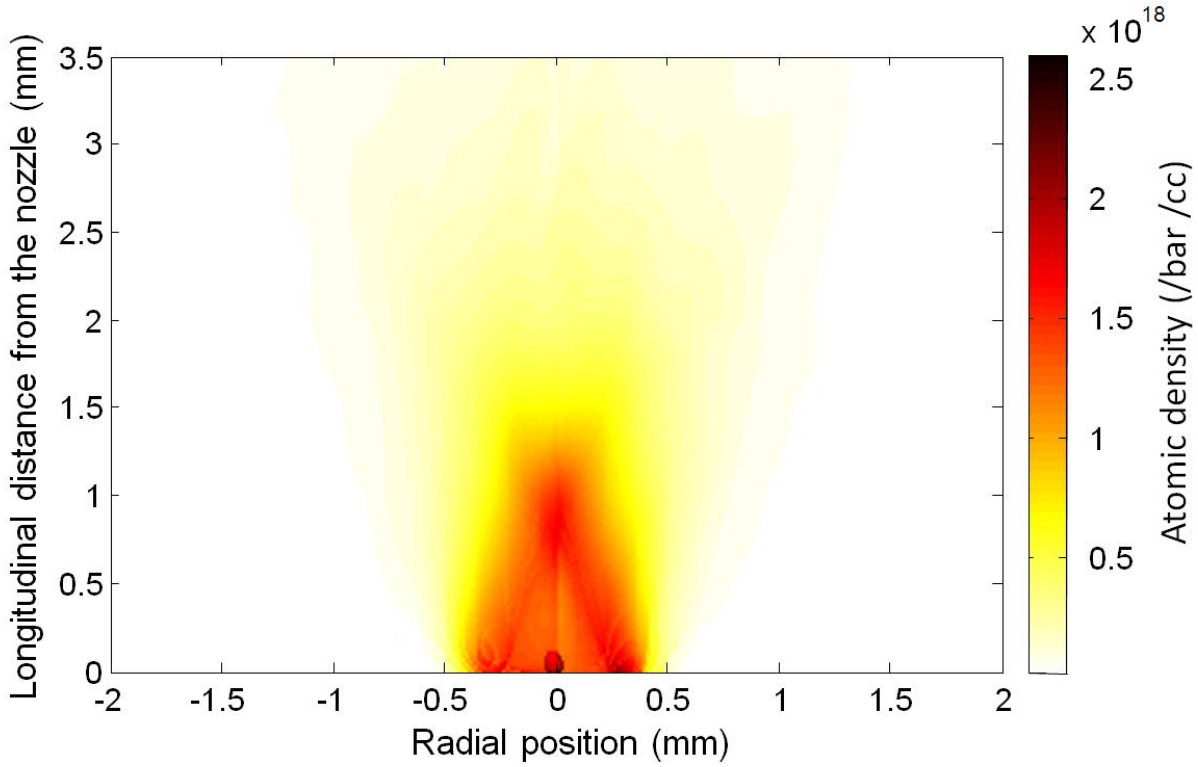

Figure III-19: Atomic density profile in the output of the nozzle relative to the pressure of the gas it is fed with.

Let us now look at the different positions of the focus of the laser we used with respect to the gas jet on the relative density curve (Figure III-20). One can clearly see that the vertical positions of the focus we used in the experiment (750 and 1000 µm) do not change fundamentally the plasma density that was experienced by the laser beam. At the opposite, depending on the radial positions of the focus we used in the experiment (0 and 0.5 mm), the density at the location of the laser focus is shown to be different. Indeed at the nozzle edge (0.5 mm), the density is twice lower than the density at the center (0 mm).

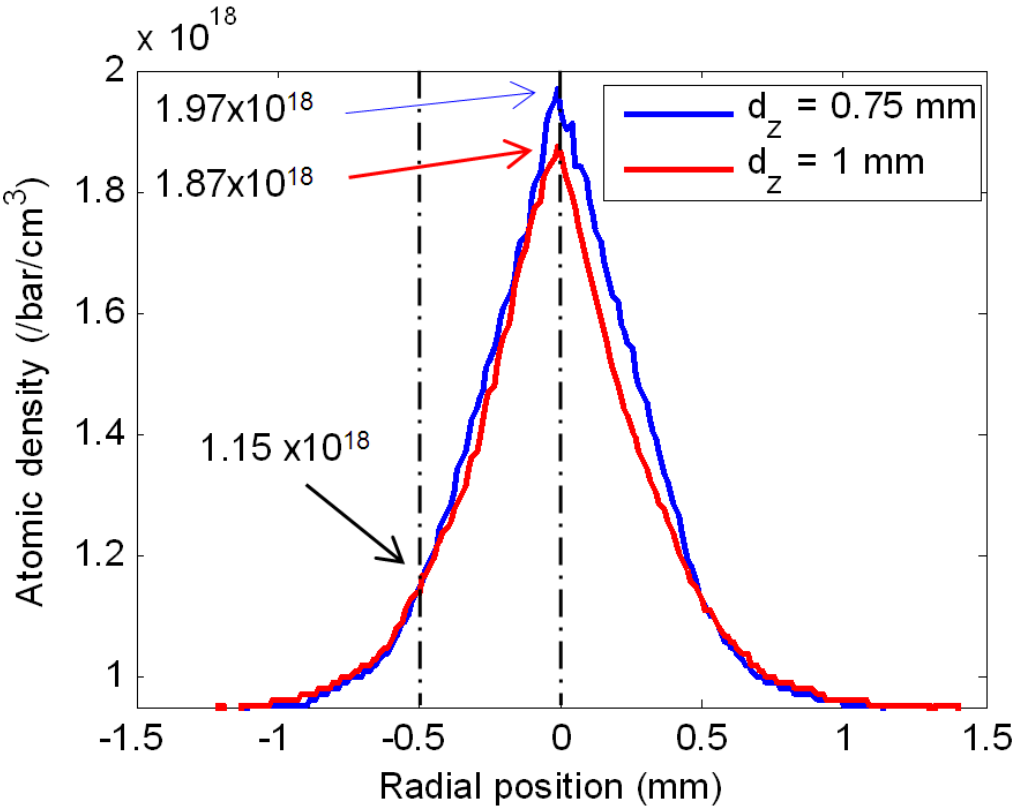

Figure III-20: Density profiles (relative to the gas pressure) at respectively 750 µm and 1 mm above the nozzle tip.

Once ionized, the gas jet reaches approximately electron densities, n_e, from 4×10^{19} to 2×10^{20} cm^{-3} depending on the gas pressure feeding the nozzle (20 to 100 bar). Since n_c at λ_0 = 1 µm is equal to 10^{21} cm^{-3}, the produced plasma remains under-critical. In the case of our experiment, the power of the laser, P, is 10-50 TW. Using Eq. (3.53), the minimum density for self-focusing to take place is estimated around 7×10^{15} cm^{-3}: this is far below the actual ionized gas jet density. Furthermore, the ratio P/P_L varies between 22 and 280. Hence, we can expect strong self-focusing.

III.3.1.2.3.2 Results: ion beam spectra

As explained before, the ion beam spectrum is measured using TPs and IP detectors. Neutral particles and radiations are not deflected by the magnetic and electric fields and form a so-called 0th order point on the IP, which is actually just the projected image of the plasma through the pinhole. In our experiment, the main and bright 0th order is accompanied by other 0th order points with sometimes their respective ion traces (see Figure III-21).

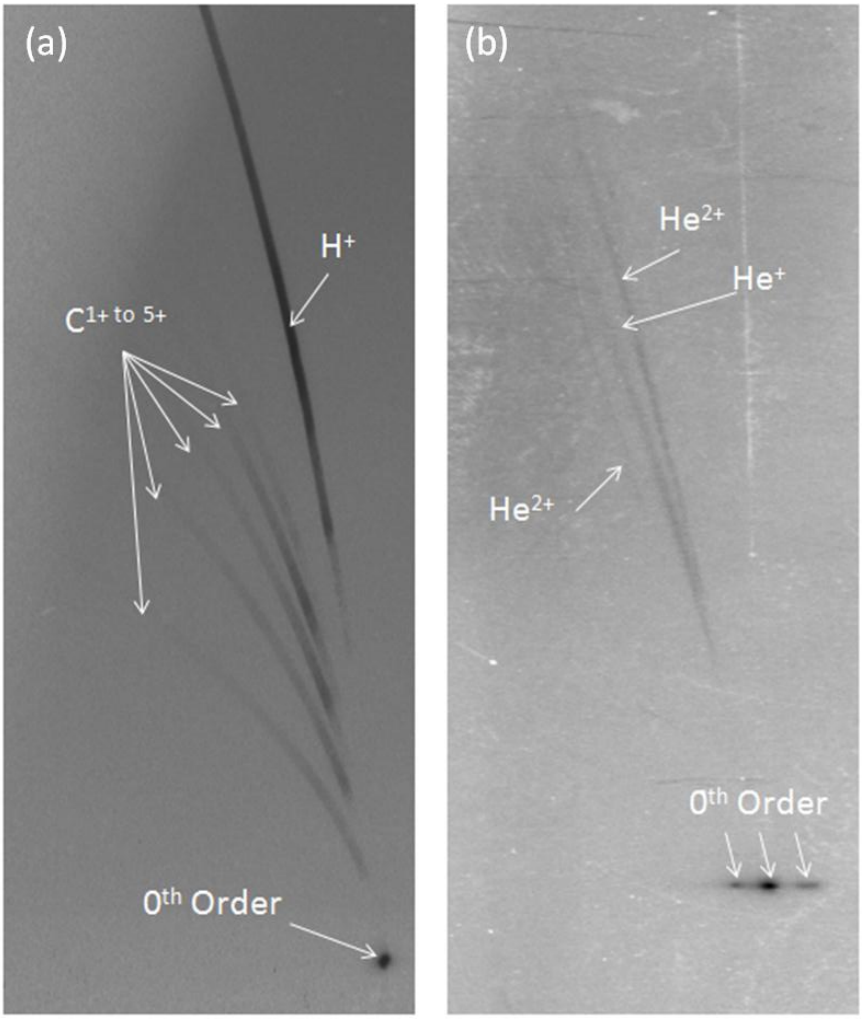

Figure III-21: Typical IPs from measurements of laser-produced ion beams. The laser is interacting, respectively, with a plastic solid-density target and the ion beam is detected normally to the target (a), with a gas of helium and the ion beam is detected normally to the laser propagation axis (b).

The signal intensity projected by the plasma along the laser beam path and printed on the IP detector in Figure III-21b is shown in Figure III-22. The spatial scaling takes into account the magnification of the diagnostic. The highest intensity peak located at 5.4 mm corresponds to the main 0^{th} order. The one located at 3.5 mm which corresponds to the 0^{th} order point accompanied by the He^{2+} ion trace is due to another laser beam focus along the beam path where the laser intensity is high enough, so that ions can be emitted radially and detected. Indeed, when the laser focuses at high enough intensity in the gas for the Coulomb explosion to occur, an ion bunch is accelerated normally to the laser axis and some ion traces appear on the IP. The fact that there are high-intensity laser focuses along the plasma has already been observed in previous experiments [114] and is attributed to the self-modulation of laser intensity inside the channel caused by SRS instabilities [115].The distance of 1.9 mm between the two points is found in reasonable agreement with the dimension of the gas jet target. The last peak is not accompanied by any ion beam: the signal is likely due to light produced by the interaction and reflected by an optical component in the chamber.

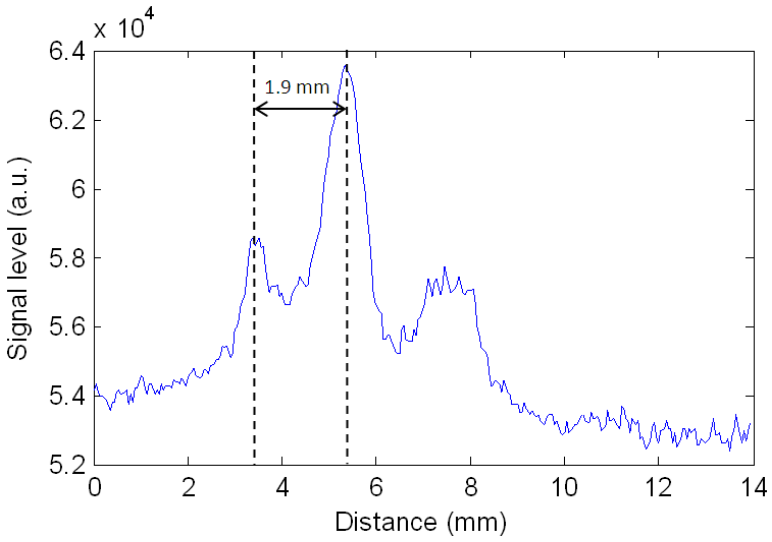

Figure III-22: Signal intensity projected by the plasma along the laser beam path and printed on the IP detector.

As shown in Figure III-23, like in the TNSA case, Coulomb acceleration generates broadband Maxwellian spectra, the number of particles decreasing exponentially with the energy. It is interesting to note the presence of both He^{+} and He^{2+} ions in the spectra. According to published ionization rates, the laser beam should interact with a fully-ionized plasma. In fact He^{+} comes from accelerated He^{2+} ions which have captured electrons from the medium when they pass through the dense and cold helium gas ejected by the gas jet. This effect is discussed in detail in chapter IV. During our experiment, we typically obtained up to 10^{12} particles /MeV /sr at 0.5 MeV as shown later in Figure III-27. The energy cut-off is measured around 2 MeV for He^{+} and 3 - 3.5 MeV for He^{2+}. The detection threshold is determined by the noise level detected on the image plate: it could come from radiations generated during the interaction or UV emissions due to electrical discharge of the high voltages electrodes. We usually could not detect ions below a number of particles around 10^{9} particles.

Let us now focus on the impact of the different experimental parameters (pressure, laser intensity and duration, position) on the accelerated ion beam. Since the TP characteristics are different, the comparison between the ions spectra recorded in different shots is made using the same parabola.

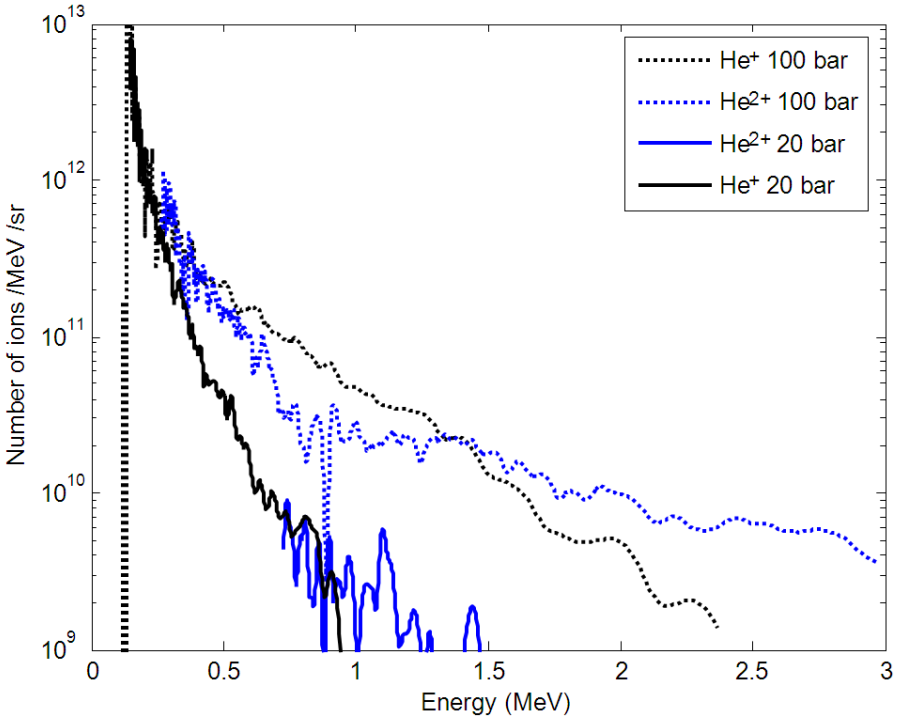

Figure III-23: Spectra of ions accelerated by focusing the laser at the center of a helium gas jet of respectively 20 bar (continuous lines) and 100 bar (discontinuous lines) backing pressure.

In Figure III-23, we compare the ion beam spectra measured when a 5 ps laser pulse is focused at the center of the gas jet with a backing pressure of respectively 20 and 100 bar, i.e., having a peak density of, respectively, 4.0×10^{19} cm^{-3} and 2×10^{20} cm^{-3}. The particles accelerated in the lower density plasma show a maximum energy around 1-1.5 MeV while the ion beam accelerated in a 2×10^{20} cm^{-3} jet reaches 3 MeV. The difference in terms of number of accelerated particles is of one order of magnitude at 0.5 MeV for He^{+} ions and keeps increasing with the energy. The difference between He^{2+} spectra is even more noticeable: He^{2+} ions generated in a 20 bar gas are barely above the noise level. The factor of 5 in the gas pressure has a strong impact on the efficiency of the accelerating mechanism: $E_{max}\sim {n_e}^{0.5}$. This is well above what gives the correlation between the ion maximum energy and the plasma density found in Ref. [21] for a lower power laser (4 TW): $E_{max}\sim {n_e}^{0.125}$, and below the one found for a 250 TW laser: $E_{max}\sim {n_e}^{0.77}$ [116].

We can also compare the impact of the density by changing the location of the laser focal spot. In Figure III-24, one can see that the ion spectra accelerated at the edge and at the center of the gas jet are very close one to another despite the difference of factor 2 in the gas density observed in Figure III-20. Their maximum energy and the total number of accelerated particle are almost identical.

Although that the gas density is higher at the center of gas (than at the edge), positioning the laser vacuum focus at the center means also that the high power laser interacts with the gas before it reaches focus. In this transit propagation zone, the laser beam likely gets affected by non-linear interactions with the gas. Hence it is probable that it does not reach its vacuum focus nominal intensity, which would explain why it produces similar energy ions as when focusing (in a clean manner) in a lower density part of the jet, i.e., at the edge.

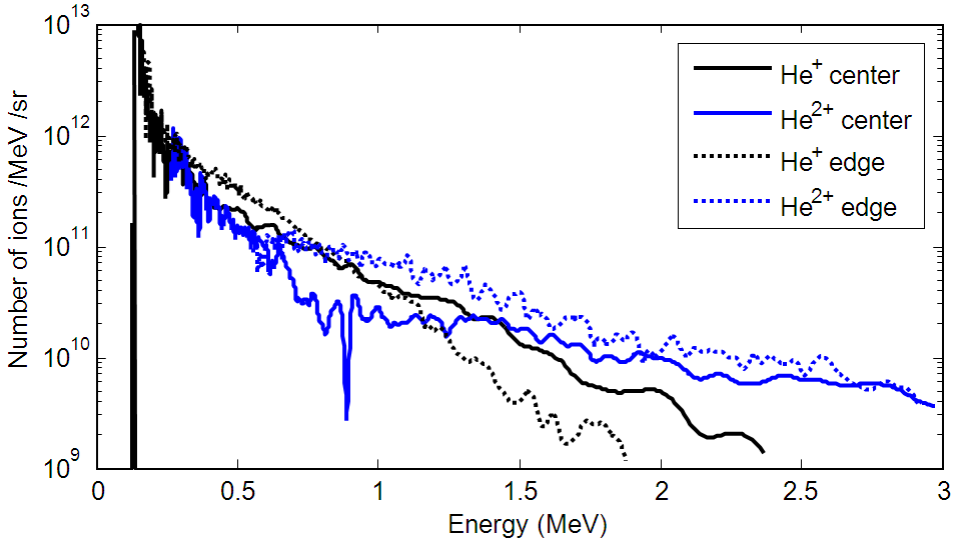

Figure III-24: Spectra of ions accelerated in a 100 bar helium gas jet by a 5 ps laser pulse focusing in the center (continuous lines) and at the edge (discontinuous lines) of the gas.

In agreement with what could be expected from the density profile shown in Figure III-20, the variation of the vertical distance from the nozzle and the laser focal spot between 0.75 and 1 mm does not have any significant impact on the ion acceleration (see Figure III-25). The difference in the maximum energy is here due to shot-to-shot energy fluctuation of the laser.

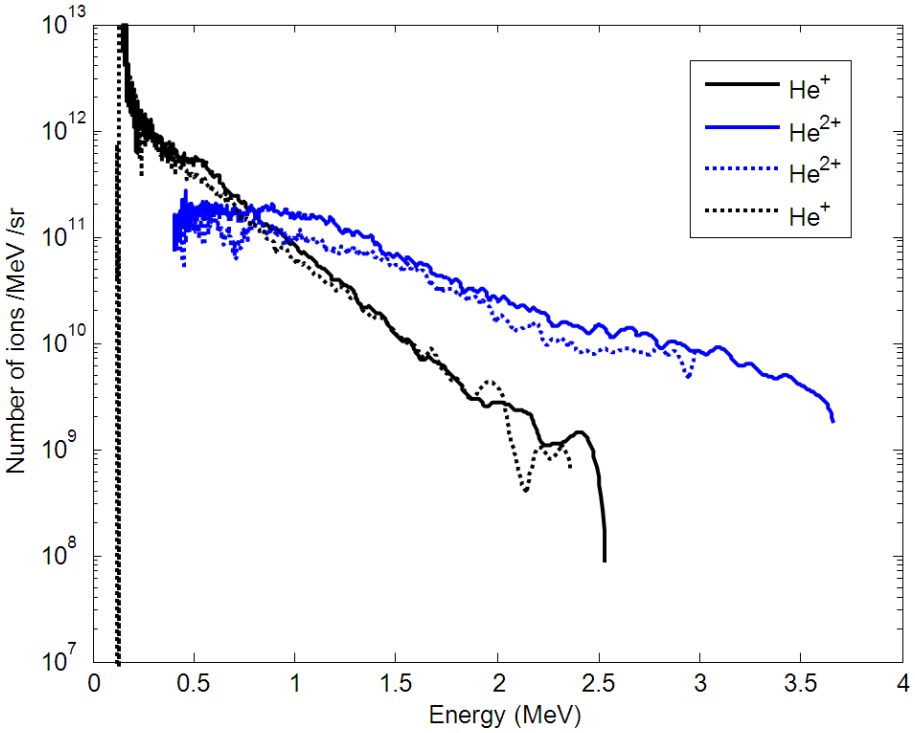

Figure III-25: Spectra of ions accelerated in a 100 bar helium gas jet by a 0.7 ps laser pulse focusing at the edge of the gas 0.75 (discontinuous lines) and 1mm (continuous lines) above the nozzle.

Let us now look at the influence of the intensity and of the duration of the laser pulse. As mentioned previously, we tested two different regimes: 5 ps / 60 J and 0.7 ps / 40 J. The maximum intensity of the beam in vacuum is then, respectively, 6×10^{17} and 3×10^{18} W/cm². When we compare several 0.7 and 5 ps shots, we observe that the highest intensity pulse commonly produces a higher number of accelerated particles with a higher energy cut-off (the maximum energy cut-off measured in each case are, respectively, 3.5 MeV and 6 MeV). In Figure III-26, one can see two typical ion spectra obtained with a 0.7 ps and 5 ps laser pulse. The ion beam accelerated by the shortest laser pulse exhibits twice more particles than in the longer pulse case. In addition, we measure energy cut-offs that are higher for both He^+ and He^{2+} for the shortest pulse duration: 2.5 versus 1.8 MeV for He^+ and 3.6 versus 2.9 MeV for He^{2+}.

To conclude, considering the shot-to-shot fluctuations of the laser beam energy and the small variations detected when varying the different parameters, finding the best combination of focal spot position, laser intensity and gas pressure, would require a higher number of shots and stronger variations of each parameter. All the same, we can conclude that, in the frame of our experiment, the best compromise to have the highest energetic ion beam is a maximum pressure of the gas jet and a maximum intensity. It is interesting to note that our results are very close to those obtained in Ref. [100] with a 50 TW laser beam focused at the edge of a gas jet in a 5×10^{19} cm^{-3} plasma.

It could be interesting for future experiments using the same platform to study more carefully the impact of the radial position of the laser focal spot compared to the center of the nozzle.

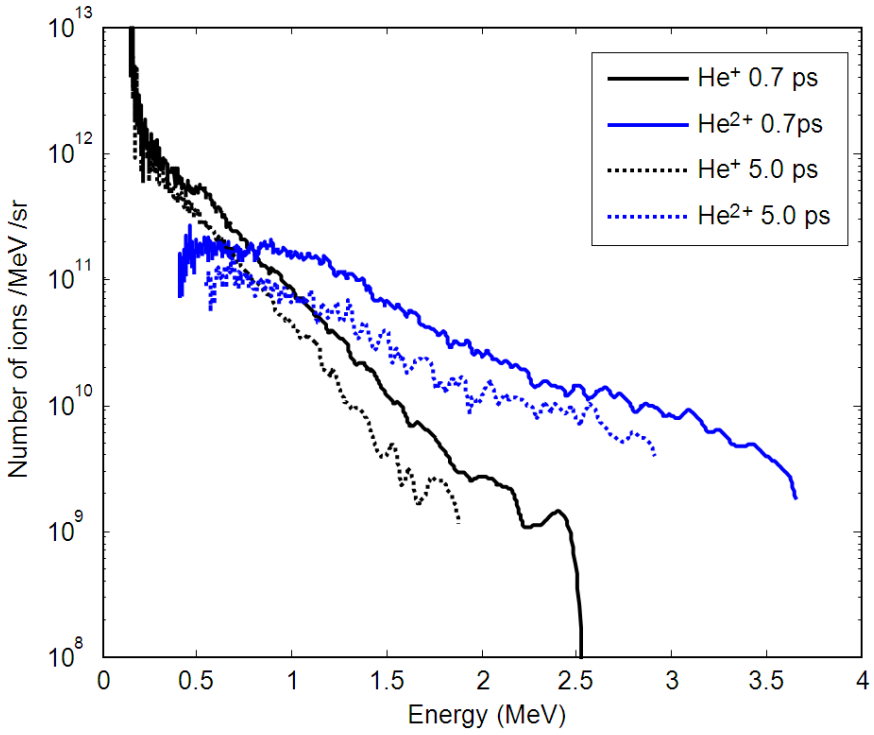

Figure III-26: Spectra of ions accelerated in a 100 bar helium gas jet by respectively 0.7 (continuous lines) and 5 ps (discontinuous lines) laser pulses focused at the edge of the gas jet.

III.3.1.2.3.3 Symmetry

Since we are looking for both high energy and similar ion beams, 20 bar shots are automatically excluded due to their low energy spectrum. Therefore, we focus this second part of our study on the highest energy shots performed at the highest backing pressure, i.e., 100 bar.

Two cases presenting the best and the worst similarity between East and West spectra are shown, respectively, on Figure III-27 and Figure III-28. To avoid the issue caused by a potential difference of the detection threshold (due to a difference in the noise level) between the two TPs, we choose to keep only the part of the spectra where the noise remains negligible compared to the signal on the IP, i.e., the particle number is above 10^9/MeV/sr.

In Figure III-27, the ion beams recorded by the West and East TPs are very alike. Indeed their numbers of particles are found to be similar in the full energy range. The only difference between them is their energy cut-off which is higher on the West beam (3 MeV versus 2.2 MeV).

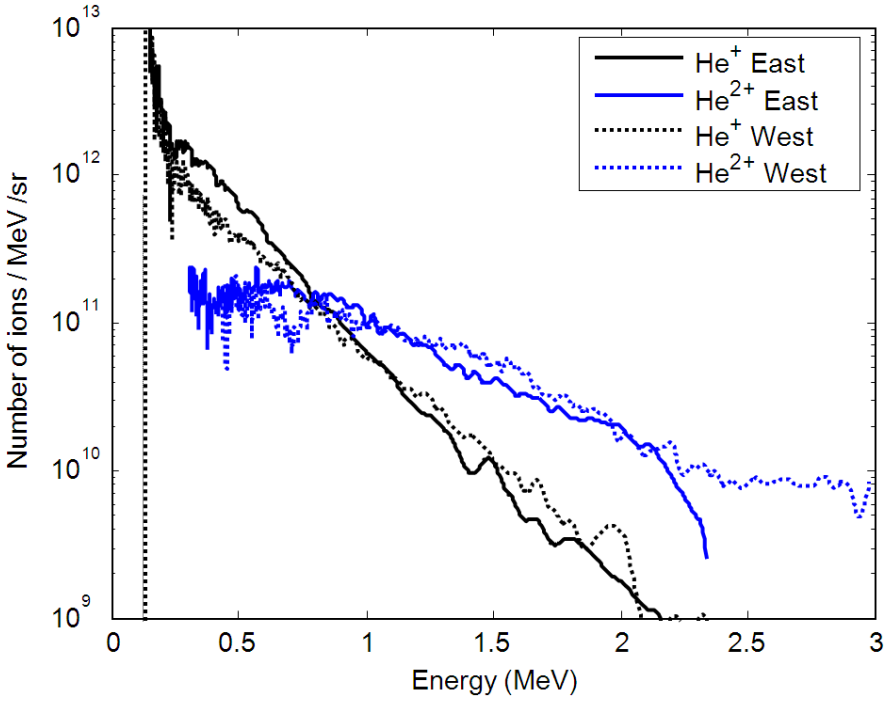

Figure III-27: Spectra of ions accelerated in a 100 bar helium gas jet recorded on the same shot, by respectively the East (continuous lines) and West (discontinuous lines) TPs.

In Figure III-28, the West beam is shown to have up to twice the number of particles measured in the East beam. Their respective energy cut-off is again different one from each other, but, in that case, the East beam is found more energetic than the West one (4.7 versus 3.7 MeV).

When looking at both spectra in Figure III-27 and Figure III-28 obtained from two consecutive shots, we observe that each parabola can exhibit the highest energy cut-off for a given shot. Since the TPs and the laser axis are not changing between two consecutive shots, the dissimilarity observed in terms of energy cut-off is unlikely coming from the imprecision of the alignment of the TP axis with respect to the laser axis. The difference is therefore more probably coming from the interaction between the laser and the gas itself. The interaction is complex and instabilities may affect the charge separation area and produce inhomogeneity in the ion density. For instance, if more particles are present in west side of the channel than in the east side, Coulomb explosion would then be more important in the west side, increasing the energy cut-off measured by the West TP compared to the one obtained by the East TP.

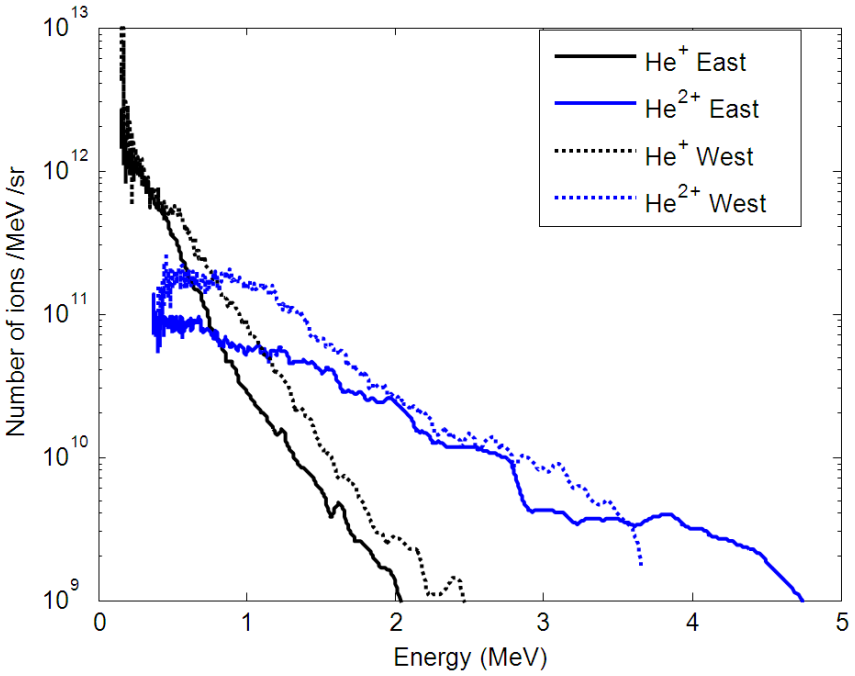

Figure III-28: Spectra of ions accelerated in a 100 bar helium gas jet recorded on the same shot, by respectively the East (continuous lines) and West (discontinuous lines) TPs.

III.3.1.3 Conclusion on Coulomb explosion

The main objective of this study was to estimate the potentialities of such a set-up to produce two similar high energetic ion beams.

We have demonstrated that, with our laser condition, we can accelerate ions to a maximum energy of 6 MeV. In average, it was however a bit smaller, i.e., around 3.5 MeV. Such energy is relatively low compared to what can be obtained with the same laser irradiating a thin solid-density foil (see section III.2). Such a problem could be overcome by using a higher density gas and a higher intensity laser beam. Indeed it has been observed that the maximum ion energy when $P/P_L > 2000$ increases with the plasma density, in which case a collision-less shock acceleration mechanism takes place [116].

Regarding the rotational symmetry of the Coulomb explosion acceleration mechanism, both ion beams generated at 90° with respect to the laser propagation axis are observed to be very similar in terms of number of particles. Nevertheless, their energy cut-offs can be different, the difference being as large as 1 MeV. In the scope of using this set-up to study stopping power, the two beams are too different to be used for direct stopping power measurements in which the precision of the energy cut-off is essential (see chapter IV). All the same, we will see in chapter IV that this similarity can be used in another kind of experiment still related to the study of the stopping power. Note that set-

ups including ions accelerated in a gas jet can also be an issue for experiments using two or more different targets (one is the gas jet): the expanding gas can contaminate or even blow-away the other targets, and so needs to be positioned far from them (at least, 1 cm in our case). This significantly reduces the flux of the produced ion beam interacting with the other targets.

III.3.2 Ion acceleration in a exploded foil

Coulomb acceleration is preferentially radial and far less ion emission is expected in the longitudinal direction of the short pulse laser. However, it has been found experimentally that under definite laser and target conditions, forward acceleration is not negligible in sub- and near-critical density target and can even produce ion beams of higher energy and of better collimation compared to the Coulomb explosion acceleration process [93, 117, 118]. The basic idea behind it is that the longitudinal acceleration of hot electrons is improved in sub- and near-critical density targets [94]; hence both laser-to-ions conversion and ions energy can be enhanced.

Several interpretations have been proposed to interpret the ion acceleration mechanism in the longitudinal direction of the laser. One hypothesis is that the ions are accelerated at the rear target-vacuum boundary through a process similar to TNSA [93]. The charge separation between the ions and the fast electrons expanding in vacuum generates a strong electrostatic field that accelerates the ions forward in the direction of the electrons expansion. Another mechanism called magnetic acceleration mechanism has been suggested to explain the ion acceleration [119]. The high current of hot electrons only partially neutralized by the return current, induces an azimuthal long-living magnetic field along the longitudinal axis at the rear target-vacuum boundary. The variation of this magnetic field on a very steep gradient generates strong inductive electric fields which enhance the ion accelerating space-charge field and also gives rise to a collimation mechanism [117, 120]. Although there is a common agreement on the presence of the magnetic field and its effect on the enhanced collimation of the ion beam, the question of whether the acceleration process is predominantly due to the strong electrostatic fields or to the magnetic fields is still a subject of debate [121, 122].

Although up to now the efficiency of this acceleration process is not high compared to what can be obtained with solid targets (e.g. see the number of ions in Ref. [93]), Particle-In-Cell (PIC) simulations [123,124] have shown that a collisionless shock acceleration (CSA) could be used in sub- to near-critical density targets to accelerate ions very efficiently, but also in higher number than TNSA with the same laser parameters. However, to reach such optimum, precise interaction conditions need to be met. With present day 1 μm-wavelength lasers, d'Humières and Tickhonchuk found that it would require near-critical density thin gas jet targets (of the order of 100 μm), which are not currently

available [123]. Rather than working on the gas jet issue, we concentrate our study on the CSA process itself. As proposed in Ref. [123] to reproduce the conditions for CSA to occur, we use as a substitute a thin foil exploded by a secondary laser.

After describing the mechanism of CSA and in which conditions it is optimized according to predictions, we present our experimental set-up and the diagnostics used to study longitudinal ion acceleration mechanisms that take place in exploded targets. Subsequently, the results we have obtained are presented followed by a discussion of our observations in the light of PIC simulations.

III.3.2.1 Collisionless shock acceleration

The collisionless shock acceleration (CSA) mechanism is different from the front-side collisionless shock in the sweeping acceleration mechanism (see section III.2.3.1) in which the laser is reflected at the front of a dense target [36, 37]. This rear-side shock acceleration mechanism can be divided in two steps [123], each step requiring specific target conditions to occur.

In the first step, a long descending rear density profile is necessary [125], i.e., the characteristic scale length of the density gradient is much longer than the hot electron plasma Debye length. The hot electrons accelerated by the short pulse laser build up strong electric fields at the rear plasma-vacuum interface. Like in TNSA mechanism (see section III.2.3.2.1.1), one can then distinguish three regions at the rear surface of the irradiated target (see Figure III-29) [51]:

- a positive sheet located at the beginning of the density decrease where the electric field promptly increase,
- a quasi-neutral zone where the electric field is quasi-uniform,
- a long negative layer in the lowest density part of the plasma density profile where the electric field gradually decrease.

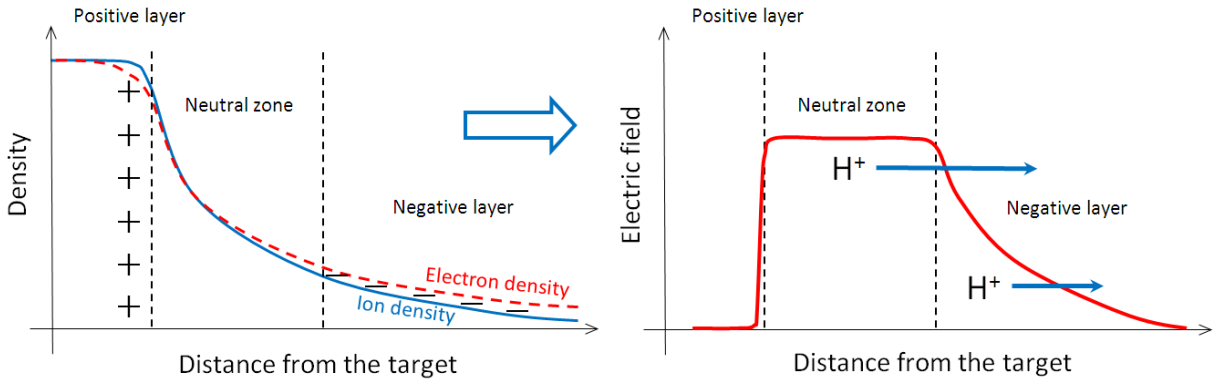

Figure III-29: Illustration of the first step of the CSA. The protons located in the high-density region experience a stronger electric field than the protons located in the low-density region.

Due to the long density profile, the peak of electrostatic field in the negative layer present in TNSA (when the plasma-vacuum interface is sharp) has disappeared. Thus, after the neutral zone, the electric field monotonously decreases with the distance from the high-density zone. Protons in the low-density region therefore experience an electric field lower than protons from the higher density region. As a result, protons from the low-density region are caught by the protons coming from higher density region leading to the formation of a shock front [51], i.e., a peak of ion density propagating inside the decreasing (low) density ramp.

The second step of the CSA mechanism consists on the propagation of the collisionless electrostatic shock through an extended exponentially decreasing density plasma [123]. In Figure III-30, the shock structure characterized by the decrease of ϕ, the electric potential induced by the ion density peak, is represented in the shock frame. The protons of the upstream background plasma, which flows from the upstream to the downstream region, are slowed down by the electrostatic potential and reflected back at velocities up to twice v_{shock}, the velocity of the shock.

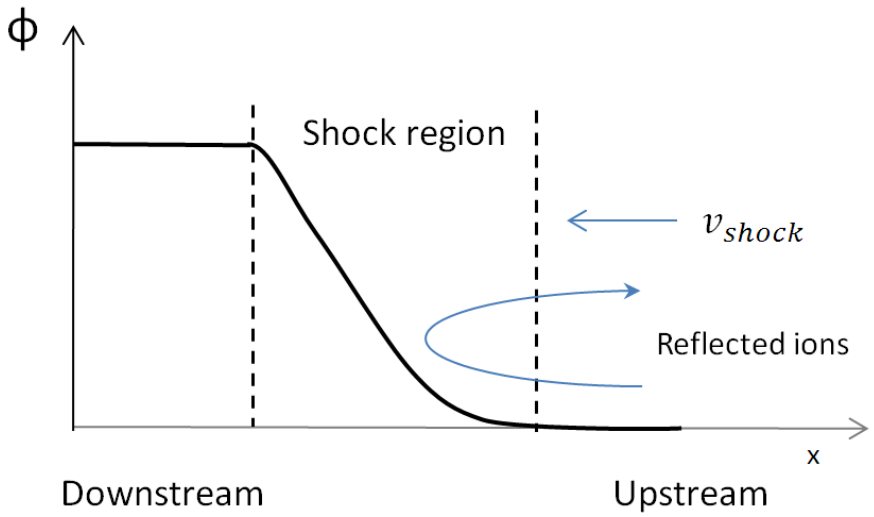

Figure III-30: Illustration of the second step of the CSA.

The CSA has been successfully demonstrated by Palmer and Haberberger with a CO_2 laser using near-critical gas targets [68, 92]. Indeed the critical density of CO_2 lasers (10^{19} cm^{-3}) is two order below the critical density of 1 µm-wavelength lasers and thus, CO_2 laser near-critical target is easier to produce compared to 1 µm-wavelength laser one[14]. Nevertheless, the proton production needs to be enhanced in order to reach the number of protons produced with TNSA when using planar foils. One

[14] Low-density targets generally consist in a high pressure gas ejected through a nozzle, the nozzle design fixing the target confinement with respect to the backing pressure. But nowadays, nozzles able to reach the pressure required to get 1 µm-wavelength laser critical density while keeping the target confined are still under development. Indeed, the gas expansion speed increases with the pressure rising.

way to improve the proton yield is to increase the intensity of the short pulse laser interacting with the smooth plasma gradient [123]. Up to now, CO_2 lasers are limited to intensities of $10^{16\text{-}17}$ W/cm², while 1 µm-wavelength lasers can reach intensities up $10^{20\text{-}21}$ W/cm² on target.

III.3.2.2 Objective and experimental set-up

The main objective of our experiment is to observe the influence of the plasma density gradient on the longitudinal ion acceleration mechanism induced by a high intensity 1 µm-wavelength laser with a particular interest toward CSA.

To overcome the issues arising with producing confined near-critical density gas jet targets, a second method to obtain such targets has been pursued in Ref. [117] with preformed targets: a very thin solid-density foil target is exploded by a long pulse (ns) laser beam. The heated plasma expands quickly into vacuum, its density decreasing in time. Controlling the irradiation of the solid foil by the long pulse laser, one is able to produce different plasma gradients, necessary for the collisionless shock to occur. A second, short pulse laser (ps) can then hit the exploded foil when the density is just subcritical and generate ions. In Ref. [117], they used the ASE pedestal of the short pulse as a tool for controlling the target parameters seen by the main short pulse. They changed the duration of the ASE before the main impulsion to modify the target density and gradient.

Our set-up is based on preformed solid-density targets as well. Instead of using the ASE pedestal to preform the targets, the near-critical density plasma is obtained by exploding thin solid foils with an independent long pulse laser beam. The use of an independent long pulse gave us a wider margin to play on the target conditions.

The experiment was carried out using the ELFIE laser facility (LULI). The experimental set-up is shown in Figure III-31. A chirped, long laser pulse (LP), of 30-40 J energy, τ = 580 ps (FWHM) Gaussian pulse duration (see Figure III-32), with a 20 µm focal spot diameter and producing on target laser intensity of $I \sim 3\times10^{15}$ W/cm² is used to irradiate a thin target under an incident angle of 45° (see Figure III-31). As targets, we used commercially available 10 µm Au and 500 nm Mylar foils. The intensity of the LP could be varied by putting neutral optical densities (OD) into the beam, achieving an energy reduction of 10 (OD 1) or 100 times (OD 2). A high-intensity short pulse laser (SP), with energy 5-8 J, 400 fs pulse duration, 10 µm focal spot diameter (FWHM) and intensity $I \sim 5\times10^{18}$ W/cm² interacted with the exploded target, accelerating protons in the laser-forward direction through various acceleration mechanisms depending on the plasma density gradient. The temporal contrast of the SP has been measured to be below 10^{-6}. The SP hit the target with normal incidence. Since the LP induces an

asymmetric expansion with respect to the target normal axis, we expect the acceleration axis to be angularly tilted with respect to the target normal axis as observed in Ref. [117].

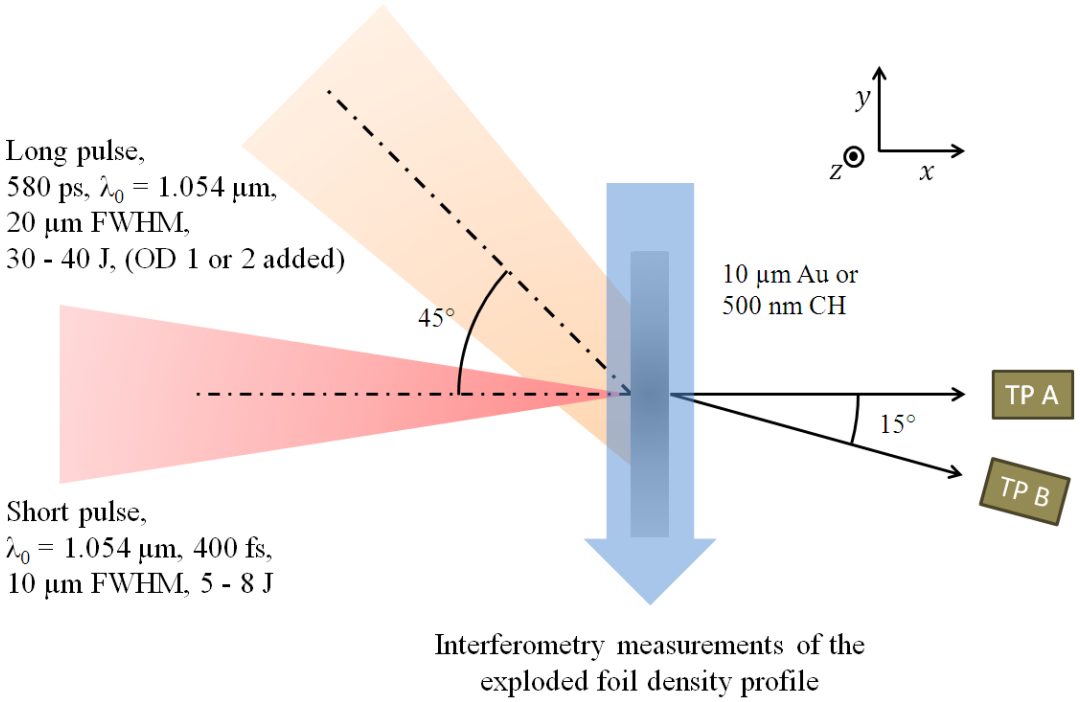

Figure III-31: Experimental set-up.

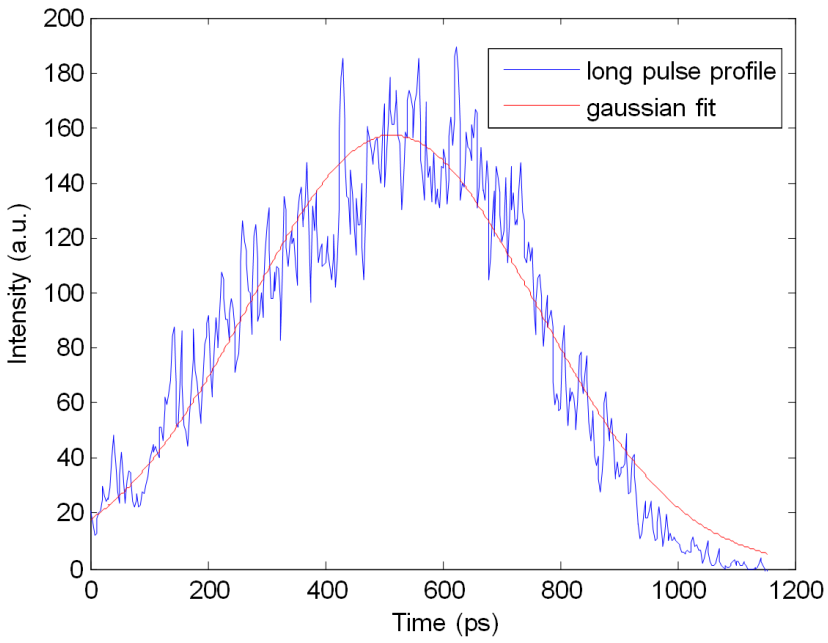

Figure III-32: Long pulse intensity profile.

By varying Δt, the time delay between the SP and the LP, as well as the LP intensity, we could vary the characteristics (gradient length, density) of the exploded target at the time of the interaction

with the SP. We choose as a convention that a 0 delay between both beams indicates that the peak of both beams are overlapping, whereas negative delays indicate that the peak of the SP arrives on the target before the peak of the LP (see Figure III-33a and Figure III-33b). During the experiment, delays were varied from -500 to 300 ps, i.e., having the SP interaction 500 ps before the peak of the LP and up to 300 ps after.

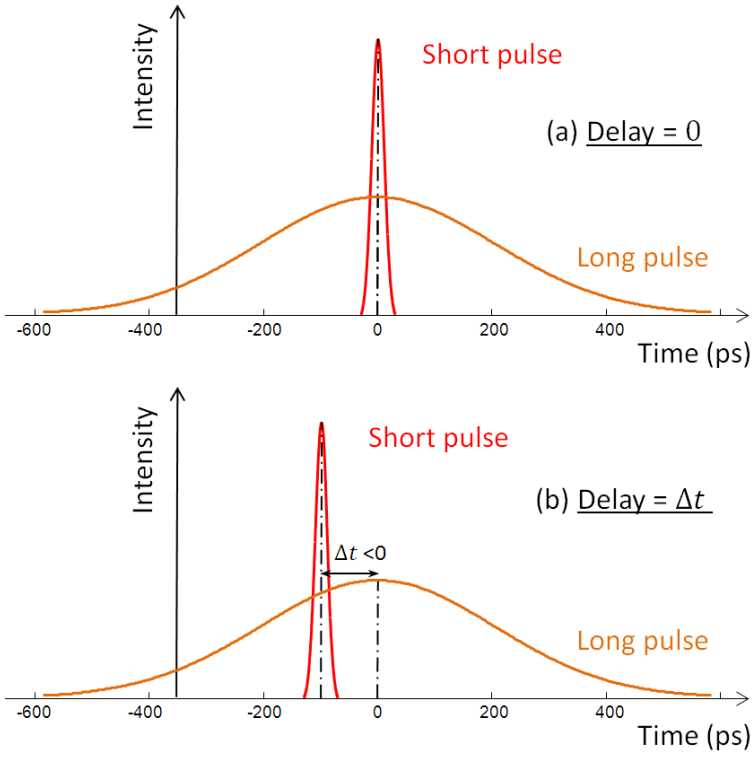

Figure III-33: Intensity temporal profile of the SP and the LP with a delay of, respectively, 0 (a) and Δt (b) between them.

III.3.2.3 Diagnostics

As diagnostics, we used two calibrated TPs A and B located, respectively, located at 0° and 15° with respect to the SP axis to measure the forward generated proton spectrum (see Figure III-31). In addition, we employed transverse interferometry to diagnose the exploded target conditions and its density gradients.

III.3.2.3.1 Thomson parabola

Like in the experiment related to Coulomb explosion (see section III.3.1.2.2.2), the two TPs are different in terms of magnetic field, electric field and distances from the target to the image plate. Both 0° and 15° ion beams are passing through a 100 µm diameter pinhole located respectively 42 and 37 cm

away from the plasma. Then they are deflected by, respectively, magnetic fields of 0.62 and 0.51 T and by electric fields, respectively, around 600 and 180 kV/m. For the TP A, the magnetic field is applied on a distance twice longer than for TP B. As a consequence, the protons are more deflected by the TP A, providing a higher resolution when measuring the high energy part of the ion spectrum. However, the lower energy protons are too deflected to be seen on the Image Plate detector. Thus all of the spectra coming from the TP A are cut below around 1.3 MeV.

III.3.2.3.2 Interferometry

A low-energy (mJ), short (400 fs), optical probe laser, which is a pick-up of the SP, probed the subcritical exploded foil when the SP is interacting. It allows us to retrieve the density map of the plasma when the interaction takes place.

The phase velocity of the wave front passing through the subcritical plasma increases with the plasma density (see Eq. (3.52)). The optical path length of the probe beam varies with the plasma density it has gone through. This induces for each ray a phase shift proportional to the linear density it has gone through. A way to retrieve the 2D map density of the probed plasma is to measure the resulting 2D phase map of the probe beam. To perform this measurement, we use a Normarski interferometer (see Figure III-34). Its working principle is as follows. Let us assume the probe laser beam is polarized at 45° to the vertical. A lens is positioned to image the interaction point, i.e., where the laser beams are interacting with the thin foil, on the chip of a CCD. The target is illuminated by a collimated and polarized low energy laser beam that probes the target transversely to the target expansion. A Wollaston prism is positioned after the lens so that the entire collimated light passes through it. The Wollaston prism splits the input light into two orthogonal linearly polarized beams, with respect to the Wollaston axis ($\vec{u}, \vec{v}$), with an angular separation, α. It is oriented so that it's the laser polarization makes a 45° angle with respect to $\vec{u}$ and $\vec{v}$ ($\vec{u}$ is vertical and $\vec{v}$ horizontal). An analyzer is positioned after the Wollaston to make both beams have the same polarization, and so make possible the interference. It is set at 45° so that it partly filters the emission from the plasma. Where the two beams overlaps spatially, they interfere and an interference pattern is observed in the overlapping zone. It should be noted that the space between the fringes, l, is fixed by the angle α and is given by $l = \lambda_0/\alpha$, where λ_0 is the wavelength of the probe. The resolution in space of the diagnostic is given by the lens magnification. The phase shift induced by the expanding plasma is deduced from the measurement of the variation of the space between the fringes in the interference pattern.

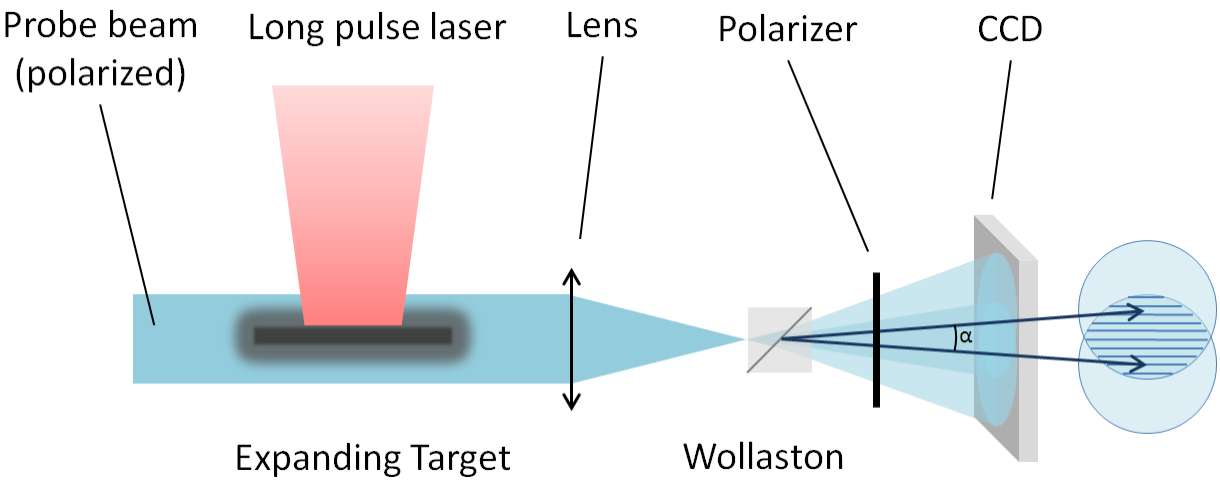

Figure III-34: Interferometer set-up.

In our case, the magnification is 1.66 µm per pixel and the fringes interspacing is comprised between 17 and 20 µm. The probe is on purpose frequency doubled so that we can cut strong scattered laser light emission (at λ_0 = 1.054 µm) using notch filters.

Assuming cylindrical symmetry for the expanding plasma, the electron density profiles are calculated from the interferometry images using "neutrino", a program written by T. Vinci based on Abel inversion [126].

III.3.2.4 Experimental results

III.3.2.4.1 Ion acceleration with the SP only

We first present the results of reference shots performed to measure the maximum energy that can be achieved in the TNSA regime using solid-density targets and the SP. We used a 10 µm gold foil since this has yielded the highest proton energy for our laser conditions [46]. Figure III-35a shows a typical spectrum measured by the TPs at 0° and 15°. With the TP A, we see a maximum proton energy cut-off around 8 MeV, whereas with the TP B, we do not observe any protons above 1.5 MeV. Comparing the particle numbers at around 1.4 MeV, we find more than 1 order of magnitude difference between the 0° and the 15° proton beams. This confirms that the acceleration process (TNSA) produces a beam strongly peaked in the target normal direction as observed in Ref. [46].

Note that we observed a variation of the energy cut-off at 0° from 4.3 MeV to 8 MeV. This is likely due to the SP intensity modulations within the focal spot or even variations of the intensity delivered by the SP.

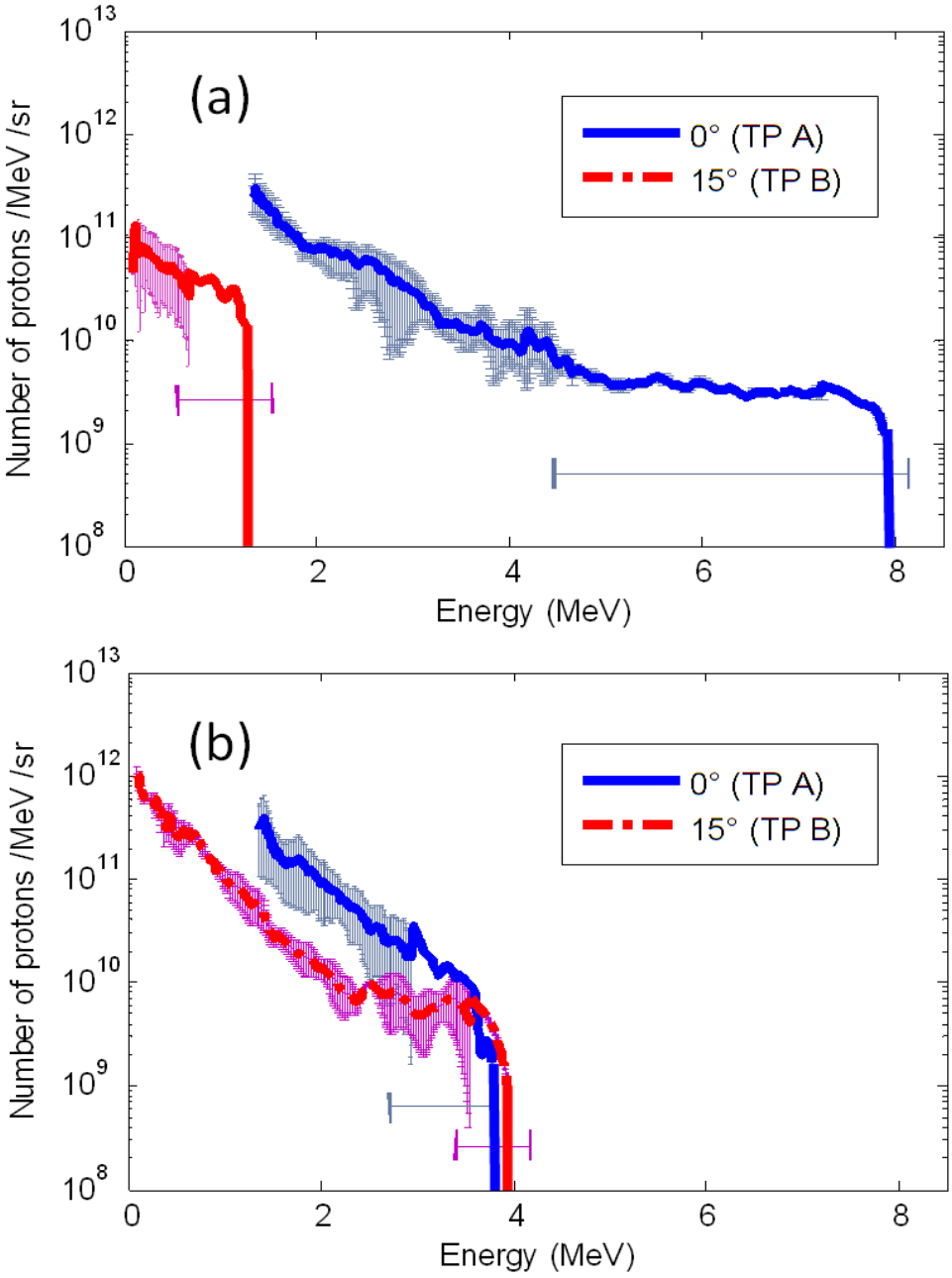

Figure III-35 : Proton spectra obtained at 0° (TP A) and 15° (TP B) with respect to the target normal axis when the short pulse (I ~ 5×1018 W/cm²) is interacting with, respectively, a 10 µm thick gold foil (a) and a 500 nm plastic foil (b). The spectra are all averaged over 3 different laser shots. The vertical error bars are related to shot-to-shot variations, while the horizontal ones are both due to shot-to-shot variations and the resolution of the diagnostic (< 5% of the proton energy).

Now we compare the shots on solid-density 10 µm Au targets to shots using as target a 500 nm Mylar foil, still irradiated solely by the SP (see Figure III-35b). The acceleration process is observed to be less sensitive to the shot-to-shot fluctuations, however it produces lower energy protons with cut-offs around 3-4 MeV for both TPs. Moreover, one observes that the beam is angularly broadened compared to the thick solid-density target case: the cut-off recorded by TP A and B are close to each other. This can be interpreted as follows. If one assumes that a shock wave is launched into the target by the ablation pressure induced on the front surface by the ASE pedestal, when it reaches the

rear side, it gives rise to a dynamic expansion of the rear surface, which thus becomes convex with a time-dependent curvature. It results in an increased of the ion beam divergence. This phenomenon has already been observed in Ref. [127] with an ASE intensity and duration similar to ours ($I \sim 10^{12}$ W/cm², τ = 1 ns) using a much thicker Al target (6 µm). We expect the effect to be even more significant in our case, since the thinner the target, the more sensitive to the pre-pulse it is. In addition, the time required for the shock to pass through the target (83 ps), estimated using the shock velocity derived in Ref. [127] (6 µm/ns) is much shorter than the ASE duration.

III.3.2.4.2 Ion acceleration using both the LP and the SP

III.3.2.4.2.1 Plasma gradients produced by the LP irradiating thin targets

During the experiment, various LP intensities and delays have been tested. Roughly, the SP interacts with exploded targets which plasma density gradient lengths at the rear and the front surface increase with the LP intensity and the delay: the higher the LP intensity, the more important the electron heating, the higher the temperature of the exploded foil, the longer the plasma gradient length is [128]. Likewise, the greater the delay between the SP and the LP, the more expanded the exploded target, the longer the plasma gradient length is.

In order to determine precisely the density profiles generated by the LP, we have performed simulations using the 2D axially symmetric radiation hydrodynamic implosion code CHIC [129] reproducing conditions similar to our experiment. The maximum LP intensity is varying within the range $I \sim 3\times10^{13-14}$ W/cm², in agreement with the LP intensities scanned during the experiment. The LP irradiates the target at 45° with respect to its normal axis, as in the experimental set-up. In Figure III-36 are shown 2D density maps of the expanding plasma at respectively, -350, 0 and +400 ps between the LP and the SP (according to the convention adopted in Figure III-33). The beam propagation direction is indicated by the black arrows. In Figure III-36a, we can see that for shorter delays, the target is still overdense: the laser deposits a part of its energy in the expanding under-dense front plasma and is specularly reflected off the target at 45° with respect to the target normal axis. The rear density gradient starts developing and the expansion is almost symmetric with respect to the normal of the target surface. After a longer time of irradiation, one can see in Figure III-36b that the plasma density becomes undercritical: the LP is no longer reflected and passes through the target. Contrary to the front expanding plasma, the expansion of the rear plasma is found to be asymmetric with respect to the target normal axis. The expanded plasma in the direction of the laser pulse is indeed observed to be less dense and the gradient smoother than on the other side with respect to the target normal axis.

At longer times (see Figure III-36c), the target density is well below the critical density and completely transparent to the LP that passes through the electron density.

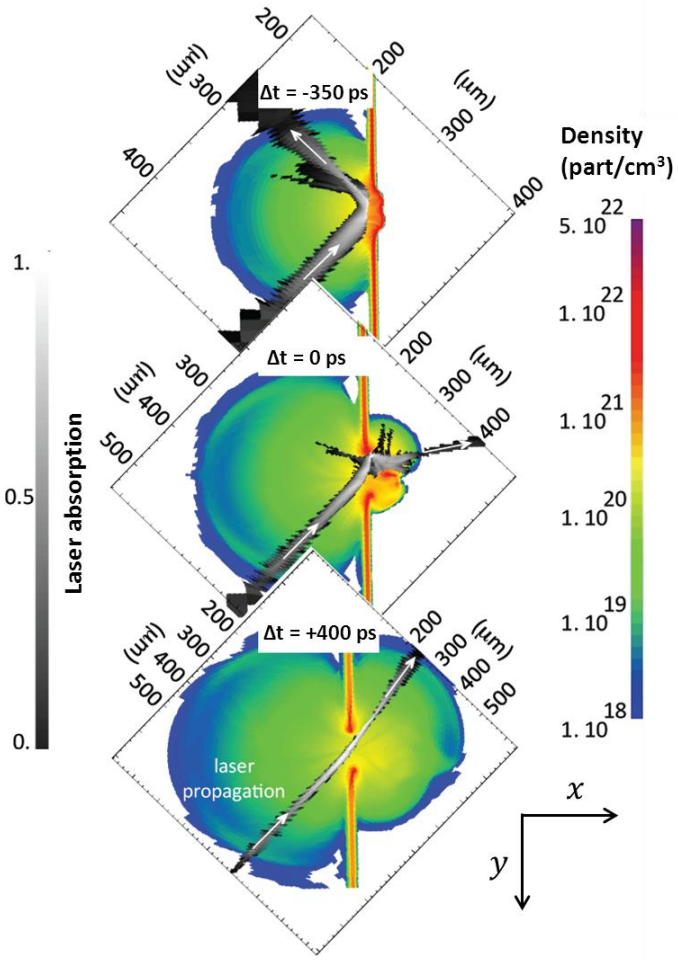

Figure III-36: Superposed density (in logarithmic scale) and LP absorption maps obtained using CHIC 2D for delays of, respectively, -350 (a), 0 (b) and +400 ps (c). The LP is coming from the left.

We now compare the front density plasma expansions simulated with CHIC to those measured by the interferometry diagnostic. In Figure III-37, two images of a 500 nm plastic target recorded by the interferometry diagnostic are shown. The image on the left has been taken before the shot, when the target has not been irradiated and is still solid, while the one on the right shows the expanding target at the time when the SP is arriving on the target (and during the LP irradiation). The black zones correspond to either overcritical plasma through which the probe laser light cannot pass ($n_c(\lambda_0$ = 526 nm) ~ 4×10^{21} cm^{-3}) or too strong density gradient inducing strong refraction of the probe. We note that the target in the left picture appears much thicker than it is (around 40 µm on the image), this is due to the fact that the target of a few millimeters width along y-axis is not perfectly planar, and hence it projects a shadow that is wider than the actual thickness. In the right picture, the LP and the SP are coming from the left. The bright light present in the center of the interferometry image is due to strong 2ω emission produced when the SP interacts with the front plasma.

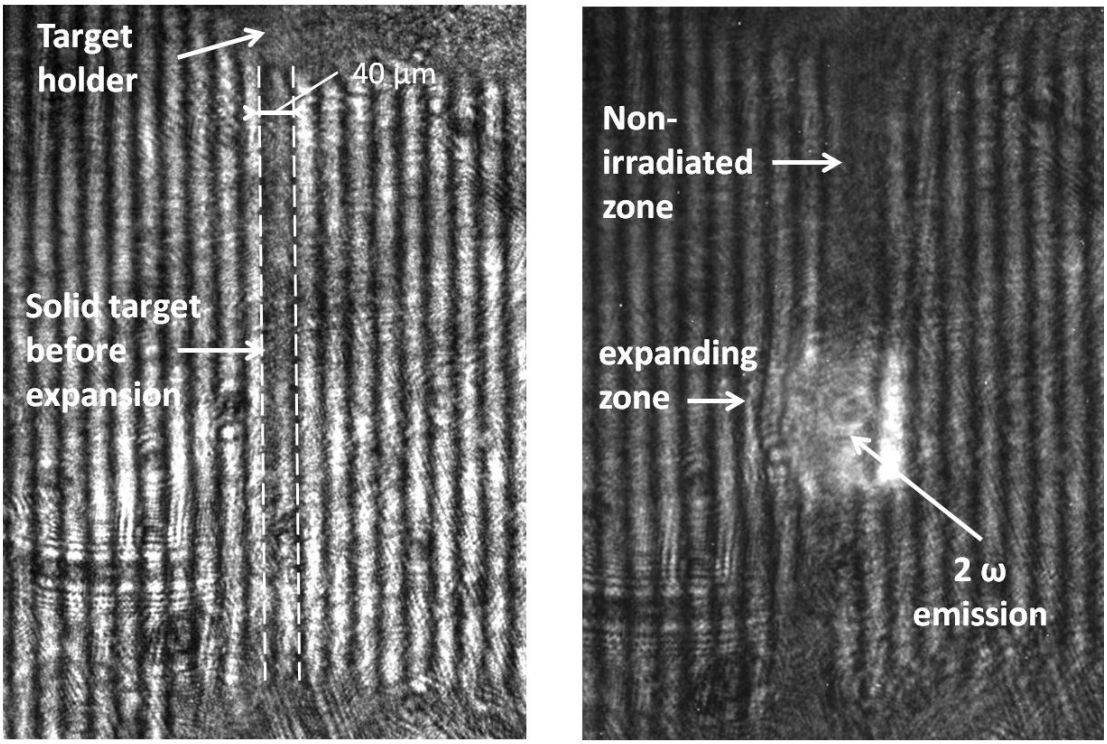

Figure III-37: Interferometry images of a 500 nm plastic target before and during irradiation by the laser coming from the left to the right. Both images have the same scale.

In Figure III-38 are presented two different experimental electron density maps deduced from interferometry pictures using Abel inversion [126], at, respectively, 400 and 0 ps prior to the LP peak ($\Delta t = -400 \text{ and } 0$ ps), with the LP intensity of 3×10^{14} and I ~ 3×10^{13} W/cm². In agreement with Abel inversion hypotheses, the electron density map has been symmetrized around the expansion direction axis. We estimate an error bar on the density up to 8 % when comparing the density obtained on each side. The observation zone of our diagnostic was limited to low-density zones of the plasma profile (below 10^{20} cm^{-3}) since at higher density the gradients are either too strong, and induce strong refraction of the probe, or the zone is inaccessible due to strong 2ω emission. When comparing both density maps in Figure III-38, we see that the expanding plasma is denser in Figure III-38a. It corresponds to a higher LP intensity and therefore to a more expanded plasma.

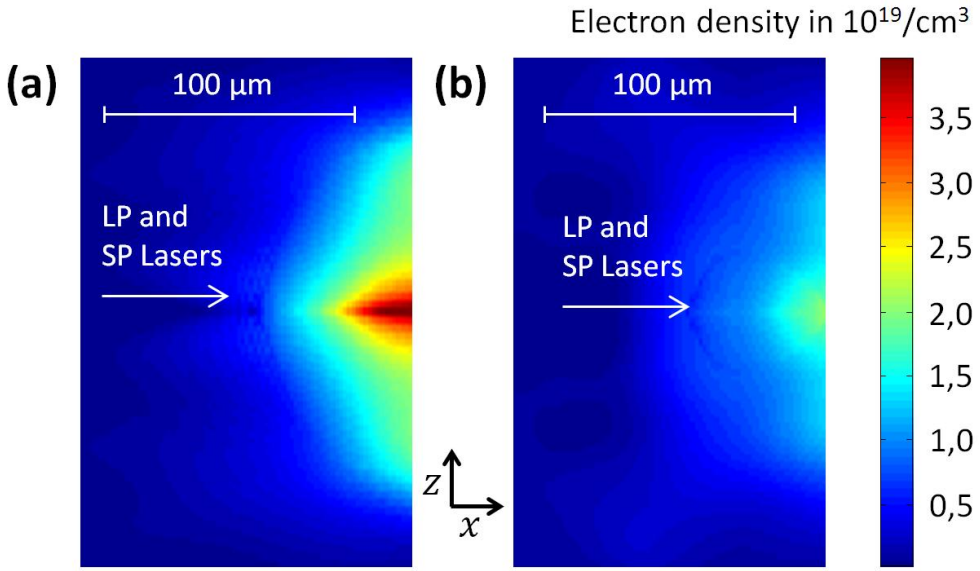

Figure III-38: Density maps obtained by Abel inversion from interferometry images. These density profiles correspond to a 500 nm plastic target irradiated by a long pulse of intensity of respectively, (a) 3×10^{14} W/cm² , (b) 3×10^{13} W/cm², 400 ps and 0 ps prior to the peak of the long laser pulse (Δt = - 400 and 0 ps).

Regarding the rear side plasma expansion of the target, we were not able to detect any expanding plasma as the non-irradiated side of the target was not sufficiently expanded so that the plasma could be detected by our interferometer.

In Figure III-39, we compare the density profile deduced from the interferometry images shown in Figure III-38 and those extracted from CHIC simulations for the same interaction conditions. Although the longitudinal density range detected by our diagnostic is very narrow, we can assess that the experimental gradient characteristic length, L_G is comprised, respectively, between 15 and 45 µm in Figure III-39a and between 30 and 48 µm in Figure III-39b. These experimental profiles are found in reasonable agreement with the results obtained by CHIC.

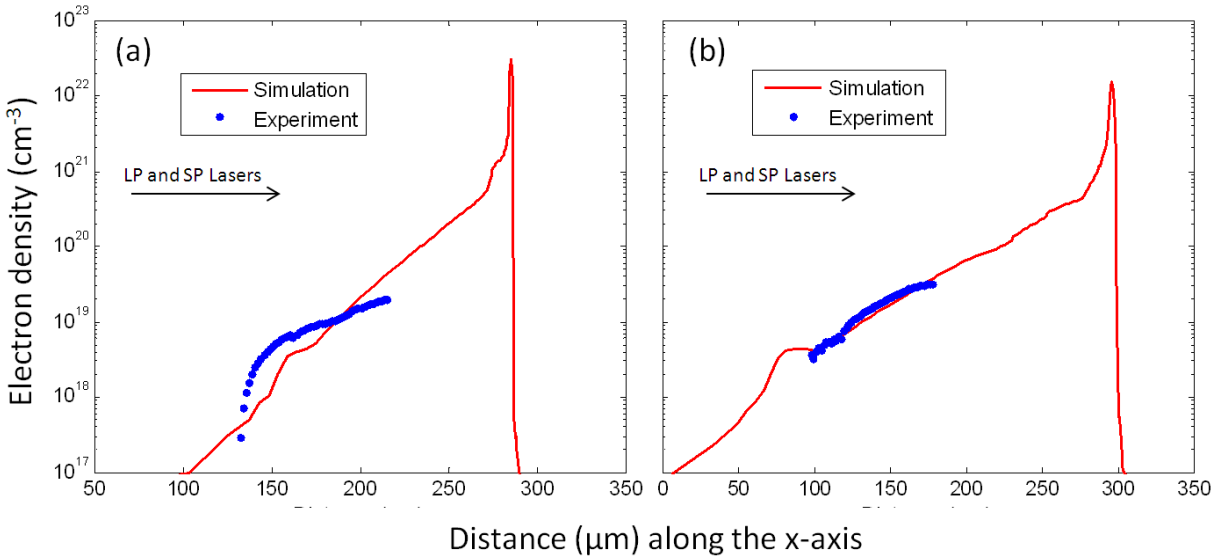

Figure III-39: Density profiles corresponding to a 500 nm plastic target irradiated by a long pulse of intensity of respectively, (a) 3×10^{14}, (b) 3×10^{13} W/cm², 400 and 0 ps prior to the peak of the long laser pulse (Δt = -400 and 0 ps). Blue dots indicate the density profiles obtained by the Interferometry diagnostic, red lines by CHIC simulations. The experimental profiles are extracted at a distance of 10 µm from the center of the expansion to avoid uncertainties caused by the Abel inversion.

Since the measurement from the interferometer is only over a limited range of densities and gradients, and hence cannot capture the entire plasma density profile, we rely on CHIC simulations to infer the front and the rear plasma gradient length.

Figure III-40 summarizes the characteristic back-side plasma gradient as obtained by CHIC for the different delays and LP intensities explored in the experiment. One can see that the gradient characteristic length strongly increases with the delay and laser intensity.

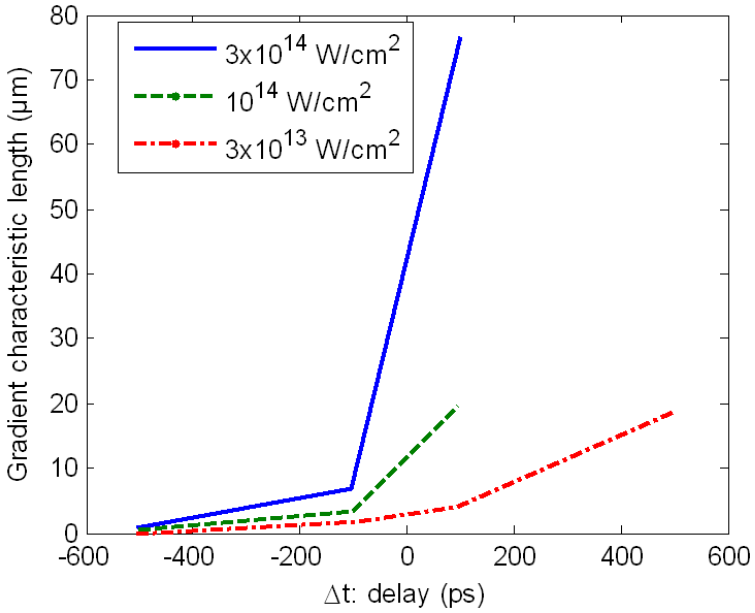

Figure III-40: Evolution of the gradient characteristic length of the rear plasma (average length to reach a decrease of the density by a factor of exp(1)) in the CHIC simulations as a function of the delay for LP intensities of 3×10^{13} (green curve), 10^{14} (red curve) and 3×10^{14} W/cm² (blue curve).

It should be noted that CHIC simulations do not take into account the ASE of the short pulse beam when estimating the expansion of the target. This is justified since the expansion induced by ASE is negligible compared to the expansion caused by the LP: Hydrodynamic scaling laws predict the ASE to heat the inside of the target to a temperature of around 300 eV. Using c_s, the ionic sound velocity and τ_{ASE}, the ASE duration (typically of 200 ps), we can estimate the distance from the beginning of the density decrease at the target surface to the front of the expansion,

$$x_{front} \sim c_s \tau_{ASE} \sim 7\ \mu\text{m}. \qquad (3.58)$$

Then, assuming the density at the front of the expansion to be equal to the critical density, we can roughly calculate the gradient characteristic length as follows,

$$L_G \sim \frac{x_{front}}{ln(n_{e,solid}/n_c)} \sim 0.07\ \mu m \ll 1\ \mu m, \qquad (3.59)$$

where $n_{e,solid}$ is the electron density of a solid-density plastic foil at 300 eV. Thus, the ASE is expected to produce a density gradient of characteristic length less than 1 µm at the front surface and even less at the rear surface (the expansion occurs later).

III.3.2.4.2.2 Proton Spectra

Using two different LP intensities and various Δt, we have measured the proton spectra accelerated by the SP (I ~ 5×10^{18} W/cm²) irradiating exploded targets having rear plasma gradients with characteristic length up to 8 µm according to CHIC simulations. As can be seen in Figure III-41, an increase of the density gradient does not decrease significantly the proton energy cut-off. Moreover, it generates higher energies than the one obtained without any target preformation and this for both observation angles (0° and 15°).

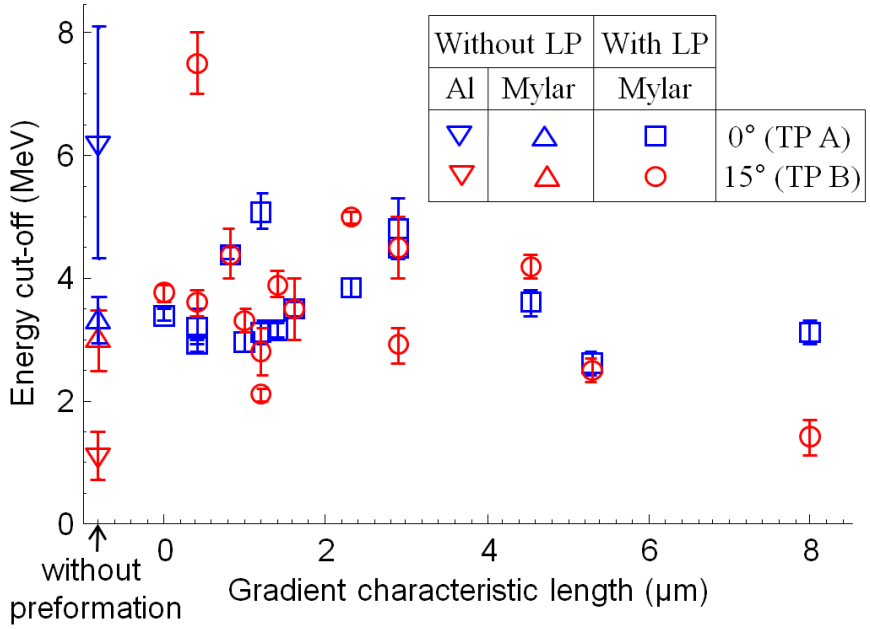

Figure III-41: Proton energy cut-off obtained using 500 nm Mylar exploded foil as a function of the characteristic length of the target rear density gradient. The proton energy cut-offs measured without target preformation either with a 500 nm Mylar foils (upward-pointing triangle) or a 10 µm Au (downward-pointing triangle) are added for comparison.

In addition, we observed that for certain gradient characteristic lengths such as 0.4 or 2.4 µm, the most energetic protons are found at 15° from the target normal, rather than at 0°. This indicates that the acceleration mechanism is affected by the asymmetric expansion caused by the LP. While the maximum proton energy is dependent on the electrostatic field, the angle with which the protons stem out of the target strongly depends on the geometry of the sheath field since ions are accelerated normally to the isopotential (see section III.2.3.2.1.3). We also observed that the most energetic protons generated using low-density targets have energies that are comparable – if not better – to those obtained in the best TNSA conditions using solid targets. For example, in the spectra measured at 0° and 15° for a delay of -400 ps (see Figure III-42), we see higher proton energy cut-off on the TP positioned at 15° (~ 7-8 MeV), however on the TP located at 0°, we only measure 2.8-3.7 MeV. Note that the number of accelerated particles is similar to the one observed in the case of a 10 µm solid-density Au target (see Figure III-35a).

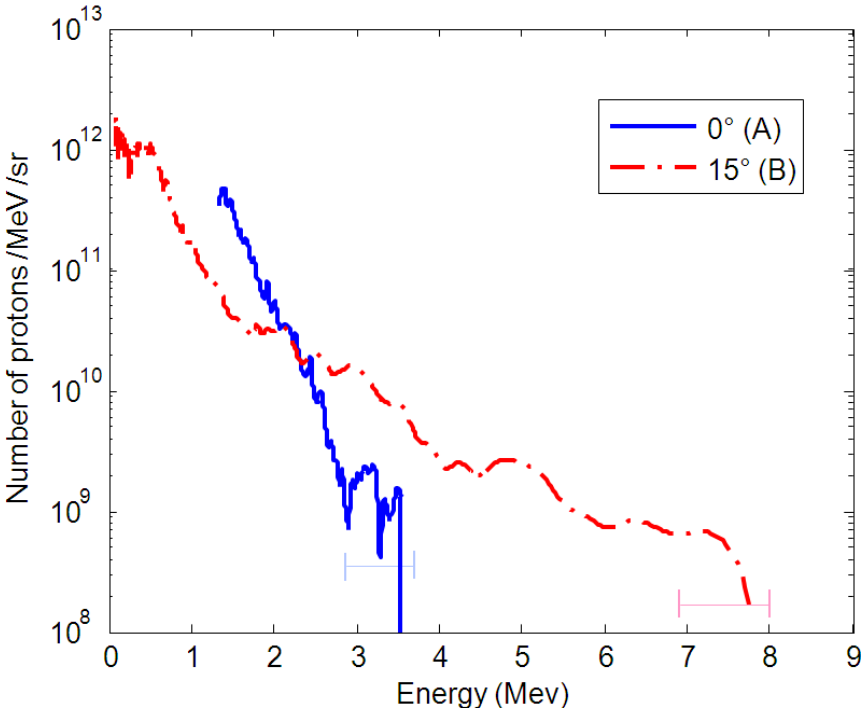

Figure III-42 : Proton spectra measured at 0° and 15° for a delay Δt of -400 ps between the SP and the LP when irradiating 500 nm plastic foils by the LP of intensity I = 3×10^{13} W/cm².

In order to further investigate the beam angular characteristics, we tilted the target at 7°, 15° 22° and 30° with respect to the initial target surface as shown in Figure III-43; the rotation angle is noted θ. We kept the other parameters fixed (LP intensity I = 3×10^{13} W/cm² and Δt = -400 ps), since in this configuration, we had experimentally obtained the highest proton energies.

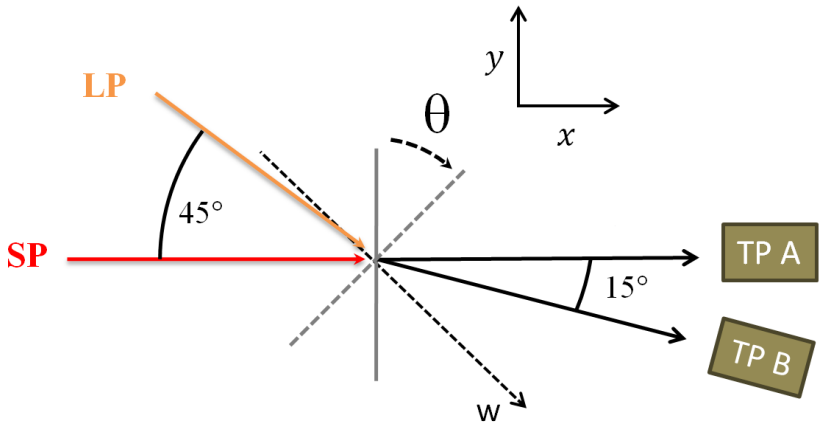

Figure III-43: Angle (θ) of the target compared to the SP axis.

A comparison of the proton energy cut-offs measured for the different target angles is presented in Figure III-44. It should be noted that for the TP A, no protons were detected when the target was tilted at θ = 15°, 22° and 30°. It means that for these shots, the maximum proton energy did not reach more than 1.3 MeV. The most energetic protons are clearly produced close to the target normal axis, but energetic protons are still found at an angle up to 15°. The accelerated ion beam is

therefore not isotropic, but less collimated than the one produced from solid-density targets [10]. This decrease of the beam collimation could be explained by the geometry of the SP. Indeed, according to Ref. [117], the protons are expected to be preferentially emitted at some angle in between the direction of the plasma expansion generated by the LP and the direction of the SP propagation: the long living magnetic field induced by the hot electron current generated by the SP slightly deflects the beam from the direction of the plasma expansion. In our experiment, the direction of the plasma expansion is given by the axis normal to the target, w (see Figure III-44), while the SP remains collinear to x. The proton beams direction is therefore tilted from w to x. This effect is not visible when both the SP and the plasma expansion are pointing in the same direction (w and x are collinear), but becomes perceptible when the angle between the two axis increases. Nevertheless, the fact that we observe clearly a decrease of the energy cut-off when increasing the angle θ means that the effect of the long living magnetic field is not strong enough to overcome the direction induced by the plasma expansion generated by the LP. It could be the case with a higher intensity or a more energetic SP producing a higher number of hot electrons and thus generating stronger magnetic fields.

It should also be noted that the highest energy is found on the TP B in the case the target is positioned at 0°, i.e., when the target is normal to the SP propagation axis. This corresponds to an asymmetric expansion of the rear plasma: the direction of the plasma is slightly modified in the direction of the LP propagation axis, tilting the proton beam in the direction given by the TP B.

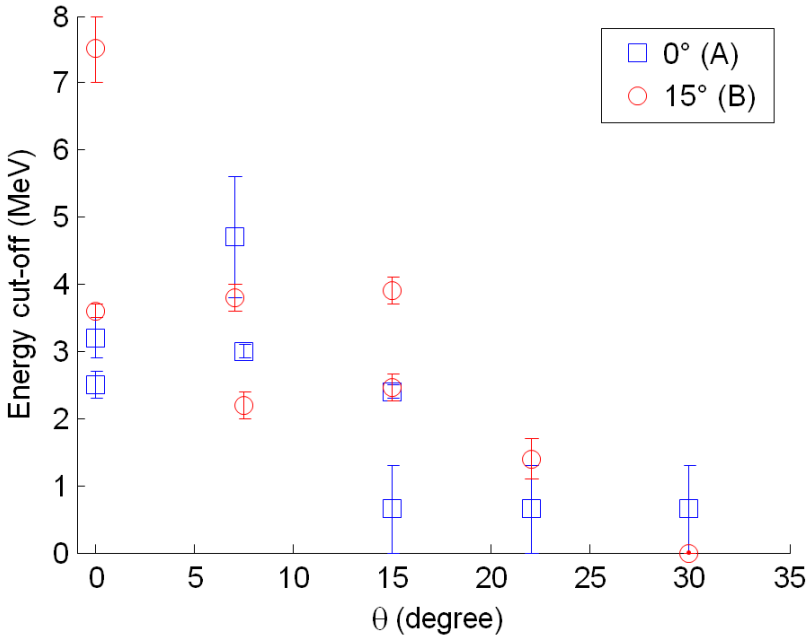

Figure III-44: Proton energy cut-off at 0° (TP A) and 15° (TP B) to the SP surface as a function of the angle between the normal of the irradiated target and the SP propagation axis.

We investigated another technique to reduce the LP initial intensity. Instead of putting optical densities on the LP path, we defocused the LP beam making the spot diameter increased from 20 µm to 200 µm and obtained a LP intensity of 3×10^{13} W/cm². In this configuration, the delay between the SP and the LP were varied from -400 to 200 ps. The proton energy cut-offs recorded by TPs A and B are plotted in Figure III-45.

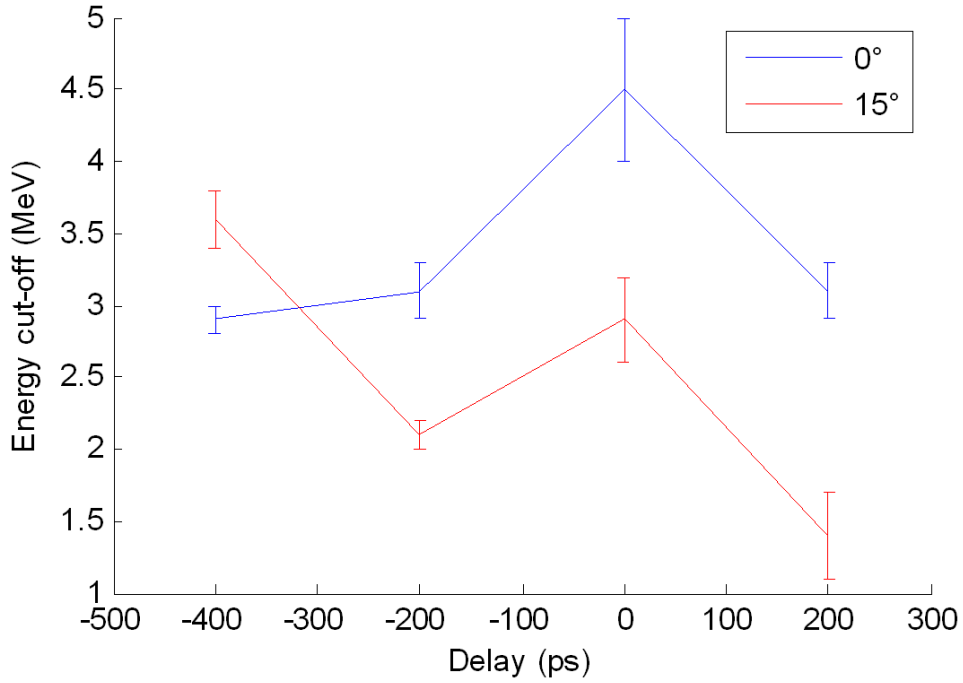

Figure III-45: Proton energy cut-off measured by the TPs A (0°) and B (15°) as a function of the delay between the SP and the LP while the LP is defocused.

The maximum proton energies are comparable but in average slightly lower to what we obtained by using ODs. Nevertheless, the protons remain as well energetic even when the preformed target presents longer densities gradients, i.e., for positive delays. The difference observed is explained as follows. On one hand, reducing the LP intensity by putting ODs in the beam path lowers the noise in the beam profile by dividing the intensity everywhere in the focal spot by a factor of 100. On the other hand, when defocusing the beam, the focal spot loses a lot in homogeneity. Hence, the SP interacts with a preformed front plasma much less regular compared to the case in which ODs are used. As a consequence, the bell-shape of the expanding plasma tends to be degraded and so the maximum proton energy is reduced.

III.3.2.5 Simulations and discussion

To study the transition between the sharp and the long gradient regime and to understand the possibility of obtaining high energy protons for various gradient conditions, we have performed 2D Particle-In-Cell (PIC) simulations with the PICLS code [130]. Depending on the gradient characteristic length, several regimes already studied theoretically can be obtained:

- For sharp density gradients, classical TNSA is dominant even when irradiating subcritical density targets [92, 122].
- For longer gradients on both sides of the targets, there is a competition between the laser absorption increase on the interaction side and the decrease of the TNSA electric field on the rear side due to the lengthening of the density gradient on this side. The acceleration regime is similar to the gradient regime studied in Ref. [51] in which the maximum proton energy decreases as the rear plasma gradient length increases.
- When the target starts to become transparent during the interaction, the coupling between the laser and the target is significantly improved. The increase of the hot electron temperature T_h can then counterbalance the characteristic scale length L_G in the accelerating electric field formula,

$$E = \frac{k_B T_h}{e L_G} \sqrt{\frac{2}{\exp(1)}}, \tag{3.60}$$

  and lead to higher energy protons [131]. In this regime, the electrostatic shock that develops in the long rear side density gradient [51] can launch the CSA mechanism [125] and enhance the maximum proton energy. This rear-side shock is different from front-side collisionless shocks already observed when the laser is reflected at the front of a dense target [36].
- For too long gradients, obtained with a strongly expanded target, the laser-to-target coupling decreases since the target is becoming too transparent to the laser light for producing energetic electrons.

The PIC simulations illustrating these regimes were performed using a 1,057 µm wavelength, 350 fs (FWHM) duration, p-polarized laser pulse focused on a 10 µm diameter spot. The spatial and temporal profiles are truncated Gaussians. The laser intensity of 8×10^{18} W/cm^2 is similar to the intensity of the SP in our experiment (~ 5×10^{18} W/cm²). The pulse is injected from the left side of the simulation box.

The density profile in the first simulation corresponds to a long negative delay between the two pulses reproducing the case of the short pulse interacting almost directly with the thin foil used in

the experiments. We used the truncated (as can be seen in Figure III-46) CHIC density profile for a delay of -500 ps and a LP intensity of 3×10^{13} W/cm². The target is composed of deuteron ions, protons (1 proton for 3 deuterons) and electrons with a 300 n_c maximum electron density. Using deuterons instead of carbon ions is less expensive in the simulations and as collision are not treated, the target is equivalent to a CH target. The initial electronic, proton and deuteron temperatures are set to zero. The plasma is located 70 µm from the left side in the 176 by 160 µm simulations box containing 12 protons, 6 D ions and 18 electrons per cell. The spatial and time steps are respectively $\Delta x = \Delta y$ = 15 nm and Δt = 0.05 fs. The boundary conditions used are absorbing in x and y. Collisions were not taken into account as the laser energy and the small target thickness leads to a quick heating of the target. The density profile we used and the obtained proton phase space on axis are shown respectively in Figure III-46a and Figure III-46b.

This simulation exhibits a standard TNSA acceleration process with the maximum energy protons coming from the rear surface and a strong laser absorption leading to high energy protons. The maximum proton energy is here 15.6 MeV at saturation. This is higher than what is measured experimentally with the SP only interacting with a 500 nm target. However, this was expected as 2D simulations are known to overestimate the final proton energy.

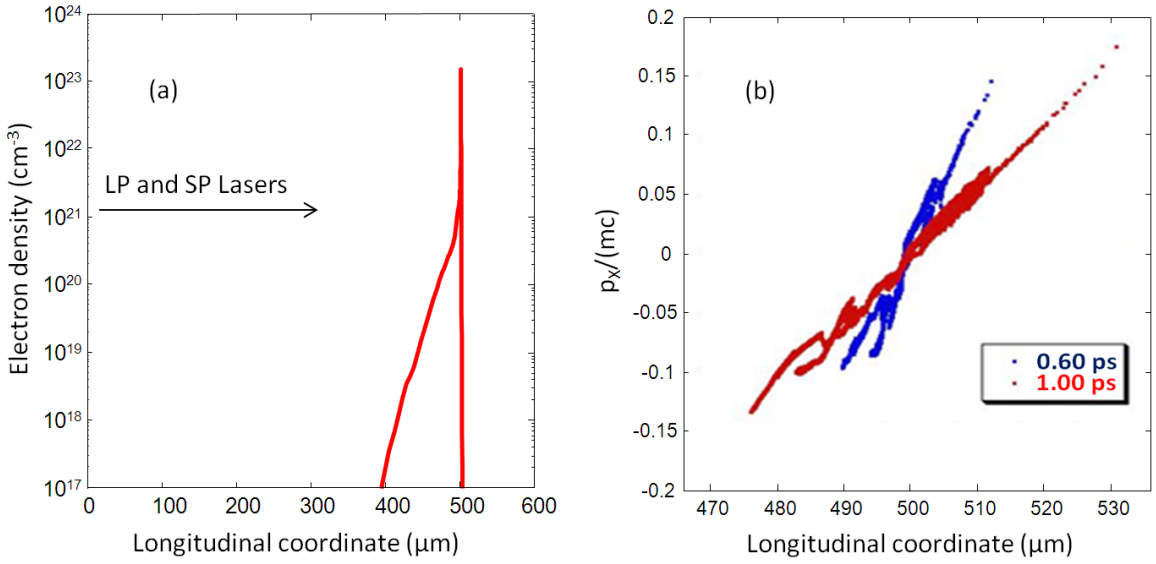

Figure III-46: Density profile obtained with CHIC for a foil exploded with a 3×10^{13} W/cm² intensity (LP) and a -500 ps delay (a) and normalized proton phase space (m is the proton mass and c the light speed) in the longitudinal direction (along the x-axis) 0.6 and 1 ps after the interaction of the maximum of the short pulse (b). The laser comes from the left. The coordinates on the left figure correspond to the CHIC longitudinal coordinates and the ones on the right figure correspond to the PICLS longitudinal coordinates.

In a second simulation, we used (as initial density profile) for the PIC simulation the CHIC density profile obtained with a LP intensity of 10^{14} W/cm² and Δt = +100 ps. In this case, as can be seen in

Figure III-47a, the density profile corresponds to a larger plasma with smoother gradients: the gradient characteristic length of the rear plasma profile is around 28 µm. We are dealing here with a plasma gradient that is much longer that those we investigated experimentally. The simulation parameters are the same as above except for the following parameters. The target has a maximum electron density slightly higher than the critical density. The target has a maximum electron density slightly higher than the critical density. The plasma is located 100 µm from the left side in the 800 by 128 µm simulations box containing 20 protons, and 20 electrons per cell. The spatial and time steps are respectively $\Delta x = \Delta y = 100$ nm and $\Delta t = 0.33$ fs.

The obtained proton phase space along the x-axis is shown in Figure III-47b. In this simulation, the maximum energy protons are also accelerated by a strong electrostatic field in the decreasing density gradient, but a secondary acceleration process occurs. The first step is not as efficient as in the case described in Figure III-46. The long density gradient at the rear surface of the target leads to a lower accelerating electric field but the strong laser-to-target coupling can compensate this decrease and still lead to high energy protons. In our case, this first step leads to a maximum proton velocity of around 0.1 c. In a second step, protons are accelerated further in the gradient by a CSA over a short distance which leads to a distinct feature in the proton phase space that is clearly visible at x = 660 µm in Figure III-47b. In this case the maximum proton energy at saturation is 13.2 MeV, which is very close to the maximum energy obtained in the case described above in Figure III-46. Depending on the density gradient at the rear surface of the target, it is therefore possible to accelerate ions to similar energies than when using sharp rear gradients target (compare Figure III-46 and Figure III-47) but through different processes.

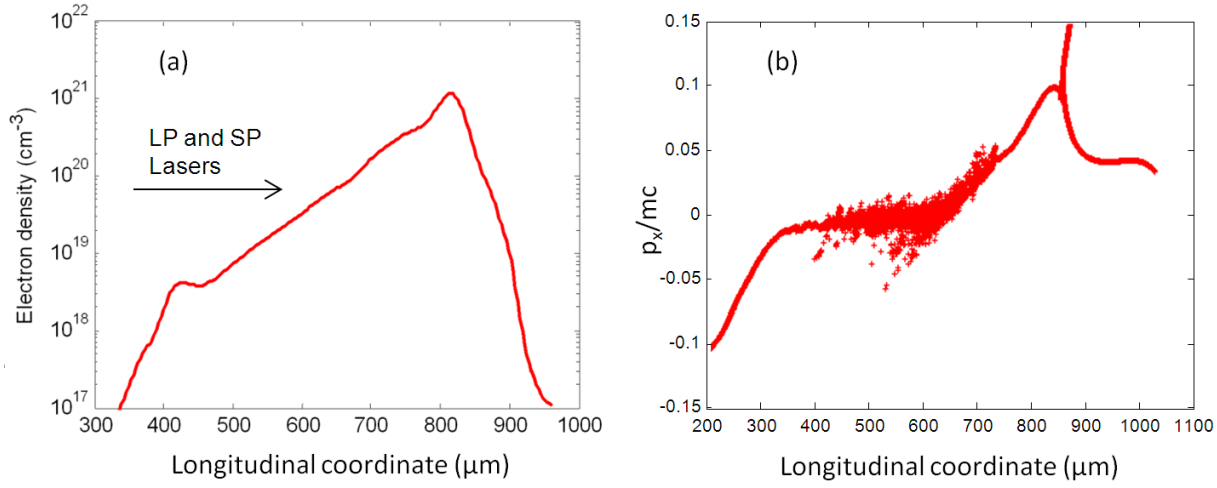

Figure III-47: Density profile obtained with CHIC for a 500 nm plastic foil exploded with a 10^{14} W/cm^2 intensity and a +100 ps delay (a) and normalized proton phase space in the longitudinal direction 7.42 ps after the interaction of the maxi-

mum of the short pulse (b). The laser comes from the left. The coordinates on the left figure correspond to the CHIC longitudinal coordinates and the ones on the right figure correspond to the PICLS longitudinal coordinates.

Figure III-48a and b respectively show the forward proton energy spectrum obtained in the second simulation and the associated divergence distribution for protons with energy higher than 1 MeV. The divergence distribution is more complex than the usual TNSA one. The low divergence part is broader and additional features are observed at ~ 35° and for angles higher than 60°. This latest feature is even observed for protons with energy higher than 8 MeV corresponding to protons that are accelerated almost perpendicular to the laser axis in the channel created by the laser.

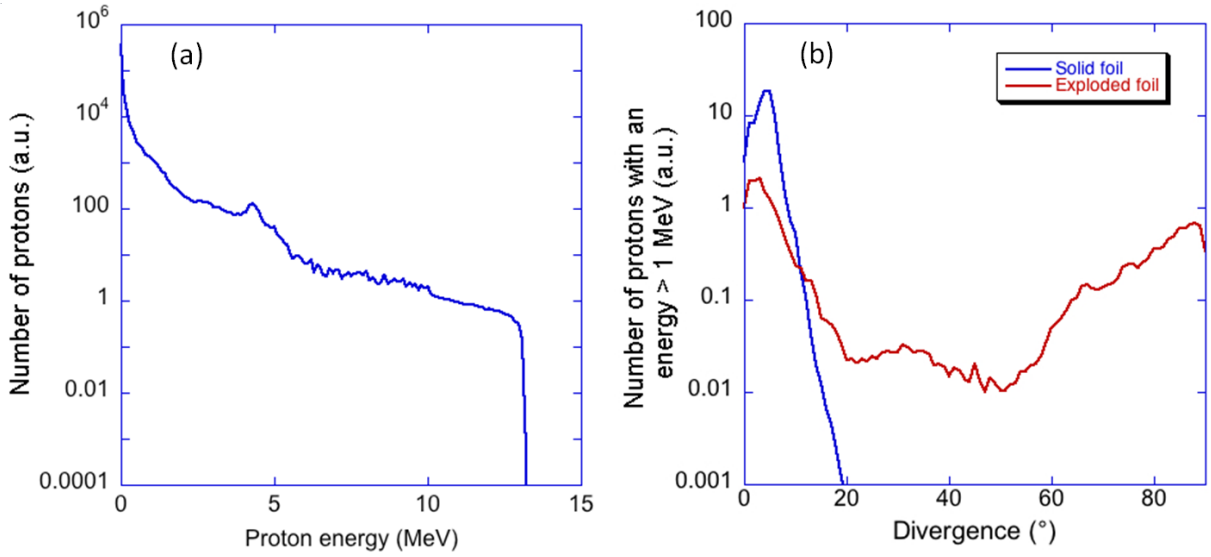

Figure III-48: (a) Proton energy spectrum in the forward direction. (b) Comparison of the divergence distribution for protons with energy higher than 1 MeV in the forward direction in the case of the short pulse interaction with a 500 nm plastic foil non-exploded and one exploded with a 1014 W/cm2 intensity and a +100 ps delay.

To study the transition between these two efficient laser proton acceleration regimes, we have simulated intermediate density gradients. Here, we decreased the plasma length used for the case illustrated in Figure III-47 by changing the rear surface profile characteristics, starting from the CHIC profile obtained for a LP intensity of 10^{14} W/cm^2 and a delay of +100 ps. In Figure III-49, we show the proton phase spaces obtained at two simulation times for characteristic gradient lengths of 5 and 10 µm. When decreasing the gradient scale length to 10 µm, the laser coupling with the target is still high but the electric field in the density gradient is weaker. This leads to moderately high energy protons (5.2 MeV) as evidenced by the lower maximum velocities reached and shown in Figure III-49a. In this case, the coupling efficiency is not enough to compare to either TNSA with thin targets (Figure III-46) or shock acceleration with exploded foils (Figure III-47).

Figure III-49b corresponds to the case of a 5 µm gradient characteristic length for which the laser coupling is decreased and the gradient length is too long to lead to high energy protons (2.8 MeV). The higher coupling efficiency in the 10 µm gradient characteristic length case is also evidenced by the enhanced backward (towards the laser) acceleration visible in Figure III-49a compared to Figure III-49b.

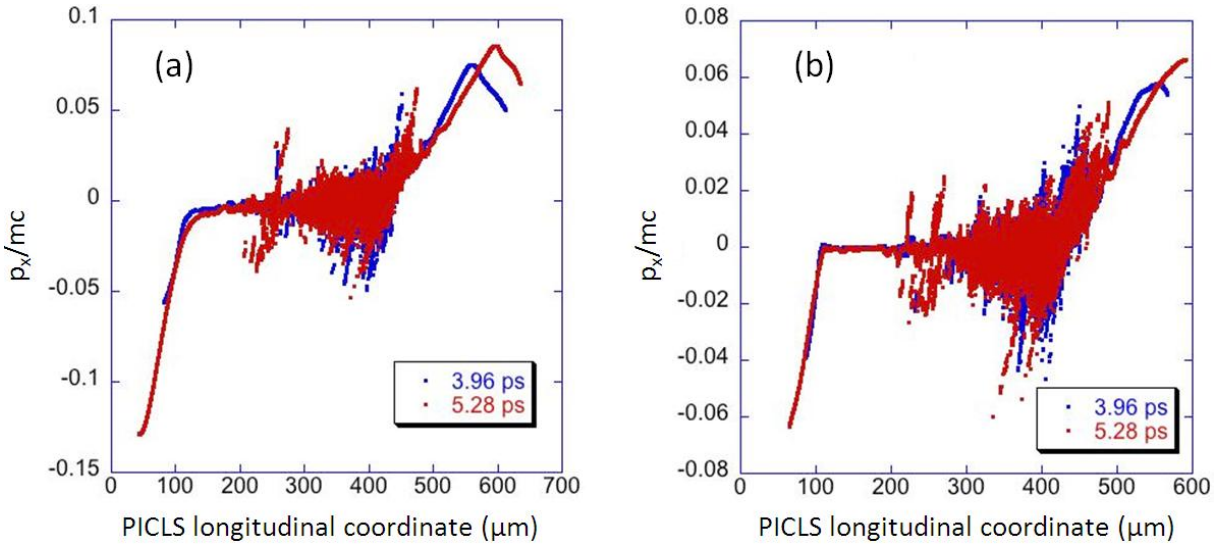

Figure III-49: proton phase space on axis at 3.96 ps (blue) and at 5.28 ps (red) in the case of the short pulse interaction with an exploded foil with rear gradient with characteristic lengths of 10 (a), and 5 µm (b).

When comparing the evolution from a steep rear surface density gradient in Figure III-46 to a longer and smoother one in Figure III-47 and Figure III-49, it is clear that it is possible to accelerate high energy protons on a wide range of target parameters in the under-dense laser ion acceleration regime. This is very similar to the experimental observation that MeV protons can be generated with various delays and various LP intensities.

In addition, these simulations indicates that there are two optimum regimes for laser proton acceleration, namely the thin target TNSA and the exploded foil CSA, generating similar maximum proton energies. For thin target TNSA, high laser contrast is necessary. One drawback of this regime is that the various techniques to improve the laser contrast also decrease the total laser energy in the focal spot (it is the case using plasma mirrors or non-linear systems laser frequency doubling). For exploded foil CSA, a small range of density gradient scale length can lead to this regime. According to simulations, in between, a large range of target parameters leads to moderately high energy protons through degraded TNSA.

III.3.2.6 Conclusion and perspectives

We have studied the longitudinal acceleration of protons using a high intensity picosecond laser pulse irradiating a 500 nm thick plastic foil exploded by a nanosecond pulse. We varied the nanosecond pulse intensity and the delay between the picosecond and the nanosecond pulses to study the acceleration mechanism in various target conditions having short to moderate plasma density gradients, i.e., with gradient characteristic lengths from 0 to 8 µm. We have shown in agreement with PIC simulations that, in these gradient density ranges, protons can be accelerated to energies comparable to solid targets. We also demonstrated that under certain laser and target conditions it is possible to produce protons of energies similar and higher than what can be obtained in the conventional TNSA regime. In addition, we highlighted that the use of exploded targets generates a broader angular proton distribution compared to solid targets and an acceleration anisotropy which still needs to be controlled.

PIC simulations have shown that, for higher SP intensities than in our experiment, we should be able to achieve higher electric fields in longer density gradients [125]. This would enhance under-dense laser ion acceleration and less stringent interaction conditions would be required for the shock to develop. As a consequence, this should allow obtaining higher energy protons than with the conventional TNSA regime. For example, for a laser intensity of 5×10^{20} W/cm^2 (intensity already achieved with SP lasers), PICLS simulations predicted protons of energy above 100 MeV (see Figure III-50).

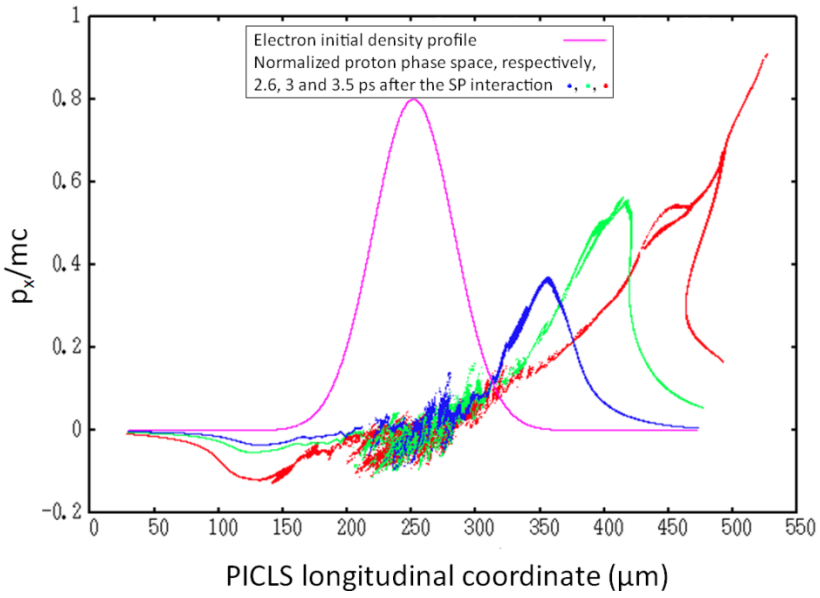

Figure III-50: Normalized proton phase space obtained predicted by a PICLS simulation for a SP of intensity 5×10^{20} W/cm^2, pulse duration 700 fs (FWHM) and the focal spot diameter of 6 µm (FWHM) interacting with a 80 µm thick (FWHM) plastic target (the electron density profile is normalized to the critical density of the laser). The laser is focused 150 µm from the left boundary.

III.4 Summary

In this chapter, we have studied the laser-generation of ion beams in the scope of optimizing those beams for measuring stopping power in warm dense matter. Throughout this chapter, we have emphasized that the generation of the hot electron population by the high intensity laser is fundamental in the various ion acceleration mechanisms whether using solid-density or lower than solid-density targets.

The first part of the chapter dealt with the most common and developed method of accelerating ions using lasers: the interaction of a short-pulse laser beam with solid-density targets. Although the two other mechanisms presented, i.e., sweeping acceleration and RPA, are promising for future enhanced laser conditions, the TNSA is up to now the best mechanism to accelerate efficiently energetic ion beams. In the scope of this thesis, we use this mechanism in particular to generate ion beams capable of heating solid-density matter in volume and produce warm dense matter samples that can be used in experiment. However, TNSA is limited due to its low laser-to-ion energy conversion mainly due to its front sharp density gradient, its sensibility to the laser contrast, the growing complexity of the targets in order to control the produced ion beam and the difficulty of solely accelerating specific ion species.

The second part was devoted to the development of new method of acceleration aiming at solving the above mentioned issues by using lower-than-solid-density targets. This section was also divided in two parts. In the first part, we focus on the most well-known ion acceleration mechanism occurring in under-critical gas jet targets based on the Coulomb explosion. Our experiment confirms its, already demonstrated, relatively low performance in terms of ion energy and number. We, however, highlight the rotational symmetry of the acceleration mechanism and its utility for ion probing purpose. Indeed, using an ion beam to probe and its symmetric as reference allows reducing the uncertainty (due to shot-to-shot fluctuations) on the initial probe beam spectrum. Such set-up is used in the next chapter. The last part concerns the experimental study of a new longitudinal ion acceleration mechanism occurring in near-critical density targets. According to PIC simulations, this collisional shock acceleration mechanism occurs in target having a smooth density gradient and would generate ions of higher energy and in higher number than TNSA under identical laser conditions. The study of such mechanism is limited by the current lack of availability of confined near-critical density targets. Nevertheless, using an exploded target as a substitute, we were able to demonstrate that under certain laser and exploded foil conditions it was possible to accelerate protons to the same energies as using solid-density targets. These results are well supported by PIC simulations using similar parame-

ters as our experiment. Those simulations also predict that, with currently available laser intensities (higher than those of our experiment), collisionless shock acceleration should be able to deliver substantially higher energy protons than with the conventional TNSA regime.

References

[1] W. I. Linlor et al., Appl. Phys. Lett. **3**, 210 (1963)
[2] F. Begay & D. Forslund, Phys. of Fluids **25**, 1675 (1982)
[3] S. J. Gitomer et al., Phys. Fluids **29**, 2679 (1986)
[4] A. P. Fews et al., Phys. Rev. Lett. **73**, 1801 (1994)
[5] E. L. Clark et al., Phys. Rev. Lett. **84**, 670 (2000)
[6] K. Krushelnick et al., Phys. Plasmas **7**, 2055 (2000)
[7] A. Maksimchuk et al., Phys. Rev. Lett. **84**, 4108 (2000)
[8] R. A. Snavely et al., Phys. Rev. Lett. **85**, 2945 (2000)
[9] P. K. Patel et al., Phys. Rev. Lett. **91**, 125004 (2003)
[10] A. Mancic et al., High Energy Dens. Phys. **6**, 21 (2010)
[11] G. Dyer et al., Phys. Rev. Lett. **101,** 015002 (2008)
[12] A. Mackinnon & P. K. Pattel, Rev. Sci. Instrum. **75**, 3531. (2004)
[13] J. Fuchs et al., Phys. Rev. Lett. **99**, 015002 (2007)
[14] B. A. Remington et al. Science **284**, 1488 (1999)
[15] B. A. Remington et al., Rev. Mod. Phys. **78**, 755 (2006)
[16] L. Lancia et al., Phys. Plasma **18**, 030705 (2011)
[17] K. Quinn et al., Phys. Rev. Lett. **108**, 135001 (2012)
[18] T. E. Cowan et al., Phys. Rev. Lett. **92**, 204801 (2004)
[19] S. V. Bulanov, Phys. Lett. A **299**, 240 (2002)
[20] M. Roth et al., Phys. Rev. Lett. **86**, 436 (2001)
[21] P. Gibbon, *Short Pulse Laser Interactions with Matter*, London: Imperial College Press (2005)
[22] T. Esirkepov et al., Phys. Rev. Lett. **92**, 175003 (2004)
[23] P. Mora, lecture notes, *Introduction aux plasmas crées par laser*, École Polytechnique, Palaiseau (2009)
[24] L. Spitzer & R. Harm, Phys. Rev. **89**, 977 (1953)
[25] W. L. Kruer, *The Physics of Laser-Plasma Interactions*, Redwood City: Addison-Wesley (1988)
[26] C. J. Startsev & E. A. McKinstrie, Phys Rev. E 56, 2130 (1997)
[27] D. Bauer, lecture notes, *Theory of Intense Laser-Matter Interaction*, Max-Planck-Institut für Kernphysik, Heidelberg (2006)
[28] W. L. Kruer et al., Phys. Fluids **28**, 430 (1985)
[29] S. C. Wilks et al., Phys. Rev. Lett. **69**, 1383 (1992)
[30] P.Antici et al., New J. Phys. **14**, 063023 (2012)
[31] F. N. Beg , Phys. Plasmas **4**, 447 (1997)
[32] M. G. Haines, Phys. Rev. Lett. **102**, 045008 (2009)
[33] F. Perez, Ph.D. thesis, École polytechnique, Palaiseau (2010)
[34] F. Brunel, Phys. Rev. Lett. **59**, 52 (1987)
[35] Y. Sentoku et al., Phys. Plasmas **10,** 2009 (2003)
[36] L. O. Silva et al. Phys. Rev. Lett. **92**, 015002 (2004)
[37] E. D'humière et al., Phys. Plasmas **12**, 062704 (2005)
[38] S. C. Wilks et al., Phys. Plasmas **8**, 242 (2001)
[39] P. Mora, Phys. Rev. Lett. **90**, 185002 (2003)

[40] NIST, electron stopping power database,
http://physics.nist.gov/PhysRefData/Star/Text/ESTAR.html
[41] M. Hegelich et al., Phys. Rev. Lett. **89**, 085002 (2002)
[42] S. Hatchett et al., Phys. Plasmas **7,** 2076 (2000)
[43] P. Mora, Phys. Rev. E **72**, 056401 (2005)
[44] C. Perego et al., Nucl. Instrum. Meth. Phys. Res. A **653**, 89 (2011)
[45] J. Fuchs et al., Phys. Plasmas **14**, 053105 (2007)
[46] A. Mancic, Ph.D. thesis, École Polytechnique, Palaiseau (2010)
[47] J. S. Green et al., Phys. Rev. Lett. **100**, 015003 (2008)
[48] A Debayle, et al., Phys. Rev. E **82** (2010)
[49] E. Bambrinck & M. Roth, laser part. Beams **24**, 163 (2006)
[50] S. Humphries, *Charged Particle Beams*, New York: John Wiley and Sons (1990)
[51] T. Grismayer & P. Mora, Phys. Plasmas **13**, 032103 (2006)
[52] P. McKenna et al., Phys. Rev. E **70**, 036405 (2004)
[53] T. Ceccotti et al., Phys. Rev. Lett. **99**, 185002 (2007)
[54] M. Allen et al., Phys. Rev. Lett. **93**, 265004 (2004)
[55] L. V. Keldysh, Sov. Phys. JETP **20**, 1307 (1965)
[56] M.V. Ammosov et al., Sov. Phys. JETP **64**, 1191 (1986)
[57] V. P. Krainov et B. Shokri, Sov. Phys. JETP **80**, 657 (1995)
[58] S. August et al, J. Opt. Soc. Am. B **8**, 858 (1991)
[59] M. Passoni et al., Phys. Rev. E **69**, 026411 (2004)
[60] D. R. Lide, *CRC Handbook of Chemistry and Physics, 84th Edition*. Boca Raton (FL): CRC Press. (2003)
[61] M. Zepf et al., Phys. Rev. Lett. **90**, 064801 (2003)
[62] B. M. Hegelich et al., Nature **439**, 431 (2006)
[63] X. Q. Yan et al., Phys. Rev. Lett. **100**, 135003 (2008)
[64] T. Esirkepov et al., Phys. Rev. Lett. **96**, 105001 (2006)
[65] A. Henig et al., Phys. Rev. Lett. **103**, 245003 (2009)
[66] S. Kar et al., Phys. Rev. Lett. **109**, 185006 (2012)
[67] A. P. L. Robinson *et al., New J. Phys.* **10,** 013021 (2008)
[68] C. Palmer et al., Phys. Rev. Lett. **106**, 014801(2011)
[69] J. Fuchs et al., Nature **2**, 48 (2006)
[70] L. Romagnagni et al., Phys. Rev. Lett. **95,** 195001 (2005)
[71] M. Borghesi et al., Phys. Plasmas **9**, 2214 (2002)
[72] U. Linz & J. Alonso, Phys. Rev. ST Accel. Beams **10**, 094801 (2007)
[73] K. W. D. Ledingham et al., Br. J. Radiol. **80**, 855 (2007)
[74] J. Weichselet al., Phys. Med. Biol. **53**, 4383 (2008)
[75] K. W. D. Ledingham et al., Science **300**, 1107 (2003)
[76] K. Nemoto et al., Appl. Phys. Lett. **78**, 595 (2001)
[77] T. E. Cowan et al., Phys. Rev. Lett. **92**, 204801 (2004)
[78] M. Roth et al., Phys. Rev. Lett. **86**, 436 (2001)
[79] S. A. Gaillard et al., Phys. Plasmas **18**, 056710 (2011)
[80] S. Kar et al., Phys. Rev. Lett. **106**, 225003 (2011)
[81] S. N. Chen et al., Phys. Rev. Lett. **108**, 055001 (2012)
[82] K. A. Flippo et al., Phys. Plasmas **15**, 5 (2008)
[83] P. Antici et al., Rev. Sci. Instrum. Meth. B **620**, 14 (2010)
[84] A. J. Mackinnon et al., Phys. Rev. Lett. **88**, 215006(2002)
[85] P. Antici et al., Phys. Rev. Lett. **101**, 105004 (2008)
[86] S. Buffechoux et al., Phys. Rev. Lett. **105**, 015005 (2010)

[87] J. Fuchs et al., Phys. Rev. Lett. **91**, 255002 (2003)
[88] T. Zh. Esirkepov et al., Phys. Rev. Lett. **89**, 175003 (2002)
[89] G. Mourou et al., Nature Photonics **7**, 258 (2013)
[90] M. Yamagiwa et al., Phys. Rev. E **60**, 5987 (1999)
[91] Y. Sentoku et al., Phys, Rev. E **62**, 7271 (2000)
[92] D. Harberger et al., Nature **8**, 95 (2012)
[93] L . Willingale et al., Phys. Rev. Lett. **96**, 245002 (2006)
[94] E. Lefebvre & G. Bonnaud, Phys. reV. E **55**, 1011 (1997)
[95] E. Esarey et al., IEEE Trans. Plasma Sci. **24**, 252 (1996)
[96] P. Agostini et al., Phys. Rev. Lett. **42**, 1127 (1968)
[97] S. Augst et al., Phys. Rev. Lett. 63, 2212 (1989)
[98] R. Fedosejevs et al., Phys. Rev. E **56**, 4615 (1997)
[99] G. Sun et al., Phys. Fluids **30**, 526 (1987)
[100] K. Krushelnik et al., Phys. Rev. Lett. **83**, 737 (1999)
[101] R. P. Drake et al., Phys. Fluids **17**, 778 (1974)
[102] A. Chiron et al., Phys. Plasmas **3**, 1373 (1996)
[103] A. B. Borisov et al., Plasma Phys. Controlled Fusion **37**, 569 (1995)
[104] E. Esarey & P. Sprangle, IEEE J. Quantum Electron **33**, 1879 (1997)
[105] J. Miyahara et al., Nucl. Instrum. Meth. Phys. Res. A **246**, 572 (1986)
[106] A Mancic et al., Rev. Sci. Instrum. **79,** 073301 (2008)
[107] K. Tanaka et al., Rev. Sci. Instrum. **76**, 013507 (2005);
[108] C. G. Freeman et al., Rev. Sci. Instrum. **78**, 013705 (2007)
[109] S. Agostinelli et al., Nucl. Instrum. Meth. Phys. Res. A 506, 250 (2003)
[110] T. Bonnet et al., Rev. Sci. Instrum. **84**, 013508 (2013)
[111] H.A. Lorentz, Ann. Phys. **9**, 641 (1880)
[112] L. Lorenz, Ann. Phys. **11**, 70 (1880)
[113] A. Shapiro, *The Dynamics and Thermodynamics of Compressible Fluid Flow*, New York: Ronald Press Co. (1953)
[114] G. S. Sarkisov et al., Phys. Rev. E **59**, 7042 (1999)
[115] Z. Najmundin et al., Phys. Plasmas **10**, 43 (2003)
[116] M. S. Wei et al., Phys. Rev. Lett. **93**, 155003 (2004)
[117] A. Yogo et al., Phys. Rev. E **77**, 016401 (2008)
[118] P. Antici et al., New J. phys. **11**, 023038 (2009)
[119] A. V. Kuznetsov Plasma Phys. Rep. **27**, 211 (2001)
[120] S. Bulanov, Plasma Phys. Reports, **31**, 369 (2005).
[121] S. Bulanov et al., Phys. Rev. Lett. **98**, 049503 (2007)
[122] L. Willingale et al. Phys. Rev. Lett. **98**, 049504 (2007)
[123] E. d'Humières & V. Tikhonchuk, AIP Conf. Proc. **1299**, 704 (2010)
[124] F. Fiuza et al., Phys. Rev. Lett. **109**, 215001 (2012)
[125] E. d'Humières et al., J. Phys.: Conf. Ser. **244**, 042023 (2010)
[126] K. Bockasten, J. Opt. Soc. Am. **51**, 943 (1961)
[127] F. Lindau et al., Phys. Rev. lett. **95**, 175002 (2005)
[128] R. Fabbro, Ph.D. thesis, Université Paris XI, Orsay (1982)
[129] J. Breil et al., J. Phys. Conference Series **112**, 022035 (2008)
[130] Y. Sentoku, A. J. Kemp, J. Comp. Phys. **15**, 056709 (2008)
[131] P Antici et al., New J. Phys. **11**, 023038 (2009)

IV. CHARGE EQUILIBRIUM OF LASER-GENERATED ION BEAMS IN WDM

While a great deal is known in cold and solid-density matter, the study of ion stopping power in warm dense matter is only beginning. Furthermore, although several theories and codes have been developed to predict it, the stopping power of ions in solid-density target in warm dense matter regime has never been measured experimentally.

In this chapter, we will present an experimental study and its results that can be considered as the core of this thesis. It gathers results from two experimental campaigns performed respectively using the LULI ELFIE and LLNL TITAN laser facilities.

The chapter is composed of two parts. The first one can be considered as an introduction to the problematic of experimental study of stopping power in warm dense matter. The current temperature-density conditions in which the stopping power could be measured with respect to the method used will be presented. Then, using the predictions provided by SCAALP calculations, an estimation of the temperature influence on observables directly linked to the stopping power will be shown. We conclude on the fact that, currently, we cannot reach with proton heating of solids, a temperature high enough to detect any visible variation of the stopping power.

As a consequence, our study will be focused on one of the most important parameter of the stopping power that is predicted to be more sensitive to our hydrodynamic conditions variations, the projectile equilibrium charge state distribution. This is the subject of the two experiments presented in the second part.

After reminding the existing theories on the equilibrium charge state distribution in both cold and warm dense matter, the experiments are presented. They follow the concept of pump-probe experiment. A solid sample is probed by an ion beam, while heated by an energetic proton beam. The charge distribution of the probe particles emerging from the heated matter is then recorded.

Since the only difference between the two experiments relies on the ion species used to probe the matter, carbon and helium, we adopt the same trend to describe the experiment and the results associated. The experimental set-up, diagnostics used are first described. Then, the experimental set-up is validated with respect to existing data measured in conventional accelerators. Last, the results we obtained when probing heated matter are presented and discussed. Note that the analysis of the results concerning the interaction between the helium probe ion beam and the heated matter is still ongoing, and thus they are not presented here.

IV.1 Experimental possibilities to measure the stopping power in WDM

IV.1.1 Review of cold stopping power experimental methods

Before studying experimentally the stopping power in WDM, it is interesting to understand the different methods that were applied in cold stopping experiments, the encountered problems, and their eventual solutions. They could be useful to design a platform able to study WDM stopping-power. Indeed, measuring precisely the stopping power of any particle is actually difficult in cold and solid-density or gaseous matter, and even more complex in hot and dense plasmas.

The problem of measuring or modeling the stopping power has been studied for over a century and still remains problematic in warm and hot dense matter [1]. Most of the work on gas and cold solid-density matter has been performed during the 50's using conventional accelerators facilities [2]. The measurement principle is quite simple using ion beams that are well-characterized in energy. It basically consists in sending an ion beam through a thin target at a given energy E_i, and then measuring the energy of the particles emerging from it at energy E_f. These direct measurements require thin enough target of thickness Δl to assume that,

$$-\frac{dE}{dl} \cong -\frac{\Delta E}{\Delta \mathrm{l}}, \tag{4.1}$$

where $\Delta E = E_f - E_i$.

For low energy measurements, targets rapidly become so thin that the relative error bar on Δl is too high to provide precise measurements of the stopping power. This experimental problem can be avoided by using a derivative approach. The stopping power is then determined from the slope of the smoothed experimental range-energy curve, *R(E),* or its mirror image, the plot of ΔE versus Δl for ions of a fixed initial energy (Figure IV-1):

$$l = R(E_0) - R(E), \tag{4.2}$$

so that,

$$\left(-\frac{dE}{dl}\right) = \left(\frac{dR}{dE}\right)^{-1}. \tag{4.3}$$

This curve is obtained by the same procedure as before. It consists in measuring the evolution of E_f while sending an ion beam of constant energy through targets with different thicknesses. Provided that the resulting curve changes smoothly (see Figure IV-1a), one can efficiently remove the inherent

noise relative to energy and thickness measurements. The stopping power at a given energy (see the red arrow in Figure IV-1b) is then deduced from its slope [2].

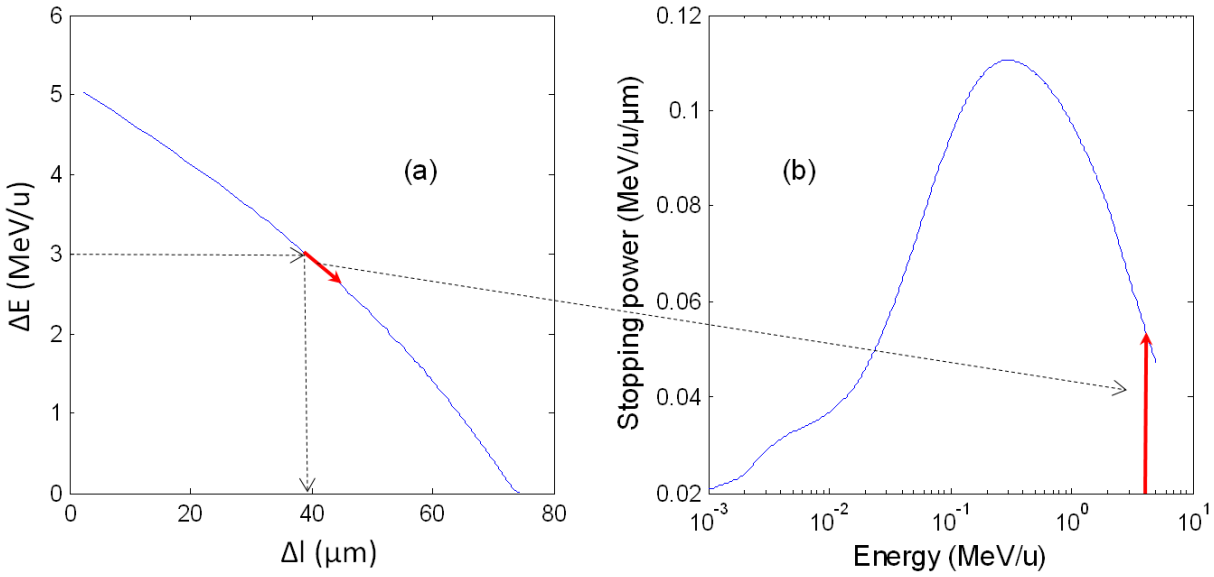

Figure IV-1 : The slope of the emerging projectile energy function ΔE related to the target thickness Δl (a) can be used to determine the projectile stopping power curve related to the same medium (b).

The last approach that has been used is even less direct. It is based on the Bethe-Bloch stopping power [3],

$$S(Q_1, Z_2, v_{10}) = \frac{4\pi\hbar^2}{m_e}\frac{{Q_1}^2 v_0^2}{{v_{10}}^2} Z_2 \left(L_0\left(Z_2, \frac{v_{10}}{c}\right) + Q_1 L_1\left(Z_2, \frac{v_{10}}{c}\right) + Q_1^2 L_2\left(Z_2, \frac{v_{10}}{c}\right) + \cdots\right), \quad (4.4)$$

where the notations are the ones of chapter II. The term in parenthesis is the stopping number L, where L_i are asymptotic developments in powers of Q_1. These correction terms, called respectively Barkas (i = 1) and Bloch (i = 2), can be estimated from stopping experimental data and their contribution to the stopping power is shown to decrease with the projectile velocity [3]: e.g. their contribution toward the stopping power of protons in aluminum is calculated below 10 % above 1 MeV protons and below 1 % above 10 MeV.

If one assumes the dependence of the stopping number on the particle charge to be negligible, i.e., one neglects the higher order in Q_1 of the Bethe-Bloch stopping number, we get:

$$\frac{S(Q_1', Z_2, v_{10})}{S(Q_1, Z_2, v_{10})} \cong \frac{(Q_1')^2}{(Q_1)^2} * \frac{L_0\left(Z_2, \frac{v_{10}}{c}\right)}{L_0\left(Z_2, \frac{v_{10}}{c}\right)} \cong \frac{(Q_1')^2}{(Q_1)^2}. \quad (4.5)$$

Once one knows the charge Q_1' of a particle traversing the matter at a given energy, its stopping power can be derived from benchmarked particle measurements such as protons or helium which

are usually used as a reference [4][15]. Indeed, they were the first energetic particles available in accelerators and their stopping power were also the first to be measured on a wide energy range. In addition since they are light particles, their penetration depth and range are the longest, making their stopping power easier to measure. Finally, the helium projectiles and even more the protons begin their neutralization only at very low velocities [3]. Also, on a wide energy range (e.g., above 1 MeV/u for helium ions [3]), these two ions are bare nucleus and their charge is equal to their atomic number.

IV.1.2 Experiments achievable on stopping power in WDM

Compared to the study of ion stopping power in cold matter, the study of ion stopping power in WDM is still in its infancy. Indeed, whereas cold measurements have been methodically performed for almost a century, no WDM set-up has ever been proved to be accurate and trustable enough so that it can be used to get at least a first measurement [5]. Following cold stopping experimental platform, the optimal set-up for WDM would consist in sending (1) a monoenergetic ion beam, which is well-characterized in energy, (2) through a homogeneous and well-characterized WDM, which conditions could be considered as fixed during the probing time. While the first part of the set-up does not change from cold stopping and is achieved on a wide energy range in conventional accelerator facilities, the second part raises an important issue.

In chapter I, we have observed that WDM created in the laboratory evolves very quickly due to thermal expansion. Particle accelerators produce well-controlled, monoenergetic ion beams on a very wide range of energy at a high repetition rate, but suffer from low flux and their duration is relatively long (1-100 ns). With respect to the duration of ion beams delivered by accelerators, only methods that can produce WDM during several nanoseconds could be used to perform measurements in WDM. Nevertheless, to the author's knowledge, there is currently only one laboratory that has the capability to couple ion accelerators and facilities in which methods to generate homogeneous WDM (see chapter I) can be used, the GSI Helmholtz center for heavy-ion research (Darmstadt). Besides a conventional accelerator, an energetic nanosecond laser beam (30 J in 7 ns at 532 nm) has recently been available there. So far, only one experiment has been conducted on stopping-power measurements [6]. In this experiment, the heating, and was performed by direct laser irradiation, which results in plasma temperatures of more than 100 eV, free electron densities smaller than 10^{21}

[15] The charge of the particle may be inferred from semi-empirical formulas. This method is related to the effective charge quantity mentioned in chapter II.

electrons/cm^3 (below 1 % of the electron density that can be found in solid-density aluminum), and strong spatial temperature and density gradients. Furthermore, experiments using Hohlraum heating hence producing tens of eV close to solid-density matter, are underway [7]. One may also report the experiments performed to measure the stopping power in coronal plasma [5 and references therein]. In these experiments, the ion beam produced by a conventional accelerator probes laser ablated plasma and dense linear plasma columns. In a dense linear plasma column, the density is typically 10^{17} cm^{-3} and temperature of a few eV. In this regime, the plasma is fully ionized and allowing free electron stopping power measurements to be performed (one should note its very long lifetime of typically 100 µs). Plasmas produced by laser ablation exhibit temperature from 1 to 150 eV and density from 10^{17} to 10^{19} cm^{-3}. The lifetime is then reduced to tens of ns. This method allows to measure stopping power in partially ionized coronal plasma.

The other way to produce collimated ion beams is to use a high-intensity short-pulse laser (see chapter II). Contrary to conventional accelerator facilities, high intensity short pulse laser source combined with energetic short- or long-pulse laser beams are more frequent. In addition, recently short-pulse lasers combined with conventional accelerators (GSI) or XFEL beam (SLAC) have been developed. As mentioned in chapter I and II, short-pulse laser interactions produce energetic ion bunches of picoseconds duration. Therefore the warm-dense heating methods mentioned in chapter I could normally be used to perform stopping power measurements. However, up to now, it has never been realized. Indeed ion beams generated by laser suffer low repetition rates and lack of reproducibility. As a consequence, to perform any stopping power measurements, (1) one needs to find a way to measure simultaneously both input and emerging ion beam energy. This is what has been designed in the course of the present work, (see chapter III). Furthermore laser-generated ion beams exhibit a broadband spectrum from very low to relatively modest energies (maximum of approximately 65 MeV). Hence, even if it is not absolutely needed[16], (2) a method to shrink the spectrum will greatly increase the precision of any measurement.

It is worthwhile to mention the important issue concerning WDM characterization (temperature, density), which remains problematic, whatever the method used to produce it [8].

[16] The measurement could only consist in measuring the variation of the maximum energy exhibited by the input and the emerging ion beam.

IV.1.3 Impact of the temperature on stopping power measurements

Now that we know in which thermodynamical conditions the stopping power could be determined with respect to the experimental method used, let us concentrate on the temperature influence on observables that can be measured in an experiment. In the following study, we use the stopping power obtained in chapter II from *ab initio* calculations. We first focus on the projectile range when the temperature increases. This value is interesting from an experimental point of view, since it gives a macroscopic value which could be directly measured in an experiment. For instance, a lengthening of the projectile range with temperature could be noticed using particles stopped in cold matter but passing through hot matter of same density and thickness. The last paragraph concerns the effect of the temperature on the energy deposition of an ion beam. This matter is treated using both the stopping power obtained via SCAALP and a hydro code, ESTHER.

IV.1.3.1 Projectile Range

The CSDA projectile range is directly derived from the stopping power. Therefore, any change in the stopping power has an impact on it. A way to demonstrate and test stopping power calculations in WDM would be to measure the evolution of the range of a projectile of a given velocity with temperature.

In Figure IV-2, the influence of temperature on the Bragg curve for, respectively, 0.5 and 10 MeV proton is illustrated. First, one can see that, in both cases, the energy deposition (or stopping power per target mass unit) loses its characteristic Bragg peak with increasing temperature. This could be expected since the maximum proton stopping power decreases with the temperature (see chapter II). The Bragg peak feature then disappeared completely when the proton energy is located below the energy which corresponds to the stopping peak (e.g. 0.5 MeV protons at 100 eV). Regarding the projectile range, one can specially display two tendencies. While the range of low-energy protons increases with temperature, at the opposite, the high-energy proton-range starts to decrease with temperature. The first point is easily explainable. Indeed the stopping power decreases in the low velocity regimes (see chapter II), hence the protons lose less energy and penetrate deeper in the material. The second observation is less evident, since it combines two effects (see chapter II):

- the decrease of the stopping power in the low velocity regime,
- the slight increase of the stopping power in the high velocity regime.

Actually, the stopping power in the low-velocity regime only affects the energy deposition at the end of the range of the particle (when its velocity is low) and its influence remains localized to the sur-

rounding of the Bragg peak. Thus, for high-velocity projectile, the decrease of the stopping has a negligible effect on the penetration length compared to the increase of the stopping in the high-velocity regime. This is what can be seen Figure IV-2b: on one hand, the decrease of the stopping power in the low-velocity regime causes the Bragg peak feature to soften when the temperature increases. On the other hand, the increase of the stopping in the high velocity regime causes the penetration length of the projectile to decrease when the temperature increases.

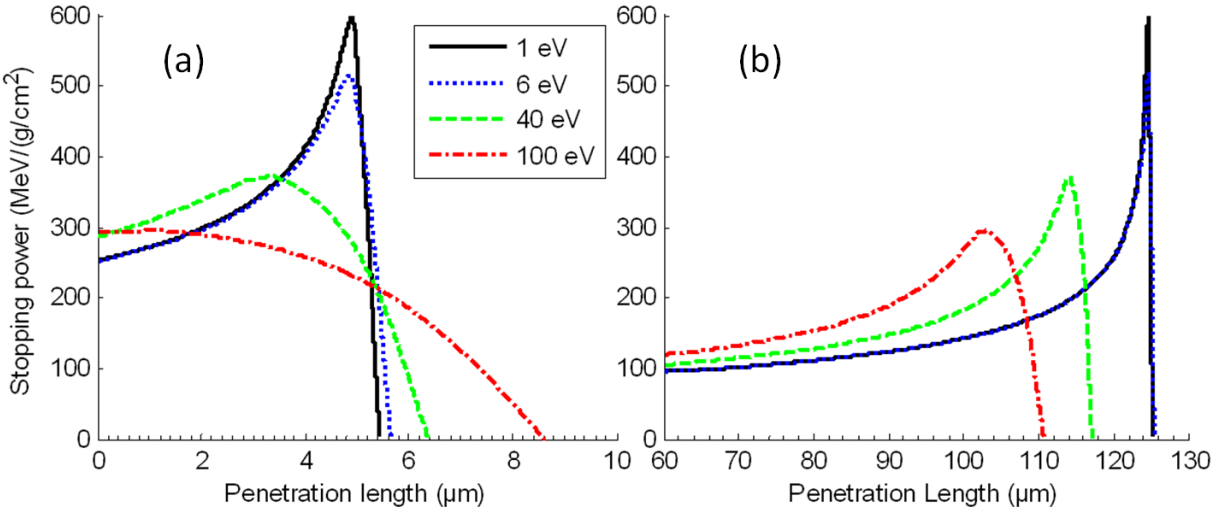

Figure IV-2: Energy deposition of (a) 0.5 MeV and (b) 4 MeV protons in solid density aluminium for various temperatures (1, 6, 40, and 100 eV).

In order to test experimentally these predictions, it should be noted that temperatures of at least 40 eV are needed, so that the range shortening/lengthening becomes significant (20 % for 0.5 MeV protons and 8 % for 4 MeV protons).

Let us now look at the influence of the temperature on the carbon range. In Figure IV-3b is plotted the carbon range in a solid-density aluminum as a function of the temperature. In order to highlight the effect of the effective charge, the proton range is plotted in Figure IV-3a. For temperature higher than 100 eV, one finds again the proton behavior: at these high temperatures, the effect of temperature on the effective charge is weak. The principal difference between proton and carbon appears at temperature lower than 100 eV. One can see that contrary to protons, the carbon range for temperature from 10 to 100 eV is shortening when the temperature increases. This is consistent with the increase of the stopping power induced by the increase of the effective charge in this temperature domain as observed in chapter II. From 1 to 10 eV, the stopping power remains constant, then rises until 100 eV and finally decreases above.

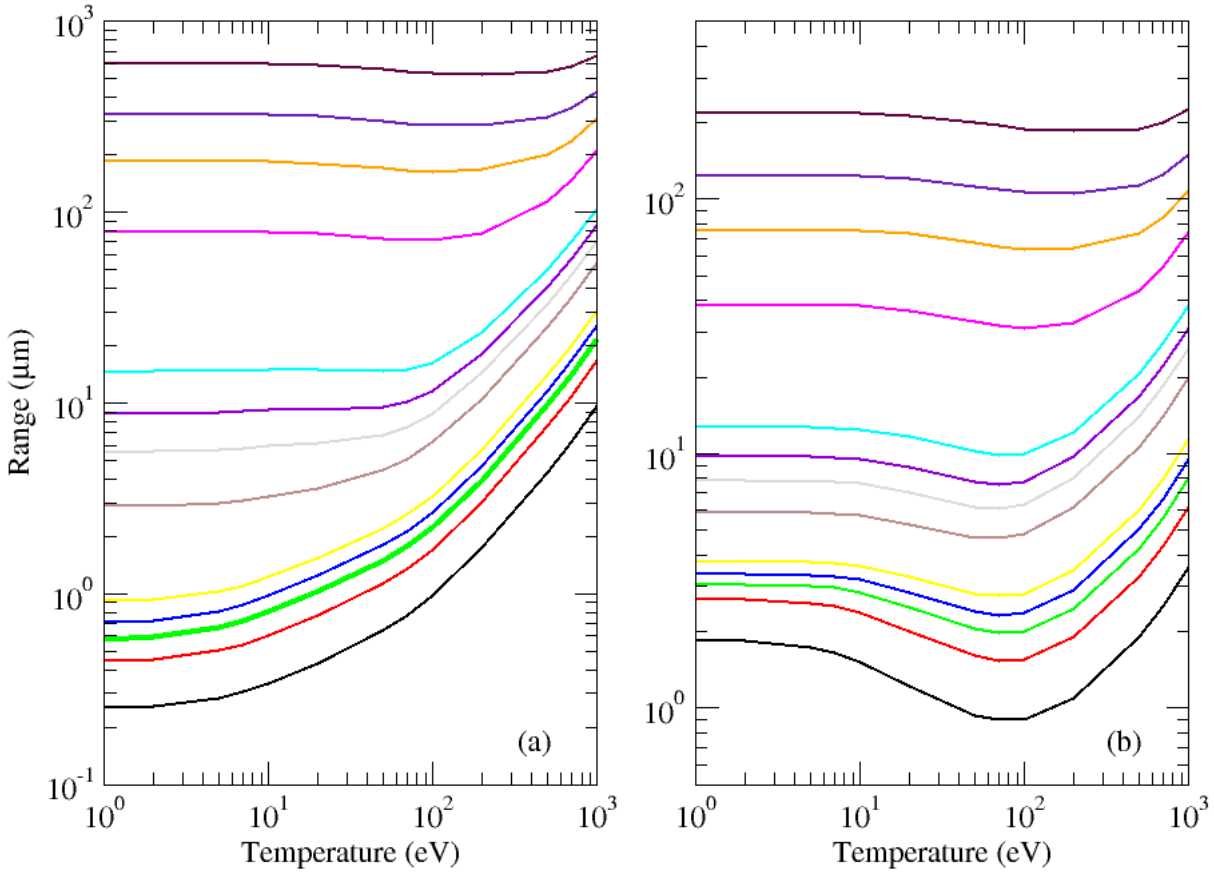

Figure IV-3: (a) Proton and (b) carbon range in solid density aluminum as a function of temperature for various projectile energies (from down to top 0.01, 0.03, 0.05, 0.07, 0.1, 0.3, 0.5, 0.7, 1, 3, 5, 7 and 10 MeV/u).

It should be noted that we discuss here of the CSDA range and that we have only access in experiment to the projected range. Therefore to compare our results with experimental results, one needs to estimate how the projectile range can be affected by straggling. In cold material, the CSDA range is close to the projected range for lower atomic number materials and projectile [9]. The difference increases for low energy particles, where the effect of straggling is more important. For instance, in solid density aluminum, the projected range shows value lower up to 15 % relatively to the CSDA ranges for energy from 0.01 MeV to 100 MeV [9]. This difference is found to be below 2 % for energies higher than 1 MeV.

IV.1.3.2 Projectile energy loss

Another way to measure experimentally the effect of temperature on stopping power is to measure the energy loss by a projectile emerging from a target of a given thickness. The stopping power is then integrated over the thickness of the sample. This observable can be considered as an extension of the previous one. As an illustration, we plot in Figure IV-4 the proton energy output after passing through a 20 eV solid aluminum sample of various thicknesses as a function of the energy input. This

target conditions corresponds to the best achievable regarding the proton heating experiments. The results are compared to the cold case using SRIM stopping power database [10]. One can clearly see that the difference between cold and heated foil is not important. Indeed, in order to see any influence of the temperature, one needs to use very thin foil (1 µm) and to look at proton energies below 50 keV. Measuring such low energy particle is very difficult and may be very sensitive to any noise. In addition, the difference predicted may be covered by uncertainties due to the projectile straggling, the error bar on the energy input, the temperature of the sample, its density …

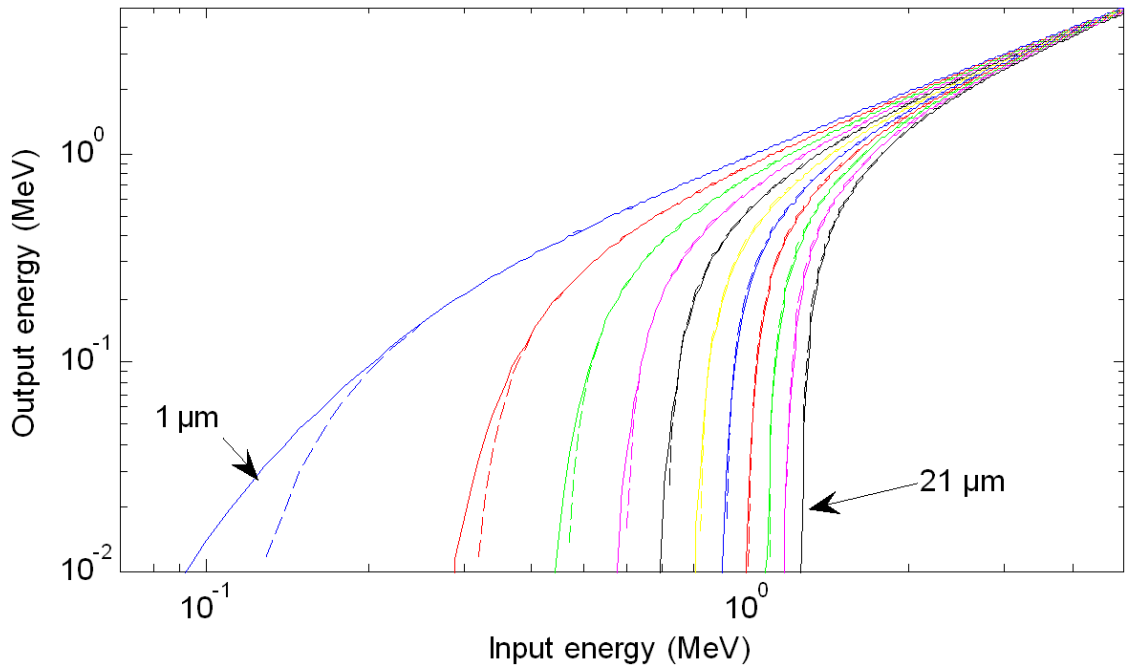

Figure IV-4: Energy of a proton emerging from, respectively, a 300 K (dotted lines) and 20 eV (plain lines) solid density aluminum foil of various thickness (1, 3, 5, 7, 9, 11, 13 15, 17, 19, and 21 µm) as a function of its initial energy.

One finds similar results for carbon as well [11].

To conclude, the energy loss by a projectile in a definite thickness hot sample does not differ significantly from the one in cold material for temperatures below 20 eV. Therefore to detect any effect of the temperature, one would need very sensitive energy diagnostics or either to heat the matter to much greater temperature such as temperatures where the peak of the stopping power is maximum (e.g., 100 eV for aluminum [11]). Note that this temperature, even if the matter was not in equilibrium, has been achieved using XFEL to heat the solid-density aluminum sample [12].

IV.1.3.3 Ion heating

The last effect we would like to investigate is the influence of temperature on energy deposition by ions in matter they propagate through. This is particularly interesting within the framework of the fast ignition scheme of ICF in which the ignition is initiated by an ion beam. Here, we focus on the heating of a solid-density target by a laser- generated ion beam. Due to different time of flight (TOF), protons of different energies but generated simultaneously do not experience the same matter condition as the matter is progressively heated by the preceding ions. Thus, while the higher energy part of the spectrum deposits its energy in cold matter, the lower part propagates inside a matter already heated. Their energy deposition, and so, the thermodynamic quantities (density, temperature) of the target they go through may then be affected by the increase of the target temperature.

In order to have access to the sample conditions during the heating process, we use a 1D hydrodynamic code ESTHER [13] (EffetS Thermo-méchaniques et Hydrodynamiques Engendrés par un Rayonnement), developed at CEA by P. Combis. With this code, we are able to perform simulations of heating and expansion of a thin aluminium foil irradiated by a laminar high-energy proton source. We follow the well-assessed procedure given in Ref. [8].

The code ESTHER solves, according to a Lagrangian scheme, the fluid equations for the conservation of mass, momentum and energy. The target material is described by the Bushman-Lomonosov-Fortov [14, 15] (BLF) multiphase EOS. This tabulated multiphase EOS for metals allows associating, for any couple of parameters like temperature (T), density (ρ), pressure (P), and internal energy, the other two parameters. The tables P(T, ρ), E(T, ρ) are generated in the code and they describe in a very precise sampling manner the phase transitions of the material, taking into account the fusion point as well [13].

In the ESTHER code, energy can be deposited in the target in different ways: via X-rays, optical laser field or ion beams. Here, we use a typical proton beam generated via short-pulse laser-interaction as an input parameter in the simulation. The proton energy deposition is taken into account using the SRIM [10] database or, recently, proton stopping-power generated via SCAALP simulation.

In order to illustrate the influence of the stopping-power on proton heating-process, we perform here simulations for the same set of parameters (same input proton spectrum, same target), but using either SRIM or SCAALP stopping power.

Here, we simulate the heating process of a 5 µm thick solid-density aluminum planar-foil heated by a laminar proton-beam generated 200 µm away from the heated foil. The simulation takes into ac-

count the TOF of the protons from the source to the target. The heated target is divided in 300 cells with the cell-size increasing in a geometric progression manner from the edges of the target toward its centre. In this way, we obtain a higher resolution of the target parameters at the edges, which is useful to describe well the target expansion process. The duration of the simulation is 100 ps with the information provided at 0.5 ps interval. We assume that the electron temperature, T_e, is always equal to the ion temperature, T_i ($T_e = T_i = T$). Physically, the electrons should first be heated by the proton beam and then only transfer their energy to the target ions. It has been shown that, with our method of heating, the target is not heated instantaneously from 0 to the maximum temperature but relatively "slowly" compared to the characteristic time of energy transfer from the electrons to the target ions (e.g. for an electrons temperature of 10 eV, the time required for equilibration in aluminum is below 0.3 ps [16]) [8]. As a result, assuming $T_e = T_i$ does not strongly affect the resulting temperature and density profile temporal evolution.

In Figure IV-5, we plot the target mass density and temperature profiles as a function of space and for different times using as an input beam a typical proton beam that has been experimentally obtained on the LULI 100 TW laser (see Figure I-14). In the graphics, the proton source is located at x= +200 µm and protons are propagating from the right to the left. Time 0 corresponds to the arrival of the protons of the highest energy in the target.

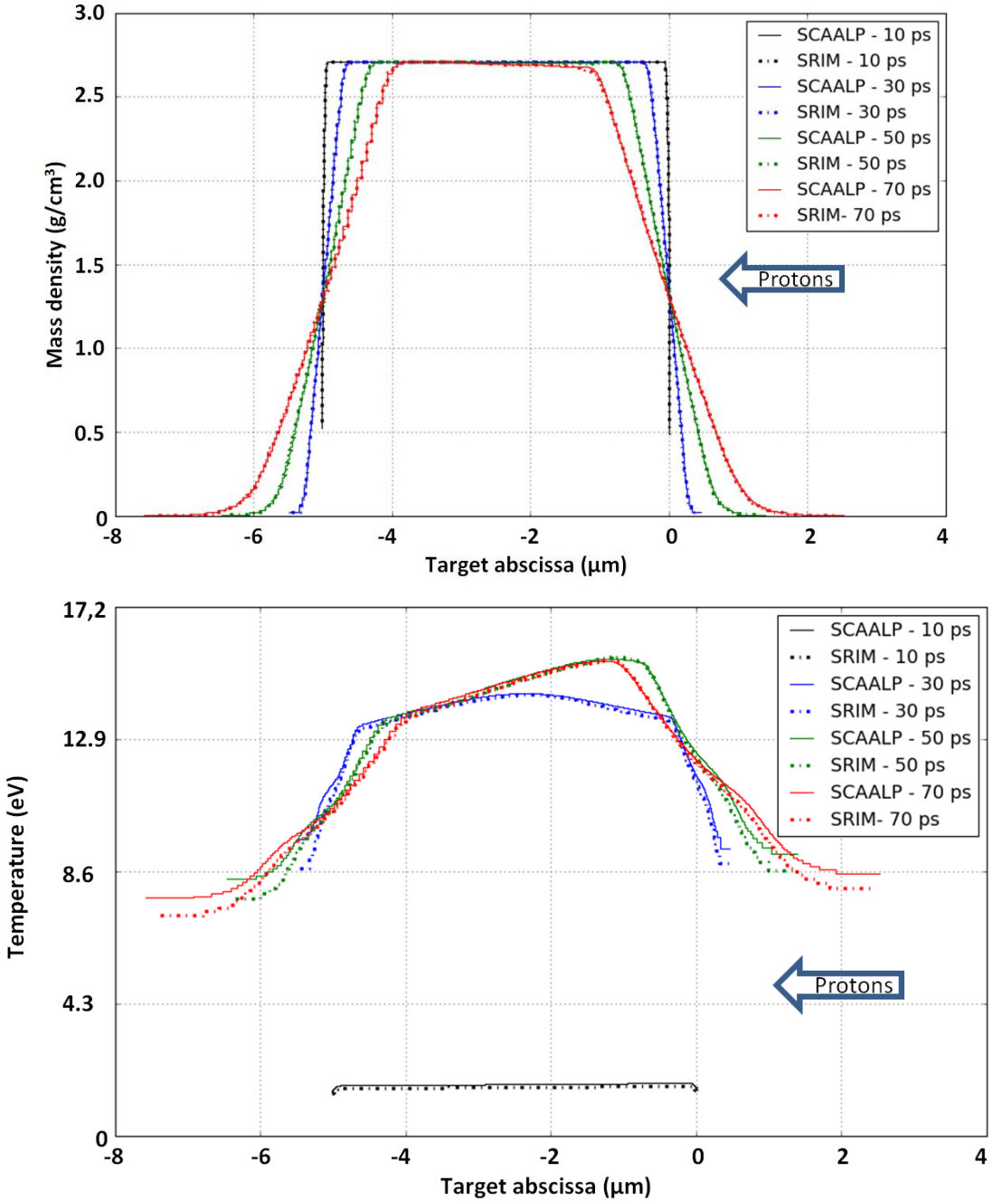

Figure IV-5: Temporal evolution of the mass density and temperature of a 5 µm target heated by a proton beam (which has been measured on the LULI 100 TW laser, see Figure I-14 using SRIM (dotted lines) and SCAALP (plain lines) stopping power.

The target temperature rises until 50 ps reaching its maximum at 15 eV. One can see that the temperature inside the target is not uniform. This is actually due to the more important proportion of low energy protons in the beam spectrum.

When passing from SRIM to SCAALP stopping power, one observes almost no changes in the mass density or the temperature profile apart from the temperature of the expanded and low density plasma at the target edges. This may be caused by the relatively low temperature (15 eV) reached

inside the target. Indeed we have seen that the stopping-power in WDM starts to significantly differ from cold above 40 eV. However, on the more powerful laser facilities, we can expect to reach higher temperatures (e.g. in Ref. [17], 81 eV was reached). In order to investigate such cases, the same simulation is run, but now using a proton beam 10 times more energetic than the one used before. In fact, we simply multiply by 10 the number of protons of the beam. The results are presented in Figure IV-6.

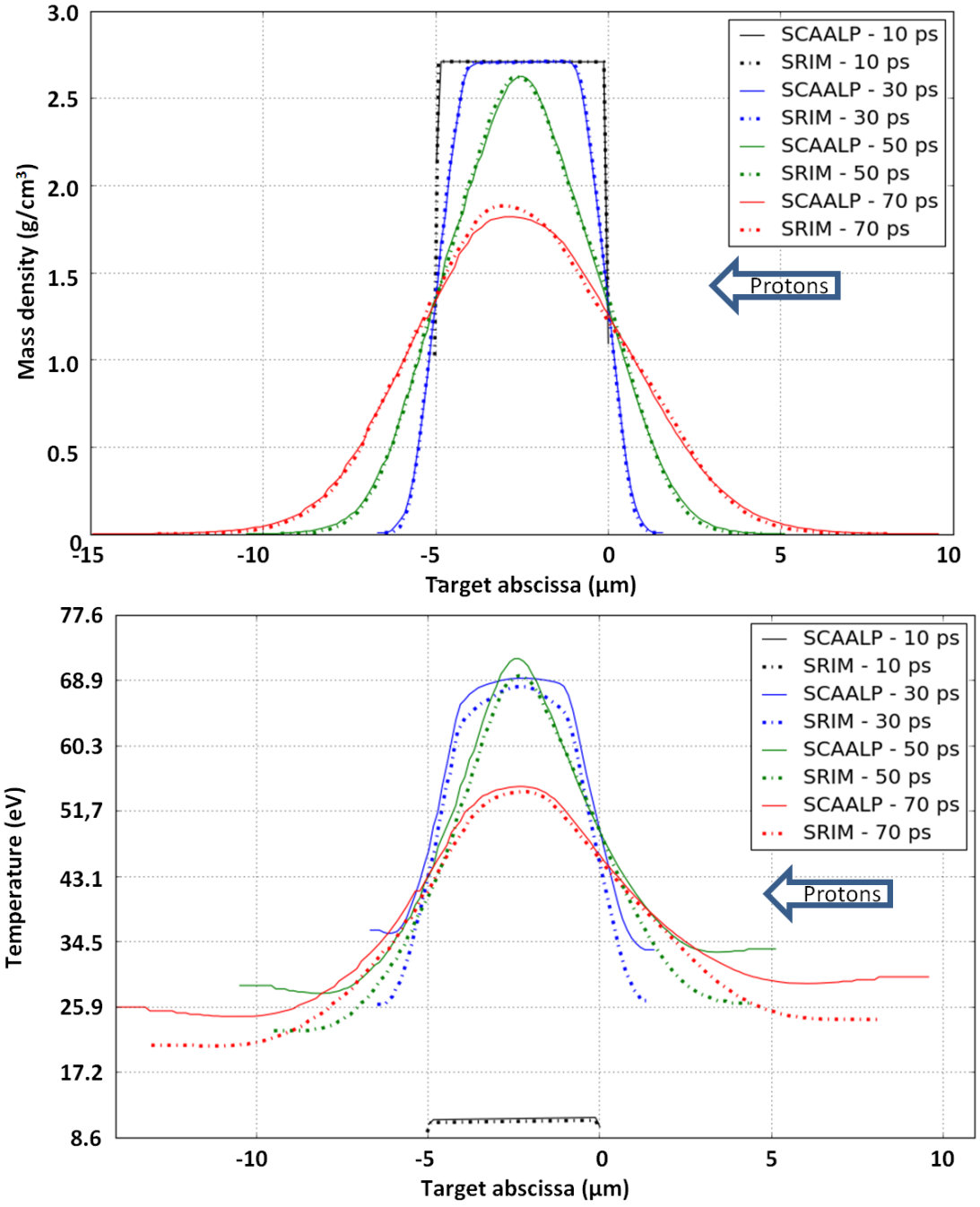

Figure IV-6: Temporal evolution of the mass density and temperature of a 5 µm target heated by a hypothetical proton beam (10 times more energetic than used for the previous figure) using SRIM (dotted lines) and SCAALP (plain lines) stopping power.

This time, the target is heated up to 72 eV. As a consequence, the target expands more quickly and the foil density tends to decrease before the end of the heating process (50 ps). Whereas the density profile remains identical in both simulations (SCAALP and SRIM), one can see that the target reaches slightly higher temperature when using SCAALP stopping-power: the temperature difference remains very small (< 5%) between the two simulations. In addition, one observes that especially at 30 ps, the temperature obtained using hot stopping power is distributed more uniformly inside the dense part of the sample. This is consistent with the observation on the energy deposition curve presented earlier (see Figure IV-2). Indeed the Bragg peak is smoothed with temperature, making the proton heating more uniform.

As a conclusion, we have seen that changing from cold to hot stopping power weakly affects the ion-beam energy-deposition process in WDM. This is, for instance, much smaller than the differences that could be induced by the use of two different EOS as shown in Ref [8]. In addition, in the frame of WDM generation, we observed that, due to the decrease of the Bragg peak sharpness with the temperature, the target heating gains in uniformity with temperature when taking.

IV.1.4 Conclusion

We have seen that, in order to detect any influence of temperature on the stopping power in solid-density aluminum, we need to reach temperatures at least higher than 40 eV, or to develop better resolved and less sensitive to noise detectors (see section IV.1.3). However, with respect to our experimental techniques exposed in section IV.1.2, this is not currently achievable.

Therefore we have decided to concentrate our study on another important parameter of the stopping power, i.e., the projectile charge distribution inside solid-density matter [18]. Indeed, this quantity is predicted to be more sensitive to temperature and is easier to measure experimentally as shown further.

IV.2 Equilibrium projectile charge distribution

As explained in chapter II, for a complete theoretical description of the energy loss of charged particles passing through matter, one is confronted with a large spectrum of physical processes. Once the target is specified, one has to deal with the aspects of the projectile-target interaction. The two main topics are [18]:

- the determination of the stopping number, i.e., how the charged particles lose their energies in the host medium,
- the determination of the charge of the projectile inside the matter, i.e., what are the changes in the electronic configuration of the projectile ion by the various processes of ionization, electron capture and excitation when interacting with the host medium.

In this chapter, we will not deal with the stopping number, for which many studies and theories have been and are still devoted for cold [9] and hot media (e.g. in Ref. [19]), but concentrate rather on the more experimentally accessible projectile charge.

IV.2.1 Definition

Ions penetrating through matter may undergo charge exchange. Their charge is fluctuating as their electrons are captured or lost in the succession of collisions with atoms of the material. As a result, a penetrating ion beam will in general exhibit a distribution of ion charges, which depend on the path length inside matter. Provided that the ion slowing down is negligible during the time of equilibrium, which is the necessary time for the projectile to reach its equilibrium charge, keeping its velocity constant, electron capture and loss processes become balanced and an equilibrium charge state distribution is established [20]. For instance, a 0.6 MeV/u carbon beam reaches equilibrium after approximately 0.1 ps with an energy loss of around 8.3×10^{-3} MeV/u (1.4 % with respect to the initial energy).This distribution depends only on the projectile species and velocity and on the medium in which it propagates [10].

We define the mean (or average) charge of a projectile at a given velocity, $\langle Q_1 \rangle(v)$ as the average charge over all the ions of the same species of a beam at the given velocity, i.e., "*the statistical net charge of the partially neutralized ion"* [3]:

$$\langle Q_1 \rangle(v) = \frac{1}{N_i(v)} \left(\sum_{i=1}^{N_i(v)} Q_{1,i} \right) = \sum_{Q_1=Q_{min}}^{Z_1} f_{Q_1}(v) Q_1 \,, \tag{4.6}$$

where $N_i(v)$ is the total number of ions propagating at a given velocity v, $Q_{1,i}$ the instantaneous charge of the i[th] ion, f_{Q_1} the charge fraction of ions of charge Q_1 and Q_{min} the recorded minimum ion charge. Figure IV-7 shows the average charge state of a 0.6 MeV/u monoenergetic carbon ion beam propagating through solid-density aluminum as a function of the penetration length. One can see that after the particle has reached a critical thickness (around 10 µg/cm²), the charge remains constant: the projectile charge state has attained equilibrium. We call this value the equilibrium mean charge, $\langle Q_1 \rangle_{eq}$. Equilibrium charge state distributions (and thus $\langle Q_1 \rangle_{eq}$) are independent of the ion charge state incident on the target. If the target thickness is further increased, the measured charge fraction will remain the same provided the total energy loss is negligible [21].

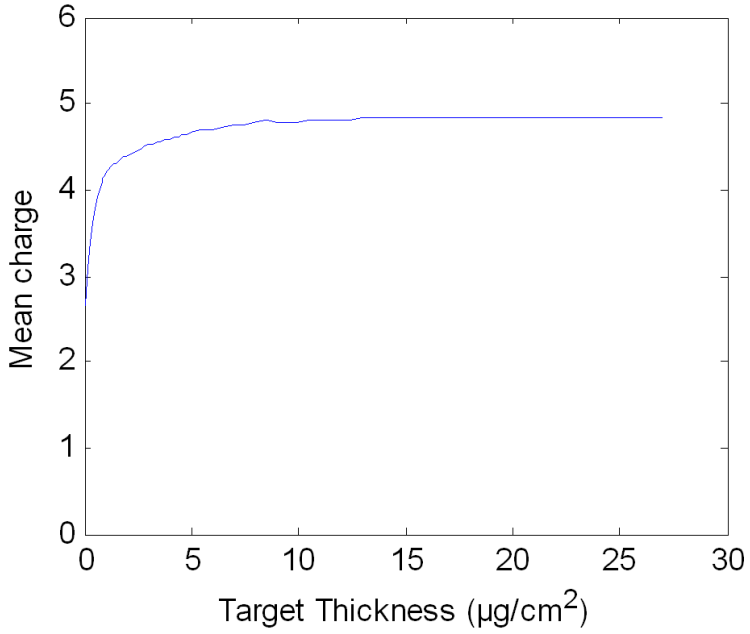

Figure IV-7: Illustration of a carbon ion going through a solid-density aluminum sample and approaching the equilibrium mean charge state $\langle Q_1 \rangle_{eq}$. The average charge state of the carbon ion beam as a function of target thickness is obtained from ETACHA calculations [22].

IV.2.2 How can this be integrated to stopping power calculation?

Assuming the energy-loss by charge exchange to be negligible, the stopping power of an ion beam under charge-equilibrium, i.e., called equilibrium stopping in Ref. [9], is equal to the sum of the energy loss for each ion of frozen-charge Q_1 weighted by the proportion of such charge in the ion charge distribution at equilibrium, $f_{Q_1,eq}$ [9]:

$$-\frac{\mathrm{d}E}{\mathrm{d}l} = \sum_{Q_1=Q_{min}}^{Z_1} f_{Q_1,eq}(v)\left(-\frac{\mathrm{d}E}{\mathrm{d}l}(Q_1,v)\right). \qquad (4.7)$$

Note that, provided that the stopping number is independent of the ion charge, we would obtain using the expression of the stopping power in chapter II,

$$-\frac{\mathrm{d}E}{\mathrm{d}l} = Q_{rms,eq}(v)^2 . \frac{4\pi\hbar^2}{m_e} \cdot \frac{{v_0}^2}{v^2} \cdot n_i \cdot L_{atom} \,, \tag{4.8}$$

where $Q_{rms,eq}(v)$ is,

$$Q_{rms,eq}(v) = \sqrt{\sum_{Q_1=Q_{min}}^{Z_1} f_{Q_1,eq}(v) * {Q_1}^2} . \tag{4.9}$$

However, Sigmund shows in Ref. [4] that, in cold solid-density foils, the correction factors in Eq. (4.4) cannot be neglected for the projectile studied in our experiment, He and C, in the energy range we cover. This fact is emphasized as well in another study conducted by Lifschitz and Arista [23] using a different approach based on a nonperturbative calculation of the stopping power. Furthermore, experimental measurements of the stopping power in a free ionized plasma [24] have shown that the stopping number and the charge distribution of a particle are strongly correlated and cannot be treated separately [25].

Therefore, we cannot *a priori* assume a strict Q_1^2-dependence of the stopping power and use Eq (1.13) to relate the projectile charge distribution to the stopping power. Nevertheless, the projectile charge distribution provides information on the different rates of the elementary processes which are essential to calculate the stopping power [23, 24, 23]. Indeed, in order to calculate theoretically the equilibrium stopping power of an ion beam in a plasma target, one needs to take into account simultaneously the cross-sections of all the elementary processes that affect the target electrons [24], these cross sections depending in particular on $\langle Q_1 \rangle_{eq}$.

This question is discussed later with respect to our experimental results in section IV.2.4.6.3.

IV.2.3 Theories and experimental difficulties

IV.2.3.1 In cold media

Significant amounts of experimental data exist on equilibrium mean charge state and on charge exchange cross-sections of various projectile elements and target materials [26]. It is well-defined and readily measurable as long as the target material is a gas, while the matter is more delicate for a solid-density material [23, 27]. Indeed charge states of ions penetrating solids are typically measured after emergence and most often ions are allowed to travel over macroscopic distances before detection occurs. The question of whether such measurements could be used to determine the equilibrium charge of ions moving inside a solid was the subject of intense discussions [9]. It has been particularly studied when equilibrium mean charge state of heavy particles was determined to be higher

when emerging from solid-density foils than their equivalent in gas, i.e., a target of the same reduced thickness (in µg/cm²) and of the same species. This phenomenon has been explained as a density effect by Bohr and Lindhard [28]. Indeed in a gas, the free-flight path between two collisions is much longer than within a solid, therefore the projectile electrons have time to decay into their ground states, while they may stay excited in a solid-density medium. Nowadays, increasing evidence appears to support this explanation [29]. Another issue regarding these measurements is the possibility of electron loss by Auger emission during the particle travel from the target to the detector [30]. This would imply that the equilibrium mean charge state during crossing in the material is lower than what is actually measured. One may add to that the problem of possible change in the charge state distribution due to collisions with residual gas if the vacuum inside the target chamber is not perfect.

Equilibrium mean charge state for heavy ions has been intensely studied and results for gas and solids have been gathered in tables [26 and references therein]. The experimental data for carbon ion emerging from a carbon foil [31] are shown in Figure IV-8 with two semi-empirical model curves.

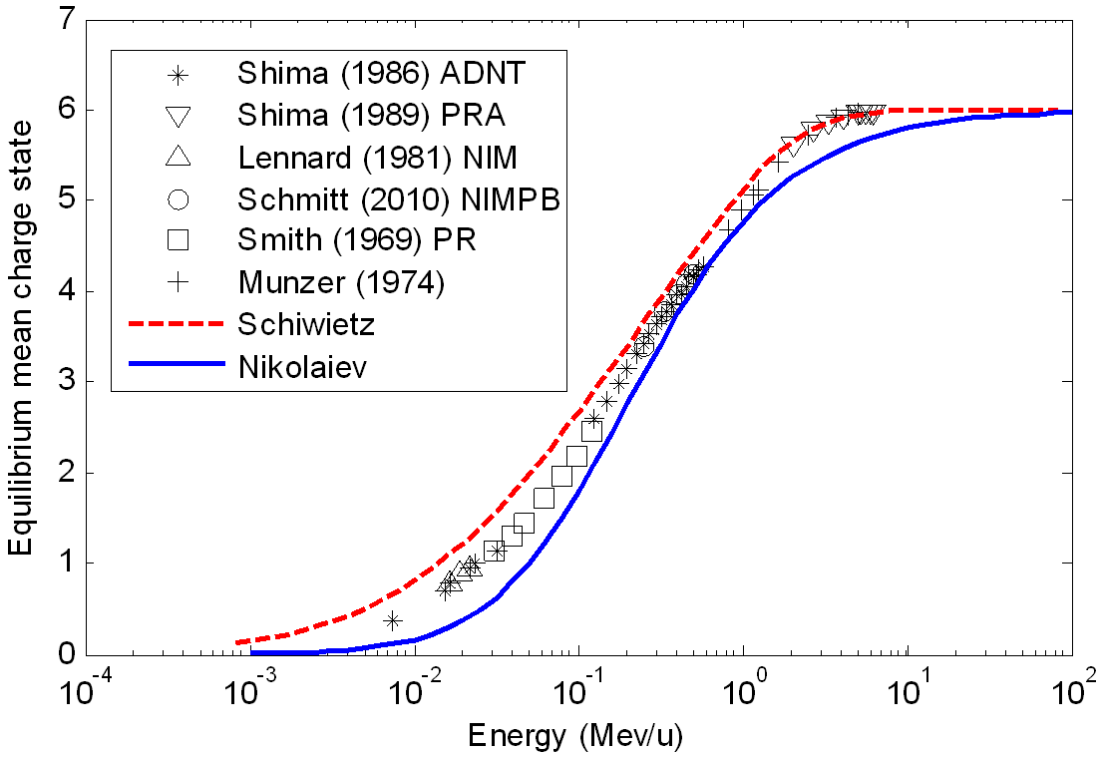

Figure IV-8: Equilibrium mean charge state of an equilibrated carbon beam emerging from a solid-density carbon foil as a function of energy. The dotted points come from experimental measurements performed on conventional accelerators; the lines are two semi-empirical curves based on Ref. [32, 33].

As for the stopping power, the equilibrium mean charge can be divided into three regimes. At very low energy (below 1 keV), the projectile is neutralized and is therefore highly-screened. This significantly reduces its energy loss per collision in the media. At the opposite, a high speed projectile

(above 10 MeV/u) is fully ionized and sees its losses per collision increasing (but the number of collisions is falling down with the speed) [9]. Between these two regimes, the charge of the projectile increases continuously with the energy. The shape of the equilibrium mean charge state is similar for other particles with different energy limits [9].

To estimate roughly the energy below which a bare projectile starts to capture electrons, one can follow the approach given by Bohr [34, 35]. Basically, an electron of an atom/ion is moving at a given velocity relative to its orbits. If the atom/ion has a velocity higher than that of the electron, the electron would not be able to follow the nucleus. Therefore, one can consider that a projectile starts to capture electrons and keep them, when its velocity become close or lower to the velocity that would exhibit one of its own electron. This approach has then been improved by using the Thomas-Fermi velocity as the projectile velocity above which the projectile is expected to be stripped of the majority of its electrons. This formalism has become the basis for most of the semi-empirical formulas that currently exist [10, 32, 33]. They are generally function of the scaling variable $\frac{v_{10}}{{Z_1}^{\alpha}\, v_B}$, where α is a constant that depends on the fitted experimental data used by the author. Most of them are compiled and described in Ref. [36].

Although the equilibrium mean charge state strongly depends on the projectile atomic number Z_1, and its velocity, experimental measurements have shown that it is varying very little with the target media that is penetrated [33]. Schiwietz et al. have recently gathered most of the experimental data points and summarized them in a semi-empirical formula using a target dependent scaling[17] (see Figure IV-9) [33]. To give a basic idea of the scaling used: in the case of a carbon projectile propagating in solid-density aluminum, 0.01 - 10 MeV/u in energy corresponds to 0.09 - 3 in the velocity parameter (x unit).

[17] The parameters in the scaling (Z_1, Z_2, v_{10}) are highlighted:

$$x = \left(\left(1 - 0.26e^{-\frac{1}{11}Z_2 - \frac{1}{9}(Z_2 - Z_1)^2}\right)\left(\frac{v_{10}}{v_B}{Z_1}^{-0.543}\right) \Big/ 1.54\left(1 + 0.03\left(\frac{v_{10}}{v_B}{Z_1}^{-0.543}\right)\ln(Z_2)\right) \right)^{1+\frac{1.83}{Z_1}}.$$

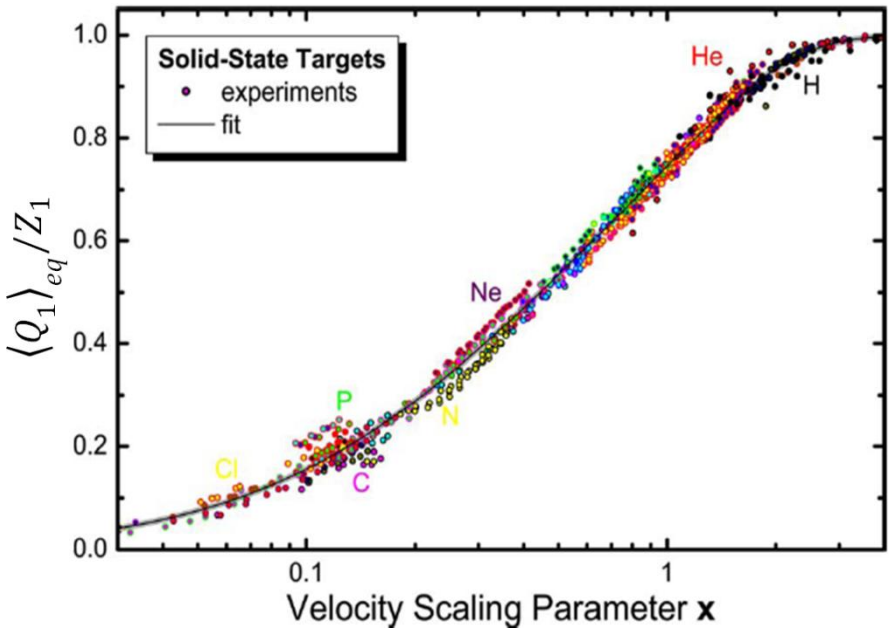

Figure IV-9: Measured equilibrium mean charge state $\langle Q_1 \rangle_{eq}$, divided by the corresponding projectile-atomic number Z_1 for various projectile species and various solid-density targets as a function of the scaling variable x; the continuous curve represents the semi-empirical formula developed by Schiwietz et al. [33]. The figure is extracted from Ref. [38].

Figure IV-10 represents the mean charge curves of a carbon beam passing through different solid media using semi-empirical formula developed by Schiwietz et al. [33]. We observe that, according to Schiwietz et al. estimation, equilibrium mean charge of a carbon beam varies very little in the different media from helium to gold. Figure IV-11 gives another view of such variation. Here, the difference of $\langle Q_1 \rangle_{eq}$ between the different media as a percentage of $\langle Q_1 \rangle_{eq}$ in aluminum is plotted. The substantial differences up to 15 % observed at low energy are mainly due to $\langle Q_1 \rangle_{eq}$ falling to 0. In addition, only a few data exist at very low energy, and all have significant error bars. Therefore the curve cannot really be trusted at such low energies. Nevertheless, for moderate energies (0.1 – 10 MeV/u) a precision better than 5 % is needed to detect any difference between the different media.

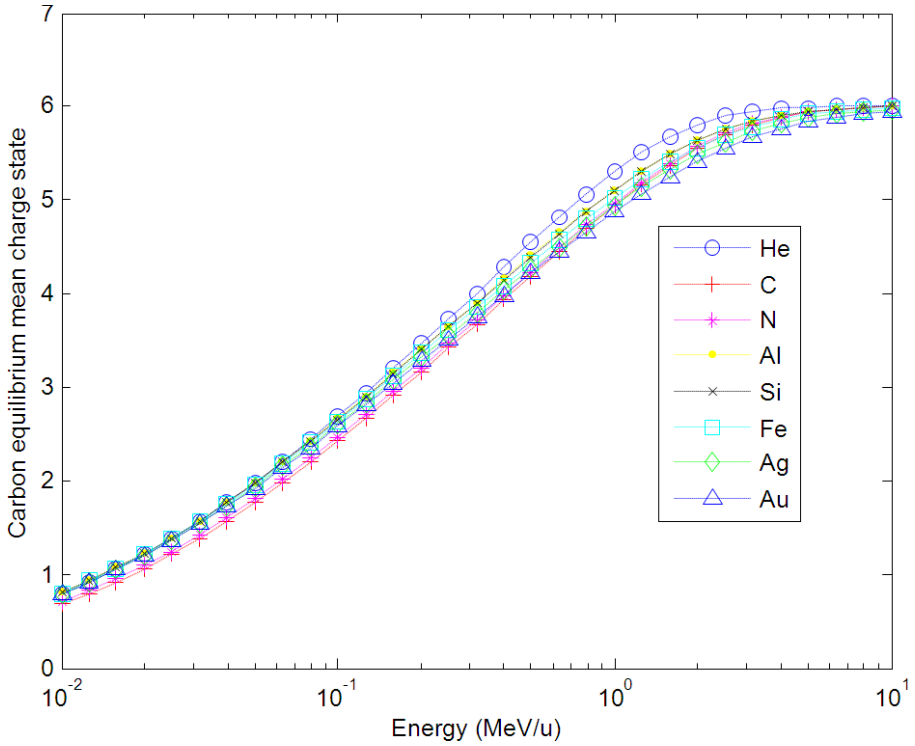

Figure IV-10: Equilibrium mean charge state of a carbon beam emerging from different solid media as a function of projectile energy; each curve represents a different medium; it goes from helium to gold.

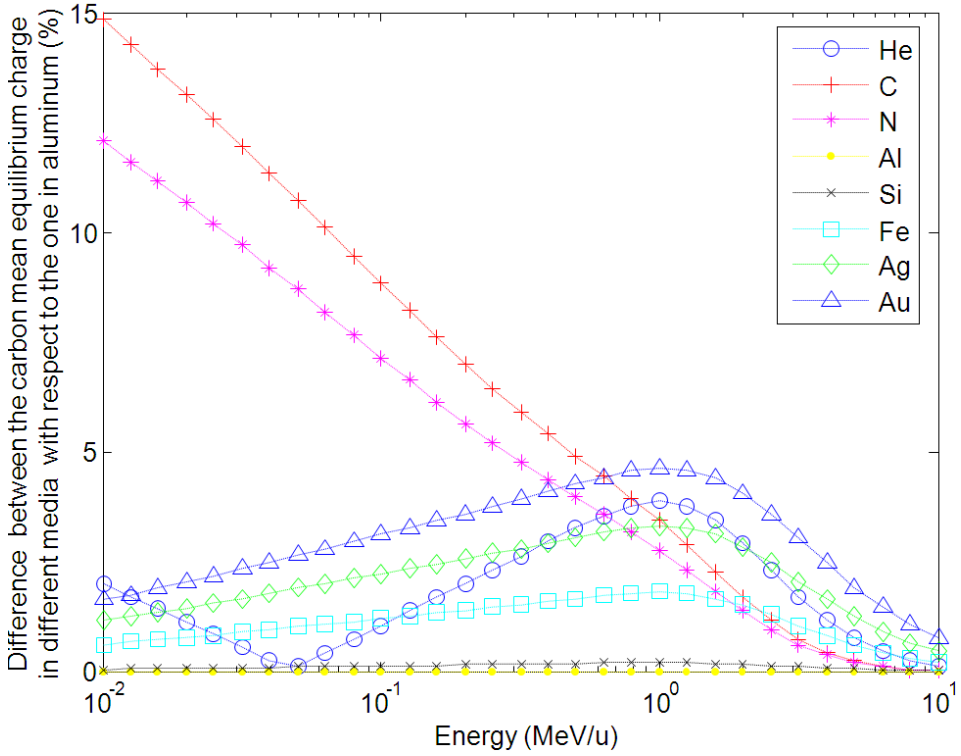

Figure IV-11: Difference between $\langle Q_1 \rangle_{eq,Al}$, the carbon equilibrium mean charge in aluminum, and $\langle Q_1 \rangle_{eq,medium}$, the carbon equilibrium mean charge in other media, as a percentage of the aluminum one: $\frac{|\langle Q_1 \rangle_{eq,medium} - \langle Q_1 \rangle_{eq,Al}|}{\langle Q_1 \rangle_{eq,Al}}$.

A few codes have been developed to predict the charge fraction of a projectile emerging from numerous cold and solid foils as a function of the target thickness. Among all, two are mainly used.

ETACHA [37] calculates the charge state distribution of the ion projectile beam considering the rates and cross-sections of electron capture, ionization, excitation, radiation, and Auger processes. It does not take into account relativistic effects whereas GLOBAL [38] does but, in it, processes such as Auger effects are missing compared to ETACHA. These two codes complement each other; ETACHA can be used for low energy particles and the other one for projectiles with near-relativistic energy range. Both codes have been tested using experimental data from accelerators. In our case, the energy of the projectile is way below the relativistic range. Thus, we will, in the following, use ETACHA to compare with our results.

IV.2.3.2 In WDM

From the theoretical point of view, the explicit calculation of the equilibrium mean charge [39] in the intermediate velocity regime from first principles is very difficult in cold matter but even more in WDM which ionic and electron structure is not well known. This is likely to affect the cross-section of the elementary mechanisms that govern the equilibrium mean charge of an ion beam propagating inside a medium [40].

As for the stopping power (see section IV.1.2), measurements of propagating ions through WDM plasma have never really been performed for the same reasons: a lack of facilities where accelerators and lasers could be coupled (only one exists at GSI, which will be fully operating in 2013) and the difficulty of generating WDM which hydrodynamic conditions remain stationary long enough compared to the duration of ion bunches delivered by conventional accelerators (so that the hydrodynamic conditions of the WDM medium are unchanged while the few ns ion beam propagates through). Up to now, only experiments in low-density plasma have been performed [41]. The experiment that is the closest related to WDM has been achieved at the GSI. The argon ions were propagating inside a non-homogeneous carbon plasma generated by laser with a temperature comprised between 300 K and 214 eV and density close to 1% of the solid-density. These conditions are far from the ones we want to explore.

High-intensity short-pulse lasers have recently brought new horizons in the pursuit of ion charge equilibrium in WDM. As mentioned in chapter I, these types of lasers generate pulsed broadband ion beams of picosecond duration off flat solid targets by the Target Normal Sheath Acceleration (TNSA) [42] mechanism where hot electrons generated by the short pulse laser creates a sheath field strong enough to ionize and accelerate hydrocarbons off the target surface (see chapter III). This new technique has opened up new possibilities for equilibrium charge state measurements. A laser-generated

ion beam can namely (i) isochorically heat thick solid-density samples during 100 ps reaching temperature up to 20 eV for mid-scale lasers like TITAN [43] or LULI [44] (see chapter I). In addition, (ii) the short duration of the ion bunch (a few ps) allows using it as a probe beam. Indeed, as long as the hydrodynamic time scale is far longer than the ion acceleration process, one can assume that ions of the same energy range are seeing the same hydrodynamic conditions. This last point is used in the proton radiography experimental technique [45, 46, 47]. Achieving both points is significantly harder with conventional accelerators since the typical ion beams produced by accelerator facilities have usually quite longer bunch lengths ~ 10 ns [48].

IV.2.4 Measurements of C-ion equilibrium charge state distribution

This is what we have aimed to undertake here: we present results on precisely using short-pulse laser accelerated ion beams to perform equilibrium charge state measurement in WDM.

IV.2.4.1 Experimental set up

The experiment was carried out using the ELFIE laser at the Laboratoire pour l'Utilisation des Lasers Intenses working in the chirped pulse amplification mode at a wavelength λ_0= 1.057 µm. The experimental set-up is shown in Figure IV-12. The first laser pulse (Beam 1) had a duration of 320 fs (FWHM) as measured after compression and before focusing. It was frequency doubled to λ_1 = 527 nm to enhance the beam contrast and then focused to a focal spot of ~ 6 µm (FWHM) using a 300 mm focal length off-axis parabola. A 1.5 µm plastic foil (mylar) used as a carbon (ion) source was positioned at focus and irradiated at 20° incidence with a peak intensity of 2.8 x 10^{18} W/cm^2. Due to the high contrast of the laser, two similar carbon ion beams were accelerated normally from the rear and the front surface of the carbon source [49]. One (front) was used as a reference, while the other one (rear) was in charge of probing an unheated/ heated secondary target. The latest was located 1 cm away from the carbon source, its normal axis making a 65° angle with the normal to the source target. During the experiment, we used secondary targets of three different thicknesses to study the possible passage from non-equilibrium to equilibrium mean charge state; they were composed of 80, 50 or 0 nm aluminum on 30 nm of Si_3N_4 substrate. The substrate surface was facing the carbon source, so the carbon beam was always emerging from the aluminum side. Considering the little difference between the mean charge of carbon ion in cold solid-density aluminum and silicon one, and their proximity in atomic number, we approximate silicon to aluminum in our study. A 10 µm gold foil, parallel to the secondary target and located 500 µm away from it, was positioned at the focus of a second laser pulse (Beam 2) working at λ_0, independently compressed to 320 fs (FWHM) and focused using a f = 300 mm off-axis parabola to a focal spot of ~ 6 µm (FWHM). The gold target, called

proton source, was irradiated at 45° incidence with a laser peak intensity of 1.1 x 10^{19} W/cm² to produce an energetic broadband proton beam in charge of heating the secondary target.

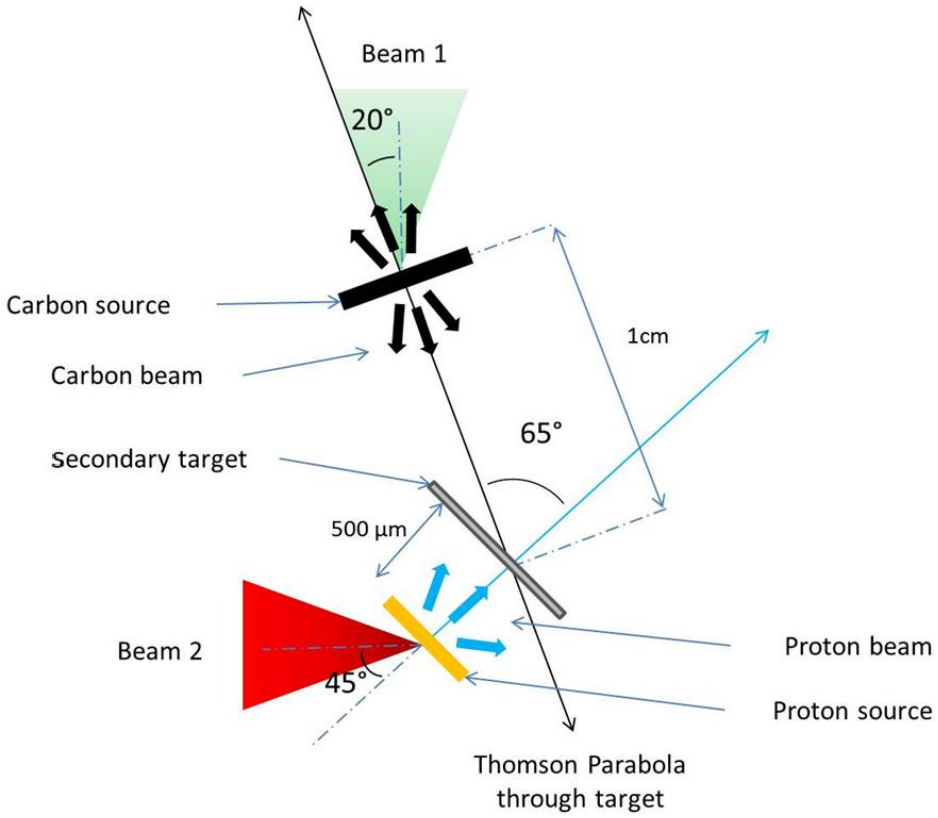

Figure IV-12: Experimental set-up.

IV.2.4.2 Diagnostics

Two TPs, specially designed to measure low energy spectrum, were used to measure the distribution charge of the carbon beam. In order to characterize the proton beam from the rear surface of the proton source target, we used alternately a magnetic spectrometer and stacks of radiochromic films to obtain in addition the angular characteristics of the beam. To get an absolute number of ions, we use image plates as detectors for both TPs and magnetic spectrometer. The absolute spectra of the heating proton beam coupled with the hydrodynamic code ESTHER [50] allows us to estimate the hydrodynamic conditions of the secondary target. A temperature diagnostic based on thermal radiation measurements was employed, but was not working at the low temperatures we reached.

IV.2.4.2.1 Thomson parabola

The principle of this diagnostic has already been shown in section III.3.1.2.2.2. In the case of our experiment, since we wanted to compare two similar ion beams, the two TPs had similar characteristics. They were both located 70 cm away from the carbon source. Their magnets and electrodes were producing a 0.32 T magnetic field and a 6 kV/cm electric field. The particles were passing through a 100 µm diameter pinhole. A vacuum of approximately 10^{-3} mbar was maintained all along the particles path from the target to a FujiFilm BAS-TR image plate detector. We used absolute calibration in number of protons [51] and carbon ions [52] to retrieve the spectra. Before measuring the spectra, calibration of the spectrometer dispersion was done using a set of Al filters. According to it, we were able to detect low energy particles from 0.0075 to 4 MeV/u. We may note that the energy resolution increases with the charge (at constant mass). Carbon ions of higher charge state are indeed more deflected than carbon ions of lower charge and of the same energy. Details on the basic working principles of particle deflection and calibration are given in appendix.

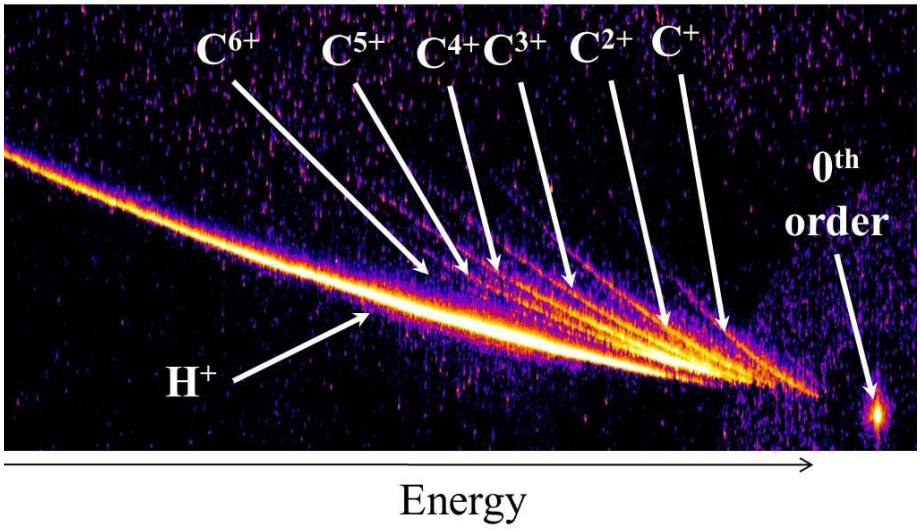

Figure IV-13: Typical ions beam signal collected by an IP. Each line represents the continuous spectrum of a particular ion within the beam, i.e., carbon ions and protons. The particles of higher energy are less deflected, so are located closer to the 0^{th} order (not deflected) point.

IV.2.4.2.2 Magnetic spectrometer

A magnetic spectrometer [53] was used to measure the heating proton beam energy spectrum. It works like a TP without any electrode. The proton beam is going between a pair of permanent magnets inside a yoke to separate the particles in energy. Instead of a pinhole, a slit is located at the entrance of the yoke to limit the particle flux on a FujiFilm BAS-TR image plate detector. As for TPs, we used an absolute calibration in number of protons [51] to retrieve the spectra. During our experiment, the spectrometer was located 120 cm away from the proton source and had a 150 µm slit. A magnetic field of 0.23 T has been estimated from the calibration performed using the same method as for the TPs. Due to the compact set-up within the target chamber, we were not able to measure the proton spectrum on every shot while heating the aluminum sample. So, we did several measurements of the proton beam produced throughout the experiment in order to get a good idea of the proton beam spectrum despite the shot-to-shot fluctuations which are detailed later in section IV.2.4.3.2).

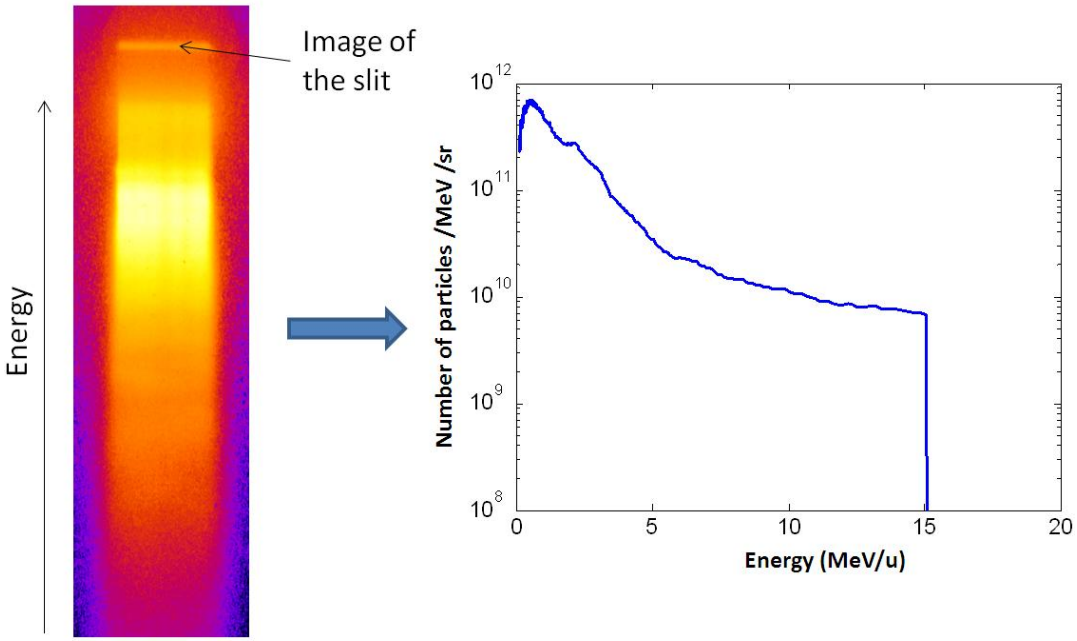

Figure IV-14: Typical proton beam signal collected by an IP and its related proton spectrum.

Note that since this diagnostic does not have any electrode, it is not able to differentiate the different ions contained in a typical laser-generated ion beam (see section III.2.3.2.3). However, since the carbon beams represent less than a few % of the total beam energy (as seen on TP e.g. in Figure IV-16), it is valid in our case to directly infer the proton spectrum from the signal recorded on the magnetic spectrometer without paying attention to the other species contained in the beam.

IV.2.4.2.3 Radiochromic film

The RCF is a radiation dosimeter that changes colour (optical density – OD) through polymerization of a di-acetylene active layer from transparent to dark blue, proportionally to the absorbed dose of ionizing radiation. It is sensitive to penetrating protons which have a large specific energy loss and produce a high contrast image. Through the measure of the change in the OD, it is possible to determine the deposited dose of the protons within the film. It should be mentioned that these films are also sensitive to electrons and x-rays, which generally appear as a diffuse low-intensity low-contrast background that extends over the whole surface of the film since they are not as collimated as the proton beam is.

RCFs of type MD-55 and HD-810 by ISP Corp were used. MD-55 is made of two active layers sensitiveto radiation and laminated between polyester film substrates (see Figure IV-15a). Since the film structure is symmetric, it can be used as a detector equally on both sides. On the contrary to the MD-55, HD-810 is not made in the sandwich form; there is just one active layer on the polyester support (see Figure IV-15b). This means that there is a difference in the stopping power when using one face or another.

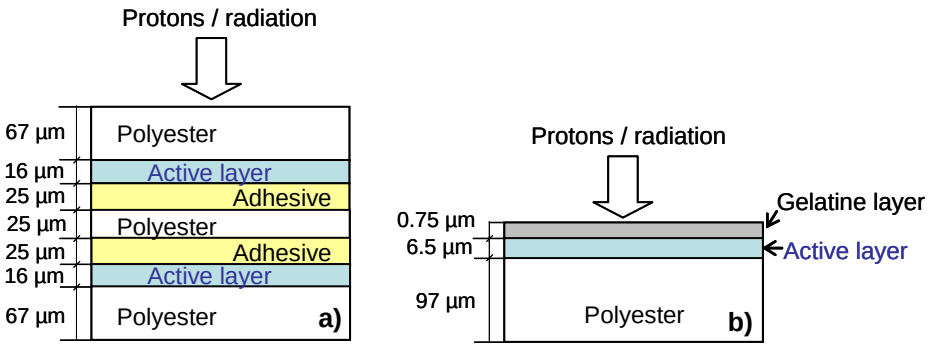

Figure IV-15: Composition of the RCF: (a) MD-55 type and (b) HD-810 type.

As proton detectors, RCFs are usually used in a stack. Because of the pronounced energy loss of protons at the end of their range (Bragg peak), different layers of RCF in the pack allow one to image the proton beam at different energies, i.e., protons can be 'filtered' by their energy. A more energetic proton will penetrate deeper into the stack than a less energetic one since the stopping power increases with the increasing thickness of the material the particle needs to cross.

IV.2.4.3 Characterisation of the generated ion beams

IV.2.4.3.1 Carbon ion probe beam

For laser intensities of some 10^{18} W/cm² and sub-picosecond pulse durations interacting with a thin (a few microns) solid-density foil, the main ion acceleration mechanism is the TNSA (see chapter II). Figure IV-16 shows the typical spectra of the ions that are accelerated normally to the mylar target surface. The beam is composed of carbon ions of charge going from 1+ to 4+ and protons. As predicted by TNSA, the protons of charge-to-mass ratio of 1 are preferentially accelerated; their number is around two orders of magnitude higher than the other ions. Let us now concentrate on the carbon ions spectra. All of the ions show bell-shaped curves, their maximum happening at energy increasing with their charge: C^{1+} 0.082 MeV/u, C^{2+} 0.086 MeV/u, C^{3+} 0.16 MeV/u and C^{4+} 0.27 MeV/u. The strong electrostatic force in charge of accelerating the projectiles is indeed proportional to the charge of the projectile. Therefore, higher charge carbon ions are more accelerated compared to lower charge ones and consequently reach higher energy. The electrostatic field was too weak to ionize higher charge states of carbon and produce C^{5+} or C^{6+}.

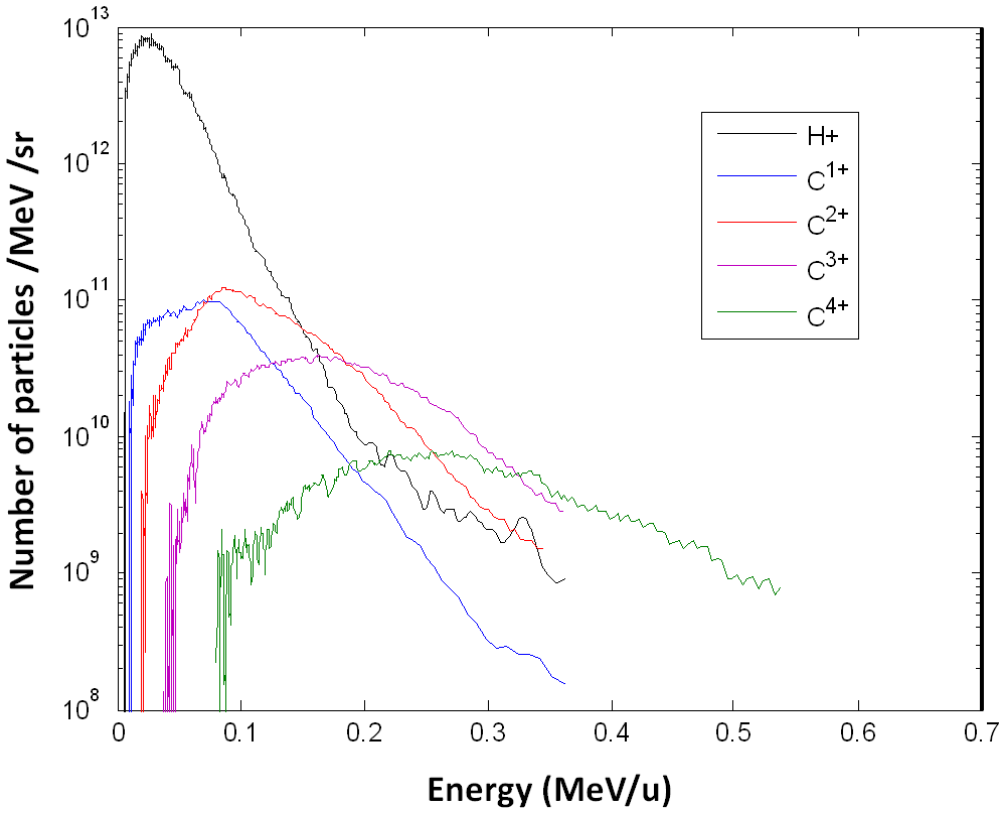

Figure IV-16: Typical ion beam spectra accelerated from a mylar target.

The objective of the experiment is basically to compare the charge state distribution of a carbon ion beam emerging from a thin aluminum foil, i.e., after equilibration, to a reference distribution, i.e.,

the one originating from the source target and unperturbed. Since the generated carbon ion beam spectra can significantly change from shot to shot, we decided to generate two carbon ion beams using a same laser beam where one would serve as a reference on every shot and the other would be sent to the secondary target (and is referred to the following as the probe beam). Ref. [49] has shown that a high-contrast laser can produce on both sides of the source very similar ion beams. This particularity corresponds exactly to what we want for our experimental set-up. To ascertain the quasi-symmetry between the probe and the reference beam, i.e., accelerated respectively from the rear and the front surface of the carbon source, we have performed several shots without any secondary target; both ion beams were then passing through vacuum only.

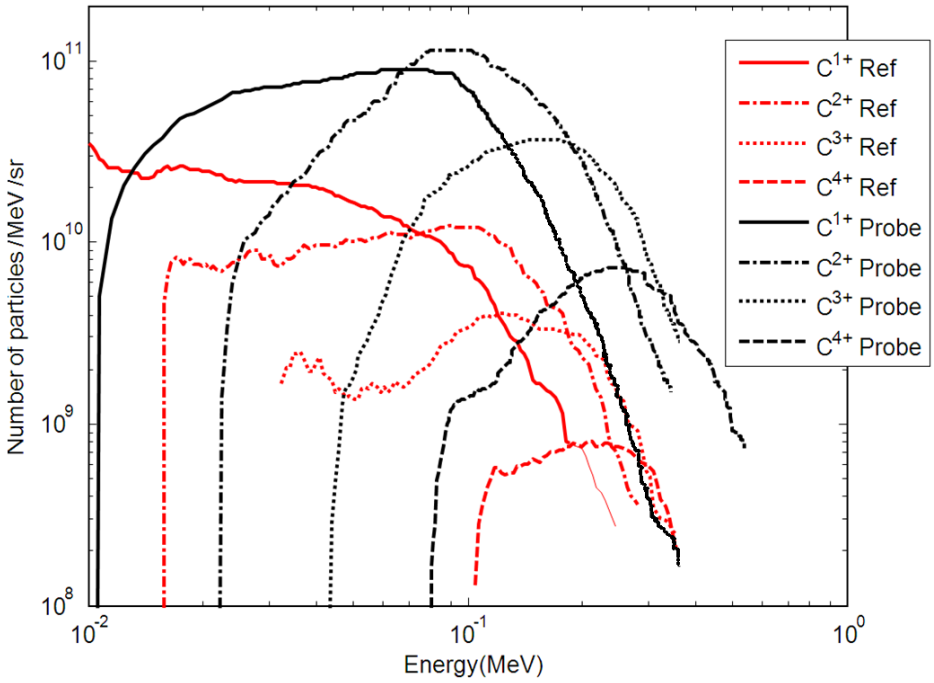

Figure IV-17: Spectra of the Probe (black lines) and Reference (red lines) carbon beam after passing through vacuum.

The number of particles in the rear spectra was most of the time found to be higher by around an order of magnitude compared to the front spectra (Figure IV-17). Regarding this observation we can propose two explanations. Firstly, since a high contrast is a stringent criterion to maintain symmetry between the electron sheaths of the two surfaces, a laser contrast lower than used in Ref. [49], despite the frequency doubling, could explain such difference. Indeed, what is observed in Figure IV-17 could be seen as typical of what is recorded with a standard contrast (10^6) laser pulse [54]. The acceleration in the backward direction is based on the same mechanism of TNSA with a disadvantage: the acceleration takes place at the front target surface that is hit by the laser (see chapter III). The laser pre-pulse then perturbs the front surface and creates a pre-plasma before the arrival of the main pulse. Hence, the sheath field is reduced by a factor L_G/λ_d, where L_G is the front plasma characteristic gradient length. In Figure IV-18, one can see that, based on calculations, our laser contrast

is however similar (or even higher) than the one obtained using a double plasma mirror, as done in Ref. [49].

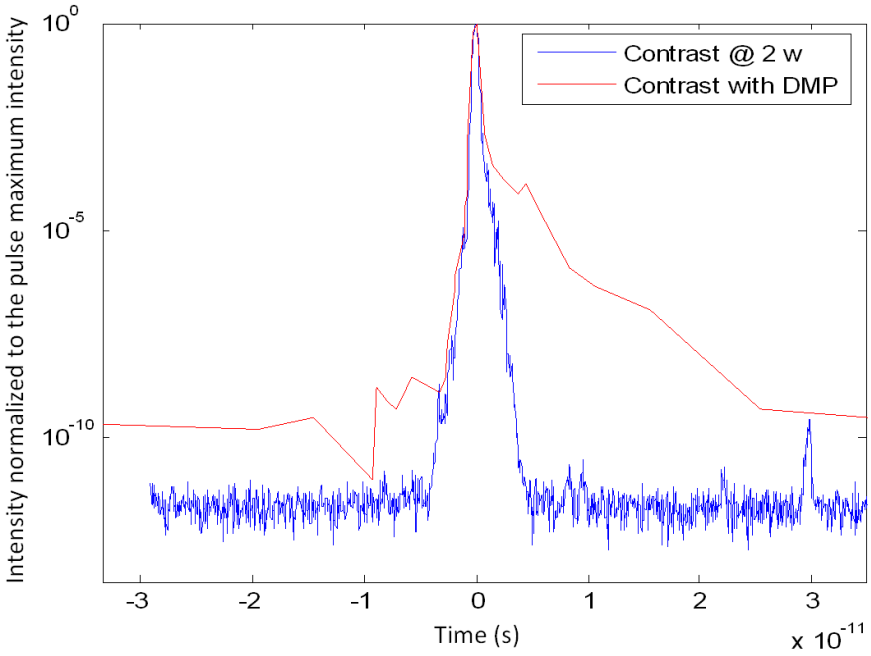

Figure IV-18 : Temporal contrast of our frequency doubled laser pulse compared to the one obtained using a double plasma mirror (DMP), as inferred from using the curve published in Ref. [55]. The contrast in our case (frequency-doubling) is inferred by taking the measured contrast at the fundamental frequency, and by squaring it.

Another explanation could then be that this quasi-symmetric acceleration is specific to very short laser pulse. The results reported in Ref. [49] have actually been performed using a laser pulse with intensity close to our (5 x 10^{18} *vs.* 2.8 x 10^{18} W/cm²), but shorter in time (65 versus 300 fs). Indeed, our longer pulse duration could lead to an asymmetry, induced by the laser irradiation, between the two target surfaces, linked to a larger blow-off plasma on the front side.

Nevertheless, what is important for us is not really the absolute spectrum, but the charge fractions, f_i and the subject of our study, the mean charge state $\langle Q_1 \rangle$. They can be computed from the beam spectra shown in Figure IV-17 using Eq. (4.6) applied to carbon,

$$\langle Q_1 \rangle(v) = \sum_{Q_1=1}^{6} f_{Q_1}(v) Q_1 \qquad (4.10)$$

where $f_{Q_1}(v) = \frac{n_i(v)}{\sum_{j=1}^{6} n_j(v)}$ and $n_i(v)$ is the number of C^{i+} of velocity *v* within the beam.

The evolutions with particle energy of these two values are plotted in Figure IV-19 and Figure IV-20. The charge fraction distribution exhibits bell-shaped curves that are more pronounced compared to the spectra shown previously. We thus find that the probe and the reference ion beams present a quasi-identical charge fraction distribution and mean charge state over the quasi-entire energy

range, except for the very low and high energy part which may differ. This can possibly come from the low number of particles on the “front IP” being barely above the noise level at very low and high energy, and so increasing significantly the error in these ranges. However, these differences remain small and localized. The two symmetrical beams show fraction and mean charge values similar enough for us to use one as a reference for the other one.

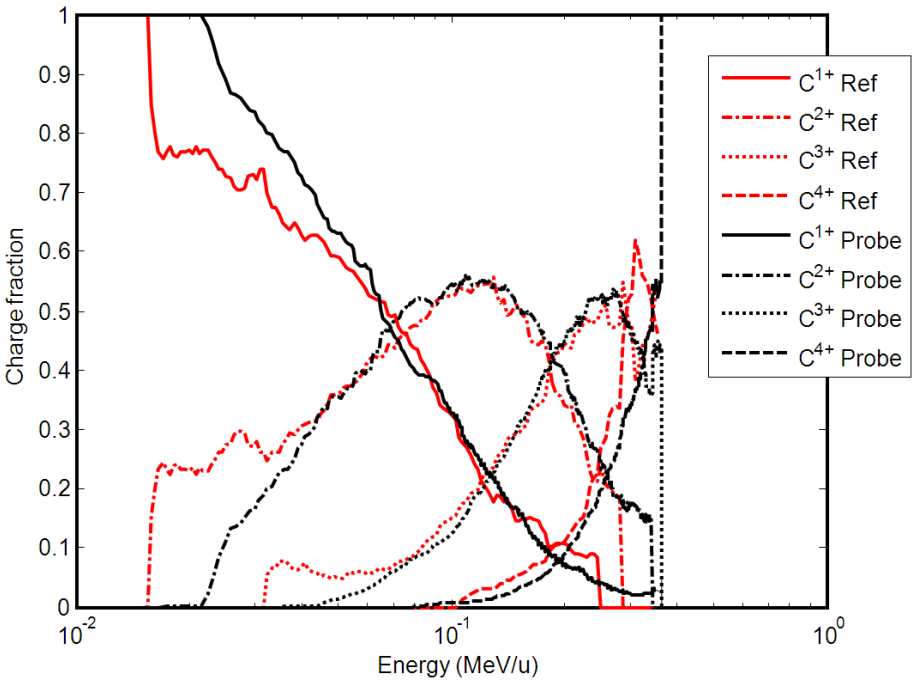

Figure IV-19: Charge fraction distribution of the probe (black lines) and reference (red lines) carbon beams after passing through vacuum.

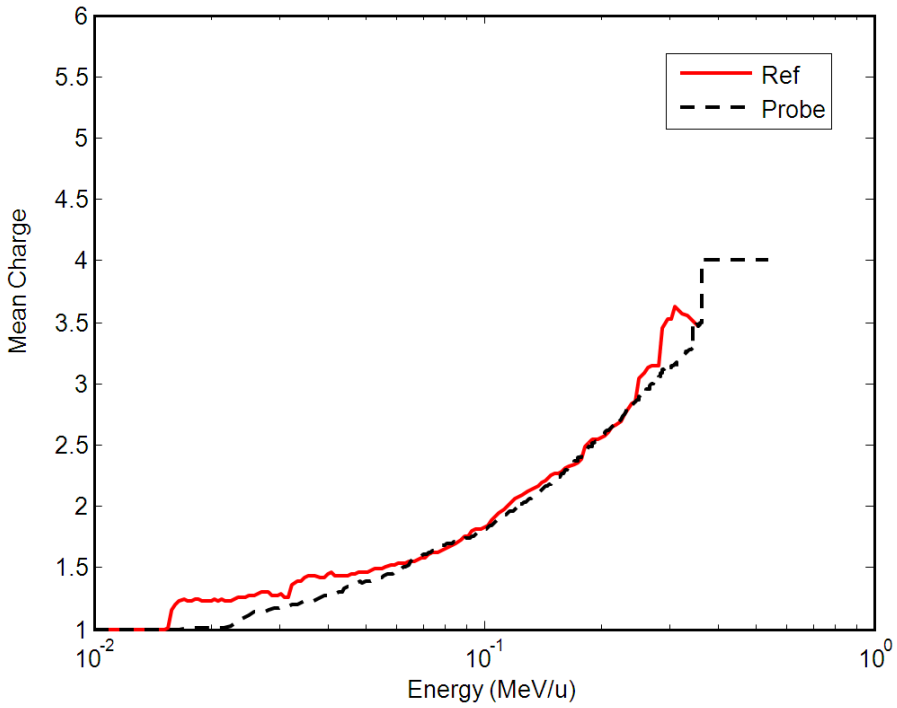

Figure IV-20: Mean charge of the probe (black lines) and reference (red lines) carbon beams after passing through vacuum.

In order to estimate the amplitude of the shot-to-shot fluctuations, we have compared the carbon ion beam spectra from two consecutive shots (# 100 and 101, see Figure IV-21) with the same laser input. We have found that the absolute number of particles remains steady. The maximum of the bell-shaped curves are quasi-identical from one shot to the other. The spectra of the probe beam at moderate to high energy range (i.e., typically ≥ 0.05 MeV/u) are well corresponding as well. One can see that C^{3+} goes to higher energy in shot 101 than in shot 100 (0.49 versus 0.36 MeV/u). This can significantly change the fraction and the mean charge at high energy where the numbers of the dominant charges, C^{4+} and C^{3+}, are close one to each other. The difference is more pronounced between reference beams with, in addition, shifts of the maxima for lower charges (C^{1+} and C^{2+}). When one compares shots taken far apart (i.e., days) from each other, a variation of the absolute number of accelerated particles up to half an order of magnitude is generally observed as well. This is explained by large fluctuations of the laser beam in energy and shape. From this short analysis, we can conclude that reference and probe beams from different shots are reproducible but only in the moderate energy range, i.e., from 0.1 to 0.3 MeV/u for reference and from 0.05 to 0.3 MeV/u for probe. The maximum of these ranges may decrease with the maximum ion energy produced on each shot.

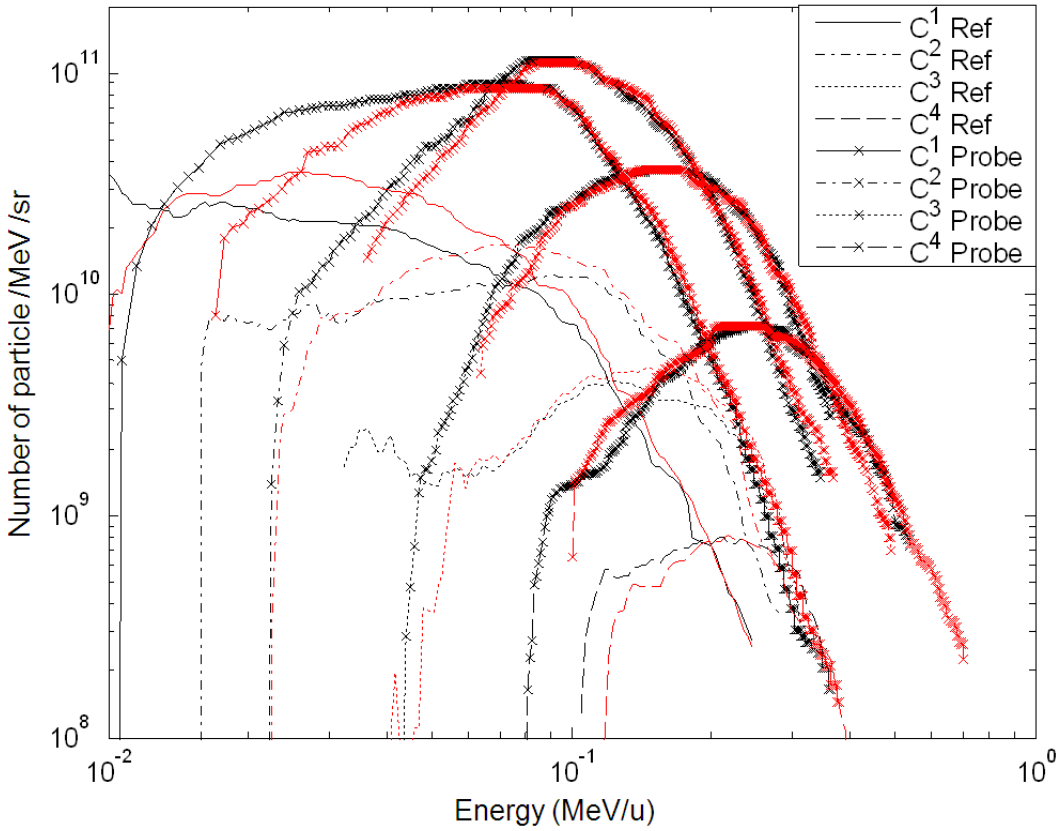

Figure IV-21: Rear (crossed line) and front carbon beam spectra for shot #100 (black lines) & 101 (red lines).

As already mentioned, in order to have the probe beam not heating the secondary target, we placed the carbon source 1 cm away from the secondary. This point has been verified with the ESTHER code using the probe beam as an input: the energy deposed on the secondary target appears to be undeniably negligible. Thus, from then, we will assume the probe beam to be a non-intrusive diagnostic. Another question might be raised about the possible interaction between the different ions within the beam. As previously written in chapter III, laser-generated ion beams are laminar, i.e., the ions of the beam do not collide one with each other after leaving the source. Furthermore, the average distance estimated between two ions within the beam when it is 1 cm away from the source, $r_{i\text{-}i}$ is much longer that the interatomic distance in solid-density aluminum, $r_{Al\text{-}Al}$[18]:

$$r_{i-i} = \sqrt{\frac{Surface}{\pi * nb\ of\ particles}} \ll \sqrt{\frac{1cm^2}{\pi * 4.6 \cdot 10^{12}}} = 2{,}6\ nm \ll\ 0.121\ \text{nm} = \text{r}_{\text{Al-Al}}\ .$$

[18] In a first estimation, we did not take into account the debunching induced by the time of flight, therefore the ion density of the beam inferred from the different spectra in Figure IV-16 (including the protons) and so r_{i-i} are overestimated.

Thus we can assume that we are not in a collective regime: a carbon ion from the beam is only interacting with the aluminum medium. Hence its instantaneous charge fluctuations are only due to the interaction with the electrons and nuclei of the medium.

IV.2.4.3.2 Proton heating beam

As mentioned above, the compact set-up did not allow us to measure the heating proton beam spectrum after it has emerged from the secondary target on every shot. Therefore we did several measurements of the input proton spectrum throughout the experimental period to get an indication of its shape. For these, we took care to reproduce exactly the same conditions as for heated shots, like the energy of the laser or the angle between the laser beam and the gold foil. The average of the proton spectra we measured during the experimental campaign and the error bars in term of number of protons are shown in Figure IV-22.

As explained in chapter III, proton spectrum can be approximated with quasi-thermal distributions. In our case, the average spectrum can be approximated by the sum of two semi-Maxwellian distributions having hot electron temperatures approximately of, respectively, 0.75 and 6.5 MeV.

The error bars at a given energy were determined using the highest and lowest number of protons measured at such energy through the proton spectra we measured during the experimental campaign. Although these variations appear important at first sight, most of the spectra we measured were actually close to the average spectrum especially in the most important part, the low energy range (see Figure IV-23), as highlighted by the similarity between the average spectrum and the spectra obtained with RCFs.

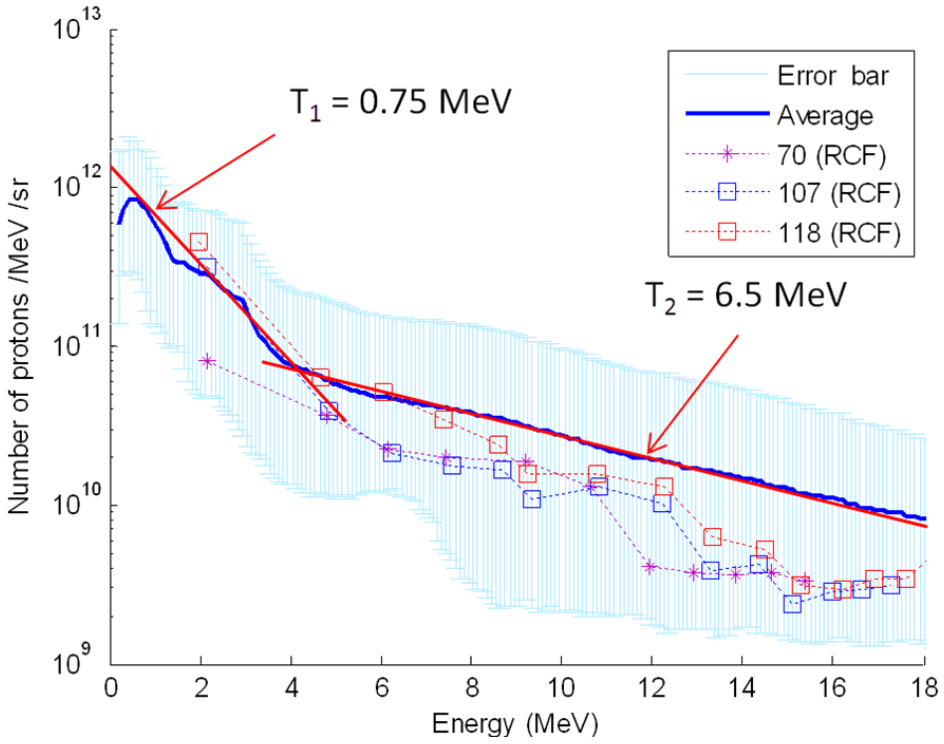

Figure IV-22: Average spectrum of the heating proton beam measured using the magnetic spectrometer and its relative error bar. This spectrum is compared with the spectra obtained with RCFs on shots # 70, 107 and 108.

Using such a spectrum, we can calculate the induced target heating. Figure IV-23 shows the energy deposition of a proton in a 100 nm aluminum target as a function of their energy. One can see that the protons which deposit the most efficiently their energy inside of the target are the ones that are located around 100 keV with a maximum of 12 keV/proton (i.e., low energy range). It should be noted that the energy of the maximum efficiency is increasing with the thickness of the target (e.g., 1 MeV for 10 µm Al).

The error on the heated target temperature and density induced by the shot-to-shot variations of the proton spectrum is evaluated later in section IV.2.4.4.2.

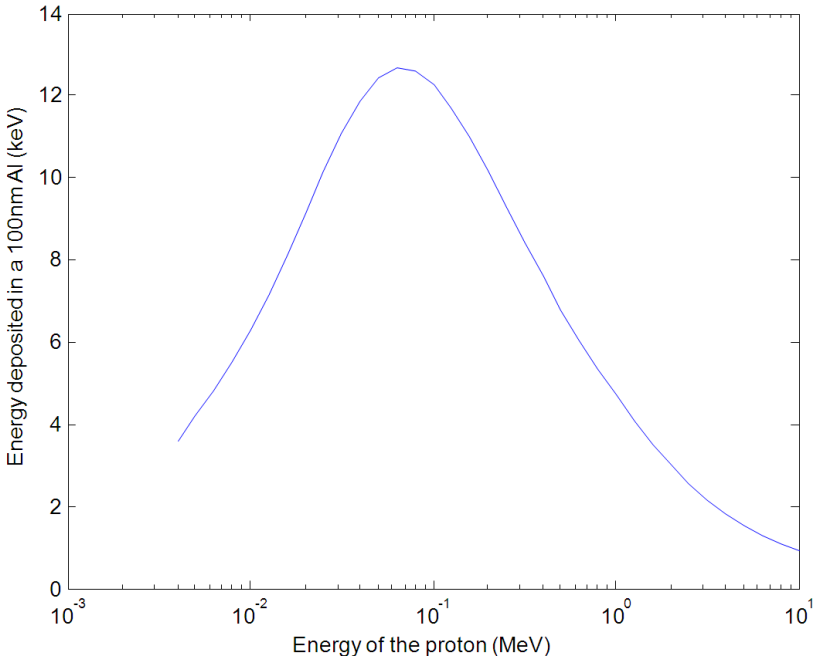

Figure IV-23: Energy deposition of protons in a 100 nm target as a function of its energy according to the SRIM code [56].

IV.2.4.4 Results

In the previous paragraphs we have described in details the set-up, all the diagnostics that have been used, the characteristics of the heating/probing beams and the conditions in temperature and density of the secondary target. We now proceed by describing the results of the experiments of carbon ions interacting with cold and heated matter. For clarity sake, the explanations and the discussion of the results will be given later in another paragraph.

IV.2.4.4.1 Interaction ion beam – cold and dense matter

We first performed the experiment in the cold and dense regime. The main purpose of this step was to test and validate our set-up by trying to reproduce mean charge measurements of carbon ion beams through cold material, as obtained on conventional accelerator facilities. Indeed this is the first time that such measurements were performed using a laser facility where the characteristics of a laser generated ion beam are far different from those produced by accelerators (see chapter I). As the probing beam is a non-intrusive diagnostic, the secondary target remains cold and dense while the whole ion beam is passing through (each particle sees the same cold and dense condition). It allows us to get a continuous mean charge curve on a single shot, while it takes numerous shots on an accelerator. Before starting with the description of the cold interaction, another important point may be added: the probe ion beam makes a 65° angle with the normal of the secondary target sur-

face (see Figure IV-12). Therefore the probe beam passes through a thicker thickness. To get the distance traveled by a probe beam particle, one has to multiply the sample thickness by a factor of ~ 2.37 ($= {}^{1}/_{\cos(65°)}$). The real distance traveled through the sample is, respectively, 71, 189 and 260.3 nm, when we use 30, 80 and 110 nm thick targets.

The measurements of the projectile mean charge state of a carbon probe beam traversing a 110 nm thick aluminum sample, from both TPs are overlaid in Figure IV-24. One may divide the data in two parts along the energy axis. For the low energy portion, below 0.11 MeV/u, both curves are very close one to each other, regularly increasing with the energy and reproducing the generated carbon ion beam trend viewed before. However, when it comes to higher energies, the two curves start diverging one from each other, this difference increasing noticeably with the energy. While the probe beam keeps its original tendency, the reference starts to display a much more disjointed layout, reaching higher values than the probe for the same energy. As observed in section IV.2.4.3.1 when we compared the front (used here as a reference) and the rear (used here as a probe) carbon beam, the reference ion beam exhibits a lower energy cut-off (0.3 MeV/u) than the probe beam (0.4-0.5 MeV/u). In addition, we observe that the reference mean charge from 0.2 to 0.3 MeV/u stops increasing and stay stable at 3. This is due to the low number of carbon ions exhibited by the reference beam in this energy range: there was a too low number of C^{4+} in the reference beam on the energy range from 0.2-0.3 MeV/u to be detected by our detector.

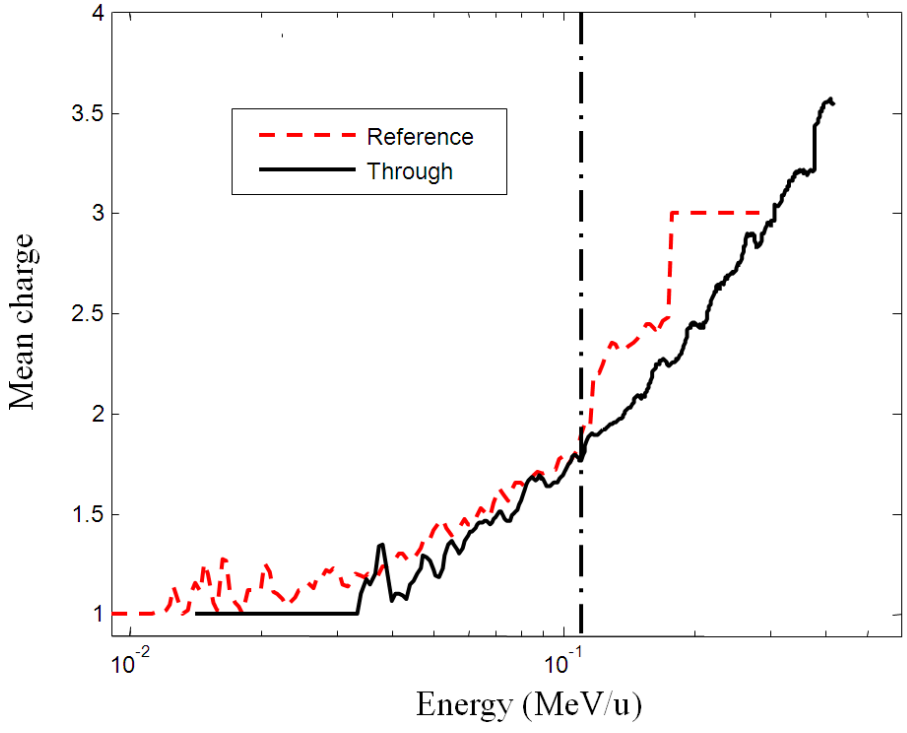

Figure IV-24: Mean charge state of the reference and the probe carbon beam emerging from a 110 nm thick aluminum foil.

We performed the experiment on three samples of different thickness in order to check the equilibration of the ion beam. The results are shown in Figure IV-25. Except for the reference mean charge, all of the curves are falling on each other from low energy to 0.5 MeV/u. The small difference at lower energy of shot #104 may just come from the resolution limit of the TP: when the particles flux of a shot is too low (in the case of a low energy laser beam), it becomes very difficult to detect them at very low energy where the deflection in the TP is important. The signal then becomes very close to the noise level. Due to the particle flux fall down, the precision of the spectrum measured by the TP at very high energy decreases as well. Consequently, very close to the ion energy cut-off, the signal of C^{3+} becomes too low to be detected. The mean charge state then invariably finishes to a constant value of 4. This explains why the different curves peak at 4 and why this occurs at different energies. We did several shots for each different thickness; we find that the 4+ peak position actually varies with the flux of the particle beams but remains close to 0.5 MeV/u.

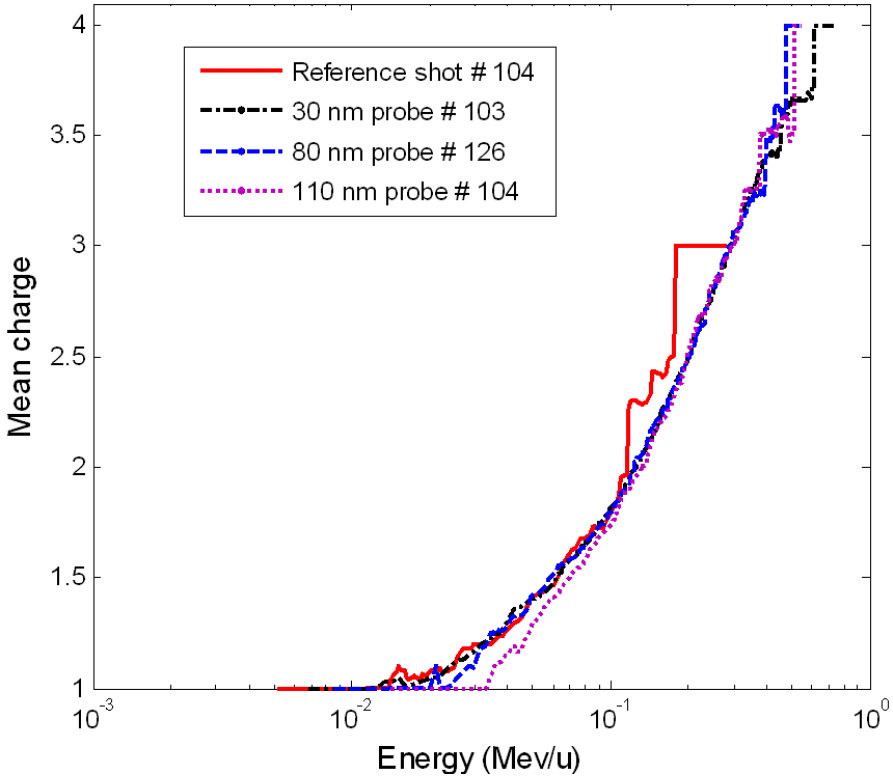

Figure IV-25: Typical mean charge state of a carbon beam emerging from an aluminum sample for different thicknesses

We can conclude from this cold interaction results, that the thickness of the traversed sample does not appear to be influencing the mean charge state of the probe beam; at least, 71 nm thick solid-density foil (30 nm thick foil) in our energy range. Furthermore, we observed that the mean charge of the reference beam matches the mean charge of the probe for energies below 0.1-0.2 MeV/u depending on the shots.

IV.2.4.4.2 Characterization of the heating

As performed in section IV.1.3.3, we ran the 1D hydro code ESTHER using the measured proton spectrum as an input to characterize the heating and so the condition of the target. This allows us to estimate the temporal evolution of the hydrodynamic conditions of the heated target, i.e., its temperature and density. The plasma characteristics of a 100 nm aluminum sample heated by protons over the course of several tens of picoseconds are shown in Figure IV-26. The origin in time corresponds to the beginning of the heating, i.e., when the first particle reaches the aluminum sample. From 0 to 60 ps, the temperature is rapidly increasing to reach its maximum at around 1 eV, while the density remains very close to solid (higher than 0.5 g/cm^3). Due to the high temperature that is achieved, the target is then thermally expanding, making the temperature stays close to constant while the density is quickly falling down. The heated target stays in the WDM regime until 140 ps (i.e., when the density goes below 1 % of the solid density) and then transform in a low-density warm plasma. ESTHER simulations predicted that the reached plasma characteristics are almost identical in the case of a 30 or 80 nm target. We ran ESTHER simulations varying the proton spectrum to estimate the potential error on target condition due to the shot-to-shot fluctuations. We have found that the maximum temperature fluctuates in average from 0.4 eV to 1.2 eV. The duration over which WDM regime prevails is a bit shorter for higher energy spectrum but stays around 140 ps (+/- 3 ps). Contrary to the temperature, the evolution of density is found quasi-identical when using one spectrum or another.

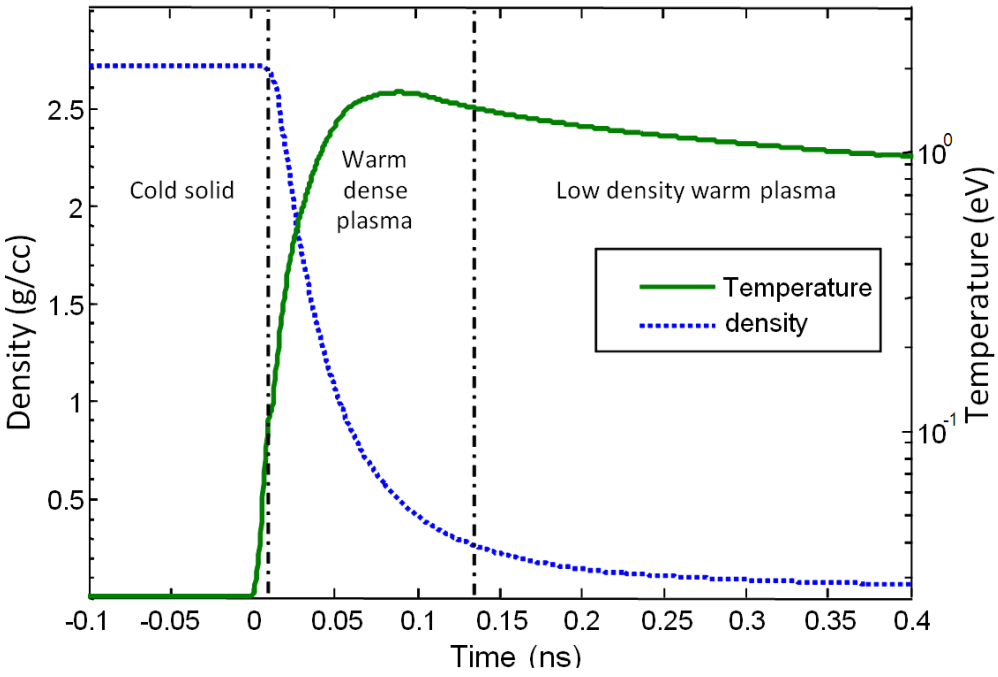

Figure IV-26: Temporal evolution in density and temperature of a 100 nm thick Al target proton-heated up to 1 eV.

From this analysis, we can say that we have a good estimate of the target conditions in density and temperature despite shot-to-shot fluctuations. However, compared to the temperature previously

reached by proton heating on the same laser facility [44], our temperature can be considered as low. This can be easily explained by the following elements:

- the laser pre-pulse was important enough to preheat the gold foil, causing the evaporation of a part of the rear side contaminant layer, so fewer particles were accelerated (one order of magnitude less) and heating the aluminum sample. Furthermore, as mentioned in chapter III, the pre-pulse perturbs the planarity of the gold foil rear surface and thus reduces the maximum energy reached by the accelerated protons.
- the most important point: due the tight target arrangement, the secondary target was located 500 µm away from the proton source, when 200 µm would have been preferable to enhance the proton flux on the secondary target, hence the low heated temperature. For instance, moving the target from 200 to 500 µm reduces significantly the heating particle flux by more than a factor of 6.

Due to the TOF of the probing broadband carbon beam, the particles do not traverse the heated target at the same time and so do not see the same plasma conditions. We have computed a maximum delay of 5 ns (at the aluminum target location) between the highest and the lowest energy particle recorded by the TP. Even if for same ions the target it is not in a WDM state, the study of ion interaction with a low-density warm plasma could give us the opportunity to learn more about the transition between plasma gas and WDM in term of charge equilibrium. Figure IV-27 shows the target hydrodynamic evolution over a longer time scale than in Figure IV-26. The dominant trend, characteristic of a thermal expansion, remains identical: a temperature decreasing slowly from 0.6 to 0.35 eV while the maximum density is falling down from 2.7 to 0.01 g/cm^3.

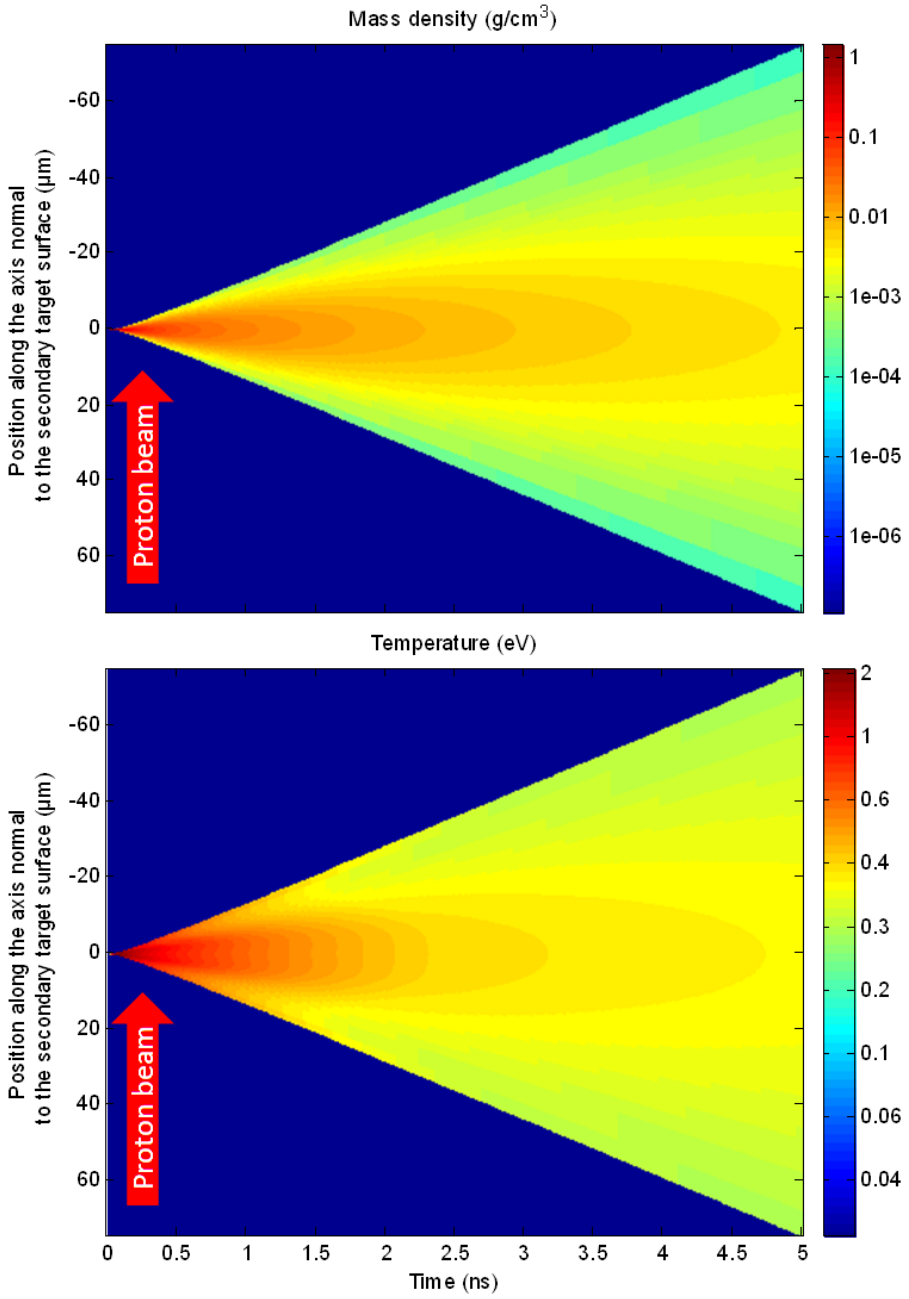

Figure IV-27: Evolution in density and temperature of a 100 nm thick Al target proton-heated up to 1 eV over ns time-scales.

IV.2.4.4.3 Interaction ion beam – heated matter

The source of carbon ions was located far from the secondary target, so that the TOF of the particles needs to be taken into account. The carbon probe beam, although broadband, is actually longitudinally laminar. This means that the beam is linearly chirped due to the difference in TOF. The high-energy particles arrive on target much earlier than the low-energy ones. At the carbon source, we can use as an estimate for the laser-generated carbon ion bunch a maximum duration of the order of

10 ps, knowing we likely overestimate the duration (see chapter III). After a travel in vacuum of 1 cm from the source to the target, the bunch is spread over approximately 5 ns if one takes into account carbon ions from 0.02 to 0.6 MeV/u, with corresponding arrival times of respectively 5.07 and 0.93 ns. We have seen in section IV.2.4.4.2 that the hydrodynamic conditions of the secondary target evolve too fast to stay constant during that amount of time. The chirp in energy allows us to consider the ion bunch as a continuous series of 10 ps monoenergetic bunches arriving at different time on the heated sample.

In our experiment, where we especially want to probe WDM (which lasts ~ 100 ps), we played on the delay between the heating proton beam and the probe carbon beam, so that the carbon energy we want to use traverses the heated sample when this one is in WDM regime. Due to the short time of our experiment, we used only three different delays or timings aiming at having these following central ion energies passing through WDM: 0.5, 0.1, and 0.05 MeV/u. These are the conditions seen by the ions:

- the ions of higher energy than the central energy are passing through cold and solid-density matter (see Figure IV-28a),
- the ions of energy close to the central energy are passing through WDM (see Figure IV-28b). Using ESTHER simulation, we estimated the energies of the ions passing through WDM to be, respectively, 0.045-0.05 MeV/u, 0.09-0.1MeV/u and 0.4-0.55 MeV/u with respect to the three different delays mentioned above.
- the ions of lower energy than the central energy are passing through a warm gas (see Figure IV-28c and d).

In Figure IV-28 is shown the temperature and density conditions of a target proton-heated up to approximately 0.5 eV probed by 0.1 MeV/u carbons for 4 different delays: -0.1, 0.05, 1.3 and 1.57 ns. The origin of time corresponds to the beginning of the proton heating. Note that we use the standard reduced thickness in $\mu g/cm^2$. This unit is more appropriate to our study about equilibration since it is proportional to the number of particles met by the projectile along its path. The standard reduced thickness is simply obtained by dividing the thickness by the mass density.

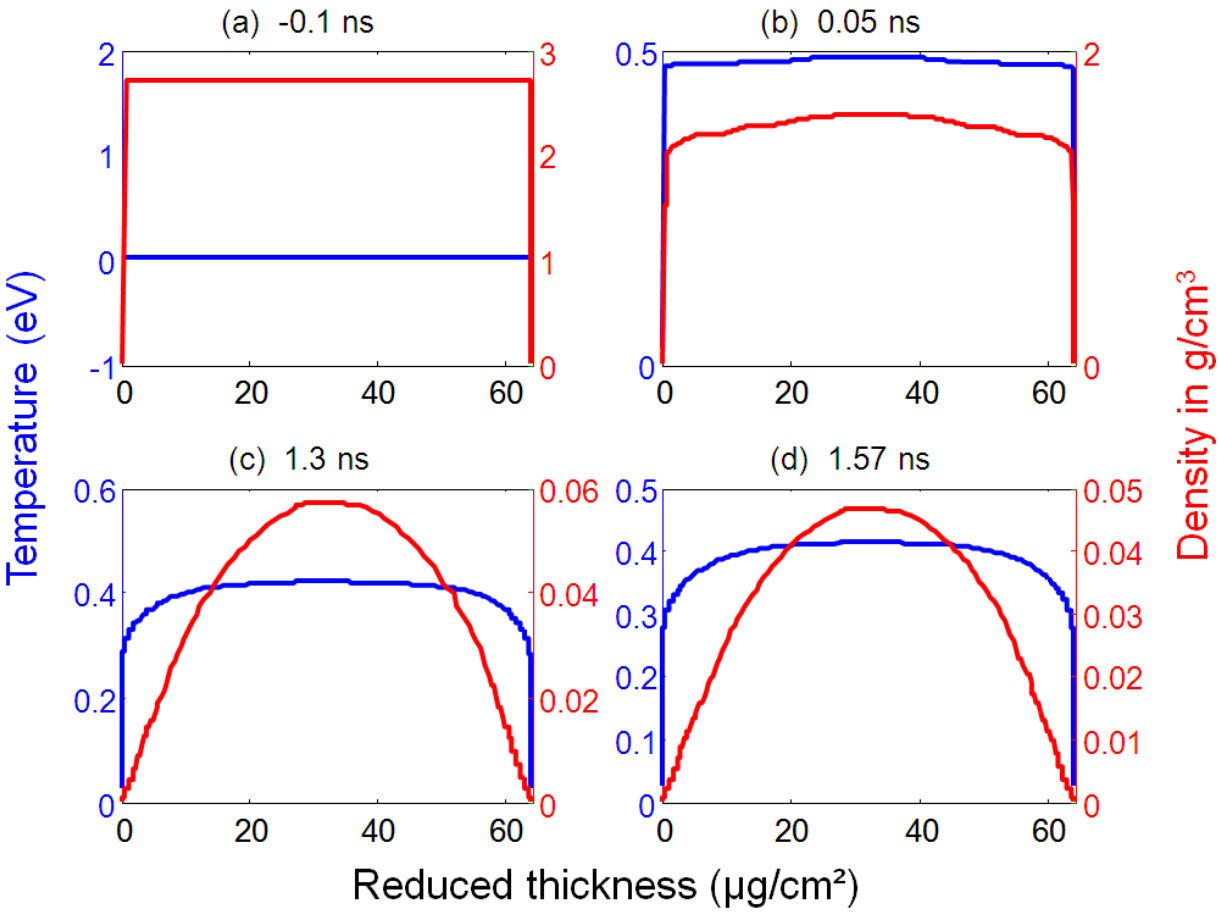

Figure IV-28: Spatial density profile crossed by a 0.1 MeV/u carbon ion for 4 different delays: (a) -0.1, (b) 0.05, (c) 1.3 and (d) 1.57 ns. The origin of time corresponds to the beginning of the proton heating. The last three delays correspond to the delay we used to probe WDM with the carbon energy of, respectively, (b) 0.5, (c) 0.1 and (d) 0.05 MeV/u.

Now that we have a better knowledge of the matter probed, we can proceed to the presentation of the results in term of charge state distribution.

In the shots where 0.5 MeV/u carbon ions were timed with WDM, i.e., according to ESTHER simulations, the carbons of energies from 0.4 to 0.55 MeV/u were propagating through WDM. The resulting mean charge curve is plotted in Figure IV-29, showing no visible difference in both low density warm plasma and WDM compared to mean charge curve we obtained in cold solid-density matter. We performed several shots using this timing and found that all the mean charge curves follow the same trend (+/- 5%) fitting well the curve obtained in cold and solid-density plasma.

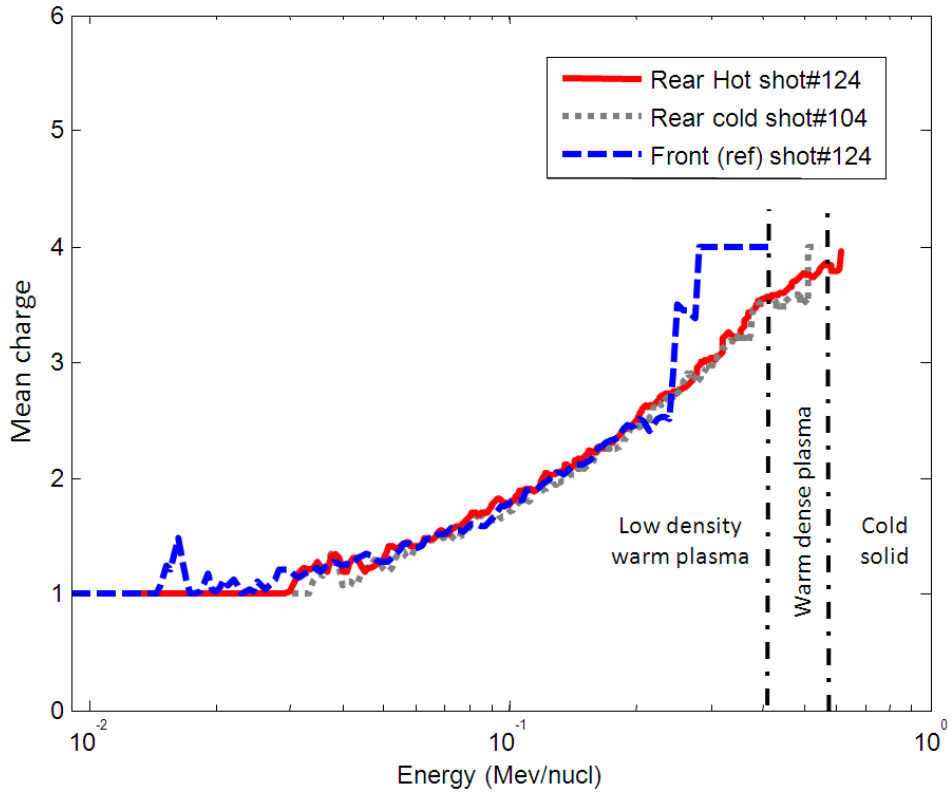

Figure IV-29: Mean charge of typical heated shot for which the laser beams were timed so that 0.5 MeV/u carbon ions were passing through WDM. It is compared with the mean charge of the reference and the mean charge we measured in cold solid-density matter.

In the shots where 0.1 MeV/u carbon ions were timed with WDM, i.e., the carbon of energies from 0.09 to 0.1 MeV/u were propagating through WDM. In Figure IV-30, the typical mean charge we measured is plotted compared to a standard cold shot. We observed again no visible difference between the mean charge in heated matter and cold solid-density matter.

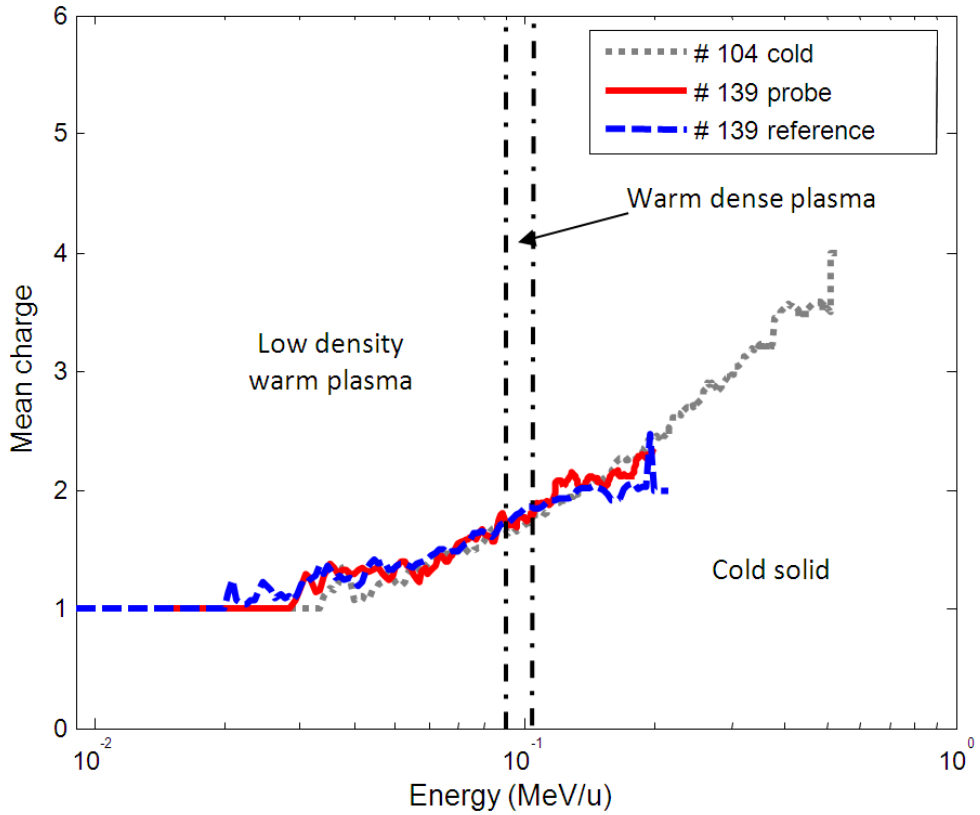

Figure IV-30: Mean charge of typical heated shot for which the laser beams were timed so that 0.1 MeV/u carbon ions were passing through WDM. It is compared with the mean charge of the reference and the mean charge we measured in cold solid-density matter.

In the case of 0.05 MeV/u, the energies probing WDM are comprised between 0.045 and 0.05 MeV/u. In this energy range, our resolution is very low. However, with respect to our error bars, we observed the same tendency.

To conclude, the difference in term of TOF between probing ions significantly reduced the energy range that can be probed in WDM in one shot. We were only able to measure the charge distribution of projectiles propagating through WDM with energy comprised between 0.4-0.55 MeV/u, 0.09-0.1MeV/u, 0.045-0.05 MeV/u. We have shown that plasma effects in WDM heated up to 1 eV do not significantly impact the mean charge of the 0.04 – 0.5 MeV/u carbon beam passing through aluminum. We believe this is mainly due to the very low temperature reached. The aluminum plasma is too cold in our experiment to see any significant change in its ionization and electronic structure (see chapter II).

IV.2.4.5 Comparison with accelerators results and ETACHA

The first main objective of our experiment was to test our platform by comparing our cold data with what had been already recorded on conventional accelerators. For this, I have reviewed what has been measured and published on charge equilibrium from accelerator facilities up to now. These cold measurements using accelerators are still ongoing, accompanying the improvement of accelerators and targets manufacturing. It started with the earliest measurement of stopping power [2, 34]. It should be noted that some of these researches are performed in order to improve accelerator stripping method rather than to study the ion charge exchange process. This explains why the equilibrium is sometimes not reached and the lack of data for low energy particles. Hence, we checked that the measured mean charges were truly at equilibrium by comparing the target thickness and the equilibrium length provided by the code ETACHA (see section IV.2.3.1). Note that it was only possible in the energy range where ETACHA is considered valid, i.e., typically above 0.1 MeV/u.

It should be noted that only few data exist for aluminum target, therefore we took the liberty to add the data corresponding to carbon target (which has been much more studied). This is justified as, according to the estimate of Schiwietz (see Figure IV-11), the difference between those, is 0 at 10 MeV/u and 15 % at 10 keV/u. In addition, so as to compare with our data where neutrals cannot be counted, we removed the neutral and negative ions from the accelerator mean charge computation.

Data from accelerators is compared with our measurement in Figure IV-31. The different types of dots correspond to measurements performed by the same team on the same experiment. First, one can see that carbon or aluminum accelerators points effectively remain very close one to each other in the energy section where aluminum points are provided. Although our experimental data are lower than the accelerator ones, one can see that they are fairly fitting, showing in particular the same slope. Interestingly, we found that the two curves would fit very well, if one divides the energy of our data by a factor of 1.5, keeping the mean charge unchanged. Since the relative error bar in energy is 2.5 %, according to the calibration of our detector (see appendix), this feature cannot be caused by a lack of precision of our diagnostic, hence cannot explain the difference observed.

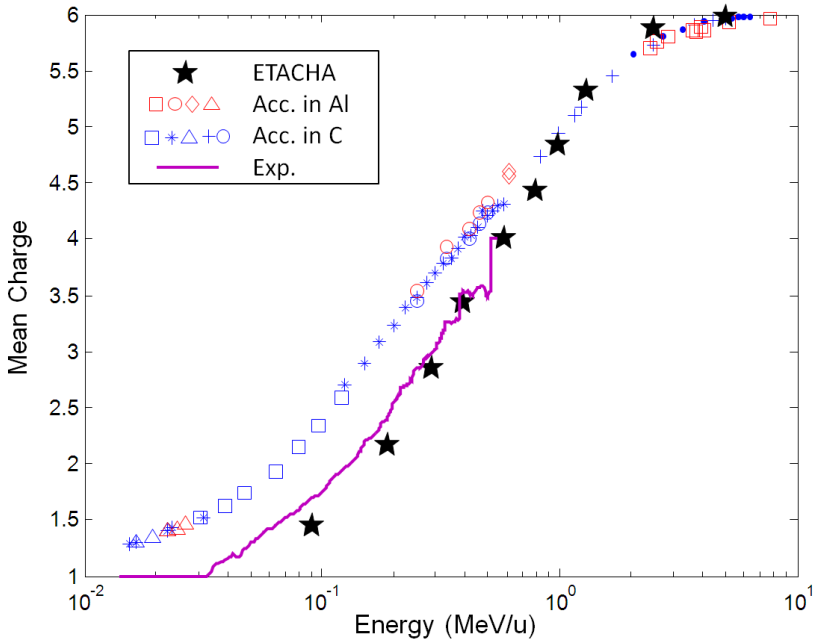

Figure IV-31: Mean charge (without counting neutral and negative ions) measurement performed on our experiment (purple line) compared to accelerator data in aluminum (red dots) and in carbon (blue dots) and ETACHA calculation (black stars). Each kind of dot corresponds to data recorded in a different experiment.

Then we wanted to compare with the code ETACHA that is commonly used in the domain to predict the charge equilibrium of a particle emerging from a cold solid-density foil (see section IV.2.3.1). The ion beam is assumed to be monoenergetic and the particles are assumed to propagate straight inside the matter, i.e., straggling is neglected. It is also possible to take into account, but separately, the effect of the energy loss inside the matter. In Figure IV-32 is shown the evolution of the charge fraction of a 0.4 MeV/u C^{2+} ion as it passes through a solid-density aluminum foil. One can see that the thickness needed for the ion beam average charge to reach equilibrium is approximately 10 µg/cm². This is way below the thickness traversed by the carbon ion probe beam in our experiment. Indeed, our thinnest secondary targets leads to a travel of 71 nm which corresponds to a relative thickness of 19.2 µg/cm².

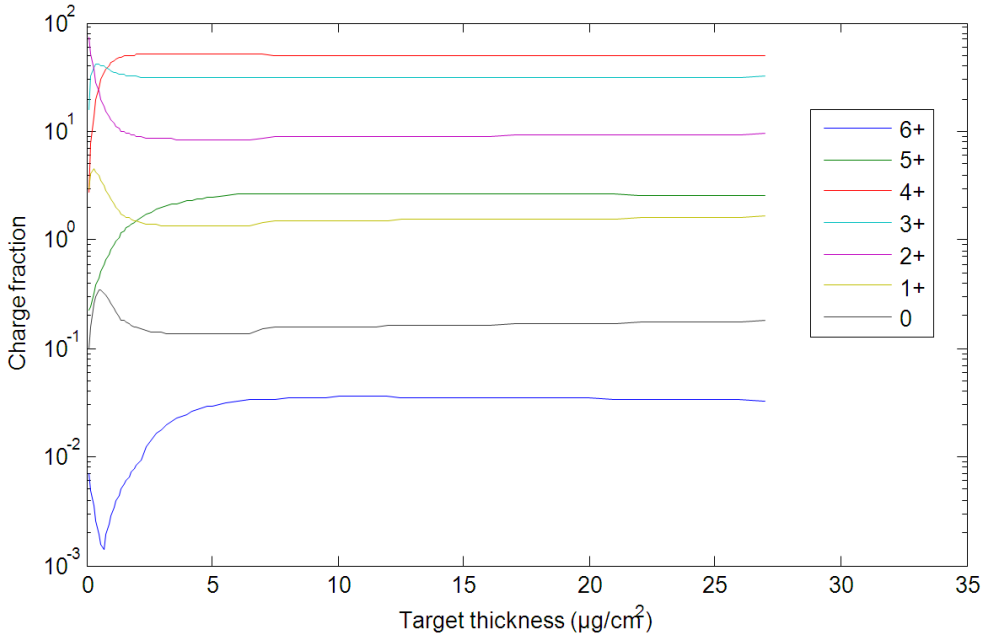

Figure IV-32: Evolution of the charge fraction of a 0.4 MeV/u carbon ion beam propagating through cold solid-density aluminum.

Hence we can compare ETACHA equilibrated results to the data without taking into account the input. To run the simulation, we arbitrarily chose a C^{2+} monoenergetic beam as input and recorded the mean charge when varying the energy. The stopping power, rather constant for such small thicknesses, was taken into account. The ensuing curve, shown on Figure IV-31, is fitting very well to our data. In order to make sure that we compare the same quantity as in the experiment, neutrals have not been counted in this case too.

When comparing the fraction distribution at equilibrium predicted ETACHA with the one we measured in experiment (see Figure IV-33), some differences arise. Although one can appreciate an impeccable fit for C^{4+}, the proportion in C^{3+} seems to be underestimated by a factor of 20 %. The shape and the position of the maximum are however preserved. C^{2+} population is also fitting well at high energy until 0.2 MeV/u, but it peaks at higher energy than measured and its proportion is underestimated by a factor of 30 %. Regarding C^{1+} population, it starts its increase at higher energy (0.3 MeV/u), but keeps the same slope than the measured one.

ETACHA is considered to provide relatively correct estimation until 0.1 MeV/u, and tend to overestimate the capture cross-section below (from comparison with accelerator data). This could explain the underlined differences when it comes to low energies.

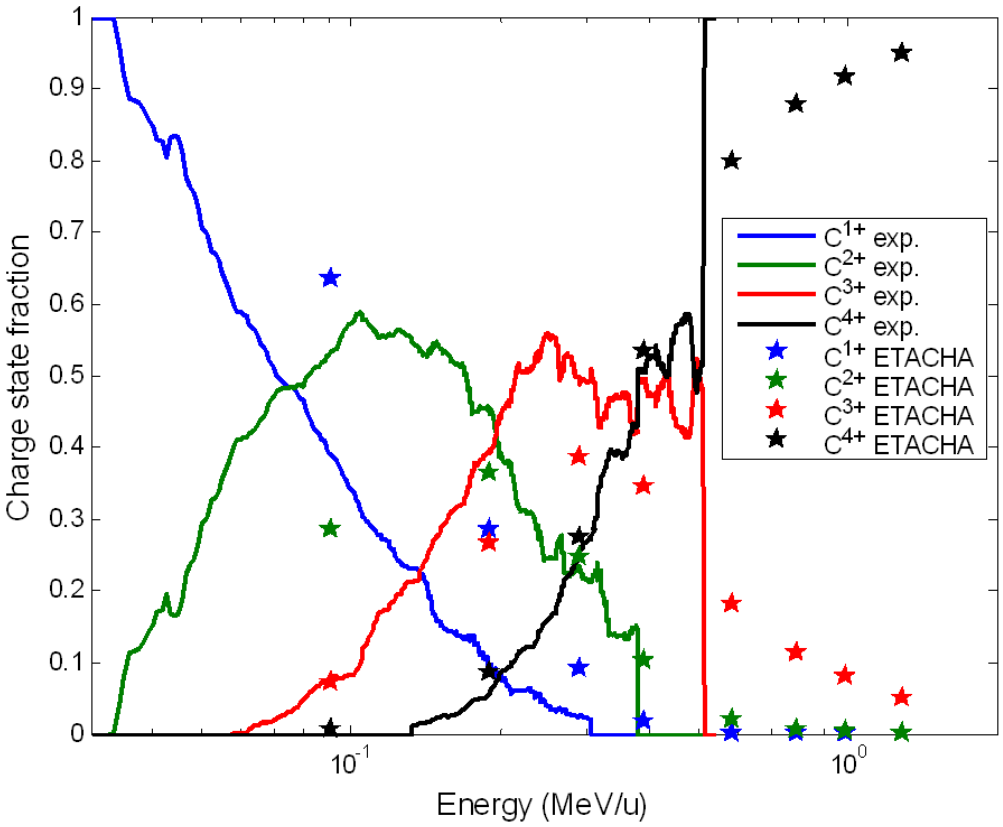

Figure IV-33: Charge fraction comparison between our results (thick lines), accelerator's records with energy multiplied by a factor of 1.5 (thin lines) and ETACHA (stars). Blue is for C^{1+}, green C^{2+}, red C^{3+} and cyan C^{4+}. The fractions have been calculated without counting neutrals and ions with higher charge than C^{4+}.

In conclusion, in the energy range from 0.1 MeV to 0.5 MeV, we observed a reasonable agreement with accelerator data and good agreement with the equilibrium mean charge computed by ETACHA. Note that others have already shown that some empirical formulae deduced from accelerator measurements overestimate the mean charge [57], even if, it is true, only for ion of higher atomic numbers ($Z_1 \geq 53$). This might explain the difference we observed between our measurements and those performed in accelerators.

IV.2.4.6 Discussion of our results

IV.2.4.6.1 Interaction with the background gas of the chamber

Before discussing about the equilibration of the carbon ion charge in, respectively, cold and heated matter, let us first concentrate on the influence of the residual gas inside the chamber on the projectile charge. In conventional accelerators, it is negligible considering the very low pressure of the residual gas, i.e., below 10^{-7} mbar. However, it is measured to be only below 10^{-3} mbar in our experiment. Therefore, it is important to investigate the impact of the interaction between the ion beam

and the residual gas from the secondary target to the detector and the possibility of an equilibration of the ion beam in the residual gas (see Figure IV-34).

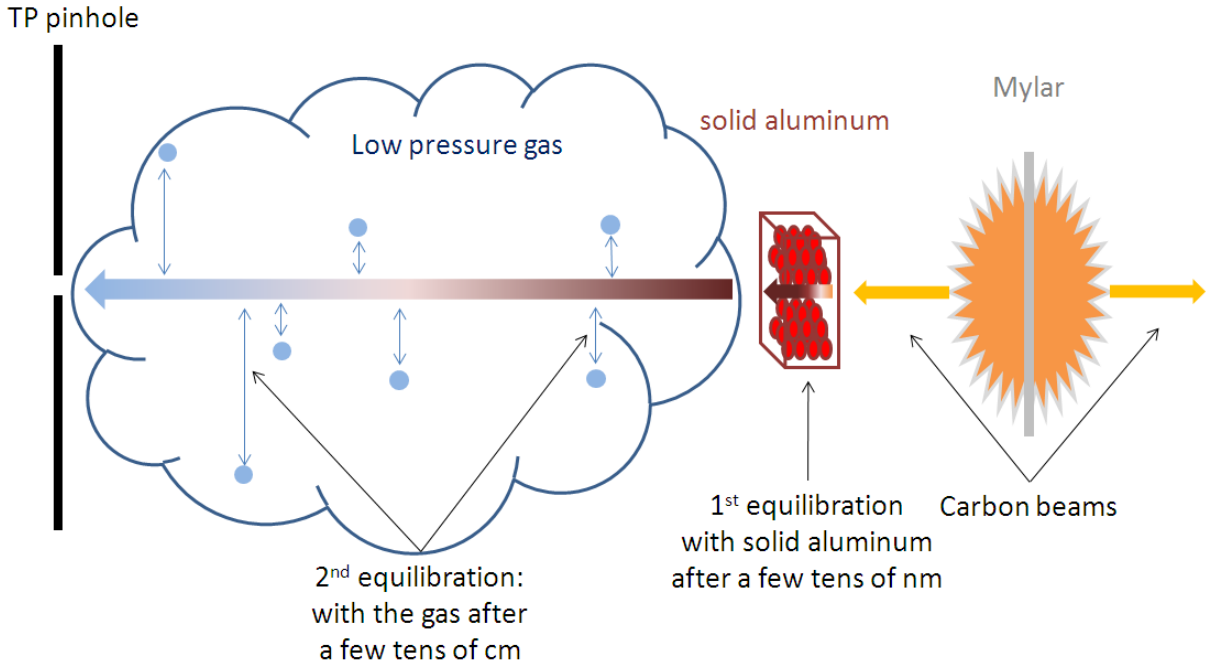

Figure IV-34: Equilibration with the target chamber low density gas of the emerging probe carbon beam.

The difference we underlined between the measurements performed in conventional accelerators is consistent with such possibility. Indeed the equilibrium mean charge of an ion passing through a gas is known to be lower than the equilibrium mean charge of the same particle passing through a solid-density target (see section IV.2.3.1). Even if only a few experimental data exist on carbon ion charge exchange in nitrogen[19] (N_2, $Z_2 = 14$) especially in the energy range we are concerned by, Grande & Schiwietz [33, 58] have developed an universal empirical formula scaling the experimental data on many projectiles (from proton to uranium) and target materials which provides equilibrium mean charges of an ion beam in both gases and solid. In Figure IV-35, we compare the mean charge we obtain experimentally with the equilibrium mean charge given by these formulas. As expected, our experimental curve is lower than the equilibrium mean charge in nitrogen and, as expected, further compared to the equilibrium mean charge in solid-density aluminum.

[19] The closest gas in term of atomic number to ambient air

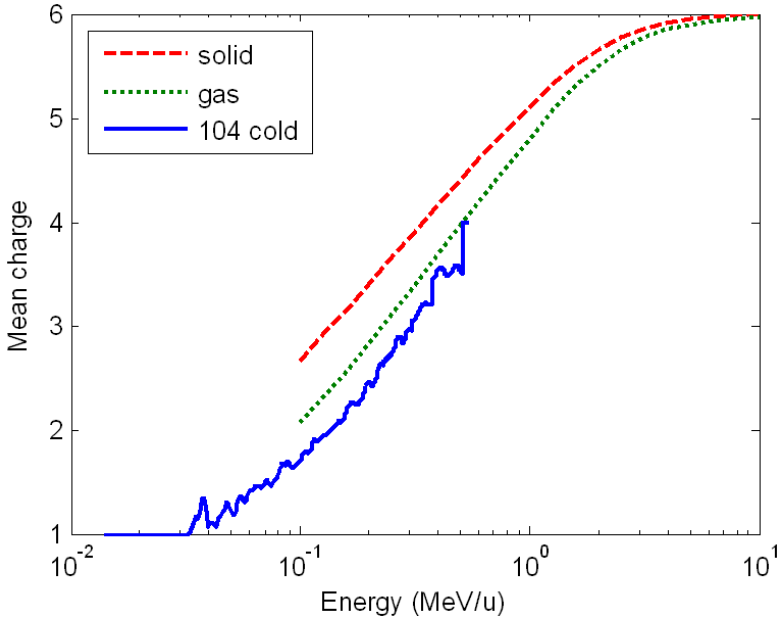

Figure IV-35: Comparison between our experimental mean charge and the equilibrium mean charge in, respectively, cold solid-density aluminum (curve) and in cold nitrogen gas (dotted curve) given in Refs [33, 58]. According to the validity range given for these two formulas, they can be used for energy above 0.1 MeV/u in our case. Their relative error bars in charge is estimated around 16 %.

Let us now explore in more detail the possibility of equilibration in the low-density residual gas. One has to know that only a few experimental data exist on carbon ion charge exchange in nitrogen [26].

Starting with the equilibrated distribution of an ion beam emerging from a solid-density cold foil, we calculated periodically along the ion beam path inside the low-density gas, the ion charge distribution of the beam considering only the electron-capture cross-sections:

$$\begin{cases} f_6(v,x_{i+1}) = f_6(v,x_i)\left[1-\sigma_{65}n_p dx\right] \\ f_5(v,x_{i+1}) = f_6(v,x_i)\sigma_{65}n_p dx + f_5(v,x_i)\left[1-\sigma_{54}n_p dx\right] \\ f_4(v,x_{i+1}) = f_5(v,x_i)\sigma_{54}n_p dx + f_4(v,x_i)\left[1-\sigma_{43}n_p dx\right] \\ f_3(v,x_{i+1}) = f_4(v,x_i)\sigma_{54}n_p dx + f_3(v,x_i)\left[1-\sigma_{32}n_p dx\right] \\ f_2(v,x_{i+1}) = f_3(v,x_i)\sigma_{54}n_p dx + f_2(v,x_i)\left[1-\sigma_{21}n_p dx\right] \\ f_1(v,x_{i+1}) = f_2(v,x_i)\sigma_{54}n_p dx + f_1(v,x_i)\left[1-\sigma_{10}n_p dx\right] \\ f_0(v,x_{i+1}) = f_1(v,x_i)\sigma_{54}n_p dx + f_0(v,x_i) \end{cases}, \qquad (4.11)$$

where $f_q(v,x_i)$ is the fraction of ions that carries the charge q (C^{q+}) at a given velocity v and at a distance x_i (along the ion beam path) from the secondary target, σ_{kl} is the electron-capture cross-section, where k and l denote the charge which the ion carries before and after the electron-capture, n_p is the density of the gas and $dx = x_{i+1} - x_i = constant$. Note that we assume the trajectory of each ion to be straight. This simple model does not take into account several elementary processes that would have tempered the neutralization. If this first estimate shows that the impact of passing

through a gas is not negligible, we would need to improve this model and indeed improve the vacuum inside the target chamber.

Instead of the few accelerator data in cold solid-density aluminum foil, we use as input the more numerous charge distribution points of an equilibrated carbon ion beam emerging from carbon foil: anyway, they remain very close one to each other. As recombination (or electron-capture) cross-sections, we used Schlachter [59] universal empirical rule based on accelerator measurements that provided predictions for a wide variety of projectile-target combinations for projectiles range in energy from 0.3 to 8.5 MeV/u, and charge states, Z_2 as high as 59+. To stick to our experiment, we evaluated the impact of a low pressure (P) gas of nitrogen applied over 70 cm, the distance between the secondary aluminum target and our detector. The 10^{-3} mbar pressure of our gas gives an upper limit for the residual gas (N_2) density of,

$$n_p = \frac{PN_a}{RT} \cong 3 \times 10^{13}/cm^3, \tag{4.12}$$

where R is the gas constant, T the gas temperature (300 K) and N_a the Avogadro constant. We fixed dx to 10 µm so that the precision gained by reducing even more dx remains negligible.

Accordingly to what we have done earlier, when computing the mean charge, we do not take into account the neutrals. The results for various gas pressures are shown in Figure IV-36.

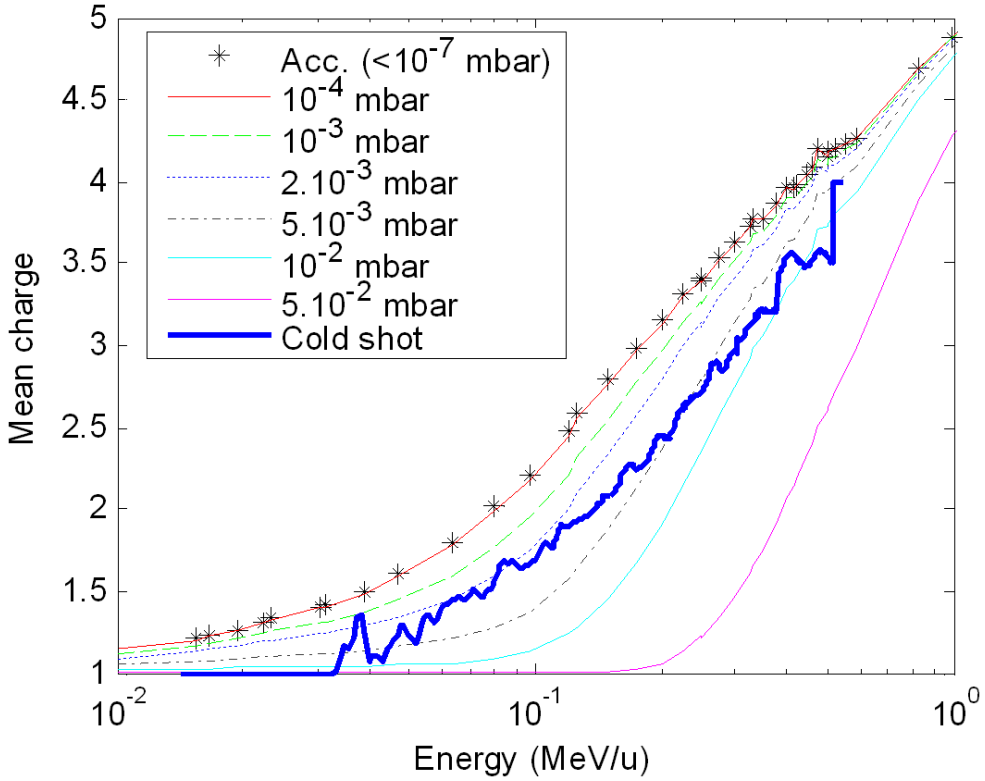

Figure IV-36: Predicted evolution of the carbon ion mean charge recorded in accelerator (pressure below 10^{-7} mbar) with the pressure inside the chamber compared to our experimental measurement; the neutral projectiles are not taken into account when plotting the curve.

First, one can see that the effect of neutralization is more important for low energy projectile. Note that the neutralization is artificially limited at very low energy due to the absence of the neutral particles in our calculation of the mean charge. Secondly, as expected, the neutralization rate is increasing with the pressure. Indeed a higher pressure means a denser gas, and so more interactions between the projectile and the atoms of the medium. One can see that the recombination is null for pressure below 10^{-4} mbar and stays negligible below 10^{-3} mbar with respect to the error bar estimated by comparing the reference and probe ion beam mean charge (+/- 0.1). The pressure is predicted to play an important role on the mean charge especially for lower energy. By comparing our experimental data with the generated set of curves, we can roughly infer what would be the chamber pressure required for the accelerator data to stick to our cold experimental curve. From the set of curves, we can deduce a pressure around 0.5 – 1×10^{-2} mbar is needed for energy above 0.2 MeV/u. For lower energy, the pressure is required to be lower, around 2 - 5 $\times10^{-3}$ mbar. It should be noted that the results for low energy projectiles have to be handle carefully, since we are no longer in the validity energy range of the empirical rule. In addition the neutral population becomes very important which can decrease dramatically the precision of our experimental measurement of the average charge.

To sum up this short study, we can say that for gas pressure higher than 2×10^{-3} mbar, the residual gas can play an important role on the ion beam mean charge measured by our diagnostic. In such case,

its impact should be clarified using experimental measurements. At the opposite, for pressure below 2×10^{-3} mbar, the impact of the residual gas pressure can be neglected. Note that the pressure is experimentally measured by a detector positioned closed to the vacuum pump and may underestimate a bit the real pressure inside the chamber. Nevertheless, the difference between the pressure we measured in our experiment and the minimum pressure required for the accelerator data to stick to our cold experimental curve is, by far, too high to be explained by such underestimation.

Another argument moving in the same direction may be added to the last one. To estimate if the recombination with the cold gas of the target chamber could affect the charge distribution of the beam, we computed the reduced thickness traversed by the particle from the source to the detector (70 cm) assuming the pressure to be 10^{-3} mbar and found it to be approximately 2×10^{-4} µg/cm². This quantity turns out to be completely negligible compared to 0.6 µg/cm², which is the equilibration length of 0.2 MeV/u carbon ions in N_2 (i.e., a situation quite similar to ours) according to the data reported in Ref. [60] using conventional accelerators. This measurement is illustrated in Figure IV-37.

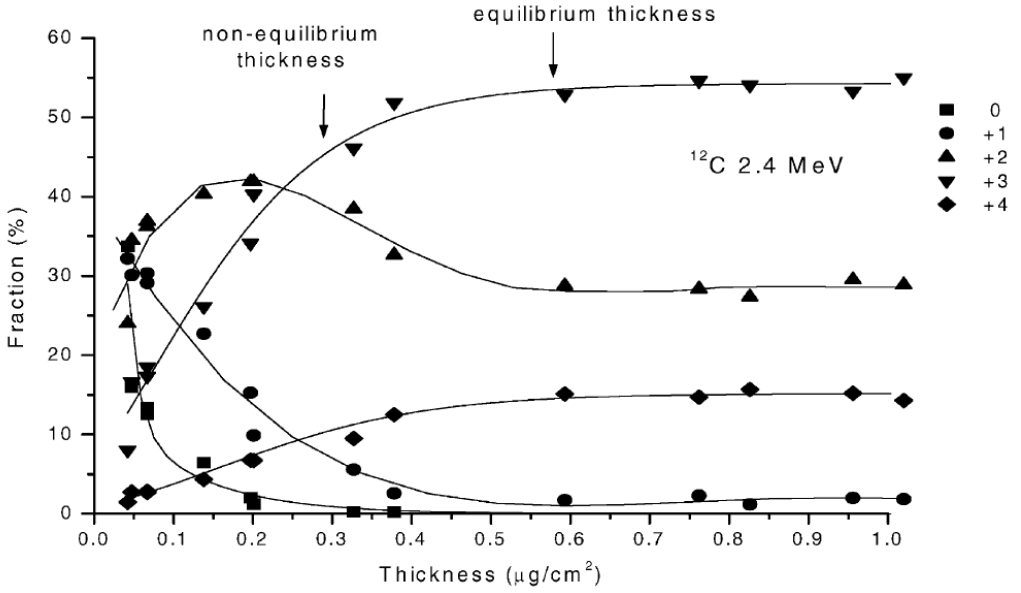

Figure IV-37: Charge fraction of a 0.2 MeV/u carbon beam as a function of the N_2 gas stripper thickness (extracted from Ref. [60]).

To conclude, it is highly unlikely that we are measuring carbon ion beam equilibrated in the low pressure gas of the target chamber. It might alter by a small amount our measurements, but this change stays within our error bars. It could be interesting for future experiments using the same platform to study more carefully the impact of low pressure gas inside the target chamber. This would result on

an estimate of a pressure limit (depending on projectile energy and Z_1) above which charge equilibrium measurements cannot be carried out.

IV.2.4.6.2 Interaction with cold matter

Let us now discuss the cold interaction results. As shown in Figure IV-24, we can divide the mean charge of the probing beam in two parts: (1) Low energies, where both reference and probe are overlapping one each other and (2) high energies where they significantly differ.

One hypothesis is that the reference carbon beam for energies typically below 0.1– 0.2 MeV/u is already in equilibrium when leaving the source target, and on the other hand, the higher energy portion of the spectrum (above 0.1– 0.2 MeV/u) is not at equilibrium after leaving the source and reach equilibrium only when propagating through the aluminum foil/plasma. Indeed, the ions produced by TNSA are accelerated within an expanded plasma where complex ionization and electron capture processes take place between the ions and the co-moving electrons. Due to the difference in term of TOF, the beam is linearly stretched in velocity. Hence, the (slow) low energy part of the beam (below 0.1 – 0.2 MeV/u) transits for a longer time in the dense part of the accelerating sheath, and thus will tend to be already in equilibrium when leaving the source target (gold foil). This is what can be seen in Figure IV-24 ; ions with energy below 0.1 MeV/u from both reference and probe beams overlap each other: this means that the reference carbon beam, for energies below 0.1 MeV/u, is equilibrated.

Another hypothesis that could explain such a behavior is that the ion charge would be equilibrated by the co-moving electrons once they had left the electrostatic sheath. To estimate, the effect of these co-moving electrons, we have to consider several points.

Let us first estimate their temperature. From a previous experimental study that was conducted on the same facility, the transverse temperature of co-moving electrons of a laser-generated ion beam was measured around 30-100 eV (see Figure IV-38). Although we have to keep in mind that this is still imperfect to evaluate the impact of these co-moving electrons on the ion beam charge, we then use the ionization and recombination rates given by the FLYCHK code [61]. For this, we assumed that the ions were at rest in a 100 eV electron gas.

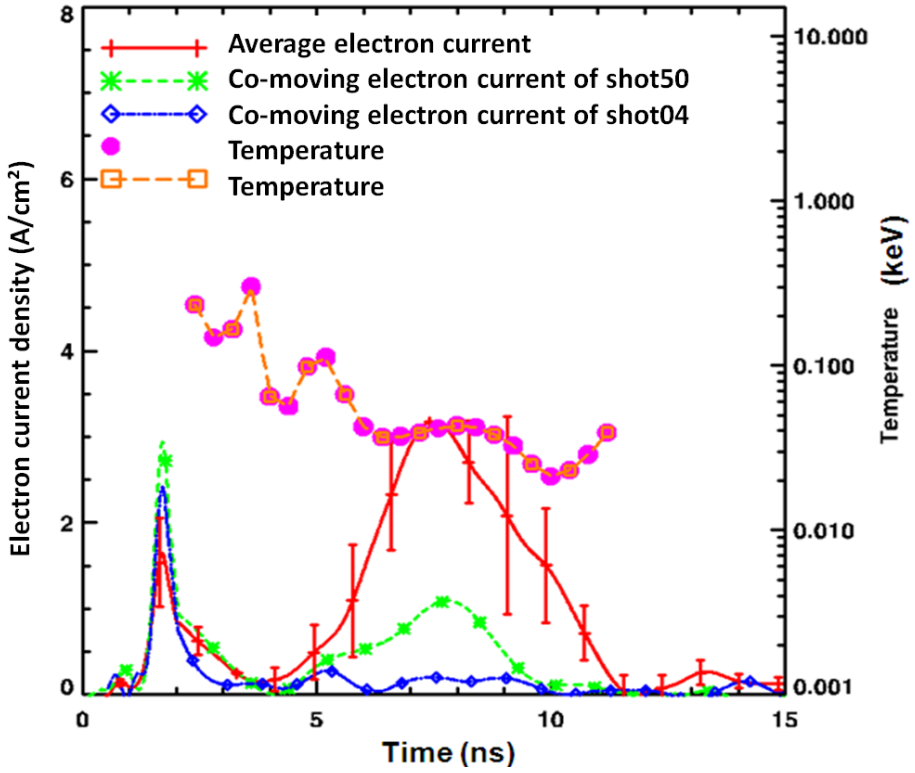

Figure IV-38: Measurements of co-moving electrons accompanying a fast, laser-produced ion beam. The measurements were conducted using the 100TW laser at LULI and performed using Faraday cups. The blue and green curves correspond to shots on which the low electrons, i.e., co-moving electrons, were filtered out, whereas the red curve corresponds to the current average of all of the shots on which they are not. The pink and brown curves correspond to the deduced co-moving electron temperature as a function of time (in ns) at the detector, i.e., to ions of different energy as they fly into the detector from the source.

To estimate the density of this co-moving electron gas along the beam path, i.e., after leaving the electrostatic sheath to the secondary target, we computed the ion charge density of the expanding ion beam. Here, we assume (which is justified by the same Faraday cups measurements) that everywhere the ion beam is spatially neutralized by the co-moving electrons; hence the density of co-moving electrons is equal to the ion charge density. Using an average beam divergence angle of 10° [44], an initial beam density at the source of 10^{19} cm^{-3} [62], a total number of accelerated charges of the order of 3.5×10^{11} (calculated using the spectra of a reference ion beam), and taking also into account the differential TOF of the ions, one can compute the co-moving electron density of the beam along the path as a function of the energy of the ions they are co-moving with. For instance, the evolution of density of the electrons co-moving with 0.1 MeV/u carbon ions as a function of the distance with the source is shown on Figure IV-39.

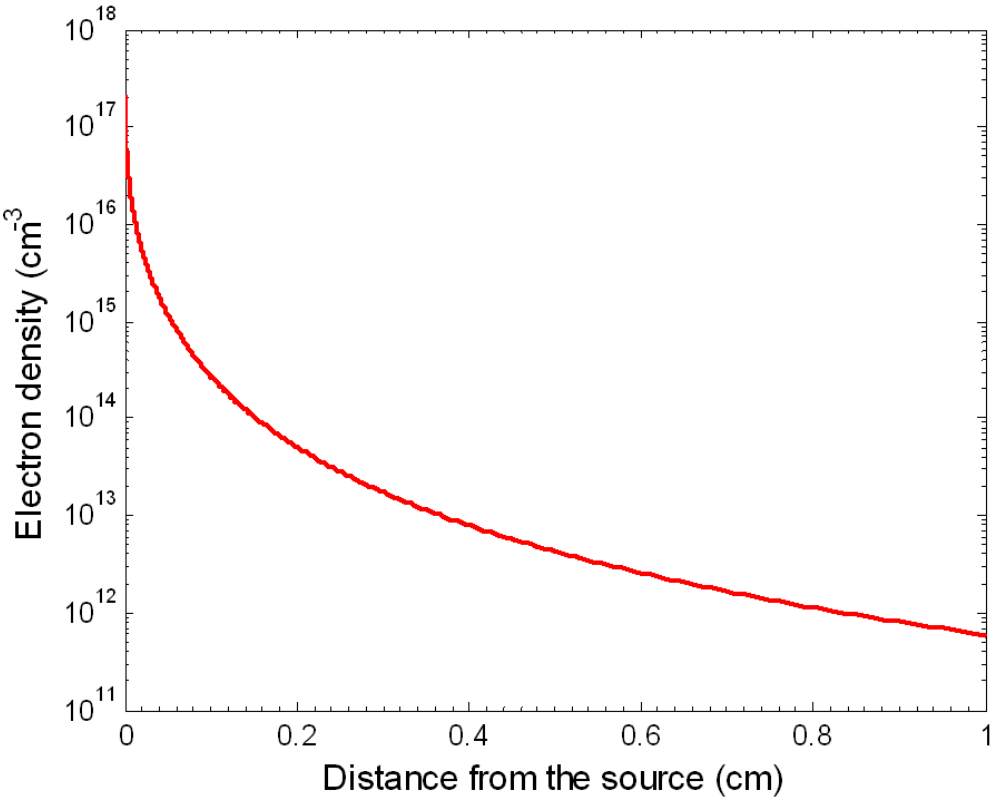

Figure IV-39: Density of electrons co-moving with 0.1 MeV/u carbon ions as a function of the distance from the source.

Now, using both recombination and ionization rates from FLYCHK and the density curve, one can estimate the evolution of the mean charge of several 0.1 MeV monoenergetic beams composed, respectively of only C^{1+}, C^{2+}, C^{3+} and C^{4+} when propagating with the co-moving electrons (see Figure IV-40) from the source (after the sheath) and the secondary target located 1 cm away. We clearly observe that, due to the decrease of the electron density with the distance from the source, the co-moving electrons between the source and the secondary target cannot modify the mean charge of the ion beam.

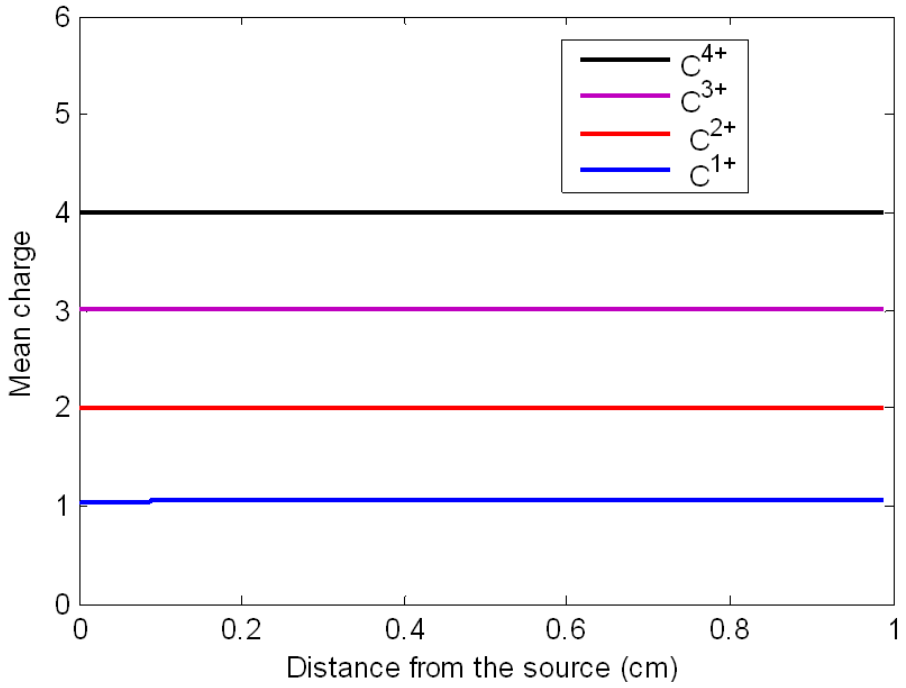

Figure IV-40: Evolution of the mean charge of several 0.1 MeV/u monoenergetic beams composed, respectively of only C^{1+}, C^{2+}, C^{3+} and C^{4+} when propagating with the co-moving electrons, according to FLYCHK.

In summary, according to our estimation, the interaction with the co-moving electrons during the propagation of the spatially-neutralized ion beam in vacuum is very unlikely to significantly affect the charge distribution and thus to explain the equilibration at low energy we observed. Although we are not in a position to fully model the dynamics leading to the observed the charge state of the ion beam, we consider that an equilibration process at low energy (as observed) is hence more likely to happen at the source, where the plasma is the densest.

Such equilibration does not affect however our capability to performed measurement of charge equilibration since we could indeed use for this the high energy un-equilibrated portion of the probe beam (i.e., $E \gtrsim 0.1\ \mathrm{MeV/u}$). Indeed, contrary to the low energy portion, one can see that the higher energy portion of the spectrum (0.1-0.8 MeV/u), was not in equilibrium after leaving the source target: the curve of the equilibrated probe beam is lower than the reference curve. Therefore, we can use this part of the ion beam to characterize the charge altering properties of the secondary target. The observed variations of the limit between equilibration/non-equilibration may be explained by the fluctuation of the laser conditions. This affects the plasma sheath density and temperature, which changes the Debye length.

IV.2.4.6.3 Comparison with semi-empirical formulas based on stopping power

Although we have explained in section IV.2.2 that the stopping power of an ion beam propagating through matter is *a priori* not proportional to $Q_{rms}{}^2$, it is interesting to compare our experimental results in cold solid-density matter with the effective charge based on stopping power measurements. We found that the difference between Q_{rms} and $\langle Q_1 \rangle_{eq}$ to be around 0.1 in our experiment, this is of the same order of magnitude with respect to our error bar. Hence, we choose to keep using $\langle Q_1 \rangle_{eq}$ for the comparison (instead of Q_{rms})[20]. In Figure IV-41, semi-empirical formulas of $Z_{eff,}$ from Northcliff [2], Brown [63], Gus'kov [64] and Basko [65] are compared with the mean equilibrium charge we obtained in cold matter. For consistency, we also plotted the mean equilibrium charge calculated from Schiwietz [33] empirical formula based on the measurements performed in conventional accelerators.

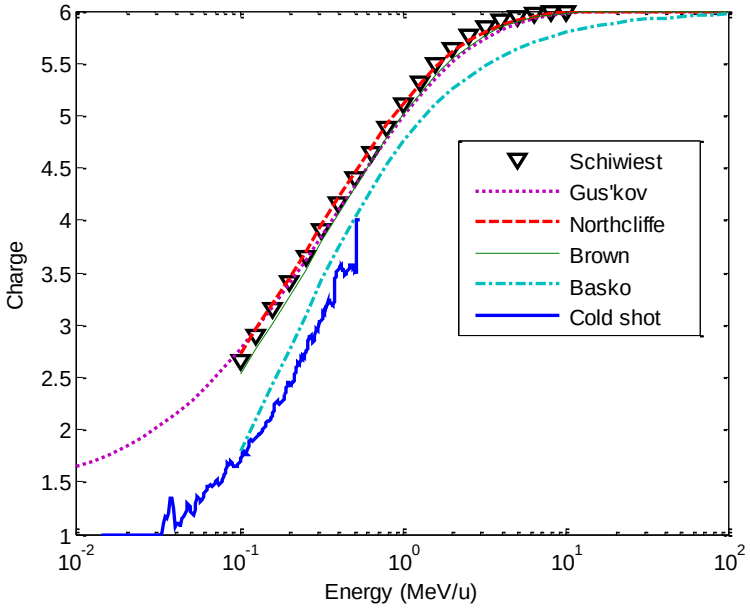

Figure IV-41: Mean equilibrium charge in cold solid-density aluminum measured in our experiment compared with semi-empirical curves from Refs. [2], [63], [64], [65] and mean equilibrium charge curve obtained from Schiwietz empirical formula [33]. Apart from Gus'kov, all formulas are only valid above 0.1 MeV/u. This validity zone roughly corresponds to the zone where the fraction of neutrals, particles that we could not measure in our experiment, is negligible.

We observe that our curve is reasonable agreement with Z_{eff} of Bakso, but lies lower than the other effective charges. It can be explained as followed. Although all Z_{eff} formulas rely only on the stopping power data, Z_{eff} of Gus'kov, Northcliffe and Brown are simply obtained from the ratio between the stopping of ions and protons as defined in chapter II. Z_{eff} of Basko is computed using a different

[20] Note that Q_{rms} is always higher than $\langle Q_1 \rangle_{eq}$.

method: first, the stopping power is calculated theoretically using an improved formula based on Bethe-Bloch stopping power for a point charge (see section IV.1.1) [4], in which the charge of the projectile is replaced by an equilibrium mean charge. The charge of the projectile is therefore not only taken into account in the prefactor, but also in the stopping number. Then, using Nikolaiev semi-empirical formula [32] for the equilibrium mean charge, the computed stopping power is compared to the stopping power measured in conventional accelerators for different projectile ions (U, Ag, Ti Al, C and Be) propagating in solid-density silver. Basko formula is eventually inferred from Nikolaiev semi-empirical formula which coefficients have been modified so that the computed stopping power overlays experimental results for energies from 0.1 to 10 MeV/u. Consequently, the effective charge calculated by Basko is actually closer to an equilibrium mean charge than an effective charge as defined in chapter II. This explained the fair agreement between Basko formula and the equilibrium mean charge we measured experimentally. Hence, this observation confirms the importance in our energy range of the dependence of the stopping number on the projectile-charge when calculating the stopping power.

Note that the good agreement between the empirical formula based on equilibrium charge measurements in conventional accelerator and Z_{eff} of Gus'kov, Northcliffe and Brown moderates this conclusion. Indeed, it indicates at the opposite, that the stopping power scaling in ${Q_{rms}}^2$ is very reasonable in our energy range.

IV.2.4.7 Conclusion

We have demonstrated that we can reproduce well, with our experimental set-up, data obtained in cold matter with accelerators on a single shot. Accordingly a very good agreement is found with the results of the ETACHA code in its recent version. Furthermore we have also demonstrated for the first time that measurements of the mean charge state of an ion beam passing in WDM under well controlled conditions can be realized. We have shown that plasma effects in WDM heated up to 1 eV do not significantly impact the mean charge of a 0.04 – 0.5 MeV/u carbon beam passing through aluminum. Next steps will be to perform similar measurements at higher temperature in WDM. Recent achievements of ultrafast isochoric heating of solids up to 100 eV using XFEL beams [12] offer interesting perspectives in this respect.

IV.2.5 Measurement of He-ion equilibrium charge state distribution

We then performed the same experiment using helium ion beam as probe instead of carbon. This is particularly interesting in the frame of ICF, since the fusion reaction produces 3.5 MeV helium-particles. Studying the stopping power, and more particularly the equilibrium mean charge, can provide us some useful information on the process of energy deposition of the produced helium ions.

We chose to use a helium gas jet as a source. As shown in chapter III, it also gives us the opportunity to generate simultaneously two similar ion beams. One is used as a reference and the other as a probe.

In the following, we only detail the results regarding the interaction with cold solid-density aluminum. Further analyses are necessary to explain and exploit what we measured in heated matter.

IV.2.5.1 Experimental set-up

The experiment was carried out using the TITAN laser at the Lawrence Livermore National Laboratory (LLNL) working in the CPA mode at a wavelength λ_0= 1.064 µm. Since only one CPA beam is available at TITAN, we use a split mirror to intercept a part of the main CPA beam, called direct beam, and reflect it on a second parabola focused at the target chamber center producing a second CPA beam, called split beam. The set-up of the "split beam configuration" is shown in Figure IV-42. We positioned the split mirror so that the split beam contained approximately 70-80 % of the total laser energy.

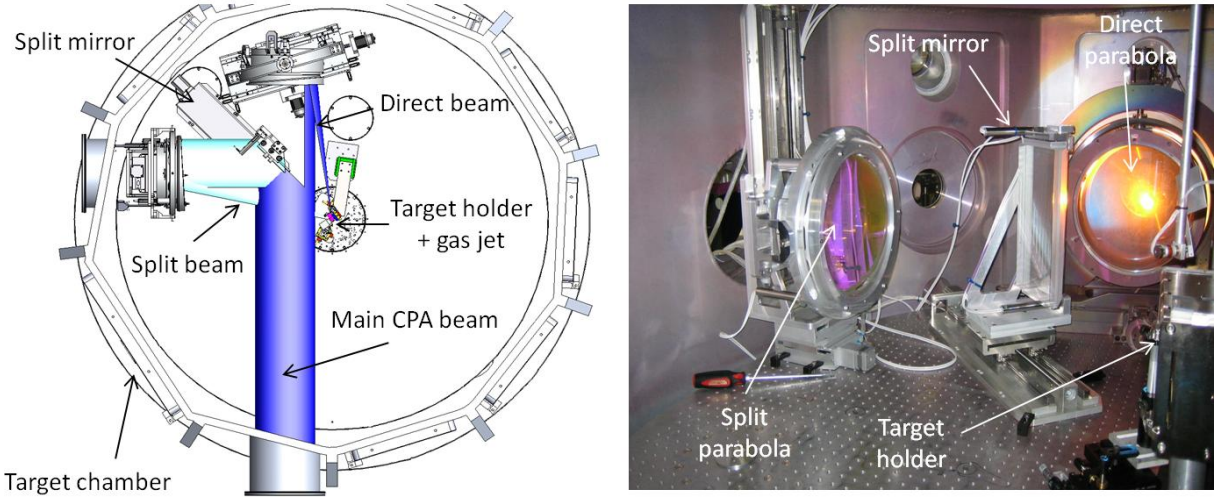

Figure IV-42: Split beam configuration.

The experimental set-up is shown in Figure IV-43. We used two regimes of the main CPA beam: (1) 200 J on target, 5 ps (FWHM) duration as measured after compression and (2) 130 J, 0.7 ps duration. The first regime allowed us to reach higher energy on target, while the second one allowed us to reach higher intensity on target. Both direct and split beams were focused to a focal spot of approximately 50 µm (FWHM) using two off-axis parabolas, one for each beam, of focal length approximately 800 mm. The direct and less energetic CPA beam was focused at the edge of helium gas jet to generate two similar helium beams perpendicularly to the laser propagation axis. The parameters of the ion beam source are already detailed in section III.3.1.2. While one of the helium beam is used as a reference, the other helium beam, called probe beam, propagates through an unheated/ heated 0.8 µm thick solid-density aluminum foil (secondary target), its propagation axis making an angle of 45° with the target normal axis. The split beam is used to generate an energetic proton beam in charge of heating the secondary target. It interacts with a 25 µm thick gold foil positioned at the laser focus and located 200 - 500 µm away from the secondary target producing an energetic broadband proton beam in the direction normal to the target surface, making an angle of 45° with respect to the surface of the secondary target. The delay between the direct and the split laser beams was fixed using a delay line located upstream in the laser line solely on the optical path of the direct beam.

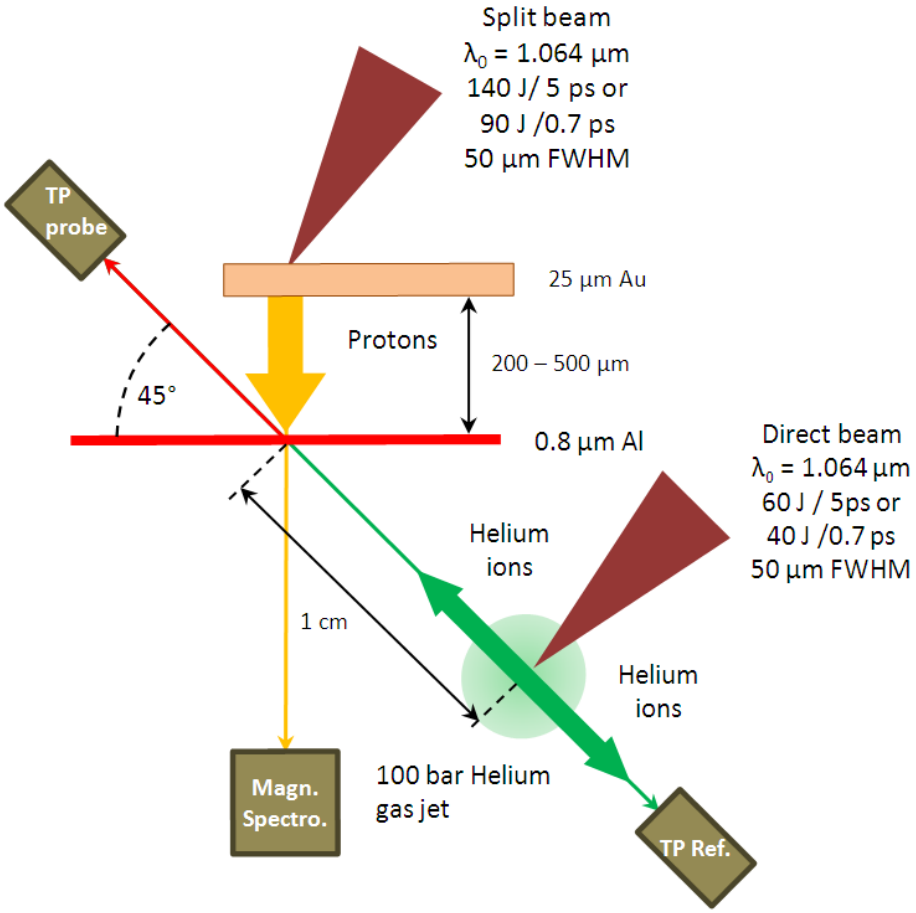

Figure IV-43: Experimental set-up.

IV.2.5.2 Diagnostics

The reference and probe spectra are measured by the same two TPs, respectively, East and West TPs already mentioned in section III.3.1.2.2. In order to measure the population of neutral, we modified the detector (see Figure IV-44): the part of the IP where the pinhole is imaged, i.e., the 0^{th} order, is covered by a solid state detector CR39 [66]. This detector not sensitive to light radiations, but particles, gives us the opportunity to separate the signal at the 0^{th} order due to neutral particles (not deflected by the magnetic and electric fields inside the TP) from the signal due to light radiation and thus, to measure the spectrum of the neutral population. However, we will see later that he neutral contribution is predicted negligible in the energy range resolved by our TPs, thus it should not affect our results.

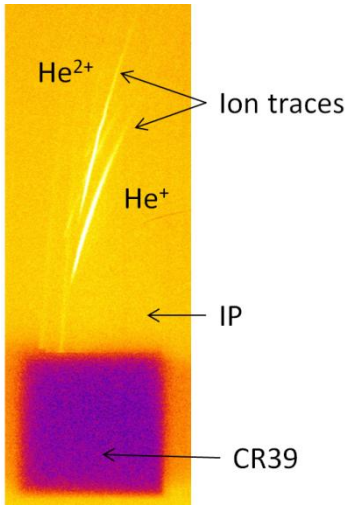

Figure IV-44: Signal of the reference ion beam detected on the IP. The signal of the 0^{th} order is obstructed by the opaque CR39 positioned in front of the IP (zone in violet).

In order to estimate the evolution of temperature and density of the heated aluminum foil, we apply the method already used in the experiment on the carbon equilibrium charge state distribution: we ran hydrodynamic simulations with ESTHER code, using as input the spectrum of the heating proton beam emerging from the secondary target recorded on each shot with a calibrated magnetic spectrometer.

IV.2.5.3 Characteristic of the helium ion-beam

The characteristics of the probe and reference helium ion-beams have already been detailed in chapter II.

We have mentioned as well that He^{+} comes from accelerated He^{2+} ions which have captured electrons from the medium when they pass through the dense and cold helium gas ejected by the gas jet. Indeed, we observed that the mean charge of the reference and probe beams without secondary target of various shots with different laser conditions are all overlapping as shown in Figure IV-46. In addition, this curve is found in good agreement with the equilibrium mean charge in helium gas measured in conventional accelerators [58].

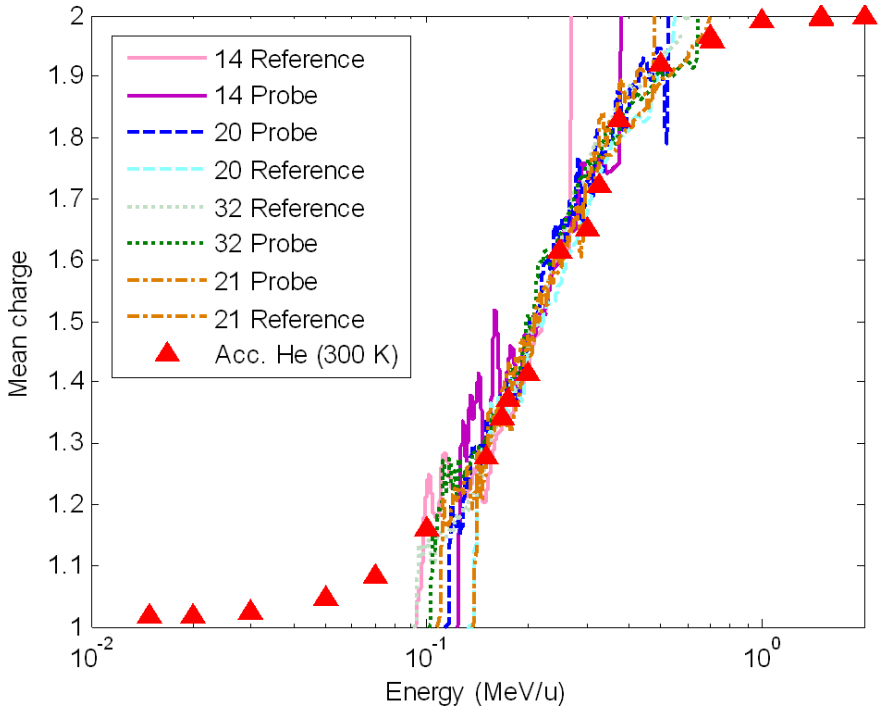

Figure IV-45: Mean charge of the reference and the probe helium beam measured in our experiment for various shot without secondary target and the equilibrium mean charge in cold helium gas measured in conventional accelerators.

Furthermore, we evaluated the equilibrium length in the helium gas using the method detailed in section IV.2.4.6.1 with the cross section of ionization and electron capture mechanisms tabulated in Ref. [26]. E.g. in Figure IV-46 is shown the evolution of the charge fraction and of the mean charge $\langle Q_1 \rangle$ along the path of a monoenegetic ion beam composed initially of 0.5 MeV/u He^{2+} and propagating in a helium gas of density 2×10^{18} cm^3. We found that the ion beam reaches equilibrium after propagating on a distance of around 1 mm. This is of the same order of magnitude than the size of the gas jet in our experiment.

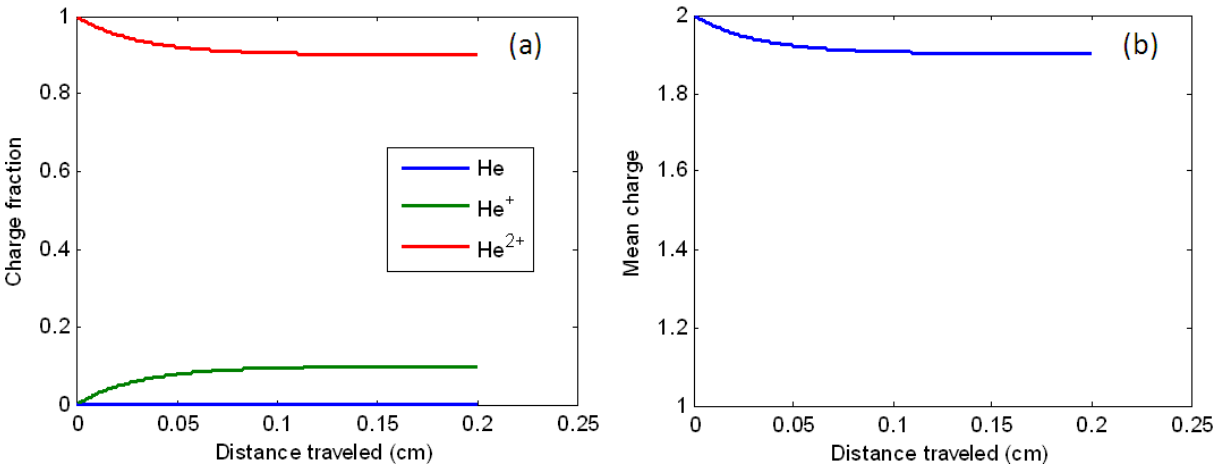

Figure IV-46: Evolution of, respectively, (a) the charge fraction and (b) the mean charge $\langle Q_1 \rangle$ (without counting the neutral) along the path of a 0.5 MeV/u ion beam, composed initially solely of He^{2+}, propagating in a helium gas of density 2×10^{18} cm^3.

Therefore, we can ascertain that our reference and probe beams without secondary target are actually equilibrated in the helium gas of the gas jet. This conclusion allows us to know with a good precision the initial charge state distribution of the probe beam before interaction with the secondary target. Moreover, it gives us also the opportunity to determine the error bar on the mean charge we measured by comparing the different curves we obtained: we estimated an error bar of +/- 0.05. Note that the precision decreases at the edges of our energy range, i.e., around 0.1 MeV/u and 0.8 MeV/u. This is due to the fact that the population of He^{2+} and He^{+} becomes too low to be detected at, respectively, low and high energy. To avoid this source of incertitude, we circumscribed our study in the energy range where both ions are present.

IV.2.5.4 Results: interaction with cold matter

Let us now focus on the interaction of the probe beam with the cold and solid-density aluminum foil. The purpose of this part of the experiment is again to validate our experimental set-up. Since the probe ion beam makes a 45° angle with the normal of the secondary target surface (see Figure IV-43), the probe beam travels inside the aluminum on a distance of approximately 1.13 µm ($\cong {}^{0.8\ \mu m}/_{\cos(45°)}$) corresponding to a relative thickness of approximately 306 µg/cm². We estimated using ETACHA the evolution of the mean charge of mono-energetic helium beams propagating through solid-density aluminum. We chose an arbitrary input a beam of charge of 1. The results are plotted in Figure IV-47. We observe that for all energies, the ion beam reaches equilibrium after a thickness of a few µg/cm² (3.7 nm). Therefore we can consider that, in our energy range, the helium ions are always at equilibrium when emerging from the cold secondary target.

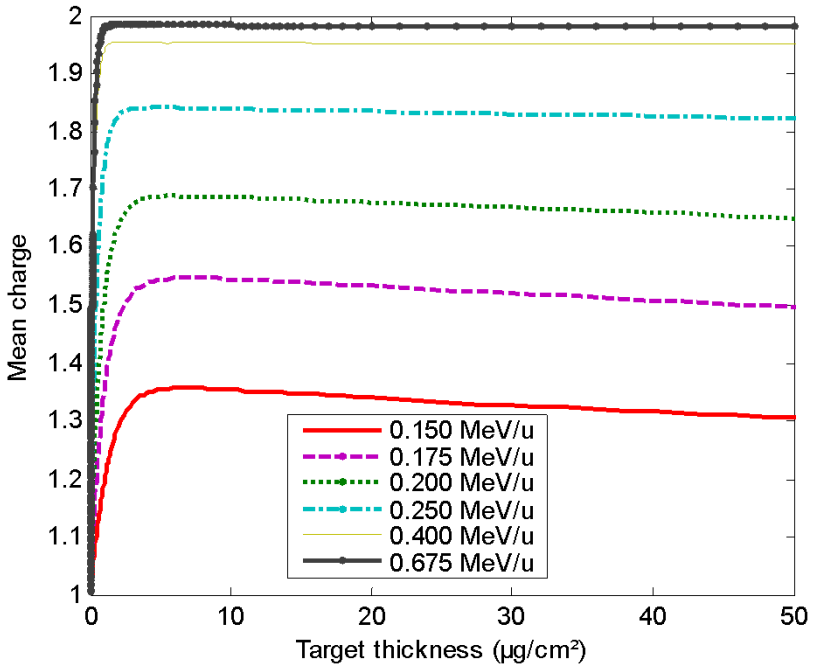

Figure IV-47: Evolution of the mean charge of mono-energetic helium beams (initially He^+) propagating through solid-density aluminum.

We notice that, after equilibration, the mean charge of all beams decreases with the target thickness. It is actually due to the energy lost by the projectiles when propagating, the stopping power being included in the simulation. Although the ion beams stay at equilibrium (with respect to their energy), this effect has to be taken in account in the analysis of the interaction with heated matter: it is of great importance to determine in the recorded probe spectrum the energies of the ions that have interacted with WDM.

Let us compare the probe ion-beam emerging from the cold aluminum foil and the reference ion-beam (i.e., the one emerging from the gas jet). Their spectra are shown in Figure IV-48 for two different shots. We can see that the probe beams after the aluminum foil exhibit a lower energy cut-off and lower number of ions for both He^+ and He^{2+} compared to their corresponding reference beams. This difference is caused by two effects: (1) the energy-loss by the probe ion-beams inside the aluminum foil, (2) the effect of scattering. Note that the lower population of ions of the probe beam noticeably lowers the signal-to-noise ratio on the IP detector and thus reduces the precision of our measurements, as highlighted by the fluctuation in the probe spectra. Considering the charge fraction, we clearly observe a higher proportion of He^{2+} with respect to He^+ in the probe beam than in the reference beam particularly at energies around 0.2 MeV/u.

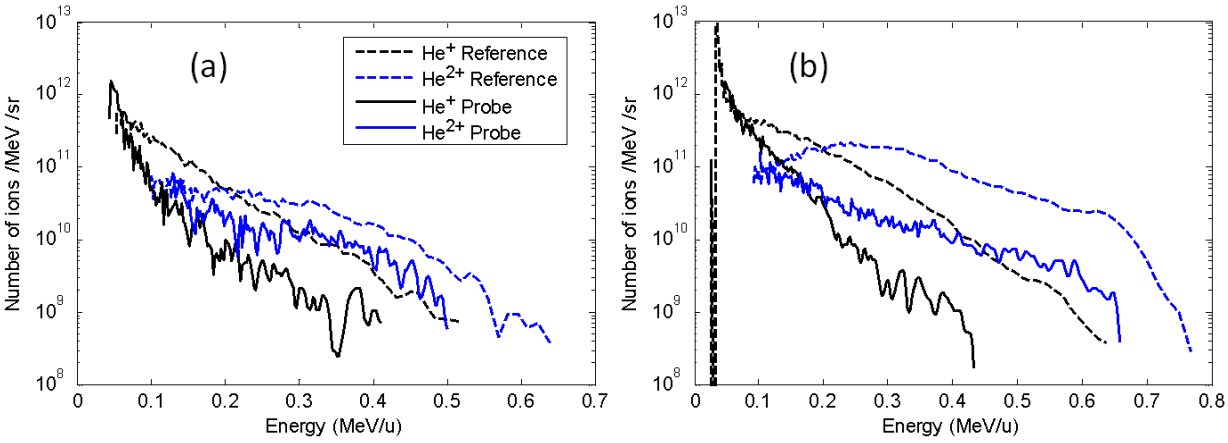

Figure IV-48: Reference and probe helium beam spectra of two different shots. The probe beam emerges from a cold solid-density aluminum foil.

The corresponding reference and probe mean charges are plotted in Figure IV-49. We observe that the equilibrium mean charge in aluminum is always higher than the one in helium in our energy range. This is due to the difference in term of free-flight path between two collisions in solid and gas (see section IV.2.3): the mean free path of the projectile in gas is longer than in solid-density matter. Hence the projectile electrons have time to decay into their ground states, while they stay excited in a solid-density medium.

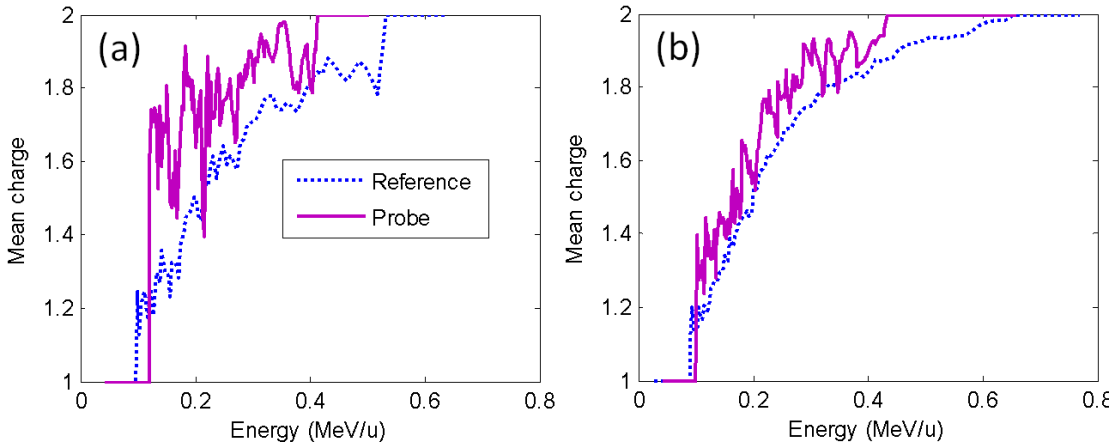

Figure IV-49: Reference and probe helium beam mean charge of two different shots. The probe beam emerges from a cold solid-density aluminum foil.

In Figure IV-50, we compare the equilibrium mean charge in solid-density aluminum we obtained (in a single shot) with the measurements performed in conventional accelerator and the results from ETACHA simulations. These are all found in fair agreement with respect to our experimental error bar. Despite the decrease of the data precision principally due to the scattering of the probe beam when propagating inside the secondary target, we are able to distinguish the equilibrium mean charge in solid-density aluminum from the one in helium gas.

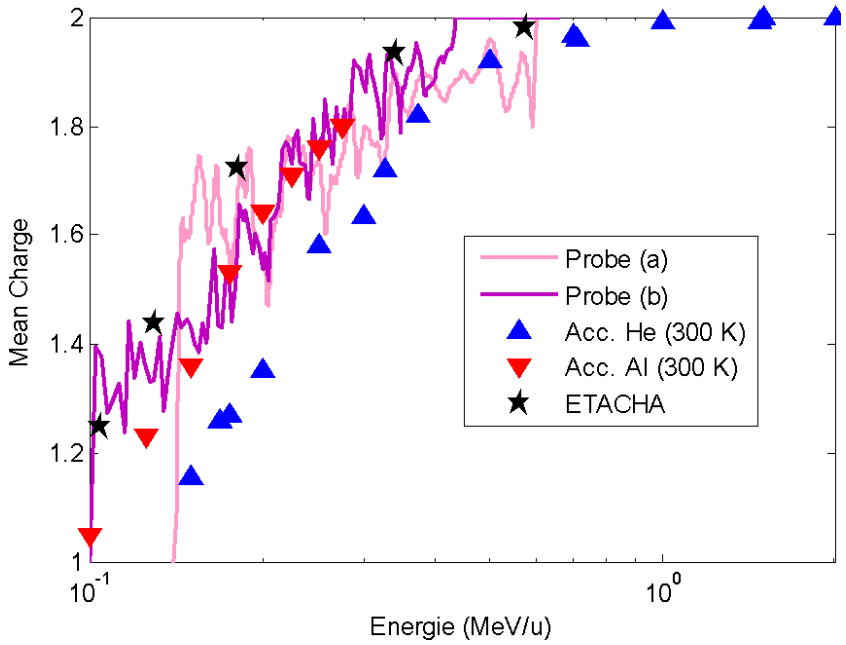

Figure IV-50: Comparison between our experimental measurements in cold solid-density aluminum, ETACHA simulation in aluminum, and accelerator data in aluminum and helium gas. Note that for all curves, the equilibrium mean charge is computed without counting the neutrals.

IV.2.5.5 Conclusion and perspectives

We have demonstrated that we can reproduce well, with our experimental set-up, the data obtained in cold helium gas and in cold solid-density aluminum with accelerators on a single shot for energies from 0.1 to 0.6-0.7 MeV/u. Our measurements in cold solid-density aluminum are also in good agreement with the results of the ETACHA code. Next step is to investigate the results we obtained in heated matter.

IV.3 Summary

In this chapter, the stopping power in WDM was studied from the experimental aspect. First, using stopping power theoretical predictions detailed in chapter II and a hydrodynamic code, we have evaluated the influence of the temperature on the stopping power of protons and carbon ions in solid-density aluminum and determined the conditions for which this effect would be detectable in the frame of our experiments. We concluded this part on the fact that we need to reach temperatures higher than 40 eV and/or to developed ion diagnostics that are better resolved and less sensitive to noise.

Since this was not currently achievable with respect to our current experimental techniques, we have focused our experimental study on an important parameter of the stopping power, i.e., the projectile

charge state distribution inside WDM. This quantity is predicted to be more sensitive to temperature and is easier to measure experimentally.

After recalling the current theories dealing with this quantity, we presented a new experimental set-up we have developed to measure the projectile equilibrium mean charge in WDM. We used simultaneously two high intensity short laser pulse: one was in charge of producing a reference and a probe ion beam, the last propagating through a secondary target. The other was in charge of producing an energetic proton beam that heated the secondary target, creating WDM. We tested this set-up through two experiments. The first, performed at LULI 100 TW facility, consisted of measuring on a single shot the equilibrium mean charge of a carbon beam propagating through either cold or heated solid-density aluminum. We reproduced well the data obtained in cold matter with accelerators and the results of the ETACHA code in its most recent version. This allowed us to validate our experimental set-up. Furthermore, we measured the mean charge state of a carbon beam passing in WDM and have shown that plasma effects in WDM heated up to 1 eV do not significantly impact the mean charge of a 0.04 – 0.5 MeV/nucl carbon beam passing through aluminum. We concluded on the importance of performing similar measurements at higher temperature in WDM, so that we can observe some modifications in the equilibrium mean charge. The second experiment, using the TITAN laser at the Lawrence Livermore National Laboratory, based on the same principle, aimed at measuring the equilibrium mean charge of a helium probe beam propagating through WDM. In this experiment, the helium ion source detailed in chapter III was used to probe cold or heated matter. We established that our helium ion source delivers an ion beam that is equilibrated in helium gas. In addition, we demonstrated that we reproduced on a single shot the mean equilibrium charge in cold solid-density aluminum obtained in accelerator for energies from 0.1 to 0.6-0.7 MeV/u. Again, our measurements in cold solid-density aluminum were also in good agreement with the results of the ETACHA code.

References

[1] F. R. Graziani et al., High Energy Density Phys. **8**, 105 (2012)
[2] L. C. Northcliffe, Ann. Rev. Nucl. Sci. **13**, 67 (1963)
[3] J. F. Ziegler, J. Appl. Phys / Rev. Appl. Phys., **85**, 1249 (1999)
[4] P. Sigmund & A. Schinner, Nucl. Instrum. Meth. Phys. Res. B **174**, 535 (2001)
[5] C. Deutsch et al., Open Plasma Phys. J. **3**, 88 (2010)
[6] A. Frank et al., Phys. Rev. E **81**, 026401 (2010)
[7] T. Heßling et al., Phys. Rev. E **84**, 016412 (2011)

[8] A. Mancic, Ph.D. thesis, École Polytechnique, Palaiseau (2010)
[9] ICRU Report 73, *Stopping Ions Heavier Than Helium* (2005)
[10] J. Ziegler et al., *The Stopping Range of Ions in Solids*, New York: Pergamon Press (1996)
[11] M. Gauthier et al., High Energy Dens. Phys. **9**, 488 (2013)
[12] S. M. Vinko et al., Nature **482**, 59 (2012)
[13] J. P. Colombier et al., Phys. Rev. B **71**, 165406 (2006)
[14] A. V. Bushman et al., Sov. Tech. Rev. B :Therm. Phys. **5**, 1 (1993)
[15] I. N. Lomonosov et al., AIP Conf. Proc. **309**, 117 (1994)
[16] NRL Plasma Formulary (2007)
[17] R. Snavely et al., Phys. Plasmas **14**, 092703 (2007)
[18] G. Zwicknagel et al., Phys. Reports **309**, 117 (1999)
[19] T. Peter & J. Meyer-ter-Vehn, Phys. Rev. A **43**, 1998 (1991)
[20] T. Peter & J. Meyer-ter-Vehn, Phys. Rev. A **43**, 2015 (1991)
[21] H. D. Betz, *Electron Capture*, In: P. Richard, Ed., *Atomic Physics Accelerators* **17**, New York: Academic Press (1980)
[22] J. P. Rozet et al., Nucl. Instr. Meth. Phys. Res. B **107**, 67 (1996)
[23] A. F. Lifschitz & N. R. Arista, Phys. Rev. A **69**, 012902 (2004)
[24] A. Golubev et al., Nucl. Instr. Meth. Phys. Res. A **464**, 247 (2001)
[25] G. Maynard et al., Nucl. Instr. Meth. Phys. Res. B **107**, 51 (1996)
[26] N. V. Novikov et al., J. Phys. Conf. Ser. **194** (2009) - http://cdfe.sinp.msu.ru/services/cccs/cccs.html
[27] H. D. Betz, Rev. Mod. Phys. **44**, 465 (1972)
[28] N. Bohr & J. Lindhard, Mat. Fys. Medd Dan. Vid. Selsk. **28**, 1 (1954)
[29] G. Maynard et al., Nucl. Instrum. Meth. B **164-165**, 139-146 (2000)
[30] S. Della-Negra et al., Phys. Rev. Lett. **58**, 17 (1987)
[31] Electronic stopping-power program CasP, http://www.helmholtz-berlin.de/people/gregor-schiwietz/casp_en.html
[32] V. S. Nikolaev & I. S. Dimitriev, Phys. Rev. Lett. A **28**, 277 (1968)
[33] G. Schiwietz et al., Nucl. Instr. Meth. Phys. Res. B **226**, 683 (2004)
[34] N. Bohr, Phys. Rev. **58**, 654 (1940)
[35] N. Bohr, Phys. Rev. **59**, 279 (1941)
[36] C. J. Schmitt, Ph.D. thesis, University of Notre Dame (2010)
[37] J. P. Rozet et al., Nucl. Instr. Meth. Phys. Res. B **107**, 67 (1996)
[38] C. Scheidenberger et al., Nucl. Instr. Meth. Phys. Res. B **142,** 441 (1998)
[39] H. D. Betz, Rev. Mod. Phys. **44**, 465 (1972)
[40] J. P. Rozet et al., Nucl. Instrum. Methods B **107**, 67 (1996)
[41] C. Couillaud, et al., Phys. Rev. E **49**, 1545 (1994)
[42] S. C. Wilks, et al., Phys of Plasmas **8**, 542 (2001)
[43] G. Dyer et al., Phys. Rev. Lett. **101,** 015002 (2008)
[44] A. Mancic, et al., High Energy Density Phys. **6**, 21 (2010)
[45] H. Ruhl et al., Phys. Plasmas **11**, 5 (2004)
[46] L. Romagnani *et al*., Phys. Rev. Lett. **95**, 195001 (2005)
[47] M. Borghesi et al., Plasma Phys. Contr. Fus. **43**, A267 (2001)
[48] C. Deutsch et al., Open Plasma Phys. J **3**, 88 (2010)
[49] T. Ceccotti et al., Phys. Rev. Lett. **99**, 185002 (2007)
[50] J. P. Colombier et al., Phys. Rev. B **71**, 165406 (2006)
[51] A. Mancic et al., Rev. Sci. Intrum. **79**, 073301 (2008)
[52] D. Doria et al., Central laser Facility, RAL, UK, Annual Report 2009/10, 78
[53] C. G. Freeman, et al., Rev. Sci. Instrum. **82**, 073301 (2011)

[54] A. Maksimchuk et al., Phys. Rev. Lett. **84**, 4108 (2000)
[55] A. Levy et al., Optics Lett. **32**, 310 (2007)
[56] Particle interactions with matter, http://www.srim.org/#SRIM
[57] R. N. Sagaidak & A.V. Yeremin, Nucl. Instrum. Meth. Phy. Res. B **93**, 103 (1994)
[58] G. Schiwietz & P.L. Grande, Nucl. Instr. Meth. B **175-177**, 125 (2001)
[59] A. S. Schlachter et al., Phys. Rev. A **27**, 3372 (1983)
[60] M. Kiisk et al, Nucl. Instrum. Meth. A **481**, 1 (2002)
[61] H. K. Chung et al, High Energy Density Phys. **1**, 3 (2005), http://www-amdis.iaea.org/FLYCHK/RATES/rt.006.dat
[62] P. Antici et al., Phys. Rev. Lett. **101**, 105004 (2008)
[63] M. D. Brown & C. D. Moak, Phys. Rev. B **6**, 90 (1972)
[64] S. Y. Gus'kov et al., Plasma Phys. Rep. **35**, 709 (2009)
[65] M. M. Basko, Fiz. Plazmy **10**, 1195 (1984) [Sov. J. Plasma Phys. **10**, 689 (1984)]
[66] S. Gaillard et al., Rev. Sci. Instrum. **78**, 013304 (2007)

V. CONCLUSION

Determining accurately the stopping power of ions in WDM is important to understand the physics that governs the energy deposition of a projectile in this particular regime, but also in the more practical context of ICF. Several theoretical attempts were made to predict the energy-loss in such a regime, but, due to the experimental complexity especially for matter of density close or higher to solid, these theories have never been tested in this thermodynamic regime. In this thesis, we took advantage of the properties exhibited by laser-produced ion beams to develop and exploit a new experimental platform that gives us the opportunity to study the stopping power of ions in WDM and more particularly the equilibrium charge of the ions in WDM, an important parameter of the stopping power.

The first chapter was aimed at introducing the concept of WDM both from a theoretical and experimental point of view. Two different *ab initio* approaches of WDM, SCAALP and ABINIT, were presented in the scope of being used to evaluate the stopping power in this regime of matter.

In the second chapter, we presented the dielectric theory of the electronic stopping power in a zero-temperature electron gas. Using the method proposed by Wang et al. to extend this *ab initio* theory, to finite temperature and dense matter, we have estimated from the electron density profile obtained with SCAALP and ABINIT the stopping power of proton in cold and heated (solely with SCAALP) solid-density aluminum. Using these results, we employed the approach proposed by Gus'kov et al. to evaluate as well the stopping power of carbon in cold and heated solid-density aluminum.

In the third chapter, the laser-generation of ion beams was studied in order to measure the stopping power in WDM. After recalling the main mechanisms of ion acceleration using a solid-density target and the properties of the generated ion beams, we presented the experimental study of two acceleration mechanisms using lower-than-solid-density targets:

- we demonstrated that, using a helium gas jet as target, we could generate perpendicularly to the laser propagation axis, two similar helium beams of energy cut-off around 1 MeV/u. These beams were used in one of the experiment presented in chapter IV.
- using a solid foil exploded by laser as target, we showed that 3-4 MeV protons can be produced with target having long gradient plasma at the back side. In addition, we observed that

under certain laser and exploded foil conditions, it was possible to accelerate protons to the same energies as using solid-density targets in the standard TNSA mechanism.

In the fourth chapter, using the estimations of the stopping power obtained in chapter II, we showed that to detect in experiment any visible variation of the proton and heavier ion stopping power, we need to heat the matter to a higher temperature than what is currently achievable with our experimental means. Then, we concentrated our study on one important parameter of the stopping power: the equilibrium charge of the projectile. We measured in two different experiments, both of them using two high-intensity short-pulse laser beams, the mean charge of a carbon and helium ion beam equilibrated in cold solid density aluminum for helium and carbon and warm dense aluminum for carbon.

In conclusion, we have shown for the first time that measurements of equilibrium mean charge state of a laser-generated ion beam passing in either cold solid-density or WDM can be realized. This demonstration of feasibility and our promising results open the way for future measurements of equilibrium charge at higher temperature and for different ion species that could be helpful as benchmarks for stopping power calculations in WDM.

In the scope of developing a more systematic method to measure the mean equilibrium charge, some points still need to be improved; all related to the ion sources:

- increasing the number of accelerated ions would give us the opportunity to reach higher temperature (heating beam) and to reduce the imprecision caused by the scattering in the probed target. This can be achieved by either using more energetic laser facilities, or by developing more efficient mechanisms of ion acceleration like the one studied in chapter III, or, only for the heating part, using a more effective method to produce WDM (e.g. X FEL).
- to increase the precision in energy of our measurement and even use our set-up to perform stopping power measurements, a monoenergetic probe beam would be preferable. In this scope, we developed a compact magnetic selector (see Figure V-1) that is able to select an energy band of a laser-generated ion beam [1]. It has already been tested in experiment and shown promising results.

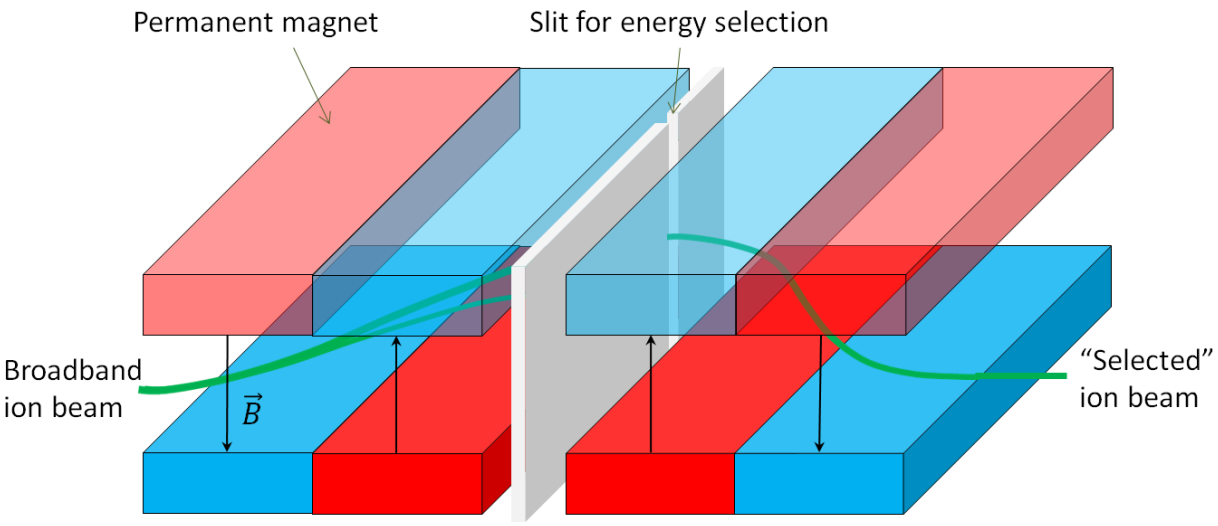

Figure V-1: Scheme of the magnetic selector. Broadband ion beam enters through a 200 mm vertical entrance slit. Then, energy selection is done with the middle slit of 500 mm. The position of the slit in the transverse direction is chosen so that the correct energy is selected. Finally, the "selected" ion beam exits close to the original entrance axis regardless of the energy selected.

References

[1] S.N. Chen et al., Rev. Sci. Instrum. Meth. (submitted)

VI. ROLE OF THE AUTHOR

This thesis, mainly experimental, has been performed in collaboration with several research groups. It is obvious that the numerous tasks necessary to manage the experiments we are dealing with require the contribution of many scientists, without mentioning the technical support brought by the technical team of each laser facility. To that you may add all the work carried out in advance to prepare the experiment and, after the experiment, the necessary and long process of analysis and interpretation of the results. In this paragraph, I describe what were precisely my own involvement and realizations in these studies.

The first chapter centered on how to model WDM and how to generate it in laboratory followed the previous work performed by Ana Mancic in her thesis. My work was therefore limited to a literature research.

In the second chapter, the code in charge of computing the stopping power in warm and hot dense matter, as well as the one used to model WDM, were already developed when I started my thesis. My work has therefore consisted on the discussion and interpretation of the results in collaboration with the CEA team associated to this subject. The code ABINIT was run by the Marc Torrent's team (CEA).

The core of my work and my main contribution to this thesis is included in the third and fourth chapter.

The theories reviewed in these chapters were the fruits of literature research, but more significantly of discussions with the scientists connected to the different domains.

From an experimental point of view, I took an important part in the design of the experiments (e.g. writing of the experimental proposals, designing the diagnostics) and in their routine operations (e.g. target alignment, analysis in real-time of the results and deciding the next steps). Furthermore, an important part of my work was dedicated to the analysis of the results (e.g. development of a Matlab program in charge of analyzing semi-automatically the spectra recorded with TP) and, in a second phase, to the discussion and interpretation of the results in collaboration with the teams associated to the experiments.

Several codes have been used during this thesis in order to predict, analyze the experimental data and interpret the results. I generated a table of proton stopping power on a wide range of density and temperature conditions in aluminum using the method described in chapter II and electron den-

sity profiles obtained with SCAALP. This table has been implemented in the code ESTHER by P. Combis in order to observe the influence of the temperature on the heating of solid-density samples with a laser-generated proton beam (chapter IV). It has also been used to estimate the conditions of the proton-heated targets in experiment. The simulations CHIC 2D and PICLS on ion acceleration (chapter III) performed, respectively, by Philippe Nikolai and Emmanuel d'Humières, were the result of a close collaboration with CELIA (Centre Lasers Intenses et Applications). I also ran the code neutrino, developed by Tommaso Vinci (LULI) to extract the electron density profile from interferometry measurements in chapter III. I ran the code ETACHA to discuss our experimental results on charge equilibration with the support of Jean-Pierre Rozet's and Dominique Verhnet's team (Université Pierre et Marie Curie). The small programs used in chapter IV to estimate the equilibration in a gas or with co-moving electrons were also my doing.

VII. PUBLICATIONS

The following resumes papers that have been published during this thesis with my contribution. They are classified from the most recent to the oldest publication.

1. S. N. Chen, M. Gauthier, R. Riquier, S. Dorard, D. P. Higginson, F. Mangia, J-R Marquès, S. Atzeni and J. Fuchs
   "Monochromatic Short Pulse Laser Produced Ion Beam Using a Compact Passive Magnetic Device"
   Submitted to Rev. Sci. Instrum.

2. M. Gauthier, A. Lévy, E. d'Humières, M. Glesser, B. Albertazzi, J. Breil, C. Beaucourt, S. N. Chen, V. Dervieux, J.L. Feugeas, P. Nicolaï, V. Tikhonchuk, H. Pépin, P. Antici and J. Fuchs
   "Investigation of Efficient Longitudinal Ion Acceleration in Near-Critical Density Targets"
   Submitted to Phys. Plasmas

3. A. Lévy, P. Audebert, R. Shepherd, J. Dunn, M. Cammarata, O. Ciricosta, F. Deneuville, F. Dorchies, M. Fajardo, C. Fourment, D. Fritz, J. Fuchs, J. Gaudin, M. Gauthier, A. Graf, H. J. Lee, H. Lemke, B. Nagler, J. Park, O. Peyrusse, A. B. Steel, S. M. Vinko, J. S. Wark, G. O. Williams and R. W. Lee
   "The Creation of Large-Volume, Gradient-Free Warm Dense Matter with an X-ray Free-Electron Laser"
   Submitted to Phys. Rev. Lett.

4. L. Lancia, C. Fourment, J. J. Santos, J.-L. Feugeas, C. Fourment, Ph. Nicolaie, G. Schurtz, M. Nakatsutsumi, S. Hulin, S. Bastiani-Ceccotti, M. Gauthier, M. Le Gloahec, P. Audebert and J. Fuchs
   "Simultaneous Measurement of Self-Generated Magnetic Fields and Electron Heat Transport in Dense Plasma"
   Accepted to Laser Part. Beams

5. M. Gauthier, C. Blancard, S.N. Chen, B. Siberchicot, M. Torrent, G. Faussurier and J. Fuchs
   "Stopping Power Modeling in Warm and Hot Dense Matter"

High Energy Dens. Phys. **9**, 488 (2013)

6. G. Faussurier, C. Blancard and M. Gauthier
   "Nuclear Stopping Power in Warm and Hot Dense Matter"
   Phys. Plasmas **20**, 012705 (2013)

7. M. Gauthier, S. N. Chen, A. Levy, P. Audebert, C. Blancard, T. Ceccotti, M. Cerchez, D. Doria, V. Floquet, E. Lamour, C. Peth, L. Romagnani, J-P. Rozet, M. Scheinder, R. Shepherd,T. Toncian, D. Vernhet, O. Willi, M. Borghesi, G. Faussurier and J. Fuchs
   "Charge Equilibrium of a Laser Generated Carbon Ion Beam in Warm Dense Matter"
   Phys. Rev. Lett. **110**, 135003 (2013)

8. Hui Chen, A. U. Hazi, R. van Maren, S. N. Chen, J. Fuchs, M. Gauthier, S. Le Pape, J. R. Rygg and R. Shepherd
   "An Imaging Proton Spectrometer for Short-Pulse Laser Plasma Experiments"
   Rev. Sci. Instrum. **81**, 10D314 (2010)

VIII. APPENDIX

VIII.1 Thomson parabola

A Thomson Parabola is a diagnostic that aims at measuring the energetic spectrum of the different ions contained in an ion beam. In practice, only different charge-to-mass ratio ions can be separated. For instance, C^{6+} and He^{2+} cannot be distinguished with this diagnostic. The principle is the following: each ion of the beam is deflected (along the x-axis in Figure VIII-1) by a constant magnetic field built up by two magnets inside a yoke, the deflection depending on the energy and the charge-to-mass ratio of the ion. Then each ion passes between two electric plates and the constant electric field deflects it along the orthogonal direction with respect to the previous direction of deflection (along the y-axis in Figure VIII-1), so that the different traces drawn by the deflected ions hitting the detector can be differentiated. In order to retrieve the different spectra from the image obtained on the detector, we use the theoretical equations of the ion motions.

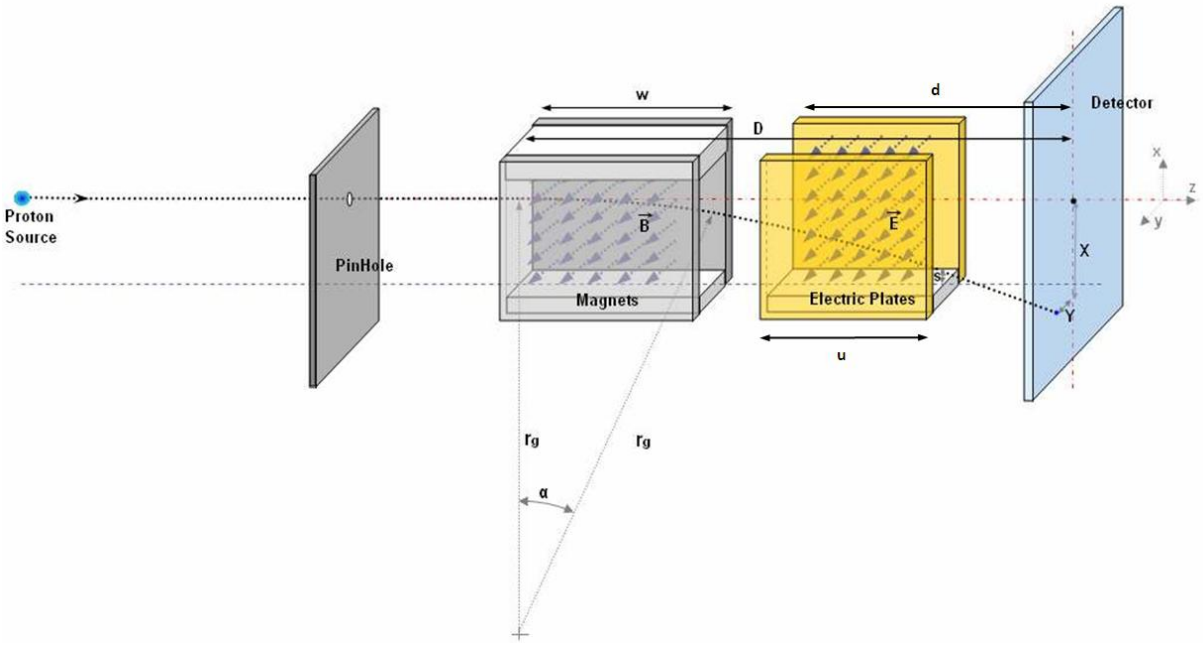

Figure VIII-1: Illustration of a Thomson Parabola [courtesy of Domenico Doria].

VIII.1.1 Theoretical equations

Let us now go through the calculations. In the first part of the trajectory, the particle of mass m and charge Q and velocity v_0 goes through a constant magnetic field, B_0. We fix its coordinates at (0,0,0) just before it passes through the magnetic field. Its equation of motion is:

$$m\frac{d}{dt}\begin{pmatrix}\dot{x}\\ \dot{y}\\ \dot{z}\end{pmatrix} = Qe\left(\vec{v}\times\vec{B}_0\right) = QB_0e\begin{pmatrix}-\dot{z}\\ 0\\ \dot{x}\end{pmatrix}. \tag{8.1}$$

where $\dot{x} = \frac{dx(t)}{dt}$. This gives,

$$\begin{aligned} y &= 0,\\ \frac{d\dot{x}}{dt} &= -\omega_c\dot{z},\\ \frac{d\dot{z}}{dt} &= \omega_c\dot{x}, \end{aligned} \tag{8.2}$$

where $\omega_c = \frac{QB_0}{m}$. We integrate the second equation and use it to remove the $\dot{x}$ term in the third equation,

$$\begin{aligned} \dot{x} &= -\omega_c z,\\ \ddot{z} &= -{\omega_c}^2\, z. \end{aligned} \tag{8.3}$$

We can integrate both equations giving,

$$\begin{aligned} z(t) &= r_g\sin(\omega_c t)\,,\\ x(t) &= -r_g(1-\cos(\omega_c t)), \end{aligned} \tag{8.4}$$

where $r_g = \frac{v_0}{\omega_c}$ is the curvature radius of the trajectory. At the end of the yoke ($z = w$), the particle is located at coordinates $\left(\sqrt{{r_g}^2 - w^2} - r_g, 0, w\right)$ and its velocity vector is $\left(-\omega_c w, 0, \omega_c\sqrt{{r_g}^2 - w^2}\right)$.

For $z > w$, the particle is no longer deflected by the magnetic field and propagates freely until reaching the electric plates. Furthermore, since the force associated with the electric field produced by the electric plates is collinear to the y-axis, it does not have any influence on the motion of the projectile along the x and z-axis. Hence, the particle propagates at constant speed along those axes. We can easily calculate the coordinates where the projectile hit the detector along x- and z-axis:

$$\begin{aligned} z &= D,\\ x &= \sqrt{{r_g}^2 - w^2} - r_g - \frac{w(D-w)}{\sqrt{{r_g}^2 - w^2}}. \end{aligned} \tag{8.5}$$

The equation of motion along the y-axis of the particle passing between the two electric plates producing a uniform electric field E_0 is given by,

$$m\ddot{y} = QE_0, \tag{8.6}$$

which gives after integration,

$$y(t') = \frac{1}{2}a_E t'^2, \tag{8.7}$$

where $a_E = \frac{QE_0}{m}$. The position and the velocity along the y-axis of the particle at the end of the electrode ($\dot{z} * t' = u$, with $\dot{z} = \omega_c\sqrt{{r_g}^2 - w^2} = cste$) is then given by,

$$y = \frac{1}{2}a_E\left(\frac{u}{\omega_c\sqrt{{r_g}^2 - w^2}}\right)^2, \dot{y} = \frac{a_E u}{\omega_c\sqrt{{r_g}^2 - w^2}}. \tag{8.8}$$

After having passed between the two electric plates, the particle is no longer deflected by the electric field and propagates freely until hitting the detector. It hits the detector at:

$$\begin{aligned} y = \frac{1}{2}a_E\left(\frac{u}{\omega_c\sqrt{{r_g}^2 - w^2}}\right)^2 \\ + a_E\left(\frac{u}{\omega_c\sqrt{{r_g}^2 - w^2}}\right)\frac{(d - u)}{\sqrt{{r_g}^2 - w^2}} \\ = \frac{a_E u}{\omega_c\left({r_g}^2 - w^2\right)}\left(\frac{u}{2\omega_c} + (d - w)\right), \end{aligned} \tag{8.9}$$

Therefore the particle hits the detector at coordinates (the origin corresponds to the 0th order):

$$\boxed{\begin{aligned} x &= \sqrt{{r_g}^2 - w^2} - r_g - \frac{w(D - w)}{\sqrt{{r_g}^2 - w^2}}, \\ y &= \frac{a_E u}{\omega_c\left({r_g}^2 - w^2\right)}\left(\frac{u}{2\omega_c} + (d - w)\right). \end{aligned}} \tag{8.10}$$

Note that for $r_g \gg w$, i.e., the curvature radius is much longer than the length of the magnet, an ion beam with a broad spectrum traces a parabola (from which the name of the diagnostic comes) on the detector:

$$y \cong \alpha\left(\frac{Q}{m}\right)x^2, \tag{8.11}$$

where α is a function decreasing with the ion charge-to-mass ratio, Q/m.

Note that the increase of the particle energy due to the work of the electric force is negligible with respect to other uncertainties such as distances or magnitudes of the fields (around 0.01 % of its initial energy for typically $E_0 = 5 \times 10^5 V/m,\ B_0 = 0.5\ T,\ u = 5\ cm,\ w = 5\ cm,\ m = m_{proton},\ Q = 1$).

Furthermore, it is quite simple to treat the "relativistic" case. Since the energy of the particle is practically constant, the Lorentz factor is a constant along the particle path depending only on the initial energy of the particle. Then, all we have to do is to replace the mass by its relativist counterpart (the changes are in bold):

$$\boxed{\begin{aligned} x &= \sqrt{\boldsymbol{\gamma}^2 {r_g}^2 - w^2} - \boldsymbol{\gamma} r_g - \frac{w(D - w)}{\sqrt{\boldsymbol{\gamma}^2 {r_g}^2 - w^2}}, \\ y &= \frac{a_E u}{\omega_c\left(\boldsymbol{\gamma}^2 {r_g}^2 - w^2\right)}\left(\frac{u\boldsymbol{\gamma}}{2\omega_c} + (d - w)\right). \end{aligned}} \qquad (1.1)$$

This effect is also negligible in our case: for instance, the relativistic corrections on the coordinates for a 10 MeV protons would be below 0.02% for the typical Thomson parabolas we used (e.g. $E_0 = 5 \times 10^5\ V/m,\ B_0 = 0.5\ T,\ u = 5\ cm,\ w = 5\ cm,\ m = m_{proton},\ Q = 1, D = 20\ cm, d = 10\ cm$)

VIII.1.2 Calibration

In order to estimate the magnetic field inside the TP, we use filters of different thickness in front of the detector to get the coordinates where protons of well-defined energy are hitting the detector. In Figure VIII-2 is shown the calibration curve obtained for the TP located at the rear side of the target. From the calibration points (blue) and the error-bar estimated taking into account the size of the pinhole and the quality of the signal, we find a magnetic field of 0.354 T +/- 0.005 T: all the calibrations points taking into account their error-bar are contained within the zone between the minimum (0.354-0.005 T) and maximum (0.354+0.005 T) magnetic field curves. These values are in fair agreement with the measure we have performed directly on the Thomson parabola ($\approx 0.28\ T$). The difference observed between the measurements and the calibration comes from the assumptions we have made on the magnetic field: in reality, the magnetic field is not uniform and not limited to the size of the magnets. However, this simple calibration allows us to determine the energy of a particle hitting the detector in this experiment with a precision of approximately 2.5 % on the energy.

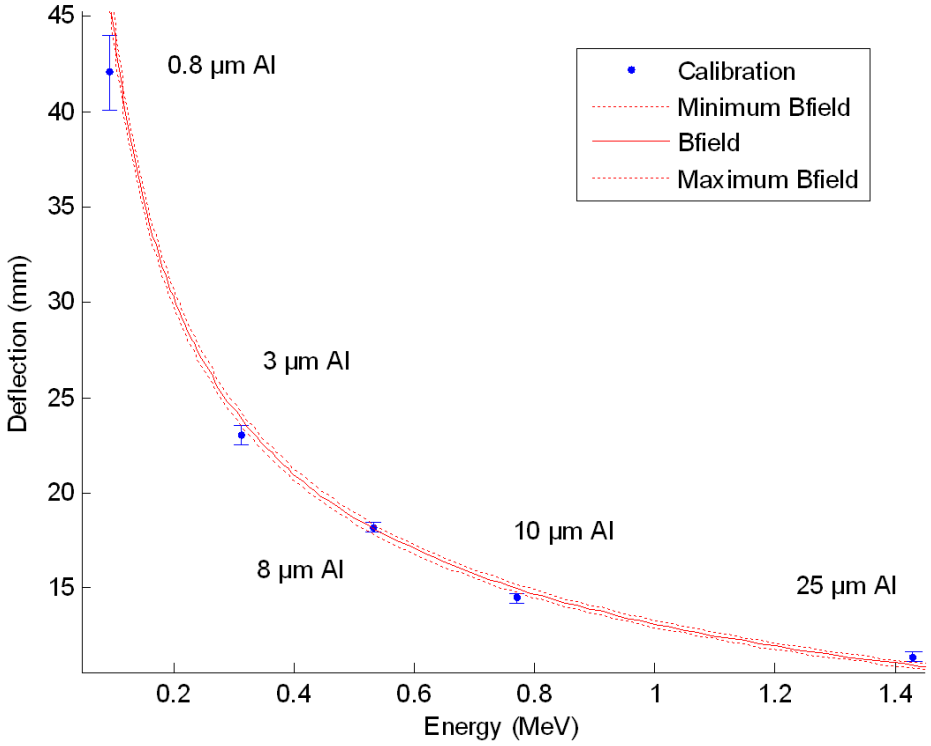

Figure VIII-2: Calibration curve of the Thomson Parabola located at the rear side of the target for the experiment on the equilibrium charge state distribution of carbon. The filters used were 0.8, 3, 8, 10 and 25 µm aluminum foils.